Prediction of Seismic Demands in Building Structures

by

EROL KALKAN

B.S. (Middle East Technical University) 1998

M.S. (Bogazici University) 2001

M.S. (Middle East Technical University) 2001

DISSERTATION

Submitted in partial satisfaction of the requirements for the degree of

DOCTOR OF PHILOSOPHY

in

CIVIL AND ENVIRONMENTAL ENGINEERING

in the

OFFICE OF GRADUATE STUDIES

of the

UNIVERSITY OF CALIFORNIA

Davis

Approved:

_____

Sashi K. Kunnath (Chair)

_____

Rob Y.H. Chai

_____

Amit Kanvinde

Committee in Charge

2006

Erol Kalkan
March 2006
Civil and Environmental Engineering

Prediction of Seismic Demands in Building Structures

ABSTRACT

The precise characterization of ground motions incorporating site, source, distance and other effects and the accurate prediction of seismic demands at the component and system level are essential requisites for advancing performance-based design and evaluation methodologies. This research effort focuses on issues related to ground motion characteristics with particular emphasis on near-fault records and its interrelationship with seismic demand and ultimately in developing enhanced procedures for estimating deformation demands in structures for performance-based evaluation. Recent earthquakes have revealed an enhanced level of hazard imposed by ground motions recorded in the vicinity of causative faults associated with directivity effects. Both forward-rupture directivity and fling effects produce ground motions characterized by a strong pulse or series of pulses of long period motions. To highlight their potential damaging effects on building structures, the energy content of near-fault records were investigated by devoting special attention to forward-rupture directivity and fling effects and the influence of apparent acceleration pulses. A new demand measure called the effective cyclic energy (ECE) is developed and defined as the peak-to-peak energy demand imparted to structural systems over an effective duration that is equivalent to the time required for reversal of the system effective velocity. This energy term led to the

evolution of a non-dimensional response index (γ_{eff}) as a new descriptor to quantify the destructive power of near-fault records. Based on validation studies conducted on numerous instrumented buildings, the ECE spectrum is proposed to estimate the input energy demand of multi-degree-of-freedom (MDOF) systems without performing nonlinear-time-history (NTH) analysis. In the final phase of the study, a new pushover analysis methodology derived from adaptive modal combinations (AMC) is developed to predict seismic demands in buildings. This procedure integrates concepts built into the capacity spectrum method recommended in ATC-40 (1996), the adaptive method originally proposed by Gupta and Kunnath (2000) and the modal pushover analysis advocated by Chopra and Goel (2002). A novel feature of the procedure is that the target displacement is estimated and updated dynamically during the analysis by incorporating energy based modal capacity curves in conjunction with constant-ductility demand spectra. Hence it eliminates the need to approximate the target displacement prior to commencing the pushover analysis. The methodology was applied to several vertically regular instrumented steel and reinforced concrete (RC) moment-frame buildings, and also validated for code-compliant vertically irregular steel and RC moment frame buildings. The comprehensive evaluation study including individual and statistical comparisons with benchmark responses obtained from NTH analyses demonstrate that the AMC procedure can reasonably estimate key demand parameters such as roof displacement, interstory drift, plastic rotations for both far-fault and near-fault records, and consequently provides a direct reliable tool for performance assessment of building structures.

This dissertation is dedicated to my parents, my wife "Narmina" and my sons "Ediz and Ronan". Their constant love and caring are every reason for where I am and what I am.

ACKNOWLEDGEMENTS

The research described herein could not have been possible without the generous support of my advisor, Prof. Sashi Kunnath. I would like to express my deepest gratitude to him for providing me with his sound and critical perspective and being a true mentor and model during my studies. I am truly indebted to him for providing me an environment to think creatively and cover different aspects of earthquake engineering problems. I also greatly appreciate the opportunities he has given me to become involved with other aspects of his work, broadening my overall scientific experience. He has contributed to this work by providing innumerable ideas and exciting intellectual challenges. Many thanks to his objective thinking, open-mind and friendship, working with him has always been a real pleasure and invaluable experience for me.

I would also like to thank Prof. Rob Chai for chairing my qualifying examination committee, providing generous support and invaluable comments during my research study. Also special thanks to Prof. Kanvinde for being always helpful to me, reviewing this dissertation and for his comments. Sincere thanks are extended to Prof. Boris Jeremic for his encouraging and continuous support throughout my PhD research.

The research study described in this dissertation was funded by the National Science Foundation under Grant number CMS-0296210, as part of the US-Japan Cooperative Program on Urban Earthquake Disaster Mitigation. This support is also gratefully acknowledged.

Lastly, but not last, I would like to acknowledge the love, continuous support, encouragement throughout my life of my parents and my brother.

My deep and greatest thanks go to my wife, Narmina, for her incredible support and companionship, her understanding and restless help as I pursued my doctoral degree. She was always there every step of the way with her inconceivable love. Also, a big “thank you” to numerous friends and colleagues who made my life at Davis enjoyable and meaningful.

TABLE OF CONTENTS

LIST OF FIGURES

LIST OF TABLES

CHAPTER 1

INTRODUCTION

1.1 BACKGROUND AND MOTIVATION

Among the key components in performance-based seismic evaluation are the accurate identification of seismic hazard and the estimation of associated seismic demands. The specification of seismic hazard in zones that are close to the causative faults of medium to large magnitude earthquakes should account for the special characteristics of near-fault ground motions. Of particular importance in the near-fault region are the effects of forward directivity and fling. Both directivity effects produce ground motions characterized by a strong pulse or series of pulses of long period motions. In recent years, many efforts have been devoted to the characterization of forward-directivity and fling motions (e.g., Somerville et al. 1997, Krawinkler and Alavi 1998; Sasani and Bertero 2000; Kalkan et al. 2004, Pamuk et al. 2005). These studies have highlighted the potential damaging effects of impulsive motions. Building on this understanding, more research is clearly needed to fully account for the detrimental impacts of near-fault ground motions on engineered structures.

Nonlinear static procedures (NSPs) are now prevalently used in engineering practice in lieu of nonlinear-time-histroy (NTH) analysis for the prediction of seismic demands in building structures. In the simplified version of NSP, a mathematical model of the

building is subjected to monotonically increasing invariant height-wise distribution of lateral forces until a predetermined target displacement is reached. The target displacement is currently determined from procedures derived using an equivalent SDOF system. Although NTH analysis is the most rigorous procedure to evaluate the seismic demands of buildings structures, it is relatively complex and onerous for routine applications due to the fact that NTH analyses require an ensemble of ground motions and an associated probabilistic assessment to account for aleatoric variability in earthquake recordings. On the other hand, NSP offers a major advantage over NTH that in NSP, demands can be computed directly from a site-specific hazard spectrum. This feature makes NSP an attractive proposition for practitioners. However, there are still several unresolved issues in identifying appropriate lateral load patterns to be used in NSPs. Current structural engineering practice uses invariant load distributions described in ATC-40 or FEMA-356. While those invariant load distributions (such as inverted triangle, uniform, or mass proportional) are based on the assumption that the response is primarily in its fundamental mode of vibration, it can lead to incorrect estimates for structures with significant higher mode contributions. This accentuates the need for improved procedures that addresses current drawbacks in the lateral load patterns that are used in pushover analyses. Recently, several improved pushover procedures have been proposed (e.g., Chopra et al. 2002; Jan et al. 2003; Chopra et al. 2004) to account for higher mode effects while retaining the simplicity of invariant load patterns. These procedures utilize the concept of modal combinations either through a single pushover analysis where the load vectors reflect the contributions from each elastic modal shape considered (for example, the upper-bound pushover analysis of Jan et al. 2003) or

through multiple pushover analyses using invariant load patterns based on elastic mode shapes where the contribution from each mode is combined at the end such as the modal-pushover-analysis (MPA) of Chopra and Goel (2002). Recently, a modified version of MPA (MMPA) has been proposed in which the inelastic response obtained from first-mode pushover analysis has been combined with the elastic contribution of higher modes (Chopra et al. 2004). Although, these procedures have been shown to provide more accurate estimates of interstory drift values than conventional NSPs using inverted triangular, uniform or other lateral load patterns based on direct modal combination rules suggested in FEMA-356, none of them can account for the redistribution of inertia forces due to structural yielding and the associated changes in modal attributes of the structure. To overcome these limitations, force-based and displacement–based adaptive pushover methodologies emerged to follow more closely the time-variant distributions of inertia forces (e.g., Gupta and Kunnath 2000; Elnashai 2000; Antoniou et al. 2000; Aydinoglu 2003, Antoniou and Pinho 2004).

Recognizing the merits and limitations of all existing methodologies, there is still a need for a conceptually robust and practically applicable adaptive pushover procedure that can particularly eliminate the use of elastic system attributes as well as approximations in target displacement computation (as described in the Displacement Coefficient Method of FEMA-356) or iterative performance evaluation procedures (as applied in the Capacity Spectrum Method of ATC-40). Such an improved adaptive procedure should also be applicable for a variety of regular and irregular, steel and concrete building structures.

1.2 OBJECTIVES

The objectives of this dissertation can be summarized as follows:

1. Evaluate the underlying assumptions, approximations and limitations of current methodologies presented in ATC-40 and FEMA-356 to estimate seismic demands in building structures.
2. Ascertain the validity of using static methods to compute dynamic demands by comparing nonlinear static responses with nonlinear time-history analyses.
3. Characterize near-fault ground motions in terms of their directivity effects and investigate the energy content of these impulsive records.
4. Quantify the damaging potential of near-fault ground motions in comparison to far-fault accelerograms through nonlinear-time-history analyses conducted on a wide range of buildings.
5. Correlate the maximum system deformation to seismic input energy input for near-fault ground motions for both SDOF and MDOF systems.
6. Develop a new adaptive pushover methodology and evaluate its ability and accuracy in estimating seismic demand parameters of both regular and vertically irregular frame buildings.
7. Compare the predictions of the proposed pushover methodology to other approaches and to results obtained from detailed time-history analyses for far-fault and near-fault ground motions.

1.3 REPORT ORGANIZATION

This dissertation is organized into nine chapters. ***Chapter One*** outlines some of the major issues in ground motion characterization and the prediction of seismic demand in building structures, and presents the motivating factors behind this research study.

Chapter Two investigates the correlation between demand estimates for various lateral load patterns used in nonlinear static analysis. It also examines the rationale for using component demands over story and system demands. The results reported in this chapter are based on a comprehensive set of pushover and nonlinear time-history analyses carried out on generic eight and twelve story steel and concrete moment frames. Findings from this study point to inconsistencies in demands predictions of different lateral load patterns used in pushover analysis and also highlight the critical issues in the current understanding of local demand estimates using FEMA-based NSPs.

Chapter Three investigates the consequences of well-known characteristics of pulse-type motions on seismic response of moment-frame buildings. The severity of inelastic demands is evaluated for three existing steel buildings subjected to near-fault ground motions having fling and forward directivity, and compared to their response to far-fault ground motions. Additionally, idealized pulses are utilized to gain further insight into the effects of high amplitude pulses on structural demands. Simple input pulses are also synthesized to simulate artificial fling effects on ground motions originally having forward directivity.

Chapter Four presents the general issues in demand estimates and ground motion characterization. Energy contents of SDOF and MDOF systems subjected to an ensemble

of ground motions from different seismic source characteristics are studied comprehensively using absolute and relative energy formulations. This chapter emphasizes the significance of local distinctive acceleration pulses that are more critical than long period velocity pulses contained in near-fault accelerograms, and investigates the abrupt energy spikes created by these pulses. The differences between two energy formulations are investigated using ground motions having distinct acceleration pulses and records without a distinguishable pulse.

In ***Chapter Five***, the maximum deformation of a structural system is related to a new measure termed "effective cyclic energy" (ECE). The intensity of this energy measure is evaluated for cyclic or impulsive ground motions using inelastic SDOF systems for a wide range of spectral periods, different hysteretic rules and ductility levels. This chapter also describes the development of a non-dimensional response index (γ_{eff}) as a new descriptor to quantify the severity of ground motions. Its accuracy and stability is examined, in a comparative way, for different types of near-fault recordings and also against commonly used response indices.

Chapter Six describes the development and fundamental precepts of a new direct adaptive pushover methodology referred to as Adaptive Modal Combination (AMC). In this chapter, the accuracy of the AMC procedure for predicting seismic performance of building structures is validated using two instrumented moment frame buildings.

Chapter Seven presents a more comprehensive evaluation of the AMC procedure. The capabilities of the proposed adaptive pushover methodology are compared with other FEMA and enhanced pushover methodologies in predicting the salient response characteristics of steel and reinforced concrete (RC) buildings. A comprehensive set of

NTH analyses are conducted to produce benchmark responses against which to compare the predictions of various NSPs. An array of time-series from ordinary far-fault records and near-fault motions having fling and forward directivity is employed to consider the aleatoric uncertainty in ground motions.

Chapter Eight evaluates the accuracy of the AMC procedure in estimating seismic demands of vertically irregular frames designed according to IBC2000 provisions, and presents the corresponding response statistics of pushover and time-history analyses.

Chapter Nine presents a summary of results and findings from this study. It also includes recommendations for future research.

CHAPTER 2

EVALUATION OF SEISMIC DEMANDS USING NONLINEAR PROCEDURES IN MULTISTORY STEEL AND CONCRETE MOMENT FRAMES

2.1 INTRODUCTION

It is now widely recognized that the concepts and guidelines embodied in FEMA-356 contain the essential ingredients of a performance-based seismic design (PBSD) procedure. Though this document was developed for use in seismic rehabilitation of existing buildings, the key elements of the methodology are designed to accommodate the provisions of a future performance-based standard. FEMA-356 is essentially a deterministic approach to PBSD. FEMA-350 (2000), on the other hand, is a guideline for new steel construction and contains a probabilistic approach to performance assessment. ATC-40 (1996) shares many common elements with FEMA-356 but is limited in scope to reinforced concrete buildings. There are other ongoing efforts to expand and enhance existing FEMA-356 guidelines (such as the ATC-58 effort) or to develop an entirely new methodology (such as the collaborative effort within the Pacific Earthquake Engineering Research [PEER] center). Though there are intrinsic differences in the various methods, they all share some common elements that are outlined below.

2.1.1 Performance Objectives

A performance objective may be regarded as the first element in PBSD and is composed of two parts: a performance level and a hazard level which describes the expected seismic load at the site. Terms such as Collapse Prevention (CP) and Life Safety (LS) are examples of performance levels. In the probabilistic format of the PEER methodology, a decision variable (such as dollar loss or downtime) is used to quantify the performance objective. Hazard levels are typically prescribed in terms of response spectra and are controlled by site characteristics. If time histories are used to evaluate the performance of a building, then the selected records must possess characteristics (including source mechanism and fault distance) equivalent to those that control the design spectra. FEMA-356 specifies the following three hazard levels:

- *Hazard Level I (Service Level Earthquake)* – A relatively frequent earthquake with a 50% probability of being exceeded in 50 years.
- *Hazard Level II (Design Level Earthquake)* – Earthquakes at this level of hazard are normally assumed to have a 10% probability of being exceeded in 50 years.
- *Hazard Level III (or a Maximum Credible Level Earthquake)* – The maximum credible event at the site with a 2% probability of being exceeded in 50 years.

2.1.2 Demand Prediction

The next step in a performance-based evaluation is the estimation of seismic demands in both structural and non-structural elements in the structure due to the imposed earthquake loads. The prediction of deformation demands is arguably the most critical step in PBSD.

Determining demands necessitates the development of a structural model of reasonable complexity. Errors in estimating the demand as a result of an inadequate structural model can propagate through and lead to misleading conclusions on the performance of the structure. FEMA-356, for example, prescribes four different analytical procedures to estimate demands in a building. This chapter is concerned primarily with nonlinear procedures and the differences between static and dynamic methods to estimate seismic demands.

2.1.3 Performance Assessment

In this third and final phase of the procedure, the seismic demands computed in the previous step are compared with acceptable levels of damage for various performance states. Performance measures are typically derived from experimental evidence which quantify a damage state with a demand value. Though this chapter is not concerned with acceptance criteria, findings from the study shed light on the conceptual basis for developing such criteria when using nonlinear analysis procedures.

2.1.4 Establishing Seismic Demands Using Nonlinear Procedures

It becomes evident from the three elements of PBD outlined above that the determination of seismic demands is a critical step in the overall process. Demands can be evaluated using linear or nonlinear procedures. FEMA-356, for example, lists four different analytical methods to evaluate demand. Since seismic forces at the design event are expected to result in nonlinear structural behavior, it is reasonable to expect nonlinear procedures to be used in calculating element deformation demands. Of the two nonlinear

methods, static procedures involving pushover analyses are obviously going to be favored over time-history procedures by design practitioners. Hence, the focus of this study revolves around the consequence of using pushover methods in seismic demand estimation.

Early literature predating FEMA-356 on nonlinear lateral load analysis include the work of Freeman (1978), Fajfar and Fichinger (1988) and Eberhard and Sozen (1993). Since the publication of FEMA-356, pushover methods have been the subject of several investigative studies (Krawinkler and Seneviratna 1998; Tso and Moghadam 1998; Satyarno et al. 1998; Wight et al. 1999; Mwafy and Elnashai 2001). Studies by Kunnath and Gupta (2000), Kunnath and John (2000) and Kalkan and Kunnath (2004) have investigated different lateral load patterns recommended in FEMA-356 and identified inconsistencies in the different pushover procedures currently in use. Previously, Iwan (1999) demonstrated the inability of pushover methods to predict demands for pulse-like near fault ground motions. A well-known issue with a pushover analysis using standard lateral load configurations (such as an inverted triangular or a uniform distribution) is that it fails to account for certain critical higher mode contributions. The drawbacks in pushover methods using invariant FEMA-based lateral load patterns have led to alternative pushover strategies. The multi-mode pushover (Sasaki et al. 1998) tries to incorporate higher modes by considering multiple pushover curves derived from different modal force patterns. The *Adaptive Pushover Method* developed by Gupta and Kunnath (2000) uses a varying load pattern that pushes and pulls the structure by combining modes at different stiffness states of the structure. More recently, Chopra and Goel (2002) proposed a modal pushover technique that combines the response of individual

modal demands (though only the first few modes are typically needed) with reasonable success.

2.1.5 Objectives and Scope

The objective of the study described in this chapter stems from the rapid popularity of pushover analysis in engineering practice facilitated in large part by the availability of nonlinear static procedures in commercial software such as SAP2000 (Computers and Structures 2005). While nonlinear procedures do represent a significant advance in the current state-of-the-practice in seismic design, it is important to recognize and document the inherent limitations in pushover methods. Ultimately, the objective of a seismic evaluation is to identify deformation demands in structural components during an earthquake and whether these demands will exceed the capacity of the element. Traditional design practice (using R-factors) examines the overall response of the system in terms of base shear and roof displacement implying that local demands are controlled by global demands. The advent of pushover procedures facilitates the estimation of demand at both global and local levels thereby providing a means of validating this assumption. But a pushover procedure is a static method. Hence, in the first part of this chapter, nonlinear static responses are compared with nonlinear time-history analyses to ascertain the validity of using static methods to compute dynamic demands. The comparison is carried out for interstory drift demands and local component demands. More importantly, three different lateral load configurations suggested in FEMA-356 are used for the pushover analyses. This is followed by a more detailed examination of local

deformation demands and the implications of cumulative damage resulting from cyclic loading. The study is limited to regular medium-rise moment frame buildings.

2.2 DESCRIPTION OF BUILDINGS USED IN EVALUATION

The findings reported in this study are based on nonlinear static and dynamic analysis of steel and reinforced concrete moment frame buildings. Both designs are based on configurations presented in the SEAOC Seismic Design Manual (SEAOC 2000). The original design of the steel frame presented in the manual pertains to a four-story building. In this study, the same floor plan is extended to eight and twelve stories. The concrete building in the original SEAOC manual is a seven-story structure. Here, the same building plan is used to develop designs for eight and twelve story buildings. The designs satisfy the minimum requirements of the Uniform Building Code (ICBO 1997) which contain provisions for limiting interstory drift and ensuring a strong-column weak-beam connection. No enhanced provisions (such as the principles of capacity design used in New Zealand) are incorporated in the final designs.

2.2.1 Steel Moment Frame Buildings

The floor plan of the building is shown in Figure 2.1(a). There are seven bays in the EW direction and 5 bays in the NS direction of the building covering a total plan of 55.8 m by 37.5 m. The first floor is 4.5 m high and the remaining floor heights are 4.1 m. Member sizes for both the 8-story and 12-story frames are provided in Table 2.1. The lateral force resisting system in each case is a perimeter moment frame. The interior frames are

designed to carry gravity loads and are pinned at the base. Exterior frames columns are supported on piles and they are assumed to be fixed at the ground level. The design roof dead load is 9194 kN (2066 kips) and the dead load of each floor is 9945 kN (2235 kips). The yield strength of steel is assumed to be 344.75 MPa (50 ksi) for all structural members of the building. The design base shear for both the eight and twelve story structures is approximately 4.8% of their respective building weights.

2.2.2 Concrete Moment Frame Buildings

The plan and elevation of a typical frame is displayed in Figure 2.1(b). Only a typical frame in the long (EW) direction along line A (Figure 2.1(b)) is evaluated in this study. Section properties of the beams and columns that constitute this frame are itemized in Table 2.2 for both the eight and twelve story structures. Each bay in both directions span approximately 9.1 m (30 ft.). The height of the first floor is 4.3 m while the remaining floors are 3.66 m each. The roof weight of the building is based on a uniformly distributed load of 7.55 kN/m2 and typical floor weights are determined from 8.9 kN/m2. Like the steel building, each frame in the RC structure is designed to UBC97 standards for Seismic Zone 4, standard occupancy, Seismic Source Type A (capable of high-magnitude frequent events), and UBC soil profile type S_D (stiff soil with a shear wave velocity between 183 m/s and 365 m/s).

2.3 DEVELOPMENT OF BUILDING MODELS

Since both structures are essentially symmetric, it was necessary to model only a typical two-dimensional frame without affecting the outcome of the study. Two-dimensional

computer models of each building frame were developed for use with OpenSees (2005). The current version of OpenSees includes a general model-builder for creating two and three-dimensional frame and continuum models using a scripting language called TCL. A typical frame is modeled as a two-dimensional framework of beams and columns. Beams and columns are modeled using force-based nonlinear beam column elements that consider the spread of plasticity along the length of the element. The integration along the element is based on Gauss-Lobatto quadrature rule. A fiber section model at each integration point, which in turn is associated with uniaxial material models and enforces the Bernoulli beam assumption for axial force and bending, represents the force-based element. Centerline dimensions were used in the element modeling for all cases. For the time-history evaluations, one half of the total building mass was applied to the frame distributed proportionally to the floor nodes.

The evaluation of the steel buildings is based on the response of a typical perimeter frame in the north-south direction. As indicated in Figure 2.1(a), this frame consists of five bays with two exterior spans of 5.94 m and three interior spans of 8.53 m. Each beam section is discretized into a series of fibers whose stress-strain response is represented by a bilinear model with an elastic slope of 200 GPa and a post-yield strain-hardening ratio of 2%. Axial-flexure interaction is included in both the beams and columns. The composite action of floor slabs was not considered.

Here, a typical frame in the east-west direction was considered. Cross-sectional properties for the fiber model are specified for each member in terms of a mesh of concrete fibers and discrete reinforcing bars. The uniaxial properties for nonlinear modeling of the concrete fibers are shown in Figure 2.2. The rebar is modeled as Grade

60 steel (yield strength of 414 MPa) with an ultimate strength of 620 MPa and Young's Modulus of 200 GPa. The nonlinear material behavior is modeled as a bilinear curve with post-yield strain-hardening ratio of 2%.

As in the case of the steel structure, the concrete building was modeled as a bare frame without considering the contribution or interaction of the floor slab. Clearly, the contribution of the slab on both the stiffness and strength of the beam is well established; however, these effects are not expected to influence the findings in this study since the same models are being used in the different analyses.

2.4 COMPARATIVE STUDY OF SEISMIC DEMANDS

The four buildings described in the previous section are evaluated using nonlinear static and nonlinear dynamic procedures to compare the resulting demands. In the case of static approaches, the following lateral load configurations were considered:

NSP-1: The buildings are subjected to a lateral load distributed across the height of the building based on the following equation:

$$F_x = \frac{W_x h_x^k}{\sum W_x h_x^k} V \tag{2.1}$$

In the above expression, F_x is the applied lateral force at level '*x*', W is the story weight, h is the story height and V is the design base shear. This results in an inverted triangular distribution of the lateral load when the period-dependent power k is set equal to unity.

NSP-2: A uniform lateral load distribution consisting of forces that are proportional to the story masses at each story level.

NSP-3: A lateral load distribution that is proportional to the story shear distribution determined by combining modal responses from a response spectrum analysis of each building model using the BSE-2 hazard spectrum as recommended in FEMA-356.

2.4.1 Target Displacement

Each of the four building models were subjected to the three lateral load patterns enumerated above until the roof reached a specified target displacement. The target displacements were computed using the provisions in FEMA-356 for BSE-2 loading. A site-specific spectrum was developed using the following parameters to characterize a hazard level corresponding to the maximum credible earthquake (or Hazard Level III): $S_s = 2.0$; $S_1 = 0.75$; $F_a = 1.0$; $F_v = 1.5$; Site Category D and 5% damping. Assuming $\beta_s = 1$, $\beta_1 = 1$, the following ranges of spectral acceleration values were obtained:

For $0 < T < T_o$: $S_a = 10.67\ T + 0.8$

For $To < T < T_s$: $S_a = 2.0$

For $T > Ts$: $S_a = 1.125 / T$

In the above expressions, T_s = 0.563s and T_o = 0.113s. This resulted in the following values of target displacements:

- Steel frame: 8-story = 1.08 m; 12-story = 1.30 m.
- RC frame: 8-story = 0.40 m; 12-story = 0.54 m.

The BSE-2 design spectrum developed using the parameters above are superimposed on the earthquake spectra shown in Figure 2.3. The fundamental periods of each building model are also identified in these figures.

2.4.2 Benchmark Demands: Time History Analyses

The validity of pushover procedures based on the three invariant load distributions is examined using the results of nonlinear time-history analyses as a benchmark. A set of seven strong ground motions, all recorded at soil sites in California and having a magnitude range of 6.6 to 7.5 were selected for the nonlinear time history evaluations. These ground motion records are recommended by ATC-40 (1996). Details of these records are given in Table 2.3, and their five-percent damped elastic acceleration response spectra are shown in Figure 2.3 for each set of building evaluations. To facilitate the comparison with pushover analyses, the selected ground motions are scaled in such a manner so that the resulting peak roof displacement is equal to the target displacement computed for each building. The scale factors are also listed in Table 2.3. A conventional technique is to scale ground motions such that the spectral acceleration at the fundamental period matches a given design spectrum. The scaling method adopted in this study is based on the FEMA recommended guideline for the expected peak roof displacement. Though the scale factors appear to be quite high in some cases, the spectral accelerations at the fundamental period of the respective structural models is comparable to the BSE-2 spectrum for the steel buildings and somewhat higher than the BSE-2 spectrum for the RC structures.

2.4.3 Evaluation of Seismic Demands

The estimated demands using the different nonlinear procedures are evaluated at the global, story and local levels. Global demands refer to the displacement profile of the building at the peak roof displacement and the base shear vs. roof displacement response.

At the story level, the interstory drift values are compared. Finally, local demands are evaluated in terms of inelastic rotations at the ends of beam and column elements. Collectively, these deformation measures provide a basis for comparing the effectiveness of static pushover methods to predict demands resulting from seismic action.

2.4.3.1 Global Demands

Estimates of global demand from the nonlinear time-history (NTH) analyses for both steel and concrete structures are shown in Figures 2.4(a) through 2.7(a). The magnitudes at each story for each record (listed as Eq-1 through Eq-7) correspond to the maximum demand at that story throughout the duration of the event. The mean and the distribution around the mean value are repeated in Figures 2.4(b) through 2.7(b) to enable direct comparison with demands estimated from the pushover procedure using the three lateral load patterns. Recall that ground motions were scaled to produce the same target roof displacement. In all cases, the inverted triangular pattern is found to come closest to the mean time-history estimates. The other two load patterns tend to overestimate demands at the lower levels because these patterns typically result in higher loads being applied at the lower floors.

The capacity curves which show the total base shear (in terms of the building weight) as a function of the roof drift is displayed in Figure 2.8 for all models. Initial yielding of an element occurs first when using NSP-1. This loading pattern also produces a response with the least system stiffness and the lowest base shear capacity. However, the difference in base shear capacity between the different patterns decreases with story height. The difference is more evident for the steel building since the increase in story

height produced a larger change in fundamental period than the RC building. The design base shear for each building is identified in these plots for comparison.

The information generated in Figures 2.4 through 2.8 represents the fundamental measures of demand at the global level. The inherent ductility of the system is typically evaluated using the response shown in Figure 2.8. This plot contains two elements of the reduction or R-factor used in modern building codes: the difference between first yield of an element and eventual yield of the system contains information on the redundancy in the system while the response beyond system yield up to the target deformation is a measure of the ductility-based reduction factor. The question that this chapter attempts to address is whether these measures are adequate to reach an assessment of the performance of the building. In the next section, additional demand measures are evaluated using the information from nonlinear time-history analyses as benchmark estimates.

2.4.3.2 Story Level Demands

The importance of interstory drift has long been recognized as an important indicator of building performance. During an earthquake, the interstory displacements vary with time as different modes dominate the response. On the other hand, pushover methods which use invariant load patterns produce a consistent pattern of interstory demands up to initial yielding following which the story demands become localized and depend on the story level to experience first excursion beyond the elastic state.

Interstory demands are plotted in Figures 2.9-2.12 for the four building models evaluated in this study. In each case, demands are shown for each earthquake followed by a plot which compares time-history estimates with pushover demands. The third plot for

each frame shows capacity curves for critical story levels (which are defined as those stories that exhibit the largest interstory drift demands).

The most important observation that results from the nonlinear time-history evaluation is that the peak story demands vary from one record to the next. While several earthquakes impose the largest demand at the lower levels, there are a number of cases when the largest demands occur at different levels. In general, pushover methods tend to over-estimate the story demands at the lower levels and under-estimate them at the upper levels. The discrepancy becomes more apparent with increasing story height (or longer fundamental periods). Story capacity curves that result from pushover procedures serve to reinforce the finding that static methods cannot adequately reproduce demands across the height of the building when compared to typical responses using nonlinear time-history analyses.

2.4.3.3 Local Element Demands

In the third and final phase of the evaluation, demands are examined at the element level. Since story demands reflect the behavior of elements at that story, it is reasonable to expect local element demands to correlate to story demands. Based on the story drifts and story capacity curves presented in Figures 2.11 and 2.12, the ductility demands at critical story levels are summarized in Tables 2.4 and 2.5. The tables include measures at the global level and at the component level. Only a set of selected stories and elements at these story levels experiencing the maximum demands are shown. In addition to the estimates computed for the different lateral load patterns using pushover analysis, the peak ductility demands resulting from the critical earthquake record (causing the largest demands) is also displayed. In the case of the 8-story steel structure, local component

demands are generally much higher than story demands with column demands exceeding beam ductility demands.

The response using time-history analyses produced smaller demands at lower stories of the 8-story buildings but caused higher peak column demands at the critical fifth story level. Similarly, no correlation between global, story and local element demands are evident for the 12-story steel frame. Findings from the steel buildings also apply to the response results obtained for the RC structures, as indicated in the data presented in Table 2.5. The component demands at the upper floors of the 12 story buildings support the conclusions reached when examining story levels demands which show pushover methods severely under-predicting deformations and the potential for yielding at the these floors.

In computing the ductility demands, the definition of yield rotation is important. For concrete structures, FEMA-356 suggests using an effective stiffness which defines the yield rotation at the yield moment. In this study, since a fiber section model is used for concrete members, the force-deformation response is nonlinear even before yielding. Hence, the yield rotation was defined at the point where the moment magnitude reaches its yield value. For steel structures, FEMA-356 proposes an expression which assumes that the inflection point is at mid-length of the element. In this study, the following expression was used to estimate the yield rotation:

$$\theta_y = \frac{M_y{}^2 \ell}{3\,(M_y + M_2)\,EI} \tag{2.2}$$

where θ_y is the yield rotation; M_2 is the moment at one end of the member ($M_2 < M_y$); ℓ is the length of member; E is the elastic modulus; I is the moment of inertia, and M_y is the yield moment given by:

$M_y = Z f_y$ for beams;

$$M_y = Z f_y (1 - \frac{P}{A_g f_y}) \quad \text{for columns;}$$

In the above expressions, Z is the plastic modulus; P is the axial load; A_g is the gross area and f_y is the yield strength of steel. In FEMA-356, M_2 is assumed to be equal to M_y. This assumption is reasonably true for beams in moment frame structures. For columns, the assumption of mid-point inflection leads to conservative estimates in pushover analyses. For time-history methods, the FEMA equation can sometimes lead to non-conservative values of the ductility demand. For example, the computed ductility using the FEMA expression in one case was 19.0 while using Equation (2.2) suggested above yields a ductility demand of 22.0.

2.4.4 Further Implications of Using Component Demands to Evaluate Seismic Performance

An issue that has not received much attention in performance-based seismic evaluation is the development of acceptance criteria. Currently, the performance of a building is governed by the performance of a single component in the system. Component performance is assessed on the basis of the peak ductility demand when nonlinear procedures are used to estimate element deformations. The consideration of peak values ignores the effect of cumulative damage resulting from cyclic deformations. The

modeling of damage has been the subject of numerous research papers and a comprehensive review on the subject has been reported by Williams and Sexsmith (1995). Damage models have examined the process of component degradation and failure using measures of deformation, measures of dissipated energy or some combination of both. The damage model proposed by Park and Ang (1985), for example, uses a linear combination of deformation damage and damage resulting from cumulative effects. Studies utilizing the Park-Ang model have shown that most of the damage is a result of peak deformation rather than the effects of cumulative energy dissipation. Such conclusions reflect on the ability of the model to simulate cumulative effects rather than offer an insight into the cumulative damage process. It is necessary to examine studies on low-cycle fatigue behavior of components to appreciate the significance of this issue (Mander and Cheng 1995; El-Bahy et al. 1999). Experimental tests carried out by El-Bahy et al. clearly show that both the energy and displacement capacity is a function of the number of cycles to which the component is subjected to at a given ductility level. Cyclic demand, therefore, is an important factor in performance-based engineering which seeks to delineate damage measures from elastic, undamaged state to post-yield response and failure. This aspect of demand is explored in this concluding section of the chapter.

Figures 2.13 – 2.16 provide a glimpse of the implications of cyclic demand and the influence of low-cycle fatigue on performance assessment of structures. Figures 2.13 and 2.14 show a set of typical responses for a beam and column in the 8-story steel frame when subjected to an earthquake load. The ductility demand on the column using the peak rotation is 22.0. However there are numerous additional cycles of deformation which exceed the yield rotation. Since the inelastic response results in a permanent drift,

it is more convenient to count the number of half cycles wherein each half cycle is the peak-to-peak magnitude. If the peak-to-peak amplitude exceeds twice the yield rotation, that half cycle is considered to have exceeded the effective yield rotation and each such cycle is referred to as a “plastic cycle”. For the critical column shown in Figure 2.13, there were 17 half plastic cycles. Similarly, for the critical beam on the fifth floor of the 8-story steel frame, there were 16 half plastic cycles. The cumulative damage resulting from these cycles is much greater than implied by the peak ductility demand.

In addition to the cyclic demands, Figures 2.13 and 2.14 also include another useful piece of information: the relationship between curvature ductility and rotational ductility. Since curvature computations are localized, they exhibit large variations. The mean ratio of the curvature to rotational ductility is 1.85 for the column element and 2.2 for the beam element. This information is helpful in arriving at estimates of plastic hinge lengths when resorting to approximate methods to analyze structural frames.

Finally, cyclic demand data is presented for typical RC components in Figures 2.15 and 2.16. Axial force effects are evident in the response of the column element which experienced 9 half plastic cycles. The beam element, on the other hand, is subjected to 14 half plastic cycles. As pointed out earlier, the cumulative effects of these cycles cannot be ignored when assessing the performance of the component. .

2.5 CONCLUSIONS

Conventional seismic practice in the U.S. is based on elastic procedures which rely on force reduction factors. Such an approach relies primarily on global demand estimates to evaluate the expected performance of a building. The emergence of FEMA-356 has now

shifted the focus from global demand to local component demands. This chapter attempts to raise questions on the validity of nonlinear static approaches to estimate local demands and to explore correlations between component, story and global demands. The focus of this chapter is not directly related to the assessment of design requirements rather it is an assessment of evaluation methods used to estimate seismic demands that play a major role in the design process. Pushover methods are undoubtedly an improvement over existing elastic force-based procedures and provide critical information on potential collapse mechanisms and the vulnerability for soft stories. For structures responding primarily in the first mode, nonlinear static methods may be a reliable option to estimate inelastic demands.

Findings from this study indicate that there is no consistent correlation between demand estimates at the local, story and global level for the intensity level considered in the study. The evaluations presented here were based on seismic events with a 2% probability of being exceeded in 50 years. The demands at lower intensity levels could present a different picture considering the lower demands, hence similar evaluations for different intensity levels are needed to make generalized conclusions. Additionally, the inelastic models and the computational tools used to derive quantities such as plastic rotation also play an important role in establishing demand measures. It is generally assumed that the story demands are reasonably correlated to element demands at that story level. Some of the discrepancies between peak story demand and peak element demands suggest that additional scrutiny of the nonlinear element models is needed before definitive conclusions can be reached on the reasons for this discrepancy.

Designing a building to achieve a certain ductility demand can result in much larger demands at the local level. Caution must be exercised when using nonlinear static procedures since the lateral load pattern used to estimate demands can have a significant influence on the computed demands. When compared to nonlinear time history estimates, pushover methods tend to underestimate demands at the upper levels signifying the relevance of high mode participation in mid to high rise structures. Nonlinear response measures, using either static or dynamic analyses, are sensitive to modeling parameters such as the definition of effective stiffness, yield rotation, plastic hinge length, etc. and must be evaluated separately prior to utilizing the results of nonlinear evaluations in performance assessment. Finally, demands based on peak values fail to take into consideration the cumulative effects of cyclic degradation.

This study was limited to standard invariant lateral load patterns recommended in FEMA-356. As indicated in the introductory section of this chapter, methods exploring enhanced pushover methods which overcome many of the drawbacks of such procedures have been developed. The next step in this research effort is to evaluate local component demands using these new procedures. Previous studies reported by Gupta and Kunnath (2000) and Chopra and Goel (2002) have been limited to investigation of interstory demands. The present study has raised new questions related to the correlation between story demands and component demands and the computational tools used to estimate these quantities. Additional research is needed to address and clarify these issues.

Table 2.1 Member details of steel frame along line A

8-Story Steel			12-Story Steel		
Levels	**Beam Section**	**Column Section**	**Levels**	**Beam Section**	**Column Section**
7 –8	W21x73	W14x132	11 – 12	W27x94	W14x132
5 – 6	W24x94	W14x159	9 – 10	W27x102	W14x193
3 – 4	W27x102	W14x211	7 – 8	W27x114	W14x257
1 – 2	W27x114	W14x283	5 –6	W30x124	W14x311
			3 – 4	W30x132	W14x370
			1 – 2	W30x148	W14x426

Table 2.2 Section details of exterior concrete frame along line A

	Levels	Exterior Columns		Interior Columns		Beams		
		Size *	Steel **	Size *	Steel **	Size *	Top Steel **	Bottom Steel **
8-Story RC	1	101x101	20-#11	112x91.5	18-#11	107x66	5 #11+5#4	5 #9+5#4
	2	101x101	20-#9	112x91.5	18-#10	112x66	5 #11+5#4	5 #10+5#4
	3	101x101	20-#9	112x91.5	18-#10	107x66	5 #11+5#4	5 #10+5#4
	4	96.5x96.5	20-#9	107x86	18-#10	107x66	5 #11+5#4	5 #10+5#4
	5	96.5x96.5	20-#9	107x86	18-#10	96.5x66	5 #11	5 #9
	6	91.5x91.5	16-#9	107x86	16-#10	91.5x61	5 #10	5 #8
	7	91.5x91.5	16-#9	96.5x76	16-#8	86x61	5 #10	5 #7
	8	91.5x91.5	16-#10	96.5x76	16-#8	86x61	5 #9	5 #7
12-Story RC	1	86x86	24-#11	107x81	18-#14	112x71	6 #11+5#4	6 #10+5#4
	2	81x81	20-#10	107x81	18-#14	112x71	7 #11+5#4	6 #10+5#4
	3	81x81	20-#10	107x81	18-#14	107x66	6 #11+5#4	6 #10+5#4
	4	81x81	20-#10	107x81	18-#11	107x66	6 #11+5#4	6 #10+5#4
	5	79x79	20-#10	107x81	18-#11	107x66	6 #11+4#4	6 #10+4#4
	6	79x79	20-#10	107x81	18-#11	107x66	6 #11+4#4	5 #10+4#4
	7	79x79	20-#10	96.5x76	18-#11	107x66	6 #11+4#4	5 #10+4#4
	8	76x76	20-#9	96.5x76	18-#11	107x66	5 #11+4#4	5 #10+4#4
	9	76x76	20-#9	96.5x76	18-#10	96.5x66	5 #11	5 #9
	10	71x71	16-#9	86x71	18-#10	91.5x61	5 #11	5 #8
	11	71x71	16-#9	81x61	16-#9	86x61	5 #10	5 #7
	12	71x71	16-#8	81x61	16-#9	81x61	5 #9	4 #7

* All dimensions are in cm

** Number of bars-diameter => #4: 13mm; #5: 16mm; #6: 19mm; #7: 22mm; #8: 25mm; #9: 29mm; #10: 32mm; #11: 35mm

Table 2.3 Ground motion ensemble

EQ. No	Year	Earthquake	Recording Station	PGA (g)	Distance (km) *	EQ. Scale Factor †			
						8-Story Steel	12-Story Steel	8-Story RC	12-Story RC
1	1971	San Fernando	Station 241	0.25	16.5	3.7	3.5	4.3	3.5
2	1971	San Fernando	Station 458	0.12	18.3	3.5	3.0	5.9	4.1
3	1989	Loma Prieta	Hollister, South & Pine	0.18	17.2	3.8	3.5	4.1	4.7
4	1989	Loma Prieta	Gilroy #2	0.32	4.5	6.1	6.8	3.0	2.6
5	1992	Landers	Yermo	0.15	31.0	5.3	5.4	5.5	4.5
6	1992	Landers	Joshua Park	0.28	10.0	3.9	5.0	3.4	2.8
7	1994	Northridge	Century City LACC North	0.26	23.7	5.5	6.0	6.7	6.7

* Closest distance to fault; † Scale factor used to achieve the target roof displacement

Table 2.4 Summary of ductility demands for 8 and 12-story steel building

8-Story RC

		NSP-1		NSP-2		NSP-3		(NTH, EQ-1)		(NTH, Mean)	
	Global		4.4		5.2	-	6.2		-		
Story-1	***Story***		5.8		8.3		11.6		-		-
	Column	*Ext.*	6.5	*Ext.*	9.5	*Ext.*	12.4	*Ext.*	4.5	*Ext.*	5.2
	Beam	*Ext.*	7.7	*Ext.*	10.7	*Ext.*	12.9	*Ext.*	5.2	*Ext.*	4.5
Story-3	***Story***		5.0		5.1		5.1		-		-
	Column	*Ext.*	1.2	*Int.*	2.5	*Int.*	3.6	*Ext.*	2.2	*Ext.*	2.2
	Beam	*Int.*	6.3	*Int.*	7.2	*Ext.*	7.2	*Ext.*	4.9	*Ext.*	5.1
Story-5	***Story***		4.5		3.4		1.5		-		-
	Column	*Ext.*	0.0	*Ext.*	0.0	*Ext.*	1.2	*Ext.*	2.5	*Ext.*	2.5
	Beam	*Int.*	5.4	*Int.*	3.7	*Int.*	1.7	*Ext.*	5.0	*Ext.*	5.0

12-Story RC

		NSP-1		NSP-2		NSP-3		(NTH, EQ-2)		(NTH, Mean)	
	Global		4.5		5.0		6.4		-		-
Story-1	***Story***		7.3		9.6		12.9		-		-
	Column	*Ext.*	8.3	*Ext.*	12.6	*Ext.*	16.5	*Ext.*	13.3	*Ext.*	8.2
	Beam	*Ext.*	8.4	*Ext.*	12.2	*Ext.*	17.2	*Ext.*	11.6	*Ext.*	5.8
Story-3	***Story***		5.8		6.1		6.8		-		-
	Column		2.3	*Ext.*	1.9	*Ext.*	1.7	*Ext.*	1.6	*Ext.*	3.1
	Beam	*Int.*	7.7	*Int.*	7.5	*Int.*	10.0	*Int.*	7.5	*Int.*	6.2
Story-5	***Story***		5.4		4.6		3.6		-		-
	Column	*Ext.*	1.4	*Int.*	2.0	*Ext.*	2.3	*Ext.*	2.5	*Ext.*	2.5
	Beam	*Int.*	7.0	*Int.*	5.3	*Int.*	3.4	*Int.*	6.7	*Int.*	5.8
Story-9	***Story***		2.4		1.1		-		-		-
	Column	*Ext.*	0.0	*Ext.*	0.0	*Int.*	0.0	*Int.*	2.5	*Int.*	2.5
	Beam	*Int.*	2.6	*Int.*	1.1	*Int.*	0.0	*Int.*	2.5	*Int.*	3.8

Ext: Exterior; Int: Interior

Table 2.5 Summary of ductility demands for 8 and 12-story steel building

		8-Story Steel				
		NSP-1	**NSP-2**	**NSP-3**	**(NTH, EQ-5)**	**(NTH, Mean)**
	Global	5.3	5.3	6.0	-	-
Story-1	***Story***	3.7	7.8	11.7	-	-
	Interior Column	4.8	14.3	17.2	6.8	8.5
	Exterior Beam	4.6	11.6	13.5	5.8	7.1
Story-3	***Story***	5.0	5.7	6.1	-	-
	Interior Column	16.9	19.7	19.7	8.9	7.5
	Exterior Beam	9.3	4.7	4.7	8.2	6.8
Story-5	***Story***	7.8	2.4	6.7	-	-
	Interior Column	17.0	5.5	5.5	22.0	16.9
	Exterior Beam	2.5	1.2	1.3	7.1	5.9

		12-Story Steel					
		NSP-1	**NSP-2**	**NSP-3**	**(NTH, EQ-6)**	**(NTH, EQ-7)**	**(NTH, Mean)**
	Global	3.4	3.9	5.1	-	-	-
Story-1	***Story***	4.1	8.4	11.5	-	-	-
	Interior Column	4.8	12.2	15.1	7.1	9.6	7.2
	Exterior Beam	5.0	11.2	14.4	7.8	10.0	7.1
Story-3	***Story***	4.8	6.4	7.1	-	-	-
	Interior Column	3.8	3.0	4.8	4.9	3.4	2.6
	Exterior Beam	8.3	9.9	9.1	8.5	10.2	6.3
Story-5	***Story***	4.9	3.5	2.4	-	-	-
	Interior Column	3.1	4.8	3.4	5.12	5.5	3.7
	Exterior Beam	8.0	3.9	2.7	9.4	7.6	5.7
Story-9	***Story***	1.5	0.0	0.0	-	-	-
	Interior Column	2.0	0.0	0.0	6.3	5.5	4.4
	Exterior Beam	1.7	0.0	0.0	10.0	6.8	5.4

NTH = Nonlinear Time History

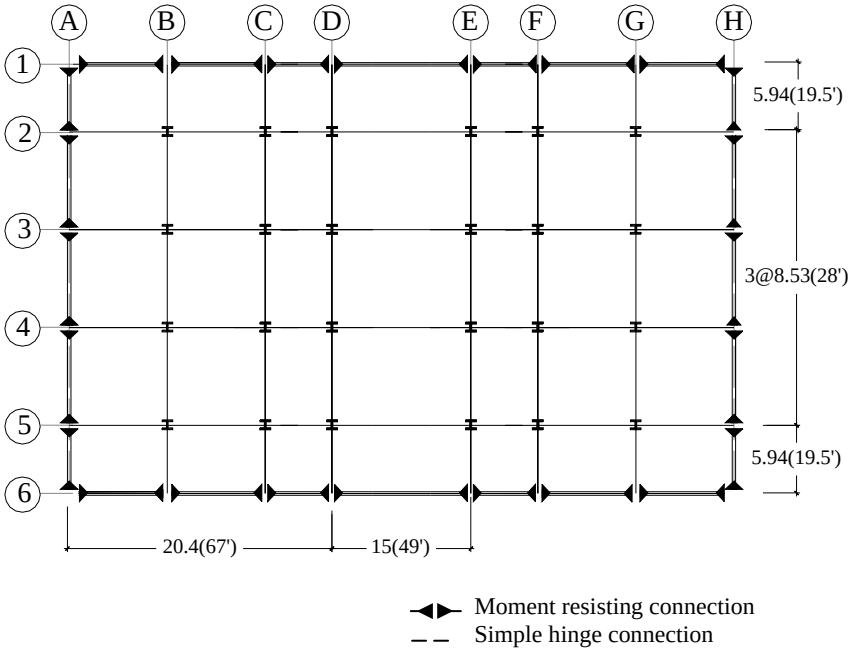

(a)

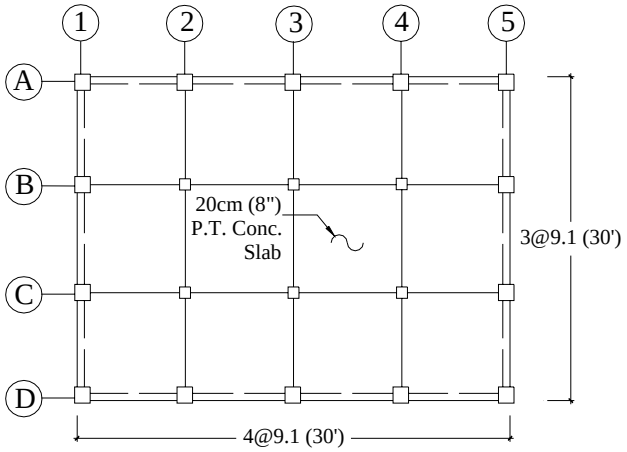

(b)

Figure 2.1 Plan view of (a) steel and (b) RC building structure

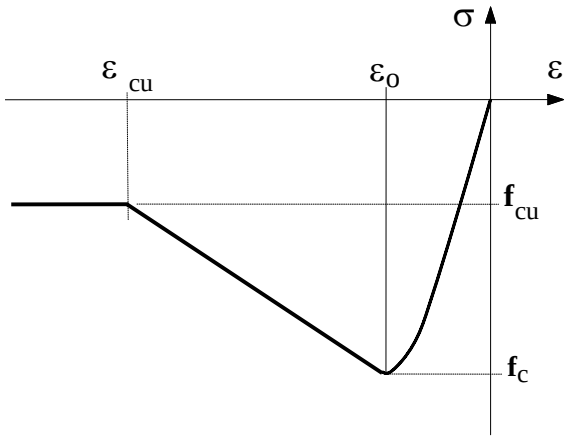

	f_c (MPa)	ε_o	f_{cu} (MPa)	ε_{cu}
Cover	*27.6*	*0.0020*	*5.5*	*0.005*
Core	*35.8*	*0.0025*	*6.9*	*0.020*

Figure 2.2 Concrete material model in compression

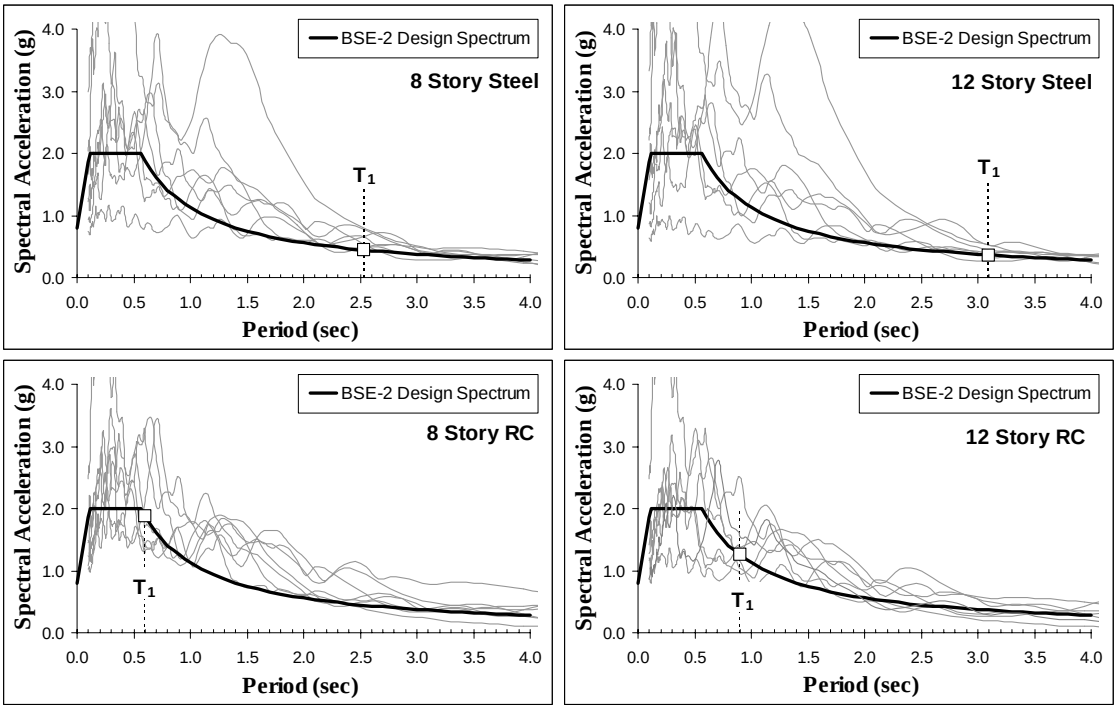

Figure 2.3 Spectra of scaled ground motion recordings used in the evaluation of each building

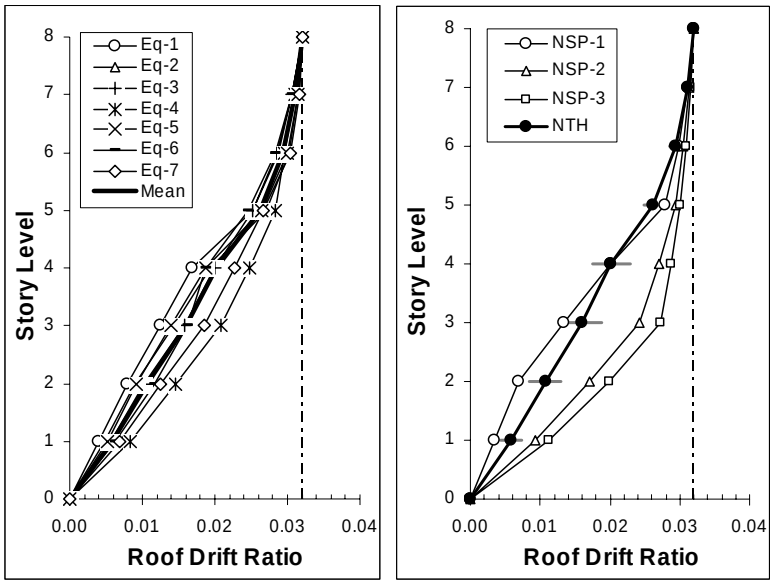

(a) Time history results (b) Pushover vs. Time history

Figure 2.4 Peak displacement profiles for 8-story steel frame under static and seismic loads (Note: Horizontal band across nonlinear time-history (NTH) estimate shows distribution of peak demands across the mean value)

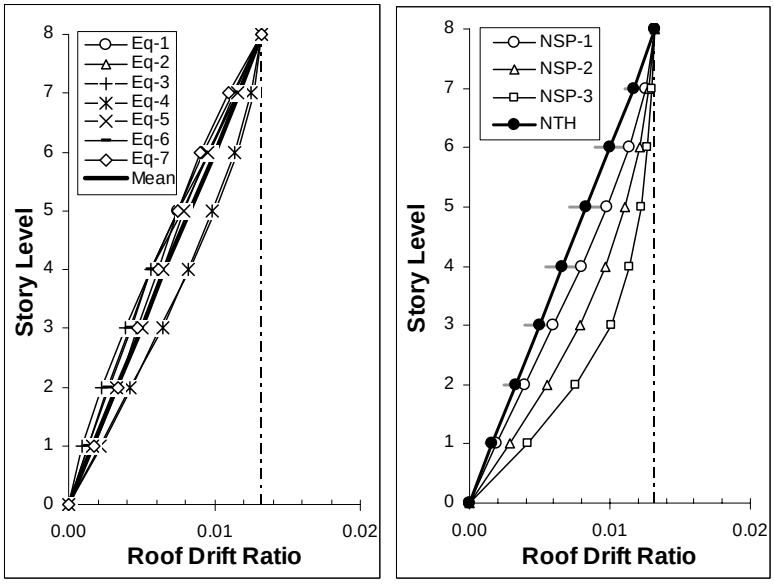

(a) Time history results (b) Pushover vs. Time history

Figure 2.5 Peak displacement profiles for 8-story RC frame

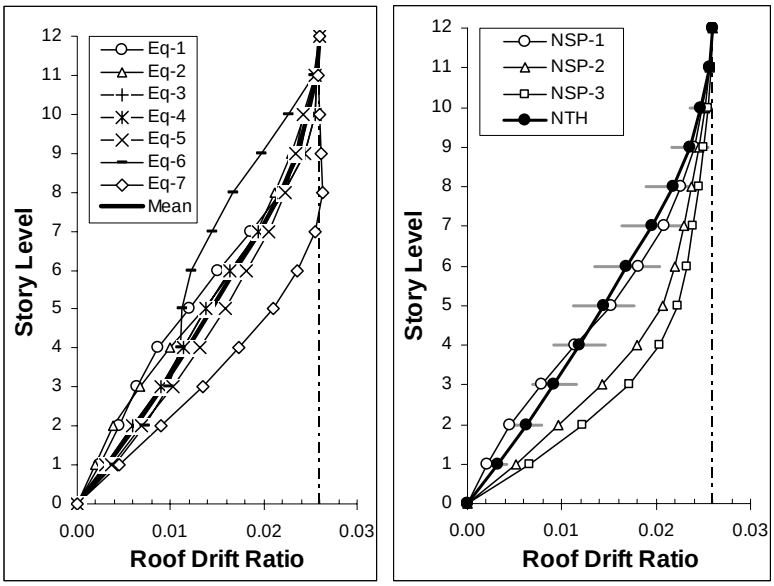

(a) Time history results (b) Pushover vs. Time history

Figure 2.6 Peak displacement profiles for 12-story steel frame

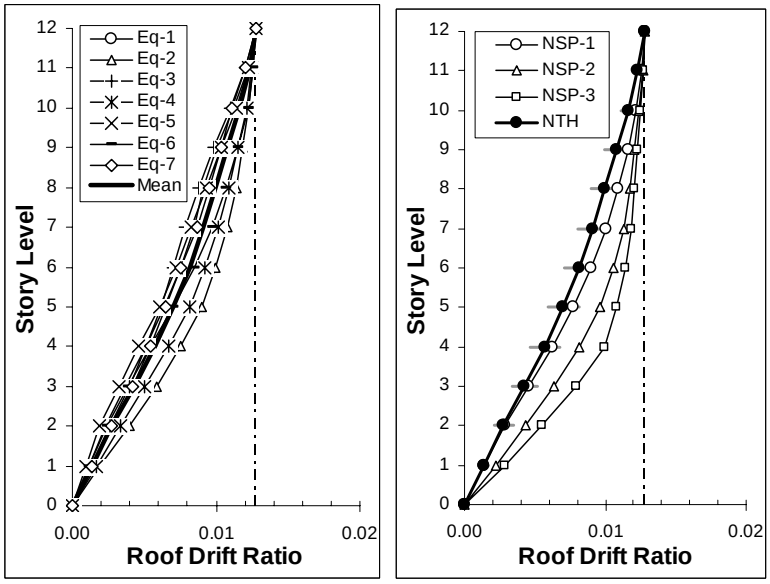

(a) Time history results (b) Pushover vs. Time history

Figure 2.7 Maximum displacement profiles for 12-story RC frame

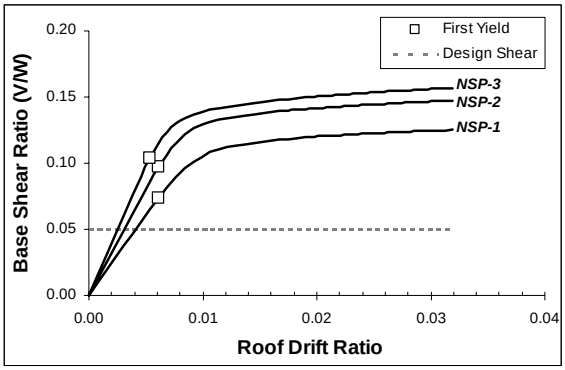

(a) 8-story steel building

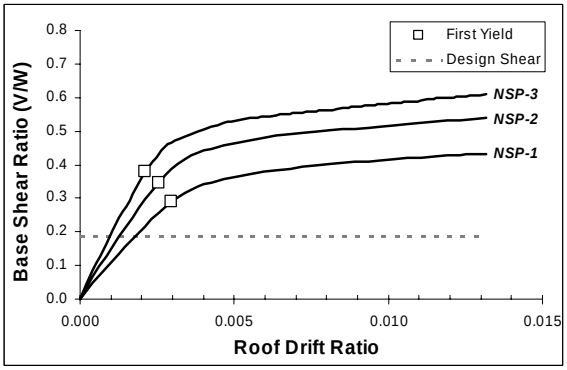

(b) 8-story RC building

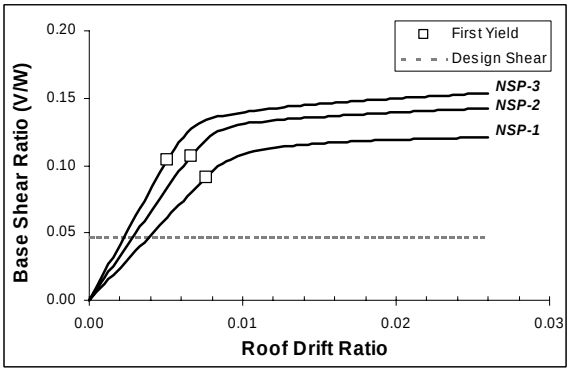

(c) 12-story steel building

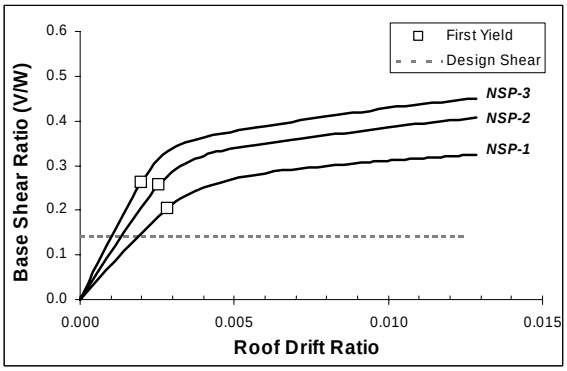

(d) 12-story RC building

Figure 2.8 Base shear vs. roof drift response using different lateral load profiles

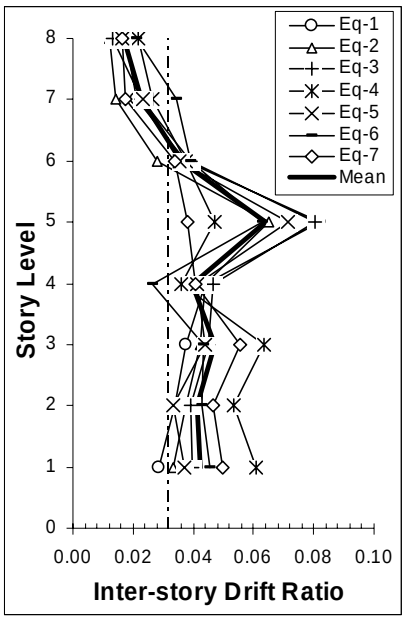

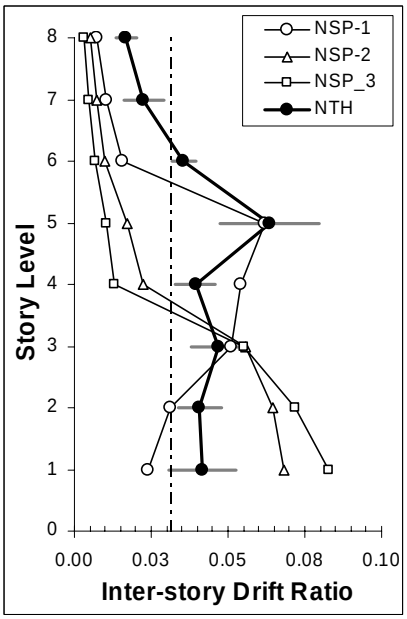

(a) Time history results (b) Pushover vs. Time history

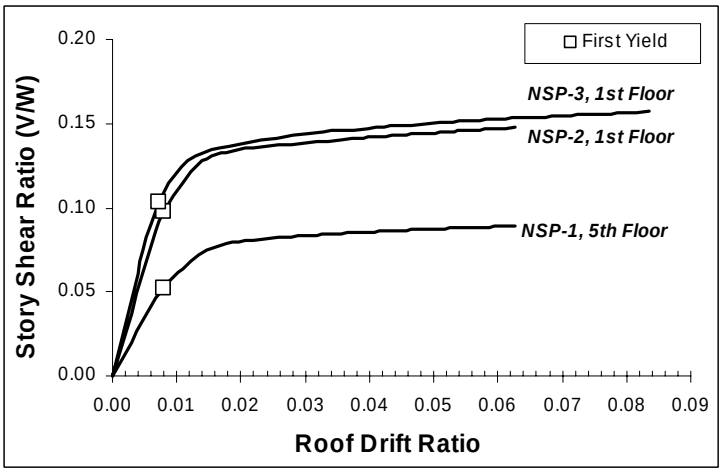

(c) Typical capacity curves for critical stories

Figure 2.9 Interstory demands in 8-story steel frame

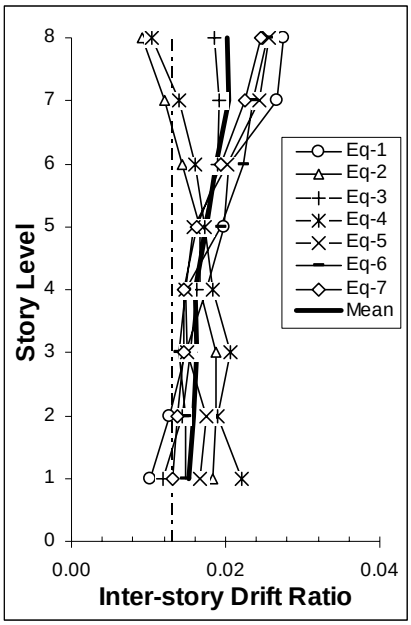

(a) Time history results

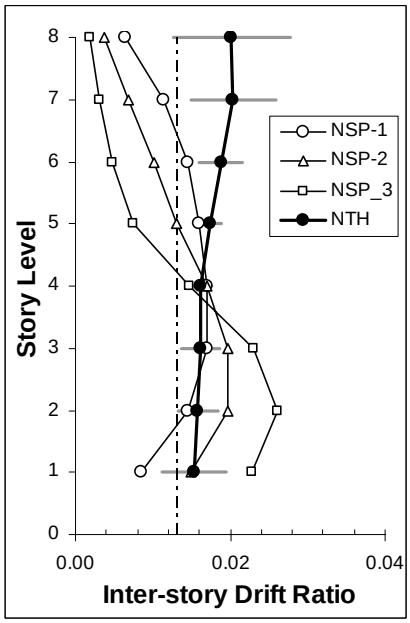

(b) Pushover vs. Time history

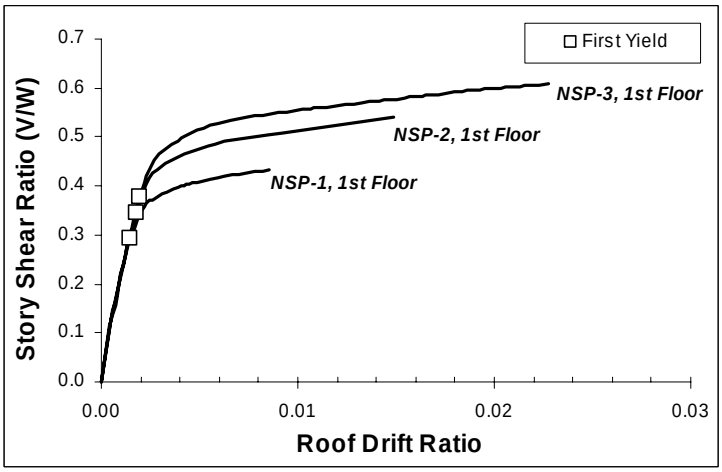

(c) Typical capacity curves for critical stories

Figure 2.10 Interstory demands in 8-story RC frame

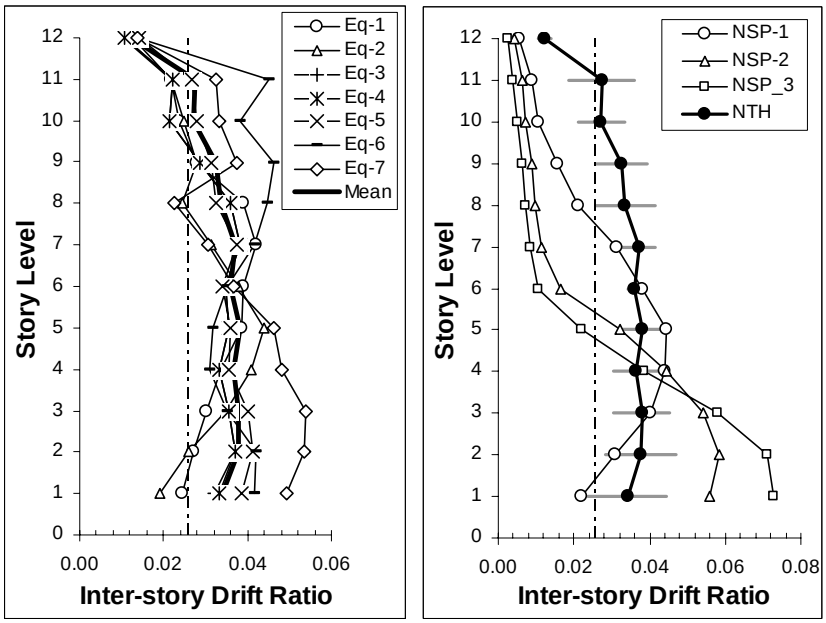

(a) Time history results (b) Pushover vs. Time history

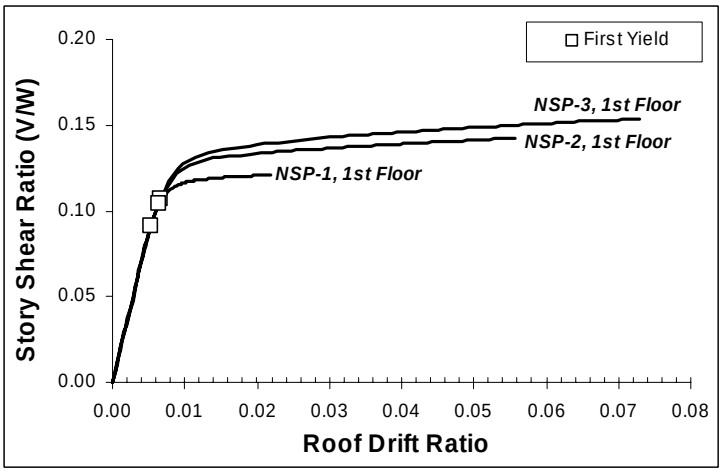

(c) Typical capacity curves for critical stories

Figure 2.11 Interstory demands in 12-story steel frame

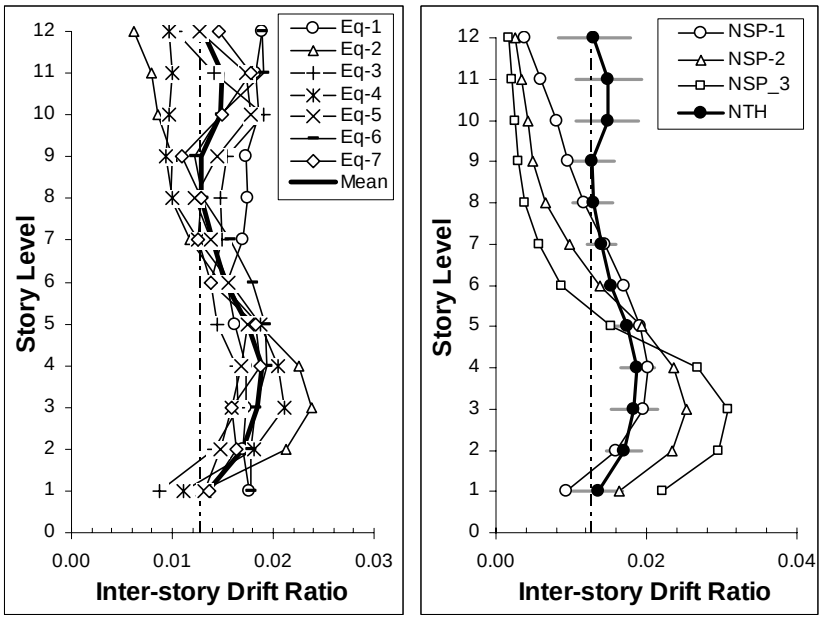

(a) Time history results (b) Pushover vs. Time history

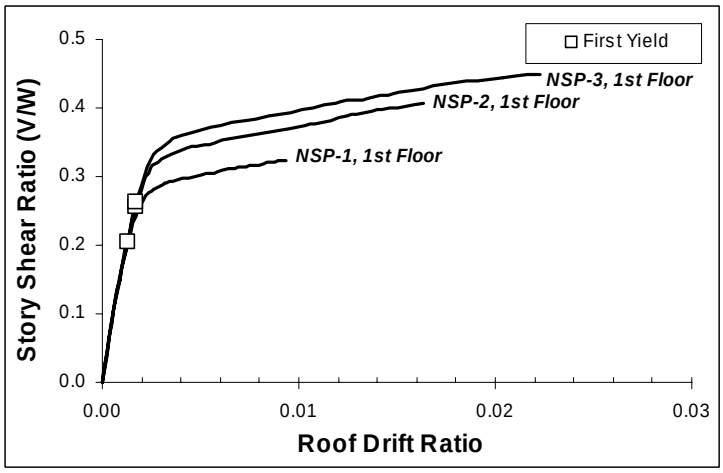

(c) Typical capacity curves for critical stories

Figure 2.12 Interstory demands in 12-story RC frame

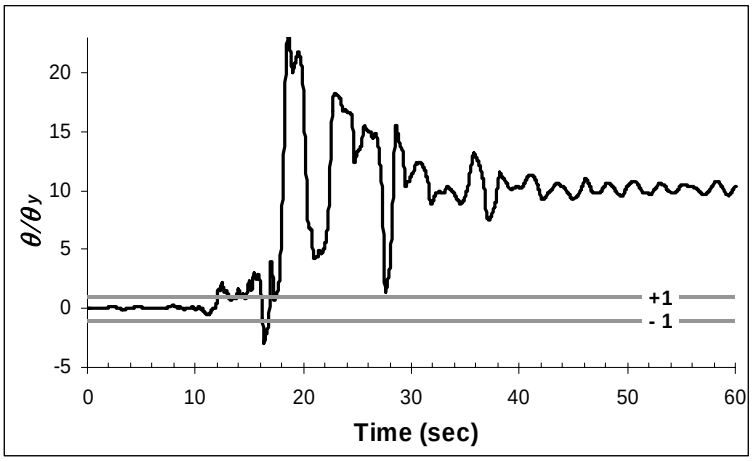

(a)

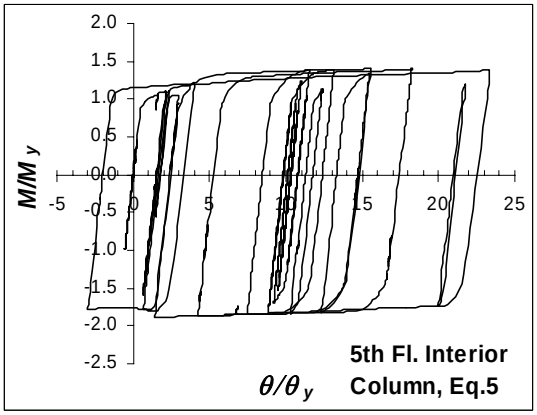

(b)

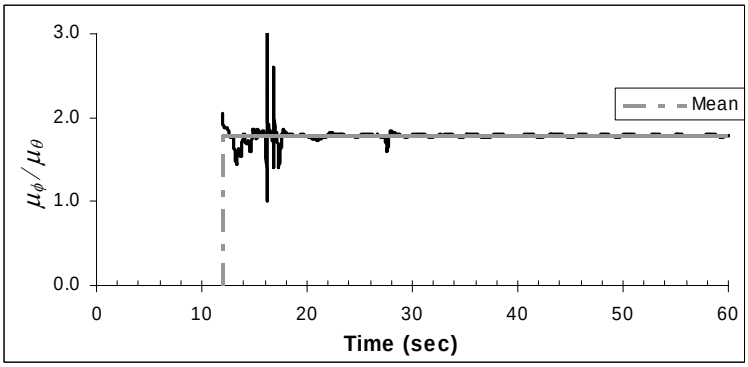

(c)

Figure 2.13 Cyclic demand in typical column of 8-Story steel building (Time history response using Earthquake #5)

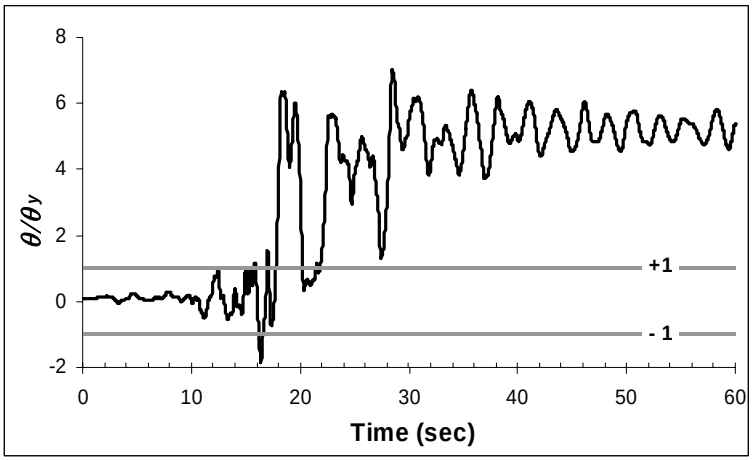

(a)

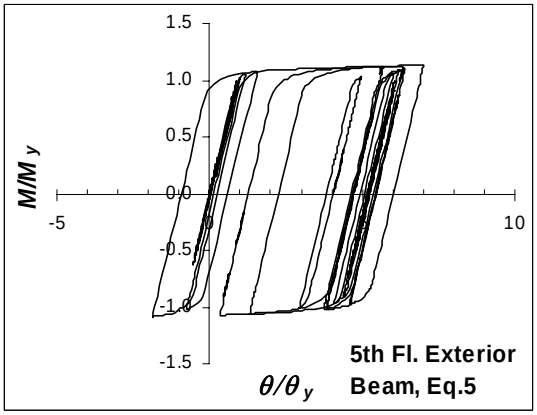

(b)

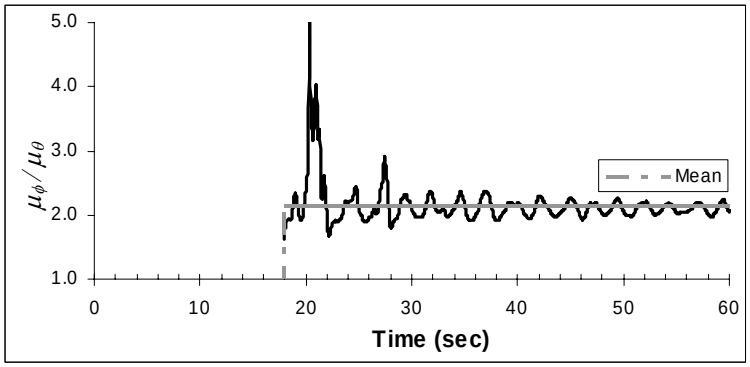

(c)

Figure 2.14 Cyclic demand in typical beam of 8-Story steel building (Time history response using Earthquake #5)

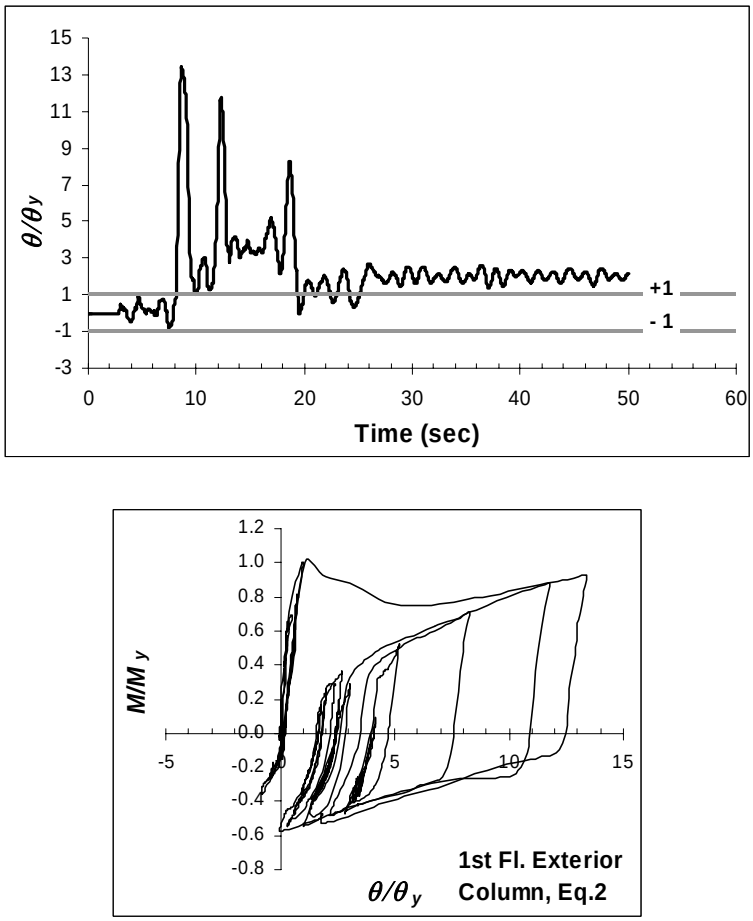

Figure 2.15 Cyclic demand in typical column of 12-Story RC frame

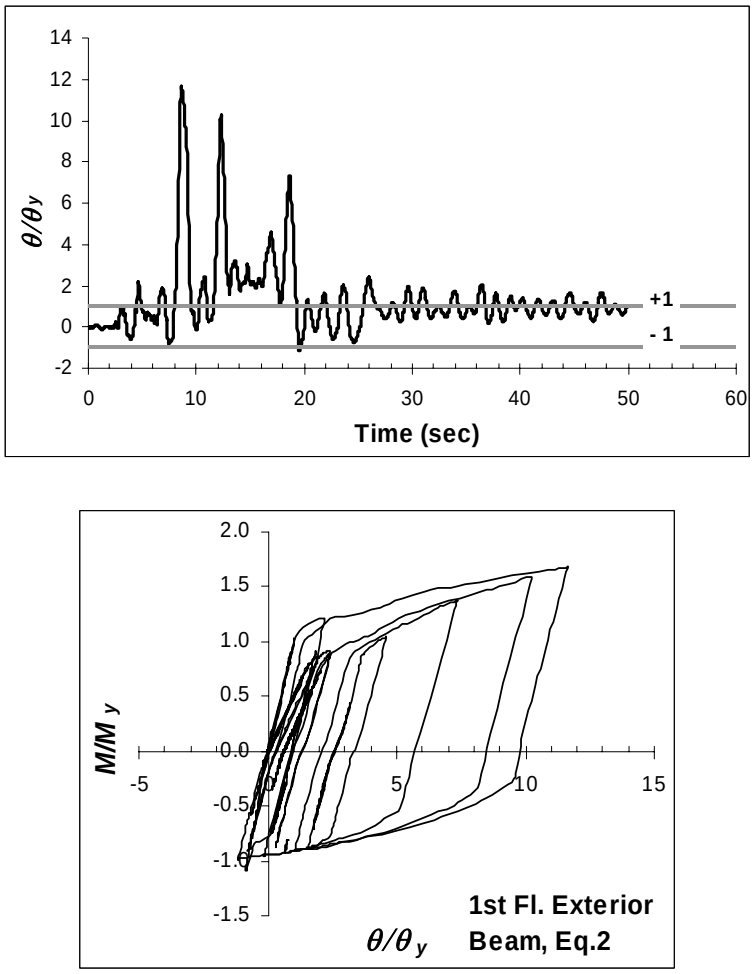

Figure 2.16 Cyclic demand in typical beam of 12-Story RC frame

CHAPTER 3

EFFECTS OF FLING AND FORWARD DIRECTIVITY ON SEISMIC RESPONSE OF BUILDINGS

3.1 INTRODUCTION

In the proximity of an active fault system, ground motions are significantly affected by the faulting mechanism, direction of rupture propagation relative to the site (e.g., forward directivity) as well as the possible static deformation of the ground surface associated with fling effects. These near-source outcomes cause most of the seismic energy from the rupture to arrive in a single coherent long period pulse of motion (note that backward-directivity records typically do not exhibit pulse-type motions). Ground motions having such a distinct pulse-like character arise in general at the beginning of the seismogram, and their effects tend to increase the long-period portion of the acceleration response spectrum (Galesorkhi and Gouchon 2000). These types of ground motions may generate high demands that force the structures to dissipate this input energy with few large displacement excursions. Consequently, the risk of brittle failure for poorly detailed systems is considerably enhanced (Manfredi et al. 2000). The detrimental effects of such phenomenon have been recognized during many worldwide earthquakes including: 1992 Erzincan, 1992 Landers, 1994 Northridge, 1995 Kobe and most recently 1999 Kocaeli, Düzce and Chi-Chi earthquakes.

In contrast to post-earthquake observations, current seismic design practice, based on response spectrum concepts to specify design ground motion, does not by itself provide an adequate representation of near-fault ground motions. This phenomenon is more important for long period buildings. Although recommended and regulatory design codes and provisions such as ATC-40 (1996), UBC (ICBO 1997), FEMA-356 (ASCE 2000) and IBC (ICBO 2000) introduce site-source and distance dependent near-source factors (N_A and N_V) to amplify the elastic design spectrum (i.e., scaling the design base shear), the effectiveness of constant amplification factors in providing adequate ductility levels to structures and components located in the proximity of fault-zones is questionable. This concern arises from the fact that current design spectra were developed using stochastic processes having relatively long duration that characterizes more distant ground motions. Therefore, the pertinent question becomes how vulnerable is the existing building stock to near-fault ground motions since they were designed accounting primarily for far-fault ground motions. Studies show that high velocity pulses can place severe inelastic demands on multi-story structures (Hall et al. 1995, Heaton et al. 1995). Most recently, Alavi and Krawinkler (2004) demonstrated that intermediate period structures can also be susceptible.

Failures of modern engineered structures observed within the near-fault region in 1994 Northridge earthquake revealed the vulnerability of existing steel buildings against pulse-type ground motions. Additionally, strong directivity effects during the 1999 Kocaeli, Duzce and Chi-Chi earthquakes renewed the attention on the consequences of near-fault ground motions on structures. The objective of this study, therefore, is to examine the response of typical existing buildings to near-fault ground motions. In the

first part of this chapter, intrinsic characteristics of near-fault ground motions are reiterated from our current understanding of these events. Three existing steel buildings (of which two were instrumented by the California Strong Motion Instrumentation Program) selected for the evaluation study are then introduced. In order to facilitate an assessment of the effects of near-fault records on structural response, a set of near-fault ground motions having forward directivity and fling are assembled. These records are used in nonlinear time history (NTH) analyses, and their results are compared to the response of buildings to typical far-fault ground motions. A perceptive comparison of component demands, story demands and global system demands for different type of ground motion recordings is presented.

The effect of the ratio of pulse period to the fundamental period of the structure on the inelastic seismic demands of the buildings is also studied. Toward this objective, simple sinusoidal waveforms that adequately describe the nature of pulse-like motions are utilized as seismic input. Additionally, artificial fling effects are synthesized into typical near-fault motions having forward directivity, and the structural response of the same buildings is reexamined. Finally a discussion pertaining to the implication of near-fault ground motions on the design and assessment of structures (and steel moment frames in particular) is presented. This work is an attempt to collate analytical evidence from nonlinear dynamic analyses on possible effects of strong velocity pulses contained in near-fault ground motions on structural demand.

3.2 CHARACTERISTICS OF NEAR-FAULT GROUND MOTIONS

Far-fault ground motions have been observed to differ dramatically from their near-fault counterparts recorded within a few kilometers of the fault rupture plane. The response of structures to near-fault ground motions can be categorized into two distinct displacement history patterns that depend on the rupture process and corresponding directivity effect. When the rupture propagates forward toward the site, and the direction of slip on the fault is aligned with the site, ground motions oriented in this forward directivity path may follow certain radiation patterns and generate long period, short duration and large amplitude pulses (Somerville 1998). Forward directivity occurs where the fault rupture propagates with a velocity close to the shear-wave velocity. Displacement associated with such a shear-wave velocity is largest in the fault normal direction for strike-slip faults. Records may also exhibit backward directivity, yet they are typically less severe, and do not have distinctive velocity pulses (Somerville et al. 1997a).

On the other hand fling, being a result of the evolution of residual ground displacement due to tectonic deformation associated with rupture mechanism, is generally characterized by a unidirectional large amplitude velocity pulse and a monotonic step in the displacement time-history. Fling occurs in the direction of fault slip, and therefore is not strongly coupled with the forward directivity (Abrahamson 2001). It arises in strike-slip faults in the strike parallel direction as in Kocaeli and Duzce earthquakes (Kalkan et al. 2004), or in the strike-normal direction for dip-slips faults as in Chi-Chi earthquake (Mavroeidis and Papageorgiou 2003).

Large displacements (permanent ground deformations in the case of fling motion) would be of little consequence if they happen slowly, unless a structure straddled the fault (Hall et al. 1995). However, the duration of these displacements is closely related to the characteristic slip time of a point on the fault, and there is evidence that this slip is rapid (Heaton 1990). Therefore both shear-wave displacements as in forward directivity and static displacements as in fling emerge as pulses. Even for moderate magnitude earthquakes, amplitude of near-fault ground accelerations, velocities, and displacements, can be quite high especially in the records having forward directivity. Peak accelerations may exceed 1.0g, while peak velocities may exceed 2.0m/s, and peak displacements can go beyond 2.0m. The velocity and displacement time series of typical near-fault ground motions having forward directivity (Rinaldi record of 1994 Northridge earthquake) and fling (Sakarya - SKR record of 1999 Kocaeli earthquake) effects are compared to that of ordinary far-fault motion (Taft record of 1952 Kern-county earthquake) in Figure 3.1. High velocity pulses are quite distinctive for Rinaldi and SKR records, such pulses do not exist in a typical far-fault ground motion like Taft. The fault parallel component of the ground motion recorded at SKR station exhibits apparent tectonic deformation at the end of the displacement time history that is a typical signature of fling.

3.3 DESCRIPTION OF BUILDINGS USED FOR EVALUATION

Three existing steel special moment resisting frame (SMRF) buildings were selected as representative case studies to evaluate their seismic demands when subjected to near-fault

ground motions with forward directivity and fling, and to compare and contrast the respective responses to typical far-fault ground motions.

3.3.1 Four-Story Building

This building located in Southern California was designed in compliance with UBC (ICBO 1988) specifications. The structural system is composed of perimeter SMRFs to resist lateral loads and interior gravity frames. The floor plan and elevation view of the building with beam and column sections are shown in Figure 3.2. The columns are embedded into grade beams and anchored to the top of the pile cap essentially restraining displacements and rotations in all directions. All columns are made of A-572 grade 50 steel. The girders and beams are made of A-36 steel. The floor system is composed of 15.9cm thick slab (8.3cm light weight concrete and 7.6cm composite metal deck) at all floor levels and the roof. The total seismic weight of the building is 10,881 kN. Further details of the building are given in Krawinkler and Al-Ali (1996).

3.3.2 Six-Story Building

This moment frame steel structure was designed in accordance with UBC (ICBO 1973) requirements, and is located in Burbank, California. The rectangular plan of the building measures 36.6m x 36.6m with a 8.2cm thick light weight concrete slab over 7.5cm metal decking. The primary lateral load resisting system is a moment frame around the perimeter of the building. Interior frames are designed to carry only gravity loads. The plan view and the elevation of a typical perimeter frame with beam and column sections are shown in Figure 3.3. The building was instrumented with a total of 13 strong motion

sensors at the ground, 2nd, 3rd and roof levels. All columns are supported by base plates anchored on foundation beams which in turn are supported on a pair of 9.75m - 0.75m diameter concrete piles. Section properties were computed for A-36 steel with an assumed yield stress of 303MPa. The total building weight (excluding live loads) was estimated to be approximately 34,644kN.

3.3.3 Thirteen-Story Building

This building is located in South San Fernando Valley about 5km southwest of the Northridge epicenter and is composed of one basement floor and 13 floors above ground. Built in accordance with the 1973 UBC code, this structure has been the subject of previous investigations (Kunnath et al. 2004, Uang et al. 1997). As shown in Figure 3.4, it has a 48.8m square plan and an elevation of 57.5m. Also shown in this figure are beam and column sections. The lateral load resisting system is composed of four identical perimeter frames. The floor plan increases at the second floor to form a plaza level that terminates on three sides into the hillside. The resulting restraint at this level has not been accounted for in this study since the objective of the evaluation is to obtain generic information on moment frames rather than quantify the response of a particular structure. A seismic weight of 140,909 kN was used in the evaluation of this structure.

3.4 DEVELOPMENT OF ANALYTICAL MODELS

The nonlinear evaluations were carried out using a typical two-dimensional frame from each of the buildings. The computer simulations were carried out using the open source finite element platform, OpenSees (2005). A force-based nonlinear beam-column element

that utilizes a layered '*fiber*' section is utilized to model all components of the frame models. A fiber section model at each integration point, which in turn is associated with uniaxial material models and enforces Bernoulli beam assumptions for axial force and bending, represents the force-based element. Centerline dimensions were used in the element modeling for all cases. For the time-history evaluations, one half of the total building mass was applied to the frame distributed proportionally to the floor nodes.

Since our objective is not to evaluate the seismic performance of these particular buildings but to utilize typical moment frames of varying height, the simulation of special features such as local connection fracture is not the primary concern. Consequently, the modeling of the members and connections was based on the assumption of stable hysteresis derived from a bilinear stress-strain model. In constructing the computer models, the columns were assumed to be fixed at the base level. In the case of the 4-story building, the exterior frame along Line-1 was modeled. Similarly, frame models for the 6 and 13-story buildings were developed along Line-1 and Line-G, respectively. Additional details of the 6 and 13-story buildings are reported in Kunnath et al. (2004). The analytical models for 6 and 13-story buildings were validated using available recorded data from different levels of buildings, and typical comparisons of recorded and computed displacement at the roof level of each building are displayed in Figures 3.3 and 3.4. Note that the simulation models of the frames used in the evaluation represent the actual state of the building and the corresponding fundamental periods are calibrated to observed response. Accordingly, Raleigh damping of 5 percent for the first two vibration modes of six-story building, and 5 percent for the first and third vibration modes of thirteen-story building were used.

3.5 GROUND MOTION DATABASE

The ground motion database compiled for NTH analyses constitutes a representative number of far-fault and near-fault ground motions from a variety of tectonic environments. A total of 21 records were selected to cover a range of frequency content, duration, and amplitude. Near-fault records were chosen so as to consider the presence of both forward directivity and fling effects. Hence, the assembled database can be investigated in three sub datasets. The first set contains seven ordinary far-fault ground motions recorded within 80km of the causative fault plane from earthquakes in the magnitude (M_W) range of 6.4 to 7.5 at soil or stiff soil sites. The second set includes seven near-fault ground motions characterized with forward directivity effect. These ground motions were populated from the SAC steel project (Somerville et al. 1997b) and the CDMG Strong Motion Instrumentation Program (Somerville 1998), and contains records either taken from soil or stiff soil sites. These records are from earthquakes having a magnitude (M_W) range of 6.7 to 7.1, and recorded at closest fault distance of 0.0 to 15 km. In the final set, a total of seven near-fault ground motions characterized with fling displacement were collected. They were recorded from 1999 (M_W 7.4) Kocaeli (Turkey) and 1999 (M_W 7.6) Chi-Chi (Taiwan) earthquakes at distances of 2.2 to 13.8 km. Pertinent information on the ground motion data sets including faulting mechanism, site classification of stations and peak ground acceleration (PGA), peak ground velocity (PGV) and peak ground displacement (PGD) of records are presented in Table 3.1. Also shown in this table is the fling displacement of near-fault records.

It is of significance to note that raw acceleration data was used for fling records of Kocaeli and Chi-Chi earthquakes, since conventional data processing procedures

eliminate or distort the original waveforms through filtering. Utilized in this study is a data processing technique proposed in Iwan et al. (1985) and refined in Iwan and Chen (1994) to recover the long period components from near-fault accelerograms, and the process has been extensively elaborated in Boore (2001) and Boore et al. (2002) during the correction of 1999 Chi-Chi and Hector Mine earthquake records, respectively. In this study, the pre-event mean was removed using the zero-order correction described in Boore (2001) prior to the application of the baseline correction.

The major concern in baseline correction is the selection of appropriate corner periods to establish the segmental polynomial fits to satisfy two requirements: First, true tectonic deformation should be represented in the displacement time history. Second, the final velocities should oscillate around zero reference after the end of the time-series. The residual displacement due to fling were computed based on the GPS measurements for Chi-Chi earthquake ground motions, this information was retrieved from the study of Boore (2001). Since such reported information is not available for Kocaeli earthquake stations, the baseline corrections of the Kocaeli records were only performed considering the requirement of the zero-velocity crossing at the end of the time-history. The purpose of applying such a correction procedure in this study is to get consistency in fling records reflecting the true permanent ground displacement, thus to investigate consequences of static offset in the displacement time history on structural response. Studies (Boore et al. 1999, Boore 2001) have shown that elastic response spectra for periods less than about 20sec are usually not affected by the baseline correction.

3.6 RESPONSE SPECTRA OF GROUND MOTIONS

For NTH analyses presented in subsequent sections, ground motions given in Table 3.1 were scaled such that the spectrum of each record matches the five-percent damped UBC (ICBO 1997) design spectrum with minimum error in the period range of 0.6sec to 4.0sec. Hence, the mean of the seven records in each ground motion category reasonably represent the design spectrum. Such a scaling procedure has been used previously (Alavi and Krawinkler, 2004), and found to be necessary to facilitate the comparison of results from the different ground motion sets in a consistent manner. Design spectrum parameters were selected so as to consider explicitly the near-fault effects via near-source amplification factors (N_A *and* N_V) introduced in UBC. Therefore the spectrum was constructed for soil type S_D and fault distance of 5km (Seismic Zone 4). The spectra of the scaled ground motions together with the design spectrum are exhibited in Figure 3.5. Also marked on this figure are the fundamental periods of each building (Figure 3.5c). The fundamental modal periods for the buildings are as follows: 4-story building, T_1 = 1.05sec; 6-story building, T_1 = 1.40sec; and 13-story building, T_1 = 3.05sec. It is observed that for near-fault motions particularly for fling records, the effect of the inherent pulse tends to increase the long-period portion of the acceleration response spectrum (Figure 5a-5b). This suggests that amplifying the design spectrum with explicit near-source factors as in UBC may not be always conservative.

3.7 SEISMIC RESPONSE EVALUATION OF BUILDINGS

In all, a total of 63 nonlinear time-history (NTH) simulations were conducted on the three buildings. Interstory drift ratio (IDR), defined as the relative displacement between two consecutive story levels normalized by the story height, is used as the primary measure of seismic demand. Additional demand measures, such as component and story ductility were also investigated. In general there is reasonable correlation between interstory drift demands and component/story level ductility demands; hence these results are not included here. The peak interstory drift profiles obtained from NTH analyses of the buildings subjected to the three sets of ground motions (i.e., far-fault motions, near-fault motions with forward directivity, and near-fault motions with fling) are presented in Figure 3.6 with their associated dispersion values. For the 4-story building, far-fault motions produce nearly uniform interstory drift demands for most records with the exception of Taft record which triggers higher mode effects resulting in increased demands in the upper stories. In case of near-fault records, they impose higher demands than far-fault records though the maximum drift is generally concentrated at the lower story levels. The largest demand is caused by the Chi-Chi record (TCU052) which produced a 3.6 percent interstory drift at the 1st story.

For the 6-story building, the maximum story demand for far-fault records is observed to be either at the 1st or 5th story levels and depends on the frequency content of the motion. Though similar observations hold for near-source records, the demands at the intermediate levels are much higher. Of the entire data set, the SKR record generated the highest demand (5.3 percent interstory drift) at the 1st story. Three near-fault ground motions in particular (Rinaldi, Erzincan, and TCU068) created significant demands at

intermediate stories. For the 13-story building, the SKR record (a typical near-fault motion with fling) generated the highest demand (5 percent interstory drift) at the 2nd story level. Higher mode effects are predominant in many of the near-fault records (e.g., YPT, TCU0129, Olive V., Rinaldi) causing a shift in demands from the lower to upper stories. The variation in story demand for the far-fault records is less significant.

While higher mode effects are expected to contribute to the response of the 6 and 13-story buildings, the response of the 4-story building demonstrates that even for low-rise buildings higher mode effects could play a role. In order to ascertain the contribution of higher modes, it was necessary to inspect both the acceleration and velocity spectra of the ground motions collectively. Figure 3.7 depicts the spectral velocity of the critical records that generated the largest demands in the three buildings. In examining the spectral content of records, it must be noted that modal periods are constantly changing in a nonlinear system and that so-called “higher mode periods” also shift as the building moves into the inelastic range. The dashed lines shown in Figure 3.7 refer to the modal periods in the elastic range. All these lines will gradually move to the right as component yielding progresses. For objective of correlating the information on the spectral demands with the observed behavior, the building responses were re-examined. Therefore for the 4-story building, though most of the records caused higher demands in the lower stories, Taft and TCU129 records are seen to activate higher mode effects resulting in increased demands in the upper and intermediate stories. The spectral velocities at the 2nd and 3rd modes for Taft and TCU129 records are more significant than their first mode counterpart. Yet for the Rinaldi record the dominant first mode response is clearly observed from the velocity spectra. Similarly, looking at the velocity spectra for Taft,

Erzincan and TCU129 records explain the observed higher mode response for the 6-story building. Finally, for the 13-story building, Cliff house, LGPC and TCU129 motions produced larger demands at intermediate and upper levels. The spectral velocities for these records at the higher modes periods are much larger than that for the fundamental period keeping in mind that a shift to the right of the spectra is to be expected as yielding of components occur.

In summary, the median maximum demands as well as the scatter (dispersion) in the peak values for the three buildings were higher for near-fault records than far-fault motions. Additionally, the demands in the lower levels for records with fling were significantly higher than records with forward-directivity. Overall, higher mode effects were more predominant in forward-directivity records.

In Figure 3.8, the severity of near-fault ground motions having forward directivity and fling are compared with far-fault motions at the component level. M/M_y is the ratio of the moment demand to the yield moment and θ / θ_y is the ratio of the member end rotation to the yield rotation. The results shown are for a typical element but convey the general difference in component demands between far-fault and near-fault ground motions. In this case, the demands on an interior column on the first story level of the 6-story building experiencing the largest demand among each ground motion category are presented.

The largest deformation demands in near-fault shaking are associated with fewer reversed cycles of loading. This effect is due to the presence of long-duration high-amplitude pulses in near-fault records causing dissipation of sudden energy in a short period of time in a single or few excursions. On the other hand, the energy demand on a

structural system subjected to a far-fault motion tends to gradually increase over a longer duration causing an incremental build up of input energy. The total input energy variation for each record is also displayed in Figure 3.8. It can be inferred from the figure that the magnitude of the input energy by itself is not a complete measure of the severity of the ground motion. For example, the peak demands can be caused by ground motions with smaller input energies. Another important observation that was alluded to earlier is the fact that the gradual build up of input energy for far-fault records results in increased reversed inelastic cyclic action and low-cycle fatigue damage while near-fault motions are characterized by fewer inelastic displacement cycles followed by several cycles of elastic action. The consequence of a single predominant peak is a well-pronounced permanent offset (displacement) and the subsequent response is essentially a series of elastic cycles about this deformed configuration. Also shown in Figure 3.8 are the inelastic and elastic components of the total deformation. It is evident that the elastic part of the rotation is almost negligible which suggests that for ductile elements with significant inelastic behavior, the peak component deformation is generally equivalent to the plastic deformation.

Figure 3.8 also provides a glimpse of the implications of cyclic demand and the influence of low-cycle fatigue on the performance of structures. The ductility demands on the column are 7.6, 6.4 and 7.7 for Taft, Olive V. and SKR records, respectively. However there are numerous additional cycles of deformation which exceed the yield rotation for the far-fault motion. Since the inelastic response results in a permanent drift, it is more convenient to count the number of half cycles wherein each half cycle is the peak-to-peak amplitude. If the peak-to-peak amplitude exceeds twice the yield rotation,

each such cycle is referred to as a “plastic cycle”. For the critical column shown in Figure 3.8, there were 20 half plastic cycles during the response to the far-fault record. The near-fault motions with forward directivity (Olive V) and fling step effects (SKR) both resulted in only 6 half plastic cycles. The cumulative damage resulting from plastic cycles is much greater than implied by the peak ductility demand, and should not be ignored when assessing the performance of the component (see Chapter 2).

From the information generated through the evaluation of the three buildings discussed above, it is clear that buildings respond differently to far-fault and near-fault ground motions. However in order to achieve a more coherent understanding of the effects of near-fault records, a systematic study was conducted on the same structures using simple pulse motions that reasonably represent forward-directivity and fling effects.

3.8 SIMPLE MATHEMATICAL MODELS FOR NEAR-FAULT GROUND MOTION PULSES

Simple pulses do not necessarily match the ground acceleration of original records (Makris and Chang 2000). It would also be unrealistic to expect that near-fault records can be represented fully by equivalent simple pulses. Since near-fault recordings come from great variations in the vicinity of an active fault system, the wave propagation pattern of ground motion is strongly affected by radiation pattern, directivity, rupture mechanism, stress drop and also by geo-morphology and lateral scatter, therefore real recordings may contain high-frequency components as well as several non-homogenous velocity peaks. Based on the complex form of near-fault records, it is not always possible to calibrate simple models to satisfy all conditions aforementioned, unless the real record

to be represented is significantly simple. For the representation of near-fault records one can utilize more complicated pulse models such as those derived based on wavelet functions (e.g., Mavroeidis and Papageorgiou 2003, Mavroeidis et al. 2004), however they still have similar limitations, and their calibration is even more difficult due to the presence of supplementary parameters in the definition of wavelet functions. Despite the stated limitations, the use of simple pulses offers a distinct advantage in distinguishing the response of typical structures to variations in pulse characteristics.

Recent studies by Sasani and Bertero (2000), and Alavi and Krawinkler (2004) have demonstrated that simple pulses can be used to capture the salient response characteristics of structures subjected to near-fault ground motions within limitations. In the following, near-fault pulse type motions are simulated using waveforms that approximately reproduce the response spectrum of actual near-fault records as a function of time domain parameters such as the duration and amplitude of the near-fault pulse. Two types of sinusoidal wave shapes previously studied by Sasani and Bertero (2000) were used to mimic near-fault records having forward directivity and fling displacement. Simplified waveform representations are defined by the number of half cycles as shown in Figure 3.9. Figure 3.9a approximates a fling type of motion where the record exhibits a static offset at the end of the displacement time history, while Figure 3.9b represents a forward directivity type of motion.

The mathematical models for the acceleration time-history of the two pulse models can be expressed as follows:

- Pulse Type-A (Fling)

$$a(t) = \frac{2\pi D}{T_p{}^2} \sin\left[\frac{2\pi}{T_p}(T - T_i)\right] \tag{3.1}$$

- Pulse Type-B (Forward directivity)

$$a(t) = \frac{\pi D}{T_p{}^2} \sin\left[\frac{2\pi}{T_p}(T - T_i)\right] \quad \text{for} \quad \begin{cases} Ti < T < (Ti + 0.5Tp) \\ (T_i + T_p) < T < (T_i + 1.5T_p) \end{cases} \tag{3.2}$$

$$a(t) = \frac{2\pi D}{T_p{}^2} \sin\left[\frac{2\pi}{T_p}(T - T_i)\right] \quad \text{for} \quad (Ti + 0.5Tp) < \mathrm{T} < (Ti + Tp) \tag{3.3}$$

where D is the maximum amplitude of the displacement obtained by double time-integration of acceleration, a(t), T_p is the period of sin-pulse, and T_i is the pulse arrival time. The acceleration, velocity and displacement (5 percent damped) elastic response spectra of the pulse models are shown in Figure 3.10 where the spectral ordinates are normalized by their corresponding peak time history values (i.e., PGA, PGV and PGD). It should be noted that for a given pulse intensity ($a_{g,max}$) for both pulse models, PGV for Type-B pulse, used to normalize the velocity spectrum is half of that for Type-A pulse, similarly for the normalization of the displacement spectrum, the ratio of PGD of pulse Type-B to that of Type-A is around 0.25. Yet, it is evident from the velocity and displacement spectra that a Type-B pulse is more damaging than a Type-A pulse. Although it is obvious for simple pulse models that the predominant period of motion coincides approximately with the peak of velocity response spectrum, it is not always possible to capture the pulse period of actual near-fault records as easily and accurately due to the presence of multiple peaks in the velocity spectrum.

3.9 RESPONSE OF BUILDINGS TO SIMPLE PULSE MODELS

The building models are re-analyzed using simple pulse models with forward directivity and fling effects to study the influence of pulse period on interstory drift demands. In this parametric study, the pulse period is varied from 0.5 to 1.5 of the fundamental period of the buildings. Prior to application of the pulses, pulse records were scaled in a manner consistent with the ground motion scaling procedure whereby the acceleration spectra of each pulse matched the five-percent damped UBC design spectrum with minimum dispersion in the period range of 0.6sec to 4.0sec by adjusting the pulse intensity. This was necessary to enable a reasonable comparison to the results obtained in the previous phase of the study. Figures 3.11 to 3.13 summarize the responses of 4, 6, and 13-story buildings to ground motions inputs characterized by both pulse types A and B. The roof drift indicated in the plots are the ratio of the roof displacement to the building height.

The distributions of response parameters collectively confirm that demand is conditioned on the ratio of pulse period (T_p) to fundamental period (T). Demands are clearly amplified as the pulse period approaches the fundamental period of the building model. In the neighborhood where T_p/T = 1.0, the maximum story demands are concentrated on the lower levels indicating a primarily first mode response. This holds true even as the ratio T_p/T exceeds unity. When the ratio is much lower than 1.0 and the pulse period approaches the second and third modal periods, the maximum interstory demands migrates to the upper stories clearly identifying the contributions of higher modes. Similar findings have been reported in Alavi and Krawinkler (2004) where

MDOF generic frames were subjected to forward directivity type pulses with various T_p/T values.

Observations synthesized from Figures 3.11 to 3.13 indicate that forward directivity pulses result in higher demands than fling pulses. This can be attributed to the forward and backward momentum acquired during the initial and final phase of the forward directivity pulse. On the other hand, fling type of motion contains only forward momentum. In case of forward directivity the maximum drift demand in the upper stories in many cases is almost two times higher than that produced by fling motions. Higher mode effects are not as evident in the response to fling type motions but are more clearly evident in all buildings for forward directivity pulses when T_p/T is less than 0.8.

Additional insight on the transient response at the story and component levels for each pulse type is demonstrated in Figure 3.14. Shown in the figure are the 3rd story interstory drift variation and interior column base rotation from 13-story building. The pulse period is equal to the fundamental period of the building for both cases. The analyses indicate that, upon arrival of the pulse, the building starts to deform and is eventually displaced into the inelastic range in the same cycle. The peak time and end time of each pulse are indicated in the figure by dash lines. Following the impact of pulse Type-B, the 3rd story displaces laterally by 40 mm which corresponds to 3.8 percent interstory drift. For reference, the elastic drift limit in the 3rd story is 0.7 percent. Initially two pulses follow the same path dictated by the forward momentum phase, but the reversing phase of pulse Type-B increases the response compared to pulse Type-A. The higher peak-to-peak amplitude of the reversing pulse represented by pulse Type-B has

greater damage potential particularly if the pulse period is close to the fundamental period of the building.

3.10 EFFECTS OF INCORPORATING ARTIFICIAL FLING EFFECT ON NEAR-FAULT GROUND MOTIONS HAVING FORWARD DIRECTIVITY

The results presented in preceding sections suggest that fling effects are less significant than forward directivity and that systems subjected to records with predominant fling step displacements respond primarily in the first mode. To further investigate the consequences of fling step effects, a final series of simulations was carried out in which actual records with forward directivity were modified to include fling displacement. As indicated earlier, this coupling is unlikely given that fling occurs in the direction of fault slip while forward directivity is associated in the fault normal direction as in strike-slip faults. However, this theoretical study will serve to provide an understanding of the severity of fling displacements and offer a conservative approximation of near-fault effects in seismic evaluation.

The artificial fling motion is generated by incorporating Type-A velocity pulse into near-fault records that are originally characterized by forward directivity only. The contribution from the pulse motion to the simulated ground motion (i.e., static offset in the displacement time history) is manipulated by changing the velocity amplitude of the pulse model. The arrival of the peak velocity (in Type-A) is adjusted to occur at approximately the same time as the peak velocity of the original ground motion. The pulse period is selected to match the building period. The amplitude of the pulse is

carefully selected so as not to distort the intensity of the original motion, but only introduce fling effects. The sequence of the procedure to create an artificial fling displacement is presented for 13-story building in Figure 3.15. One of the records from the Rinaldi station during the 1994 Northridge, California earthquake is selected for illustration. Also shown in this figure are the acceleration, velocity, and displacement histories of the original and modified motions.

The pulse periods of the fling motions added to the Rinaldi records were based on the fundamental periods of each building, therefore for each building a new record was generated. Figure 3.16 shows the Fast-Fourier amplitude spectrum of the original and fling-added motion. It is observed that the spectral shapes are generally preserved with small amplitude changes in the spectral demands at periods between 1.0s to 2.5s. Conversely, the addition of fling amplified the first mode spectral amplitude, however reduce the spectral amplitudes at periods less than 1.0s. The consequence of this alteration is to further excite the fundamental mode while suppressing the contribution of the higher modes. This effect is clearly evident in the response of the three buildings shown in Figure 3.17. The original records containing forward directivity clearly show the influence of higher modes with significant interstory demands in the upper stories. When the fling-modified motions are applied to the frames, the demands in the upper stories are visibly reduced indicating a suppression of higher mode effects. It should be noted that similar scaling procedure as described before is applied to fling added motions prior to NTH analyses.

3.11 CONCLUSIONS

Although observed damage and failure of engineered structures during recent earthquakes have revealed the susceptibility of the existing building stock to near-fault ground motions, there is still considerable uncertainty on the consequences of near-fault ground motions on the response of typical building structures. Current practice is not adequately equipped to incorporate the effects of coherent long-period pulses in the design process. Methods to implicitly consider inelastic demands by amplifying the design spectra do not provide a reliable basis for representing near-fault ground motions. Hence the purpose of this study is to provide new insight and additional data on the response of moment frames to near-fault ground motions, and contrast the demands with far-fault records.

The analytical simulations carried out in this study show that typical steel moment frames can be subjected to large displacement demands at the arrival of the velocity pulse that require the structure to dissipate considerable input energy in a single or relatively few plastic cycles. This demand will impact structures with limited ductility capacity. In contrast, far fault motions build input energy more gradually and though the displacement demands are on average lower than the demands in near-fault records, the structural system is subjected to significantly more plastic cycles. Hence cumulative effects are more pronounced in far-fault ground motions.

Studies with simple pulses clearly demonstrated the migration of demands from lower to upper stories when the ratio of the pulse period to building period was below 0.8. Records with forward directivity resulted in more instances of higher mode demand while records with fling displacement almost always caused the systems to respond primarily in

the fundamental mode. For all the near-fault pulses investigated in this study, the severity of the demands is controlled by the ratio of the pulse to system period.

It has been long recognized that near-fault motions characterized by forward directivity effects are potentially more damaging but the consequences of fling displacements have not been as well understood. In the present study fling effects were considered in several ways: by examining the response of buildings to recorded ground motions that contain fling effects, by using equivalent half sinusoidal pulses and by artificially introducing carefully calibrated pulses into actual near fault recordings. Although simple pulse waveforms do not contain all the characteristics of recordings from real earthquakes, they provide a convenient means of understanding and correlating the relationship between pulse periods, system characteristics and inelastic demands. Findings from this study indicate that near-fault records with fling can be more damaging than far-fault records but they tend to accentuate first mode behavior.

Finally, it can also be concluded that a careful examination of acceleration and velocity spectra, collectively, can provide engineers with a reasonable assessment of the damage potential of near-fault records. Demands in the fundamental and higher modes must be evaluated by taking into consideration the fact that modal periods shift to the right of the spectrum as the system moves from the elastic to inelastic state.

Table 3.1 Ground motion ensemble

No.	Year	Earthquake	M_W	Mech.*	Station	Comp.	Source**	Site Class	PGA (g)	PGV (cm/sec)	PGD (cm)	Fling Disp. (cm)
(a) Far-Fault Recordings												
1	1952	Kern county	7.5	TH/REV	Taft	111	1	Soil	0.18	17.50	8.79	-
2	1979	Imperial-Valley	6.5	SS	Calexico	225	1	Soil	0.27	21.24	9.03	-
3	1989	Loma Prieta	7.0	OB	Presidio	00	1	Soil	0.10	12.91	4.32	-
4	1989	Loma Prieta	7.0	OB	Cliff House	90	1	Stiff soil	0.11	19.79	5.02	-
5	1992	Big Bear	6.4	SS	Desert Hot Spr.	90	2	Soil	0.23	19.14	4.53	-
6	1994	Northridge	6.7	TH	Century CCC	90	2	Soil	0.26	21.19	7.85	-
7	1999	Kocaeli	7.4	SS	Ambarli	EW (90)	1	Soil	0.18	33.23	25.85	-
(b) Near Fault Recordings (Forward-Rupture Directivity)												-
1	1989	Loma Prieta	7.0	OB	LGPC	00	1	Stiff soil	0.56	94.81	41.13	-
2	1989	Loma Prieta	7.0	OB	Lexington Dam	90	1	Stiff soil	0.41	94.26	36.66	-
3	1992	Cape Mendocino	7.1	TH	Petrolia	90	1	Stiff soil	0.66	90.16	28.89	-
4	1992	Erzincan	6.7	SS	Erzincan	EW	1	Soil	0.50	64.32	21.93	-
5	1994	Northridge	6.7	TH	Rinaldi	275	2	Soil	0.84	174.79	48.96	-
6	1994	Northridge	6.7	TH	Olive View	360	1	Soil	0.84	130.37	31.72	-
7	1995	Kobe	6.9	SS	KJMA	00	1	Stiff soil	0.82	81.62	17.71	-
(c) Near Fault Recordings (Fling-Step)												
1	1999	Kocaeli	7.4	SS	Sakarya (SKR)	EW	3	Stiff-soil	0.41	82.05	205.93	186.76
2	1999	Kocaeli	7.4	SS	Yarimca (YPT)	NS	3	Soil	0.23	88.83	184.84	145.79
3	1999	Chi-Chi	7.6	TH	TCU052	NS	4	Soil	0.44	216.00	709.09	697.12
4	1999	Chi-Chi	7.6	TH	TCU068	EW	4	Soil	0.50	277.56	715.82	601.84
5	1999	Chi-Chi	7.6	TH	TCU074	EW	4	Soil	0.59	68.90	193.22	174.56
6	1999	Chi-Chi	7.6	TH	TCU084	NS	4	Soil	0.42	42.63	64.91	59.43
7	1999	Chi-Chi	7.6	TH	TCU129	NS	4	Soil	0.61	54.56	82.70	67.54

** Faulting Mechanism = TH: Thrust; REV: Reverse; SS: Strike-slip; OB: Oblique*

*** Data Source = 1: PEER (http://peer.berkeley.edu/smcat); 2: Cosmos (http://db.cosmos-eq.org);*
3: ERD (http://angora.deprem.gov.tr/); 4: http://scman.cwb.gov.tw/eqv5/special/19990921/pgadata-asci0704.htm

Note: Original fling ground motions from data sources (3) and (4) were reprocessed.

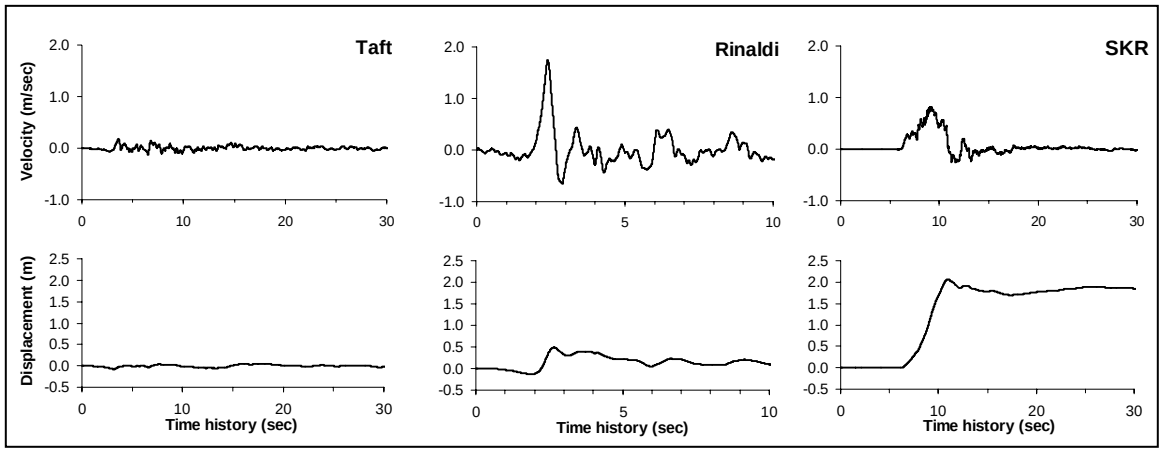

(a) (b) (c)

Figure 3.1 Typical velocity and displacement time histories of (a) Far-fault, (b) Near-fault (forward directivity), and (c) Near-fault (fling) ground motions.

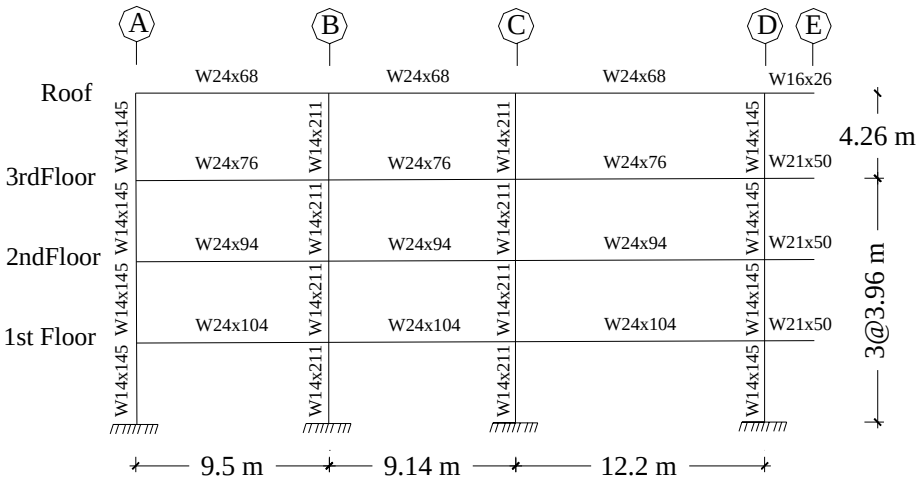

(a) Elevation view

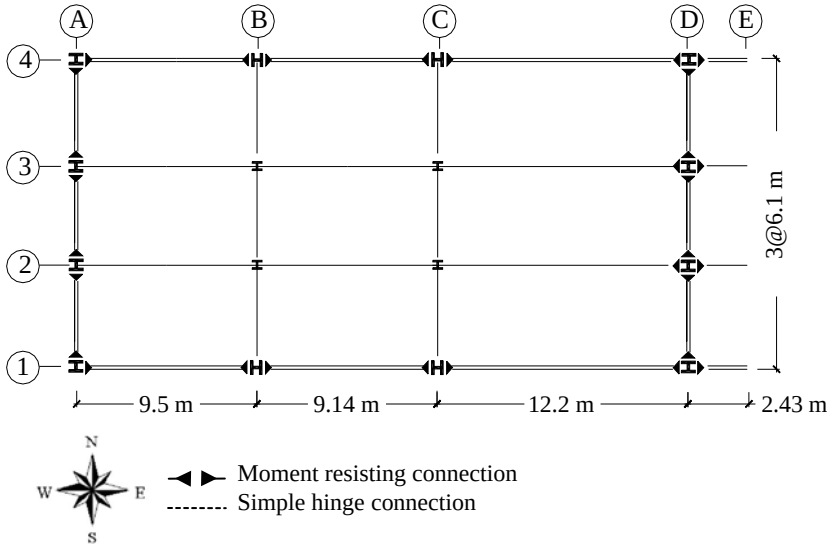

(b) Plan view of perimeter frames

COLUMNS				
Story	**A**	**B**	**C**	**D**
1	W14x145	W14x211	W14x211	W14x145
2	W14x145	W14x211	W14x211	W14x145
3	W14x145	W14x211	W14x211	W14x145
4	W14x145	W14x211	W14x211	W14x145

BEAMS				
Story	**A-B**	**B-C**	**C-D**	**D-E**
1	W24x104	W24x104	W24x104	W21x50
2	W24x94	W24x94	W24x94	W21x50
3	W24x76	W24x76	W24x76	W21x50
4	W24x68	W24x68	W24x68	W16x26

(c) Column and beam sections

Figure 3.2 Structural configuration of 4-story building.

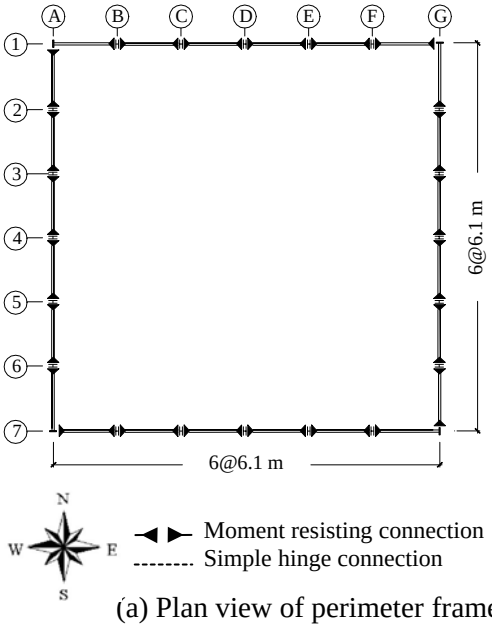

(a) Plan view of perimeter frames

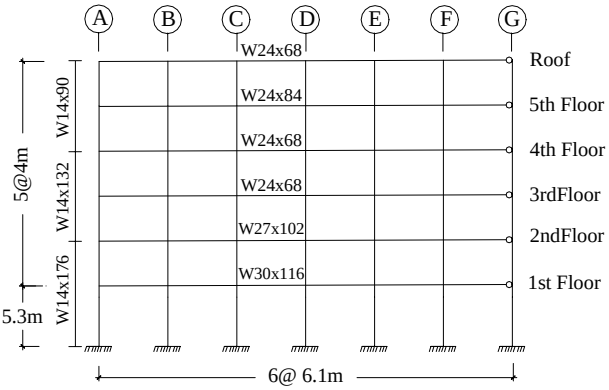

(b) Elevation

COLUMNS

Story	A	B	C	D	E	F	G
1	W14x176	W14x176	W14x176	W14x176	W14x176	W14x176	W14x176
2	W14x176	W14x176	W14x176	W14x176	W14x176	W14x176	W14x176
3	W14x132	W14x132	W14x132	W14x132	W14x132	W14x132	W14x132
4	W14x132	W14x132	W14x132	W14x132	W14x132	W14x132	W14x132
5	W14x90	W14x90	W14x90	W14x90	W14x90	W14x90	W14x90
6	W14x90	W14x90	W14x90	W14x90	W14x90	W14x90	W14x90

BEAMS

Story	A-B	B-C	C-D	D-E	E-F	F-G
1	W30x116	W30x116	W30x116	W30x116	W30x116	W30x116
2	W27x102	W27x102	W27x102	W27x102	W27x102	W27x102
3	W24x68	W24x68	W24x68	W24x68	W24x68	W24x68
4	W24x68	W24x68	W24x68	W24x68	W24x68	W24x68
5	W24x84	W24x84	W24x84	W24x84	W24x84	W24x84
6	W24x68	W24x68	W24x68	W24x68	W24x68	W24x68

(c) Column and beam sections

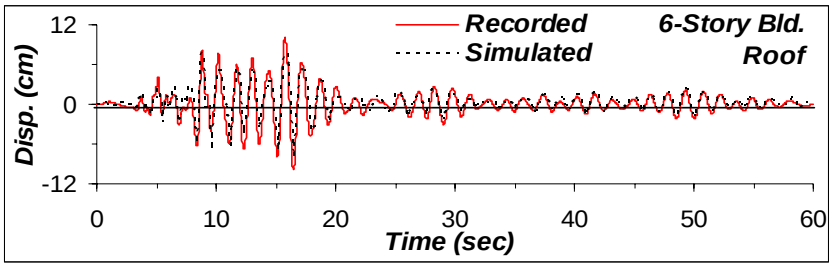

(d) Recorded and computed response at the roof level

Figure 3.3 (a-b-c) Structural details of 6-story building and (d) model validation

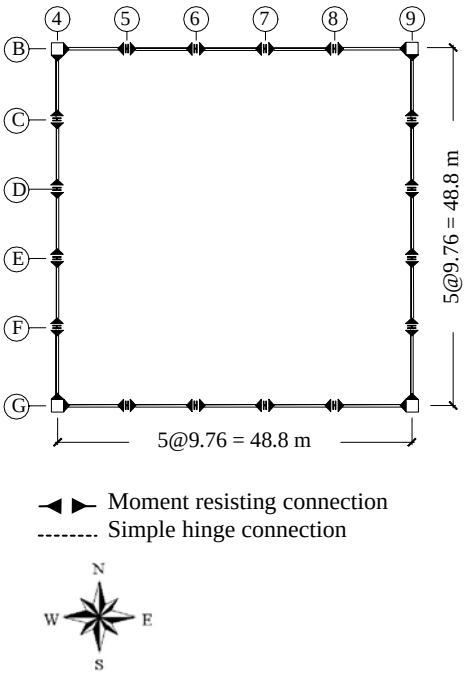

(a) Plan view of perimeter frames

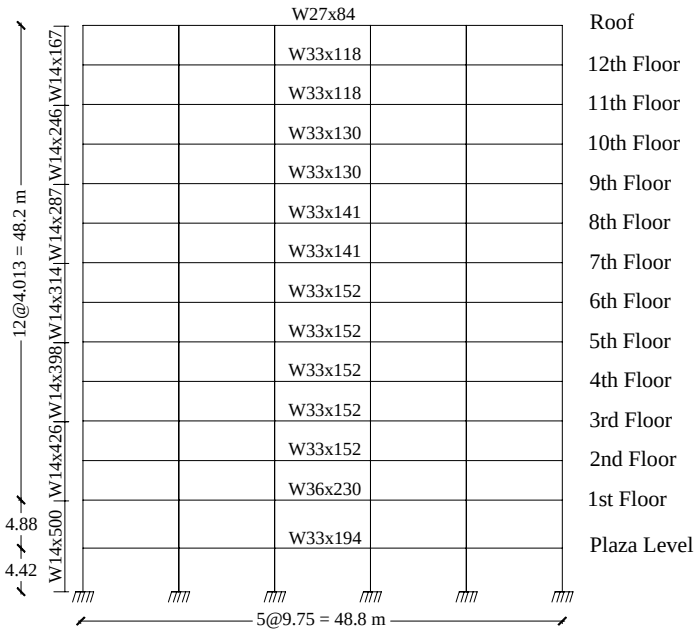

(b) Elevation

COLUMNS

Story	A	B	C	D	E	F
Plaza Level	W14x500	W14x500	W14x500	W14x500	W14x500	W14x500
1	W14x500	W14x500	W14x500	W14x500	W14x500	W14x500
2-3	W14x426	W14x426	W14x426	W14x426	W14x426	W14x426
4-5	W14x398	W14x398	W14x398	W14x398	W14x398	W14x398
6-7	W14x314	W14x314	W14x314	W14x314	W14x314	W14x314
8-9	W14x287	W14x287	W14x287	W14x287	W14x287	W14x287
10-11	W14x246	W14x246	W14x246	W14x246	W14x246	W14x246
12-13	W14x167	W14x167	W14x167	W14x167	W14x167	W14x167

BEAMS

Story	A-B	B-C	C-D	D-E	E-F
Plaza Level	W33x194	W33x194	W33x194	W33x194	W33x194
1	W36x230	W36x230	W36x230	W36x230	W36x230
2-6	W33x152	W33x152	W33x152	W33x152	W33x152
7-8	W33x141	W33x141	W33x141	W33x141	W33x141
9-10	W33x130	W33x130	W33x130	W33x130	W33x130
11-12	W33x118	W33x118	W33x118	W33x118	W33x118
Roof	W27x84	W27x84	W27x84	W27x84	W27x84

(c) Column and beam sections

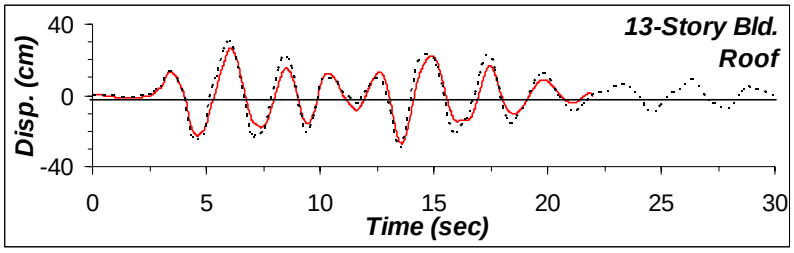

(d) Recorded and computed response at the roof level

Figure 3.4 (a-b-c) Structural details of 13-story building and (d) model validation

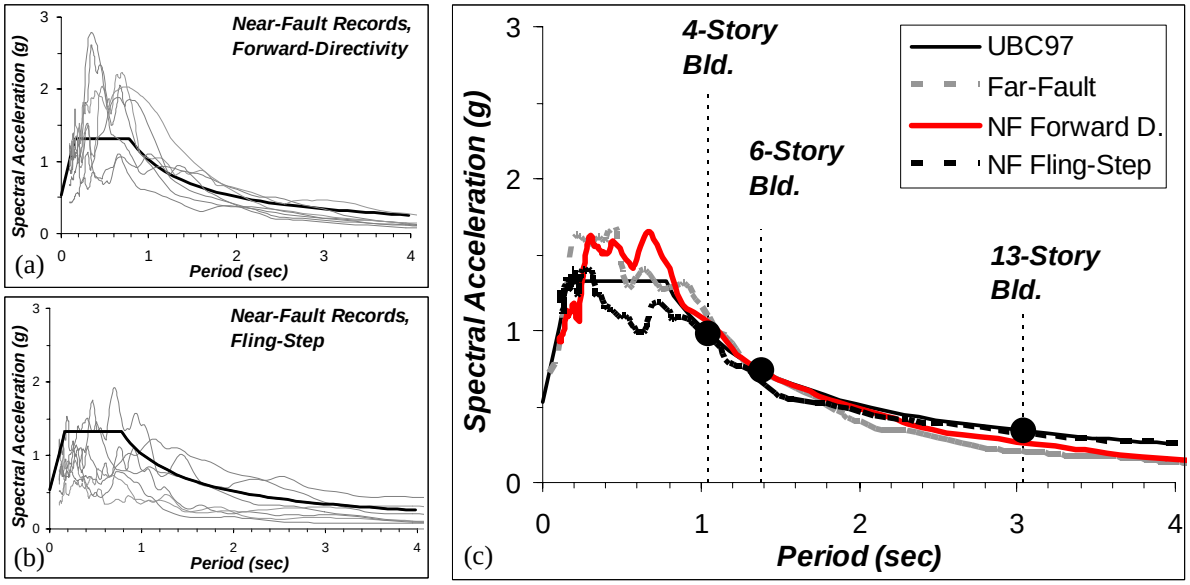

Figure 3.5 UBC (ICBO 1997) design spectrum and response spectra of (a) original forward-directivity records (b) original fling records, c) design spectrum and mean response spectra of scaled ground motions (*Note that the dash lines indicate the fundamental period of each building*).

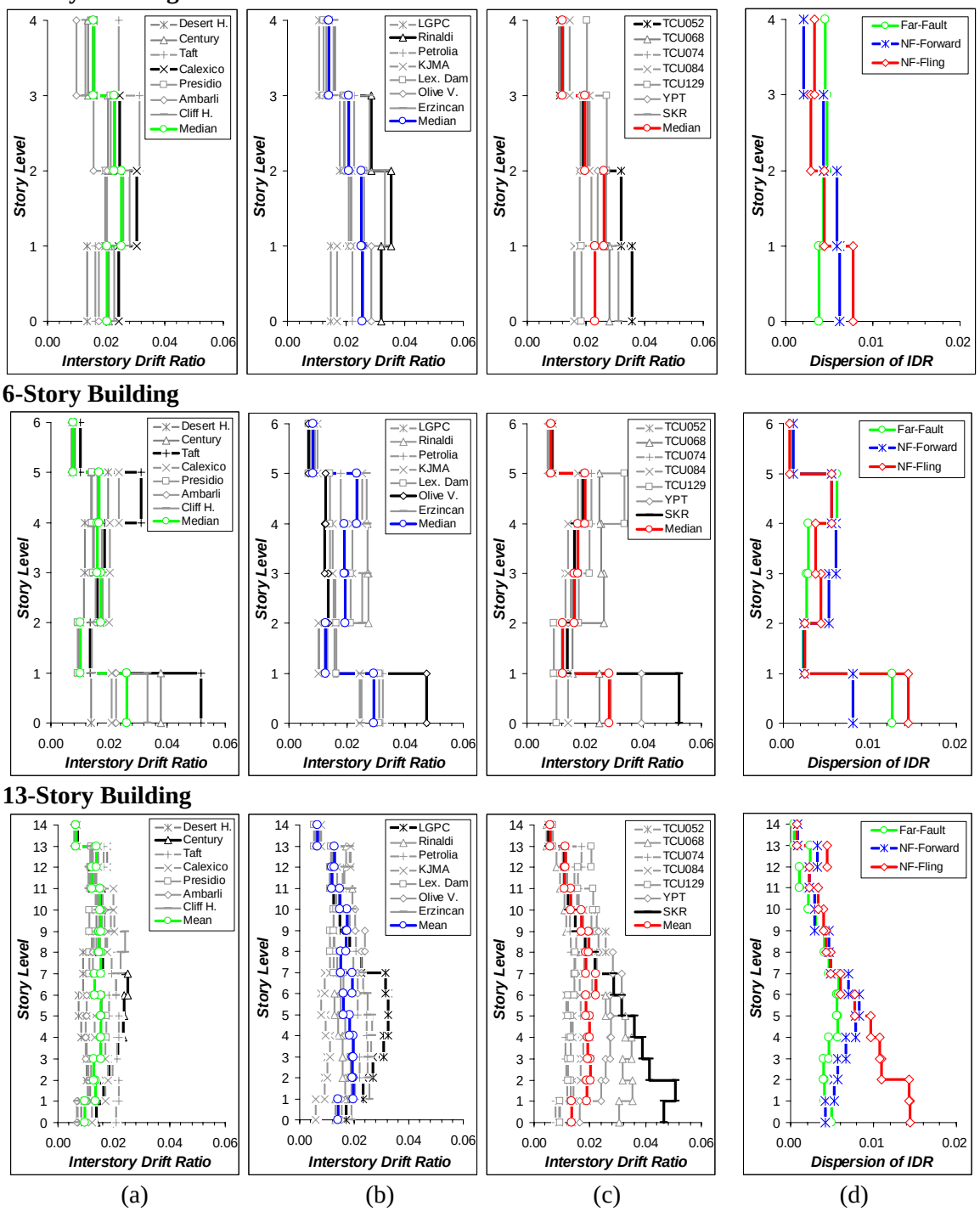

Figure 3.6 Maximum interstory drift for each building subjected to spectrum-compatible (a) Far-fault motions, (b) Near-fault motions with forward directivity, (c) Near-fault motions with fling, and (d) dispersion of interstory drift ratio.

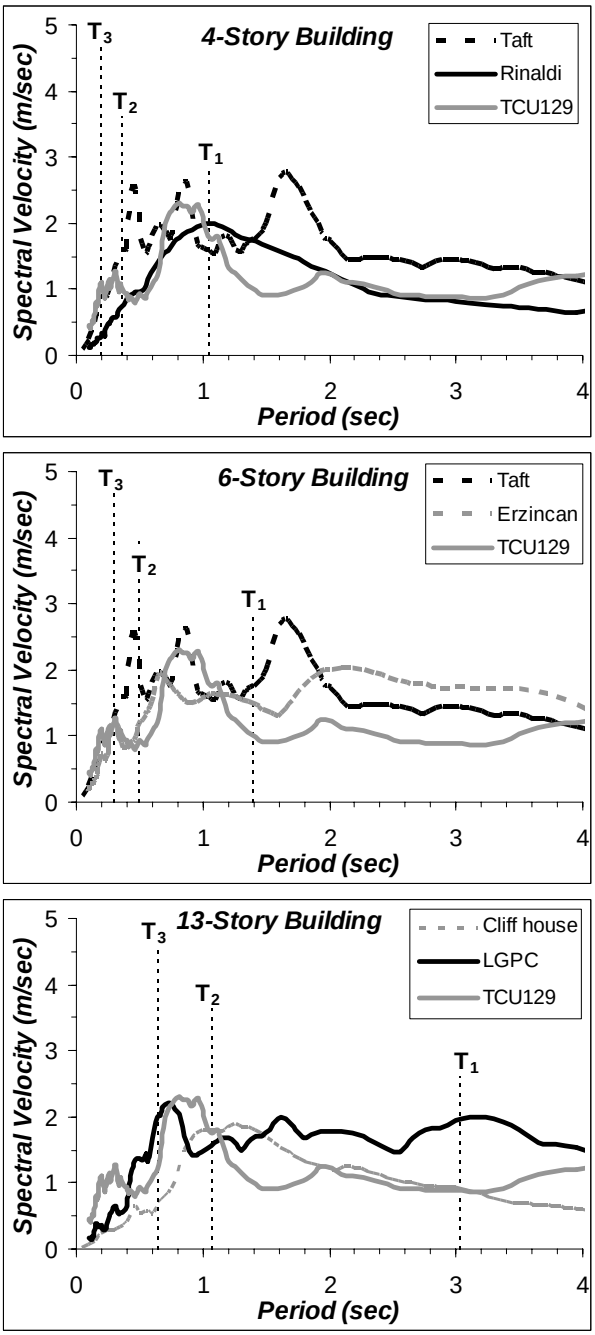

Figure 3.7 Velocity spectra of selected ground motions.

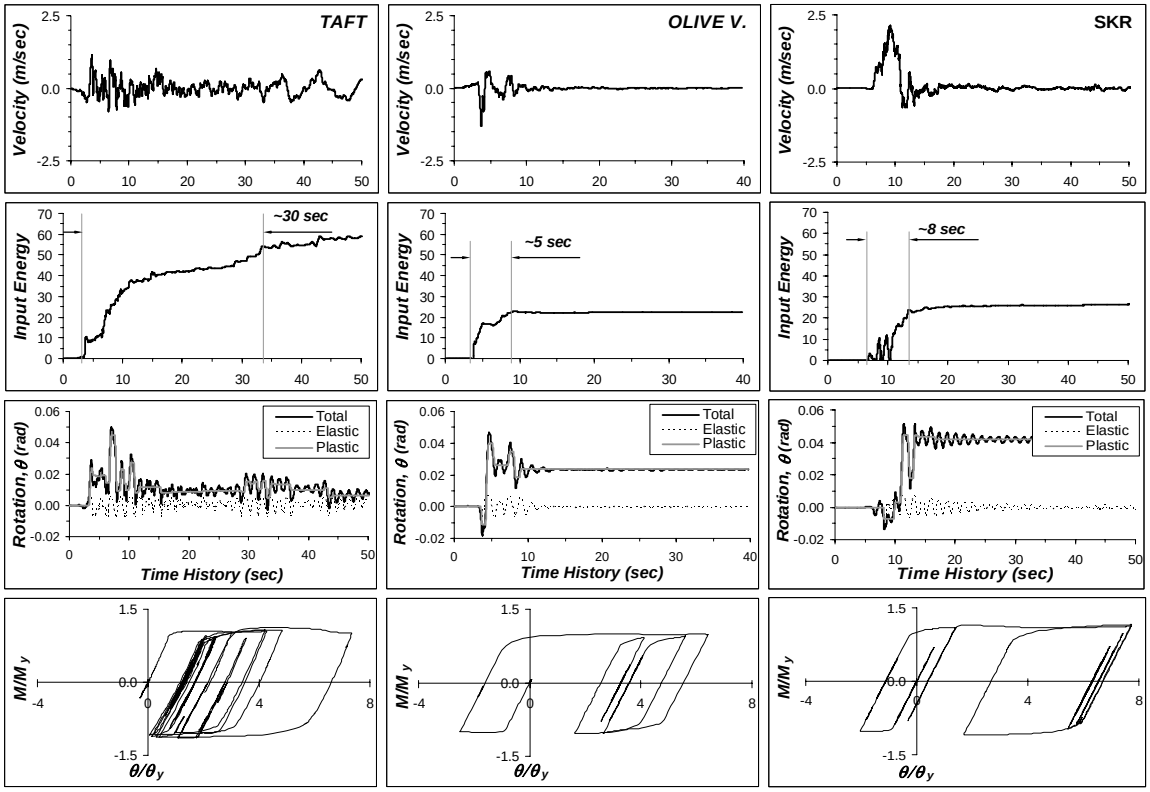

(a) (b) (c)

Figure 3.8 Cyclic demand for a typical column subjected to: (a) Far-fault motion (Taft), (b) Near-fault motion with forward directivity (Olive V.), and (c) Near-fault motion with fling (SKR).

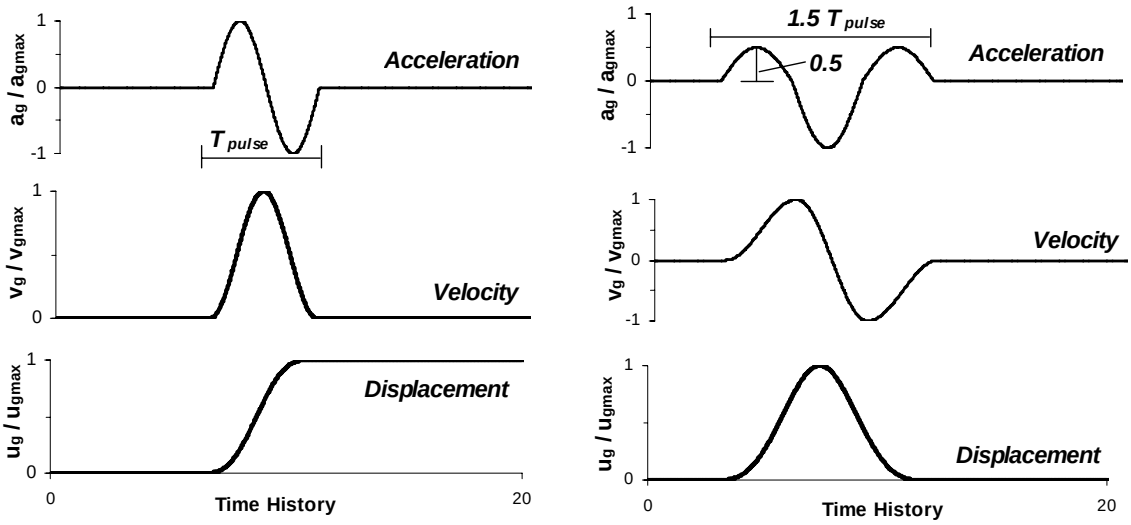

Figure 3.9 Idealized sinusoidal pulses, (a) Fling (Type-A), (b) Forward directivity (Type-B) (*Note that curves are normalized by maximum acceleration, velocity, and displacement*).

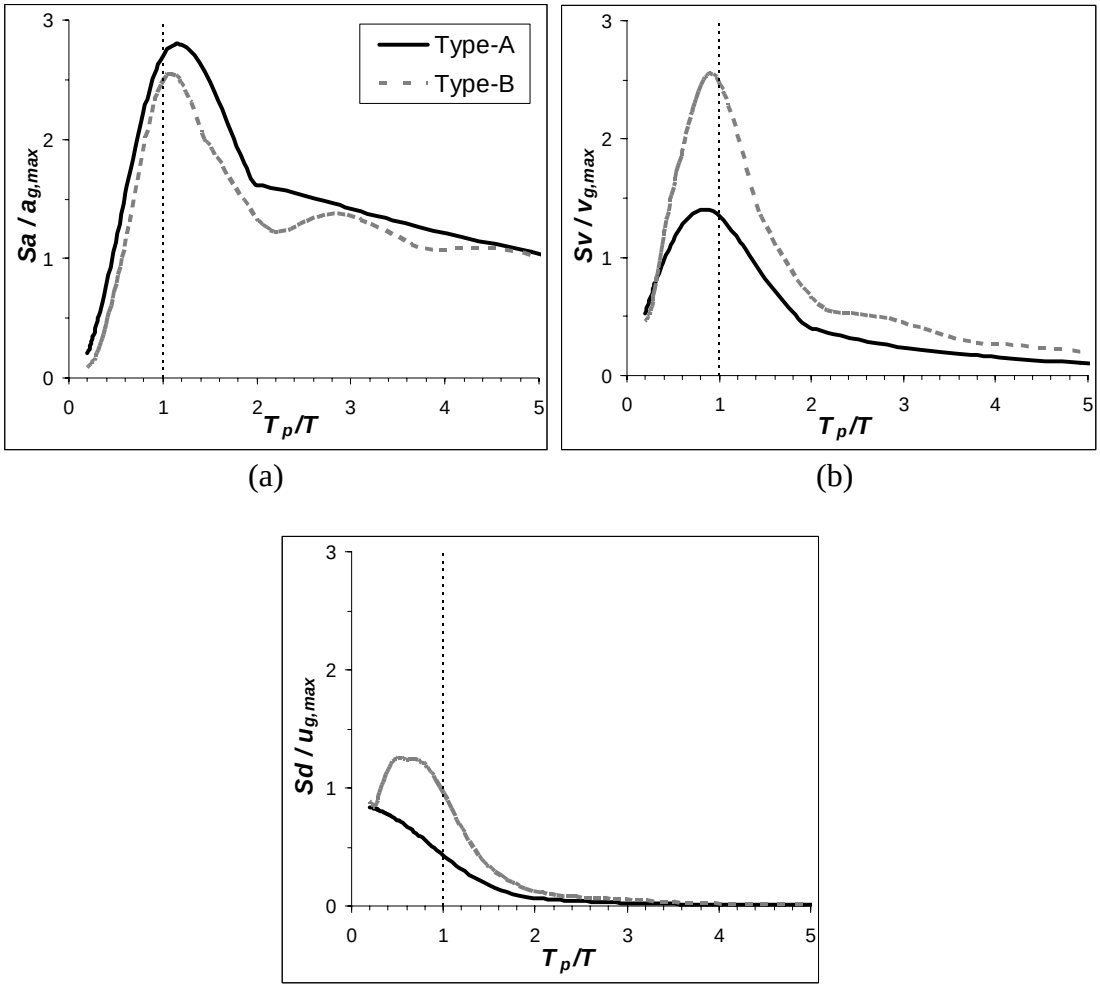

Figure 3.10 Five percent damped normalized (a) Acceleration, (b) Velocity, and (c) Displacement response (elastic) spectra for idealized sinusoidal pulses (*Type-A: Fling-step, Type-B: Forward directivity*).

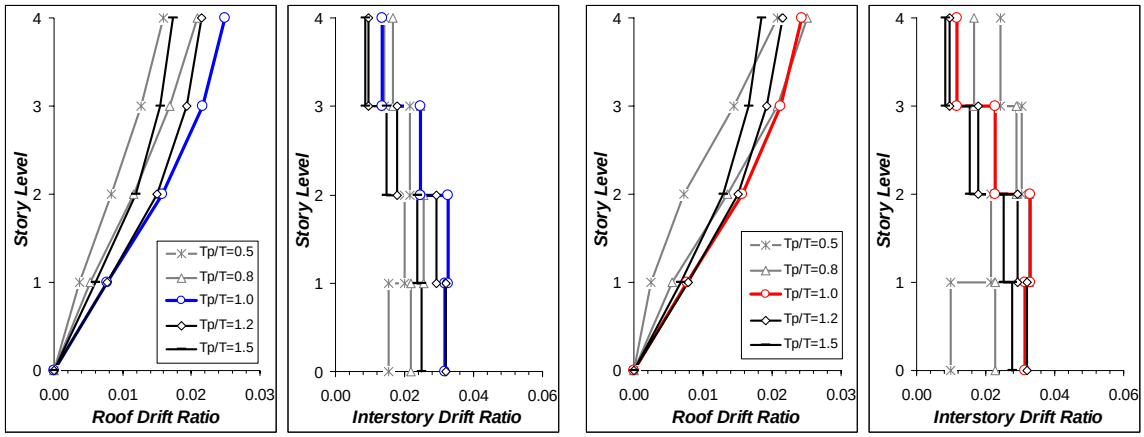

(a) (b)

Figure 3.11 Dependence of roof drift ratio and interstory drift ratio on T_p/T for 4-story building subjected to idealized pulses (a) Type-A, (b**)** Type-B.

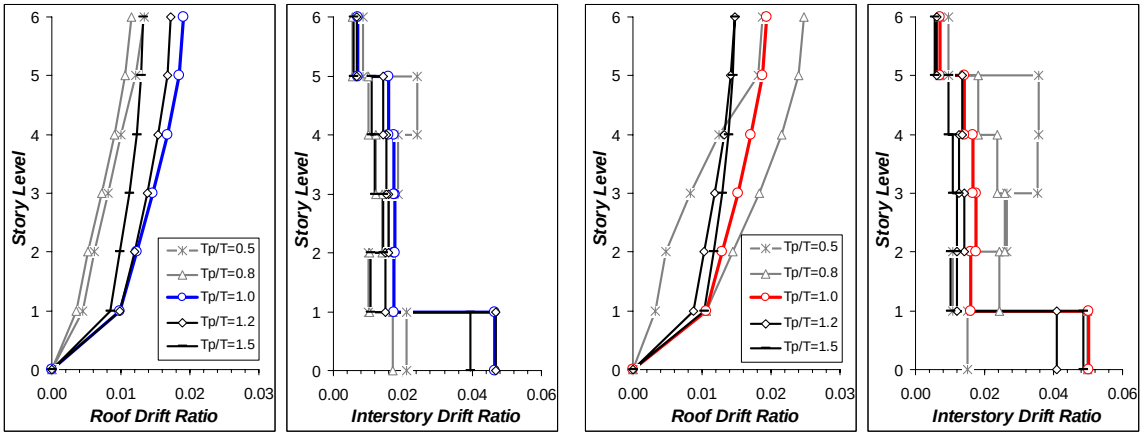

(a) (b)

Figure 3.12 Dependence of roof drift ratio and interstory drift ratio on T_p/T for 6-story building subjected to idealized pulses (a) Type-A, (b**)** Type-B.

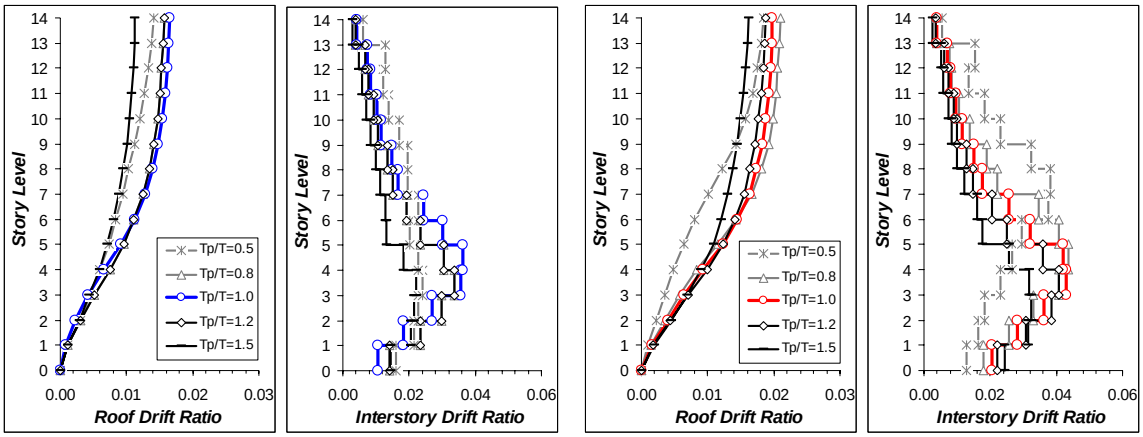

Figure 3.13 Dependence of roof drift ratio and interstory drift ratio on T_p/T for 13-story building subjected to idealized pulses (a) Type-A, (b) Type-B.

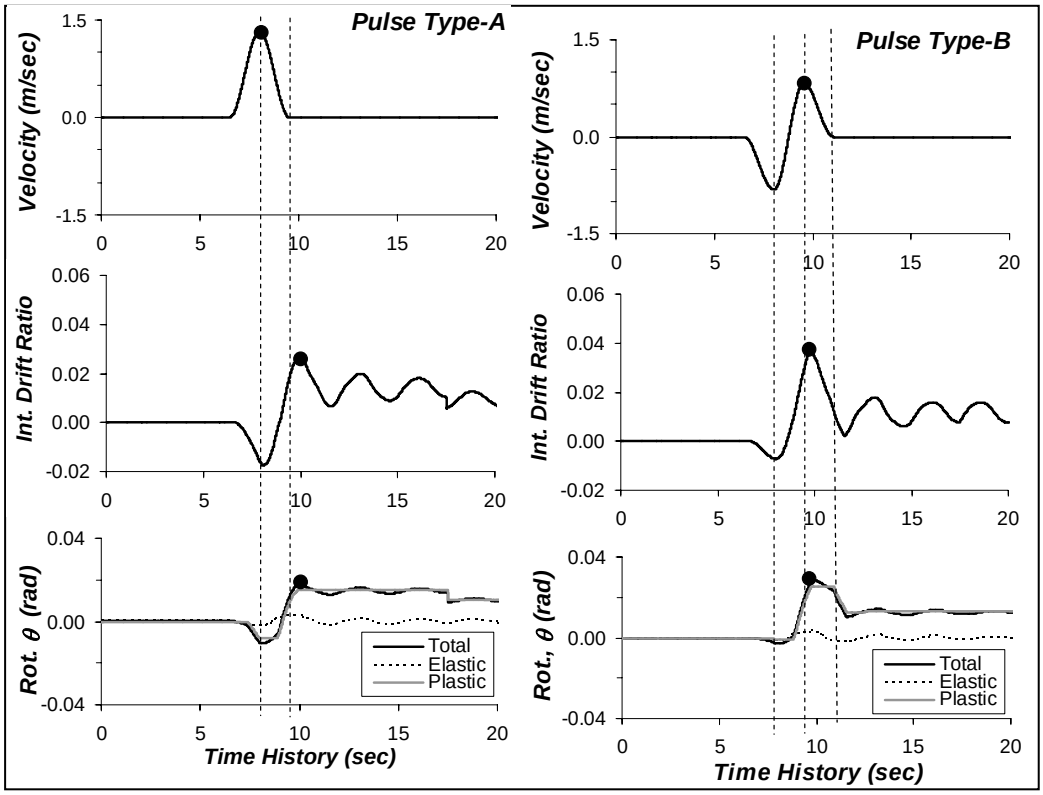

Figure 3.14 Interstory drift variation at critical (3rd) story level and rotation time history of interior column experiencing maximum demands at same story level of the 13-story building subjected to pulse type A and B (*Dashed lines denote the time at peak magnitude and the end time of pulses*).

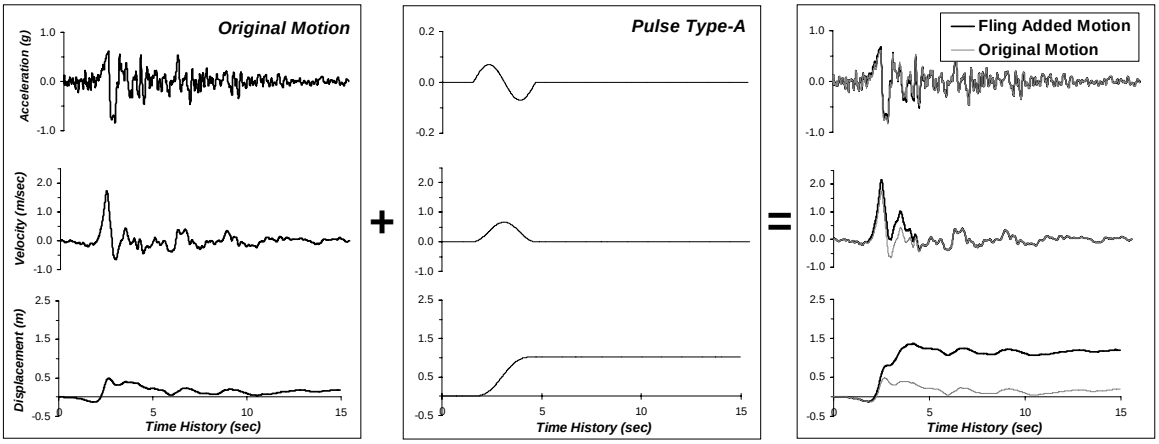

(a) (b) (c)

Figure 3.15 Sequence of generating an artificial fling effect using original Rinaldi record and pulse Type-A (*Note that T_p of pulse Type-A = fundamental period of target building*).

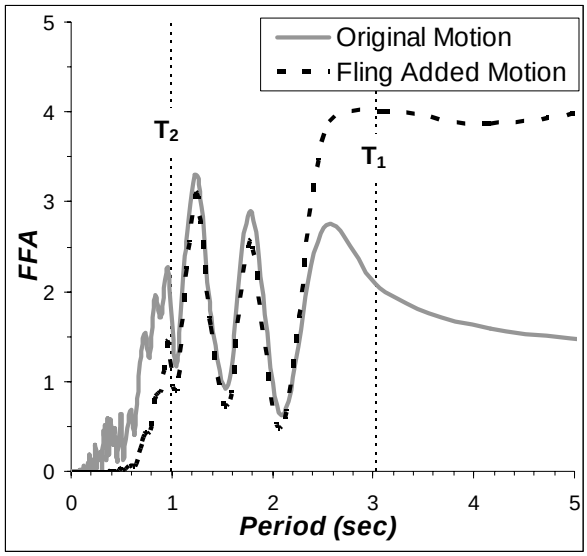

Figure 3.16 Comparison of Fast-Fourier amplitude of original and unscaled fling-added motion (T_1 and T_2 denote the first and second fundamental period of 13-story building).

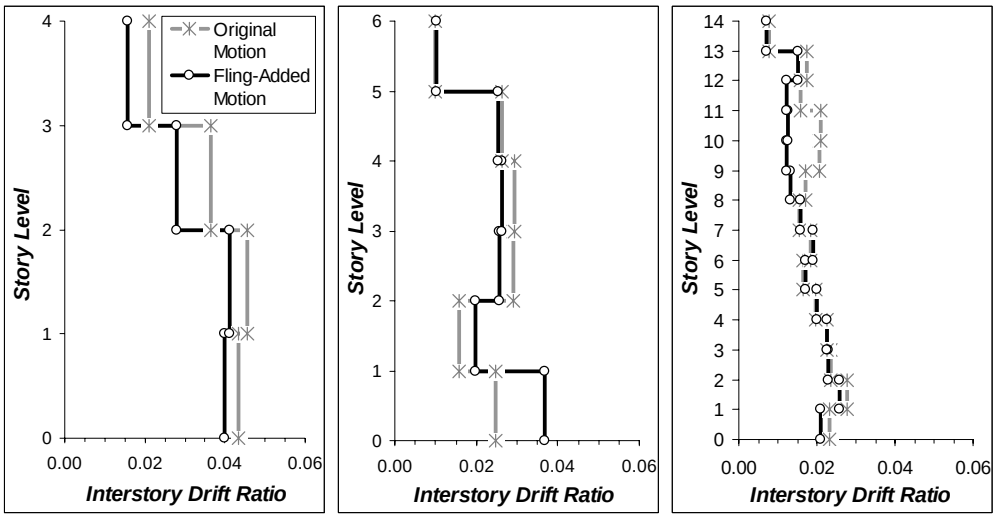

(a) (b) (c)

Figure 3.17 Comparison of response of (a) 4-story building, (b) 6-story building, and (c) 13-story building to original and fling added motion.

CHAPTER 4

ENERGY CONTENTS IN NEAR-FAULT GROUND MOTIONS

4.1 INTRODUCTION

Since the mid 1950s when Housner (1956) first proposed a limit-state design methodology to provide adequate energy-dissipation capacity to structural components, energy-based design approaches have gained considerable attention. Several papers that utilize energy-based concepts in evaluation and design have been proposed (Park et al. 1984; Krawinkler 1987; Tembulkar and Nau 1987; Minami and Osawa 1988; McCabe and Hall 1989). However, the definitive work that re-examined the concepts of relative and absolute input energy and renewed interest in using input energy as a potential measure of structural demand was the paper by Uang and Bertero (1990). Their work demonstrated the importance of absolute input energy and identified the presence of large spikes in the energy history. Since then, a great deal of effort has gone into the estimation of energy demands and dissipation mechanisms in structures resulting in the development of energy based spectra (Decanini Mollaioli 2001; Chou and Uang 2000; Chai and Fajfar 2000; Riddell and Garcia 2001) and input-energy-controlled procedures for seismic design (Otani and Ye 1999; Leelataviwat 2002; Chou and Uang 2003). The fundamental premise behind energy-based design methods are that energy dissipation capacity of

structural elements can be established based on the predicted energy demand from earthquakes. To quantify the energy imparted to structures, both relative input energy and absolute energy definitions have been used. Fajfar and Vidic (1994), Riddell and Garcia (2001) and Ordaz et al. (2002) used relative input energy in their work while Berg and Thomaides (1960), Goel and Berg (1968), Mahin and Lin (1983), Teran-Gilmore (1998), Chapman (1999) and Takewaki (2004) opted for measures based on absolute input energy. However, none of these studies explicitly consider ground motion characteristics in distinguishing the two definitions of input energy.

This chapter re-visits the input energy definitions in light of the recent findings related to near-fault ground motions. Given the large number of near-fault records that are now readily available, this study aims to add to the knowledge of directivity effects on imparted energy to structures. Near-fault records having either fling effects or forward directivity are judiciously compiled from different seismic events with particular emphasis on acceleration pulses. Recent studies of near-fault motions (Hall et al. 1995; Heaton et al. 1995; Iwan 1997) have generally paid more attention to velocity pulses alone thereby overlooking the acceleration content that leads to the build up of the velocity pulse. In fact, the significance of local acceleration pulses in generating damage was first identified by Bertero (1976). Recently, acceleration pulses have been mentioned in the studies of Bonelli (1998) and Sucuoglu et al. (1998), and their consequences on linear and bilinear SDOF system responses have been investigated by Makris and Black (2004).

The relationship between ground motion characteristics and input energy resulting from long period coherent velocity pulses produced either by a distinct acceleration pulse

or a succession of high-frequency acceleration pulses are explored to further expand our understanding of the destructive potential of near-fault ground motions. Additionally, simple sinusoidal pulse models to simulate forward directivity and fling effects are employed to illustrate the consequences of pulse period and pulse shape on input energy. Finally, this chapter investigates the correlation between interstory drift demands of MDOF systems and input seismic energy computed using absolute and relative energy formulations.

4.2 BASIC ENERGY FORMULATIONS

The equation of motion of a damped SDOF system is:

$$m(\ddot{u}_t) + c\dot{u} + f(u) = 0 \tag{4.1}$$

where m is the mass, c is the damping coefficient, $f(u)$ is the restoring force (= ku for linear systems), u_t ($u_t = u+u_g$) is the absolute (total) displacement, u_g is the ground displacement, and u is the relative displacement of the system with respect to the ground. It is also possible to express Eq. (4.1) in the following form:

$$m(\ddot{u}) + c\dot{u} + f(u) = -m\ddot{u}_g \tag{4.2}$$

Integration of Eqs. (4.1) and (4.2) with respect to relative displacement u leads to two definitions of input energy. Integrating Eq. (4.1) with respect to u gives the absolute energy formulation of a viscous damped SDOF system subjected to horizontal motion (Figure 4.1a) as follows:

$$\frac{m(\dot{u}_g + \dot{u})^2}{2} + \int c\dot{u}du + \int f(u)du = \int m(\ddot{u}_g + \ddot{u})du_g = \int m(\ddot{u}_g + \ddot{u})\dot{u}_g dt \tag{4.3}$$

Eq. (4.3) can also be written in a general form which identifies the different energy components:

$$E_K + E_\xi + (E_S + E_H) = E_I \tag{4.4}$$

where E_I is the absolute input energy, E_K is the absolute kinetic energy, E_ξ is the damping energy, E_S is the elastic strain energy and E_H is the plastic strain energy (irrecoverable hysteretic energy). As a corollary, integration of Eq. (4.2) with respect to u results in the relative energy formulation of a fixed-based SDOF system (Figure 4.1b):

$$\frac{m(\dot{u})^2}{2} + \int c\dot{u}du + \int f(u)du = -\int m\ddot{u}_g du = -\int m\ddot{u}_g \dot{u}dt \tag{4.5}$$

which can be expressed in terms of the following energy components:

$$E_K^{'} + E_\xi + (E_S + E_H) = E_I^{'} \tag{4.6}$$

where $E_I^{'}$ is the relative input energy, and $E_K^{'}$ is the relative kinetic energy. E_I represents the work done by the inertia force ($m\ddot{u}_t$) acting on the structure, which is equivalent to the work done by the total base shear on the ground displacement. On the other hand, $E_I^{'}$ represents the work done on a fixed based system by an equivalent lateral force, thereby excluding rigid body translation effects. The difference between the two energy formulations is a result of the different definitions of kinetic energy ($E_K^{'}$ vs E_K) while damping and strain energy terms remain identical in both definitions. The difference between the two energy terms can be written as:

$$E_I - E_I^{'} = E_K - E_K^{'} = \frac{1}{2}m\dot{u}_g^2 + m\dot{u}_g\dot{u} \tag{4.7}$$

The right hand side of Eq. (4.7) has two terms, the former is the kinetic energy due to ground velocity, while later is the work done by ground acceleration ($m\ddot{u}_g$) on the respective incremental system displacement (*du*). It is now generally well-known that absolute and relative energies tend to differ in magnitude for very flexible or very rigid systems. For flexible systems where the vibration period is significantly larger than the predominant ground motion period, the mass of the system preserves its original position while the ground moves. In this case, the absolute energy approaches zero while significant relative input energy builds up. Conversely, in case of rigid systems, the relative movement of the mass with respect to the ground is negligibly small and results in near zero relative energy, yet considerable absolute energy may develop.

4.3 SEISMIC ENERGY INPUT TO SDOF SYSTEMS

While interpretation of far-fault strong motions during the last three decades has evolved considerably, the recent 1994 Northridge (Calif.), 1999 Chi-Chi (Taiwan) and 1999 Kocaeli and Duzce (Turkey) earthquakes uncovered significant differences between near-fault and far-fault ground motions in terms of their distinct acceleration and velocity pulses. These pulses, associated with directivity effects, originate from kinematic characteristics of the ground in the vicinity of the fault rupture plane. Velocity pulses and the characteristics of acceleration pulses that lead to the development of a coherent velocity pulse, as will be demonstrated in this chapter, also play a significant role in determining the absolute and relative input energy outcomes of near-fault records and are remarkably different than those produced by far-fault records.

For ordinary far-fault ground motions, the input energy cumulatively increases and reaches a peak at the termination of the ground movement and this peak energy value, typically used to generate conventional input energy spectra, is similar for both relative and absolute energy measures. Figure 4.2 is an example of the energy response history and resultant input energy spectrum computed for ordinary far-fault records of selected components from the Northridge and Kern County earthquakes. In order to facilitate comparison between different records, the input energy is converted into an energy equivalent velocity as $V_{EQ} = \sqrt{2E_I / m}$ and $V_{EQ}^{'} = \sqrt{2E_I^{'} / m}$ for absolute and relative energy definitions, respectively. Henceforth, the energy equivalent velocity will be used as the measure of input energy. The two different input energy definitions result in almost similar energy response histories and input energy spectra as portrayed in Figure 4.2. Ordinary far-fault records contain typical random high-frequency content in the acceleration trace that result in multiple spikes in the velocity time-series. These spikes progressively increase the input energy and are associated with damage accumulation by inducing multiple inelastic deformation cycles (a low cycle fatigue phenomenon). Therefore, the effective duration of motion becomes an important parameter to estimate the peak input energy.

Near-fault ground motions, on the other hand, contain coherent long-period intense velocity pulses as evident in the Tabas and Rinaldi Receiver Station records shown in Figure 4.3. These two records are characterized by forward directivity which occurs when the fault rupture propagates with a velocity close to the shear-wave velocity. The displacement associated with such a shear-wave velocity is largest in the fault normal direction for strike-slip faults. The important distinction between the two forward

directivity records displayed is the initiation of the velocity pulses. These pulses may originate either due to succession of high frequency acceleration peaks that resemble far-fault records (as in the case of the Tabas record where the acceleration time-history is packed with high frequency spikes without a distinguishable acceleration pulse) or a distinct acceleration pulse (as in the case of the Rinaldi Receiver Station record). This difference can influence the resultant input energy depending on whether the relative or absolute input energy definition is used. Forward directivity records without a distinctive acceleration pulse have generally similar energy histories and spectra. However, the presence of a distinct acceleration pulse generates smaller or larger relative energy magnitude in the short and long period ranges, respectively, than absolute relative energy. While the difference in the intermediate period range becomes negligible, relative energy is generally higher than absolute energy in the long period range. Consistently similar results were obtained for a number of near-fault forward directivity records.

Comparison of energy-time history of the two records elucidates another important feature of acceleration pulses. In contrast to records without a noticeable acceleration pulse wherein the input energy gradually builds up and reaches a maximum near the termination of the ground motion, records with distinct single acceleration pulses result in instantaneous energy input to the system with minimal accumulation of energy afterwards. To be more specific, the difference between relative and absolute energy become largest during sudden energy spikes. This difference is influenced by two components: the kinetic energy of the ground motion which is independent of the system response and corresponding spectral period (always a positive quantity); and secondly, the incremental work done by the ground acceleration on system relative displacement

which becomes a positive value only if the ground velocity is in-phase with the system relative velocity. Hence, the difference between the two energy definitions reaches a minimum when the ground velocity remains mostly out-of-phase with the system relative velocity.

Figures 4.4 and 4.5 portray the acceleration, velocity, energy time-history, and corresponding energy-spectra of fling motions recorded during 1999 Kocaeli (Turkey) and Chi-Chi (Taiwan) earthquakes. Fling, being a result of the evolution of residual ground displacement due to tectonic deformation associated with the rupture mechanism, is generally characterized by a unidirectional large amplitude velocity pulse and a monotonic step in the displacement time-series. Fling takes place in the direction of fault slip thereby it is not strongly coupled with forward directivity. It arises in strike-slip faults in the strike parallel direction as in Kocaeli and Duzce earthquakes or in the strike-normal direction for dip-slips faults as in Chi-Chi earthquake. The difference between forward directivity and fling records is more clearly observable in the velocity and displacement time-series. Unlike fling motions, forward directivity records are characterized by double sided velocity pulses. Despite the difference in the velocity pulse shape, the initiation of these pulses is similar regardless of the directivity effect. As such, Sakarya and TCU074 records consist of compressed acceleration spikes, whereas in TCU052 and TCU068 records, they contain a distinct single pulse. Figures 4.4 and 4.5 also show the energy response history and input energy spectra of fling motions computed using absolute and relative energy notations. Similar to the forward directivity record of Tabas, Sakarya and TCU074 ground motions (both of which do not contain a distinct acceleration pulse) generate absolute and relative input energy input somewhat

similar to each other (though occasional spikes in the absolute input energy history may be present simply by virtue of the fact that it is a near-fault record, as in the case of the Sakarya record). Conversely, TCU068 and TCU052 records with a dominant acceleration pulse produce significantly larger instantaneous absolute energy spikes following the dominant pulse arrival. This noticeable difference between absolute and relative energy contents is more clearly seen in the resultant input energy spectrum at different spectral periods and more severe than for forward directivity records. In fling motions, the single-sided velocity pulse due to tectonic deformation of the ground surface manifests itself in the absolute energy plot as the work done by the rigid body translation, which cannot be captured by relative input energy.

The above findings are further substantiated by examining the ratio of absolute to relative input energy for a much larger subset of records. Figure 4.6 presents the statistical correlation of near-fault ground motion characteristics on input energy measures. These results are based on analyses of 66 near-fault forward directivity records (in which 20 records contain a dominant acceleration pulse) and 41 near-fault fling records (in which 6 contain a distinguishable acceleration pulse). As is evident from the figure, absolute energy measures are critical in most cases with the exception of forward directivity records containing a coherent acceleration pulse wherein relative input energy is more significant.

4.2.1 Ground Motion and Energy Response Characteristics

Table 4.1 lists some essential characteristics of the primary ground motions used in this study, including the peak energy equivalent velocity values ($V_{EQ}^{\max}$ and $V_{EQ}^{'\max}$) together

with the V/A ratio and strong motion duration (t_D). V/A ratios indicate the average duration of the acceleration pulse provided that PGV is reached immediately following the dominant acceleration pulse. This parameter was shown to be well correlated with the damage potential of earthquakes (Sucuoglu et al. 1998). Similarly, the records having distinct and dominant acceleration pulses in Table 4.1 exhibit remarkably larger V/A ratio than the records crowded with acceleration spikes. Fling records of TCU068 and TCU052 have V/A ratios more than twice that of the forward directivity record of Rinaldi Receiver Station, although their PGA values are much less than that of the Rinaldi record.

Strong motion duration (t_D) is another parameter used commonly to identify the severity of ground motions (Uang and Bertero 1990; Amiri and Dana; 2005; Shoji et al. 2005). It was first defined by Trifunac and Brady (1975) as the interval between times at which 5 and 95 percent of the value of the Arias intensity ($I_A = \frac{\pi}{2g}\int_0^{t_d} \ddot{u}_g^2 dt$, where t_d is the duration of record) is achieved. Based on the five ground motions investigated, Uang and Bertero showed a linear correlation between the strong motion duration and the amplification factor $\psi(\mu,\xi)$, defined as the ratio of maximum absolute energy equivalent velocity ($V_{EQ}^{\max}$) to PGV. Figure 4.7 compares the distribution of data used in this study (Table 4.1) in terms of their computed amplification factor and strong motion duration with the linear relationship given by Uang and Bertero (i.e., dashed line in Figure 4.7 (Left)). The filled marks indicate the records having apparent acceleration pulses. The data is not well distributed around the dashed line and the amplification factor and strong motion duration are not statistically well correlated as shown in the figure. However, statistically better correlation was obtained between the amplification factor and V/A

ratio of the records as displayed in Figure 4.7 (right). Distribution of data around the best-fit curve indicates that an increase in the V/A ratio (i.e., average duration of the acceleration pulse) has a diminishing effect on the amplification factor. Smaller amplification factors, meaning that the energy equivalent velocity approaches the PGV, were obtained for the two fling records characterized by distinct acceleration pulses at the tail of the best-fit curve. These two records produce the largest V/A ratios in contrast to motions composed of compressed (high-frequency) acceleration spikes without a conspicuous acceleration pulse. Therefore, it is possible to approximate the peak input energy imparted to a structural system based on the PGV to PGA ratio as indicated by the best-fit expression given in Figure 4.7 (right).

4.2.2 SDOF Energy Response to Pulse Inputs

A practical assessment of the above issues is facilitated through the use of simple sinusoidal pulse models, wherein pulse duration and shape can be effectively varied while their collective influences on absolute and relative input energy response and respective energy spectra can be systematically examined. Double sided and unidirectional sinusoidal waveforms to represent velocity time traces are, therefore, used to imitate respectively forward directivity and fling records as illustrated in Figure 4.8. The basis and formulations of these pulses are given in Chapter 3. Similar wave-form models have also been utilized in many other studies (Makris and Black 2004; Sasani and Bertero 2000; Alavi and Krawinkler 2003; Mavroeidis et al. 2004), and have been shown to provide reasonable representation of important characteristics of impulsive near-fault records.

Figure 4.9 compares the equivalent velocity spectra (5% damping) of simple forward directivity and fling pulse models having pulse periods of 0.5, 1.0, 2.0 and 4.0s computed using absolute and relative input energy formulations. All pulse records were scaled to the same PGA of 0.5g. Comparisons of energy-spectra demonstrate that simple pulse models consistently impart larger absolute energy than relative energy for spectral periods less than the pulse period (*Tp*). Conversely, relative input energy becomes larger for periods larger than about 2*Tp* for forward directivity and about 3*Tp* for records with fling characteristics. In the period range of *Tp* to 2*Tp* for forward directivity and *Tp* to 3*Tp* for fling, both energy notations generate similar results. As noted for real earthquakes, the difference in input energy using relative and absolute energy definitions becomes more severe in case of fling. The vertical line in the spectra plots indicates the spectral period corresponding to pulse period. For each energy-spectrum, the peak spectral value is observed to be in the proximity of the pulse period. The shape of the energy-spectrum is significantly affected by the type of pulse and its period. Compared to forward directivity, fling models results in higher input energy in the spectrum for a wider range of spectral periods. Another influential parameter on the spectral shape is the duration of the acceleration pulse (i.e., T_{pulse}). Increase in pulse period associated with larger V/A ratio results in increased seismic energy input irregardless of pulse type. Similar to real recordings (Figure 4.4 and 4.5), difference between absolute and relative energy spectrum is more pronounced in fling pulses than forward directivity pulses. This significant energy difference is attributed to higher PGV and associated kinetic energy of ground in fling motions wherein the single sided velocity pulse produces larger incremental work while being more in-phase with system relative velocity (see Eq. 4.7).

4.4 SEISMIC ENERGY INPUT TO MDOF SYSTEMS

The general form of the absolute input energy for SDOF systems defined in Equation (4.2) was expanded by Uang and Bertero (1990) to a multi-degree-of-freedom (MDOF) *N*-story system as follows

$$\frac{1}{2}\dot{\boldsymbol{u}}_{\boldsymbol{t}}^{T}\boldsymbol{m}\dot{\boldsymbol{u}}_{\boldsymbol{t}}+\int\dot{\boldsymbol{u}}^{T}\boldsymbol{c}d\boldsymbol{u}+\int\boldsymbol{f}_{s}^{T}d\boldsymbol{u}=\int(\sum_{j=1}^{N}m_{j}\ddot{u}_{t(j)})\;du_{g}=\int(\sum_{j=1}^{N}m_{j}\ddot{u}_{t(j)})\;\dot{u}_{g}dt \quad (4.11)$$

where $\boldsymbol{m}$ is the diagonal mass matrix, $\boldsymbol{c}$ is the damping matrix and $\boldsymbol{u}$ is the story relative displacement vector. Accordingly, $\boldsymbol{m_j}$ is the lumped mass of the j^{th} story and $\ddot{\boldsymbol{u}}_{\boldsymbol{t(j)}}$ is the absolute (total) acceleration recorded at the j^{th} story, and N is the number of story. Left hand side of Equation (4.11) (i.e., E_I) corresponds to total work done due to a sum of inertia force $(m_j\ddot{u}_{t(j)})$ at each storey level for a given ground displacement of u_g at the foundation level (see Figure 4.9, Left).

By the same token, it is possible to express the relative energy imparted to MDOF system (see Figure 4.9, Right) as

$$\frac{1}{2}\dot{\boldsymbol{u}}^{\boldsymbol{T}}\boldsymbol{m}\dot{\boldsymbol{u}}+\int\dot{\boldsymbol{u}}\boldsymbol{c}d\boldsymbol{u}+\int\boldsymbol{f}_{s}\,d\boldsymbol{u}=\int(\sum_{j=1}^{N}m_{j}\ddot{u}_{g})\;d\boldsymbol{u}=\int(\sum_{j=1}^{N}m_{j}\ddot{u}_{g}\dot{u}_{(j)})\;dt \quad (4.12)$$

The difference between the absolute and relative energy formulation (Eqs. 4.11 and 4.12) for a MDOF system is originated by the difference in kinetic energy formulations and can be expressed as

$$E_I-E_I^{'}=\frac{1}{2}m\dot{u}_g^2+\sum_{j=1}^{N}m_j\dot{u}_g\dot{u}_{(j)} \quad (4.13)$$

4.4.1 Input Energy and Damage Potential of Near Fault Ground Motions

In this section, the correlation between damage potential of near-fault ground motions and their input energy contents are examined using the response of two real buildings. Analytical models of existing and instrumented 6-story and 13-story steel moment-frame buildings were created and calibrated to recorded data. Details of the building models including calibration studies are reported before in Chapter 3. Table 4.2 summarizes the predominant vibration properties of the buildings.

The buildings were subjected to a variety of near-fault recordings having forward directivity and fling effects in an effort to investigate the correlation between the two input energy measures and seismic demand. Accordingly, Figure 4.11 shows the peak interstory drift profiles along with the relative and absolute energy time history responses of the 6-story building subjected to fling records. Recall that the TCU052 record contains a distinguishable acceleration pulse in contrast to TCU074 which does not. Since the pulse period matches the first mode period of the building (see Table 4.2), the TCU052 record triggers a primarily first-mode response resulting in accumulation of damage at the first story level, whereas the TCU074 record (wherein the input energy gradually accumulates over an interval of almost 11 sec) activates higher mode effects and results in larger story drifts at the fifth story level. Much of the energy in TCU052 is imparted in a short duration (approximately 3 sec) which appears to be another contributing factor in limiting higher mode contributions since the predominant pulse period is outside the range of the higher mode periods of the building. These results are consistent with observations by Uang and Bertero on the significance of absolute input energy measures over relative input energy in estimating the damage potential of the records. In the

present study, this observation is further substantiated by examining the characteristics of the near fault records, viz. the presence of a dominant acceleration pulse and the proximity of the pulse period to the vibration period of the structure.

A very different scenario emerges for the response of the 13-story building presented in Figure 4.12. This building was first subjected to the forward directivity records of Rinaldi Receiver Station and Tabas. Note that the former record contains a distinguishable acceleration pulse that is absent in the latter. In this case, the Rinaldi record produces significant demands in the upper levels while the Tabas record creates higher demand in the lower levels. Despite the fact that the Tabas record imposed significantly larger energy over a longer duration, the fact that the relative input energy reaches its peak value in a much shorter period of time is more indicative of the damage potential of the Rinaldi record. Additionally, the pulse period of the Rinaldi record is closer to the second mode period of the building.

A more comprehensive comparison of absolute and relative energy and corresponding response is presented in Figure 4.13 for again 13-story building subjected to forward directivity record of Rinaldi Receiver Stn. and fling record of TCU068. For objective of producing comparable peak demands by two records, TCU068 record is scaled by 0.65, while Rinaldi Receiver Stn. record is used in its original form. This figure manifests alteration of modal participation factors and interstory drift demands at representative lower and upper stories during the dynamic response. The peak interstory drift profile for Rinaldi Receiver Stn. shows that considerable peak drift concentrates at the upper level stories (10 and 11), a clear indication of higher mode effects, whereas the significant interstory drift demand at the first story level is the result of first mode contribution to

response. It is instructive to note that the peaks of modal participation factors (associated with yielding and inelastic behavior) for first and second modes strongly correlate to the time-steps at which the story peak demands occur at the first and tenth stories (follow the vertical lines in Figure 4.13). Another important observation is that the second and third mode modal participation factors are in-phase but both these modes are out-of-phase with respect to the first mode participation factor. That implies that the peak deformation associated with the first mode (at the first story in this case) is not coupled with higher mode contributions.

For TCU068 record, interstory drift profile implies the significant contribution of first mode effect on the response, while higher mode contributions are almost insignificant. This can be also captured from spontaneous peaks in the modal participation factor plots and peaks in interstory drift demands of lower and upper level stories (i.e., third and twelfth stories).

Also portrayed in Figure 4.13 is the relative and absolute energy input computed using MDOF energy formulations. Distinctive energy spikes in the energy time-history plots are direct artifacts of the apparent acceleration pulses contained in these records (see Figures 4.3 and 4.4). While such energy spike takes place in relative energy content incase of Rinaldi Receiver Stn. record, it appears in absolute energy plot incase of TCU068 record. The energy plots also imply that maximum deformation in structural components takes place following the dissipation of this instantaneous intensive energy within a short time interval.

To summarize the above findings, energy demand manifests itself either in the relative or absolute energy content depending on the dominant pulse period of the ground

motion, the characteristics of the acceleration pulses and the vibration periods of structural system. But most importantly, the sudden spikes in the input energy history (relative or absolute) are indicators of the severity of near-fault records.

4.5 CONCLUSIONS

The fundamental principles and consequences of two commonly used energy measures (i.e., absolute and relative) using SDOF and MDOF systems subjected to far-fault and near-fault ground motions were studied. For far-fault records, energy accumulates gradually over the duration of the record and both relative and absolute energy definitions yield comparable results. In contrast, the difference between relative and absolute energy can be considerable for near-fault records. The energy difference is a function of three primary parameters (i) the characteristics of the acceleration pulses that lead to the initiation and build up of the velocity pulse (ii) pulse period and (iii) pulse shape. Velocity pulses are initiated either as a result of a succession of high frequency acceleration peaks (resembling ordinary far-fault records) or a dominant and distinctive acceleration pulse. For the records without an apparent acceleration pulse, both notions of input energy yield similar results. On the other hand, distinctive acceleration pulses have a significant impact on the absolute or relative energy imparted to a structural system. Records containing such acceleration pulses produce abrupt energy spikes in the early phase of response and are significantly larger than the energy accumulated at the termination of the ground movement. While absolute energy is generally a good measure of seismic input for most earthquakes, it is established that relative input energy is more

meaningful for forward directivity near-fault records that contain a distinguishable acceleration pulse.

Based on the study employing simple pulse models, peak relative energy becomes larger than peak absolute energy for periods larger than 2*Tp* for forward directivity and for periods larger than 3*Tp* for records containing fling effects. Both measures of input energy produce similar demands in the period range from *Tp* to 2*Tp* for forward directivity and *Tp* to 3*Tp* for fling records.

Near-fault ground motions with apparent acceleration pulses consistently exhibit larger V/A ratio, a parameter which can be used to identify the impulsive character of accelerograms. For the limited data set investigated in this study, it is found that the V/A ratio is better correlated with the Uang-Bertero amplification factor (Ψ). Therefore, it is possible to approximate the peak input energy imparted to structural system using the PGV to PGA ratio of earthquake records. An empirical expression between the amplification factor and V/A ratio is proposed in this study based on the data set used to calibrate the relationship.

The amplitudes of energy spikes (i.e., difference between the two energy measures) become minimal for the system whose fundamental period is close to the dominant pulse period. Interestingly, the minimum discrepancy between the two energy terms occurs only if the sign of work done by the ground acceleration on the respective incremental system displacement becomes negative and its amplitude is close to the kinetic energy due to ground movement. This condition is possible only if the system velocity remains mostly out-of-phase with respect to ground velocity, meaning that the system tends to move in the opposite direction with respect to the ground movement. Finally, this study

provides supporting data on the response of realistic systems subjected to the near-fault records which reveals that the correlation between seismic demand and the two definitions of input energy depends on the dominant pulse period and the vibration properties of the system.

Table 4.1 Earthquake records used in this study

Year	Earthquake	M_W	Mech.[1]	Recording Station	Comp.	Directivity	Dist.[2] (km)	Site Class[3]	Data Source[4]	PGA (g)	PGV (cm/s)	V_{EQ}^{max} (cm/s)	$V_{EQ}^{'max}$ (cm/s)	V/A	t_D (s)
1952	Kern county	7.5	TH/REV	Taft **	111	-	36.2	D	1	0.18	17.5	80	80	0.10	28.8
1978	Tabas	7.4	TH	Tabas	TR	Forward	3.0	D	1	0.85	121.4	457	462	0.15	16.1
1994	Northridge	6.7	TH	Rinaldi Rec. Stn.	S49W	Forward	8.6	D	2	0.84	174.8	411	409	0.21	7.0
1994	Northridge	6.7	TH	Century CCC **	090	-	23.7	C	2	0.26	21.2	120	120	0.08	13.6
1999	Kocaeli	7.4	SS	Sakarya	EW	Fling	3.2	C	3	0.41	82.1	191	204	0.20	14.6
1999	Chi-Chi	7.6	TH	TCU068*	EW	Fling	3.0	D	4	0.50	277.6	412	402	0.57	12.4
1999	Chi-Chi	7.6	TH	TCU074	EW	Fling	13.8	D	4	0.59	68.9	408	405	0.12	11.8
1999	Chi-Chi	7.6	TH	TCU052*	NS	Fling	1.8	D	4	0.44	216.0	457	342	0.50	15.9

[1] *Faulting Mechanism = TH: Thrust; REV: Reverse; SS: Strike-slip; OB: Oblique*

[2] *Closest distance to fault*

[3] *NEHRP Site Class = C for V_S = 360 to 760 m/s; D for V_S = 180 to 360 m/s*

[4] *Data Source = 1: PEER (http://peer.berkeley.edu/smcat); 2: Cosmos (http://db.cosmos-eq.org); 3: ERD (http://angora.deprem.gov.tr/); 4: http://scman.cwb.gov.tw/eqv5/special/19990921/pgadata-asci0704.htm*

** Records contain appearent acceleration pulses*

*** Far-fault ground motion recordings*

Table 4.2. Vibration properties of buildings

	1st Mode	2nd Mode	3rd Mode
6-Story Steel	1.40	0.51	0.30
13-Story Steel	3.03	1.08	0.65

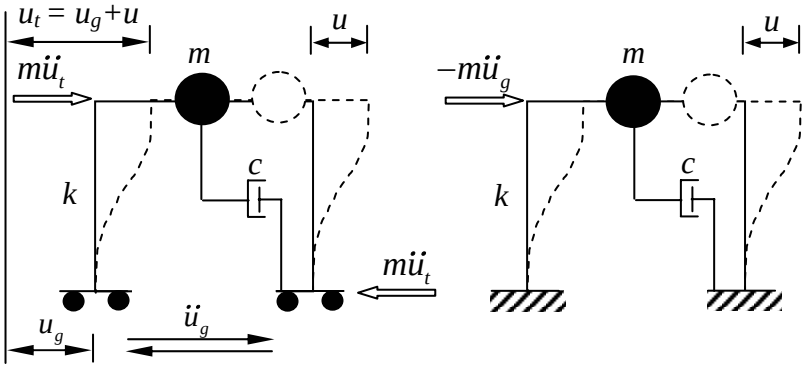

Figure 4.1 Idealized mathematical models of SDOF system used for absolute (Left) and relative energy formulations (Right)

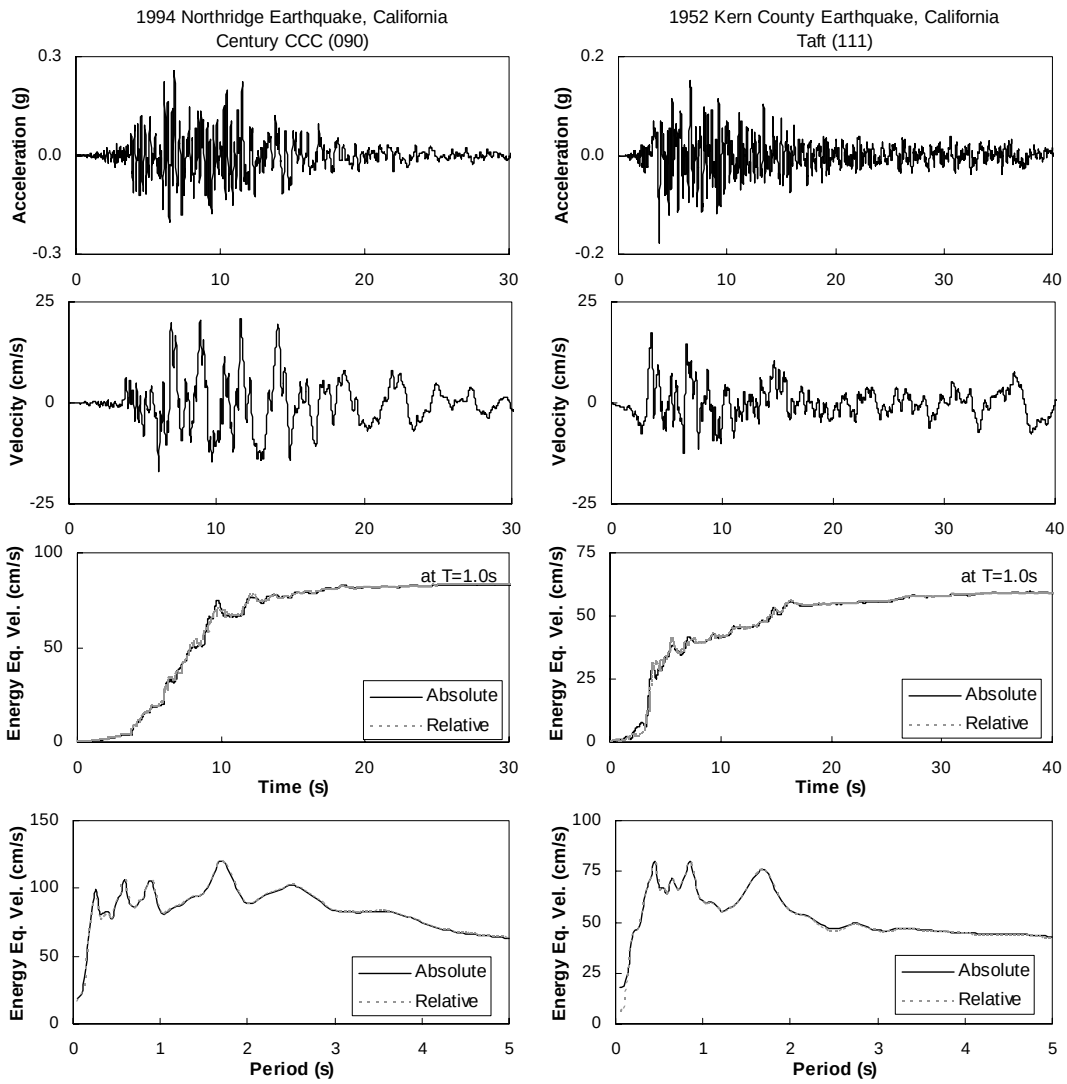

Figure 4.2 Acceleration, velocity and energy equivalent velocity time history plots, together with energy equivalent velocity spectra (5% damping) for typical far-fault records

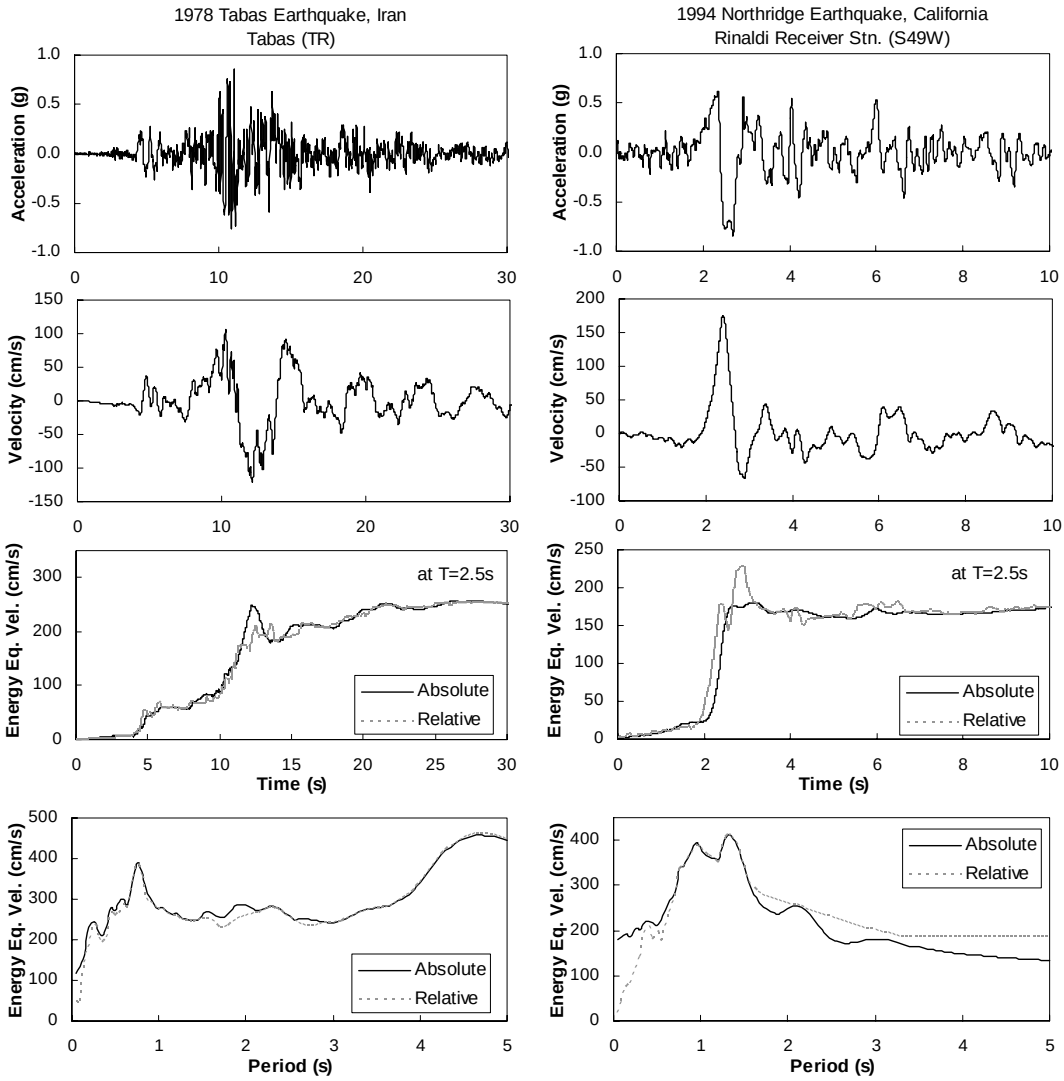

Figure 4.3 Acceleration, velocity and energy equivalent velocity time history plots, together with energy equivalent velocity spectra for typical near-fault forward directivity records

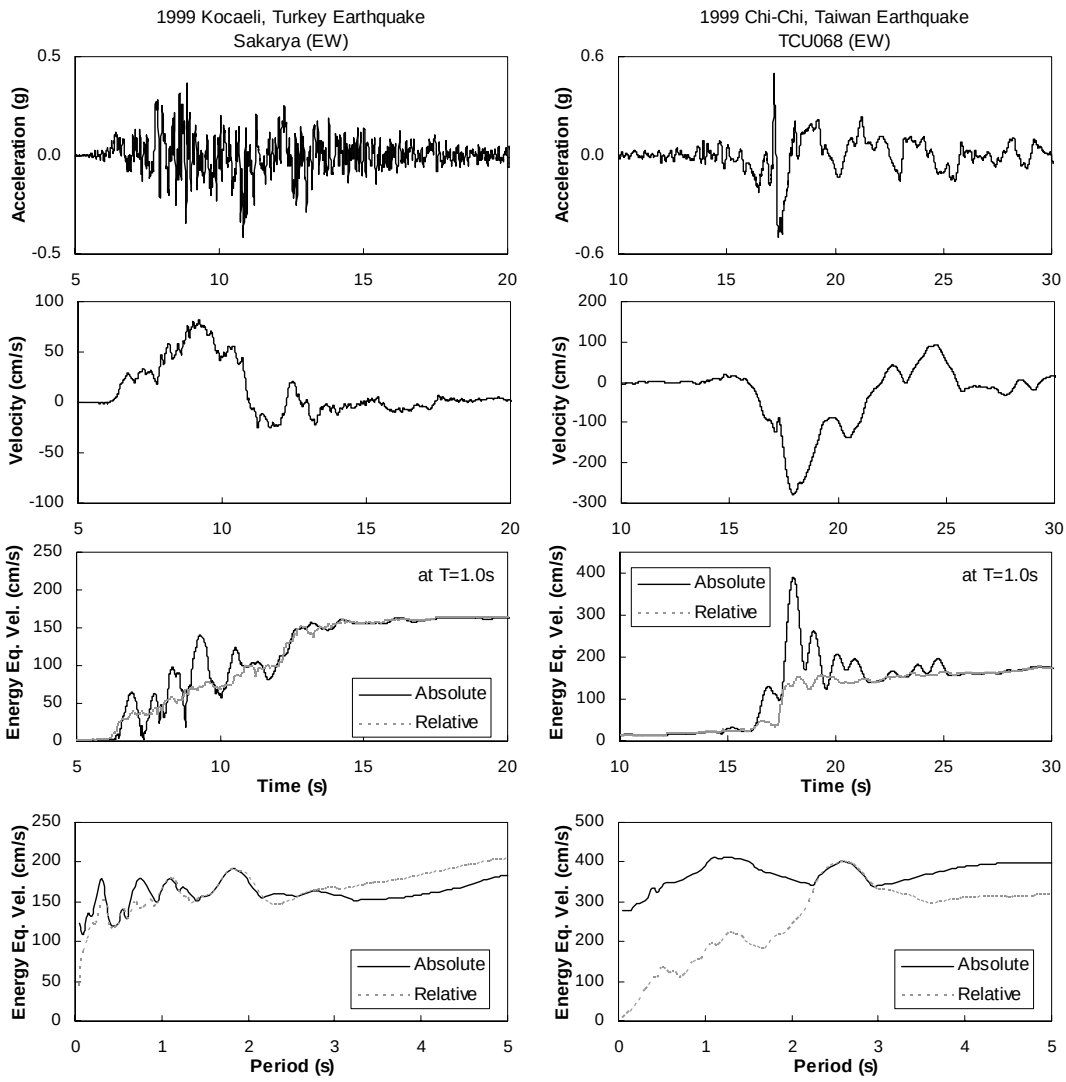

Figure 4.4 Acceleration, velocity and energy equivalent velocity time history plots, together with energy equivalent velocity spectra (5% damping) for typical near-fault fling records

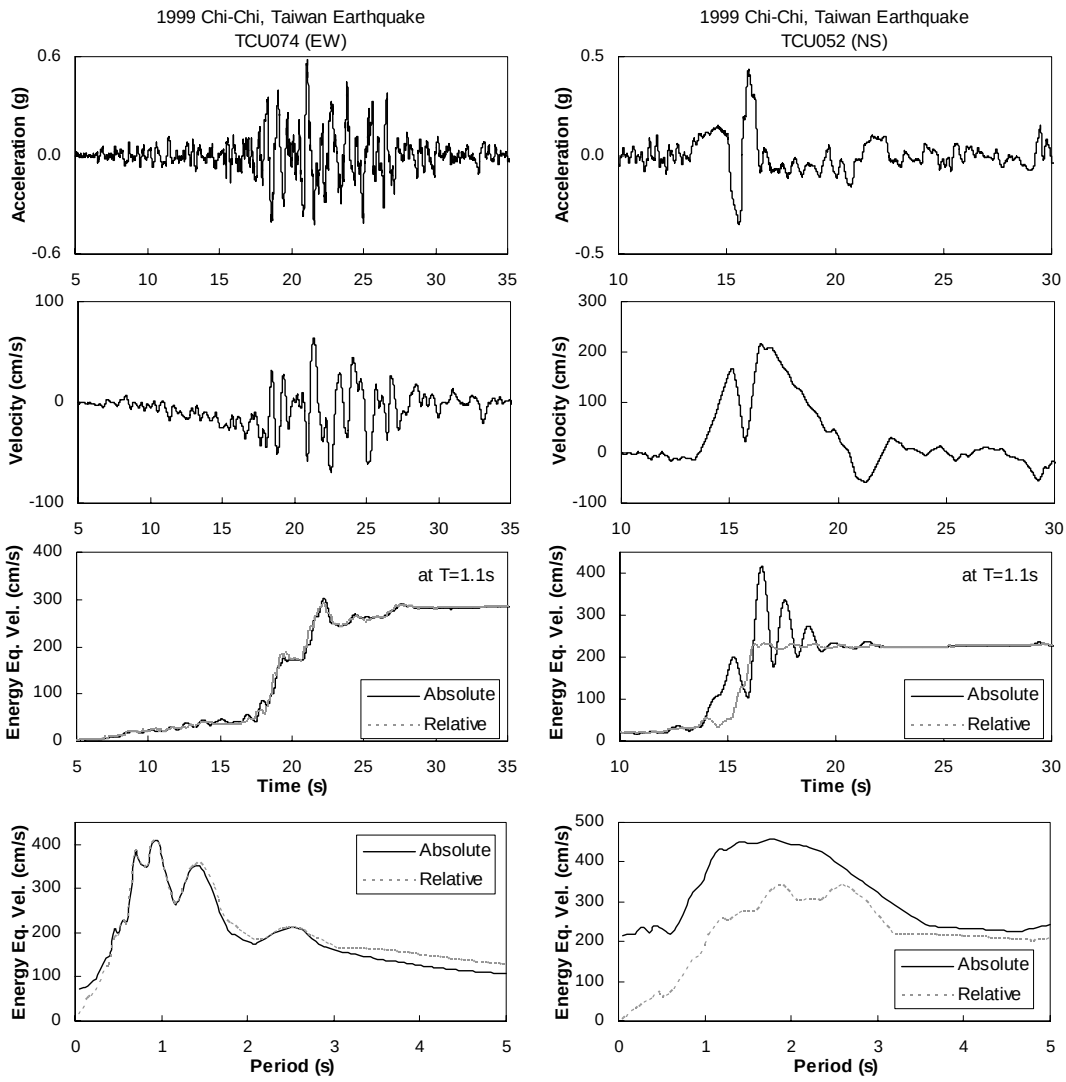

Figure 4.5 Acceleration, velocity and energy equivalent velocity time history plots, together with energy equivalent velocity spectra (5% damping) for additional near-fault fling records used in this study

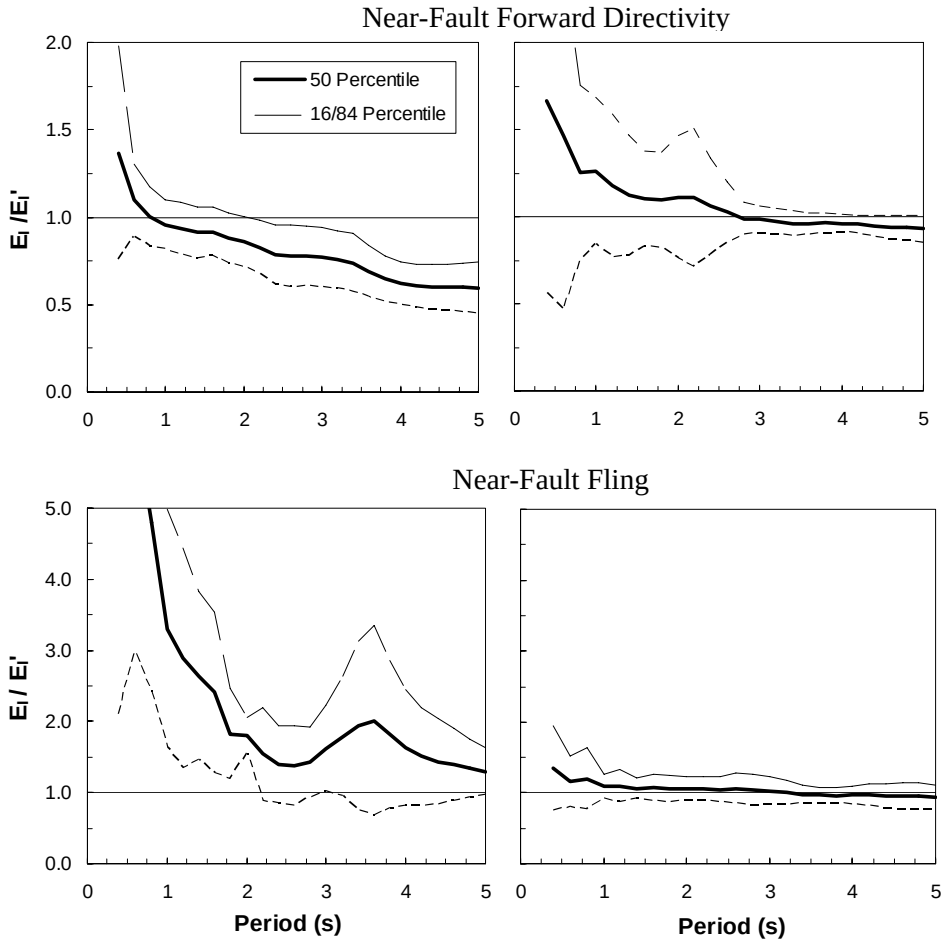

Figure 4.6 Mean and variation (16 and 84 percentiles) of absolute to relative energy ratio for near-fault records with distinguishable acceleration pulses (left) and for records with random high frequency acceleration spikes (right)

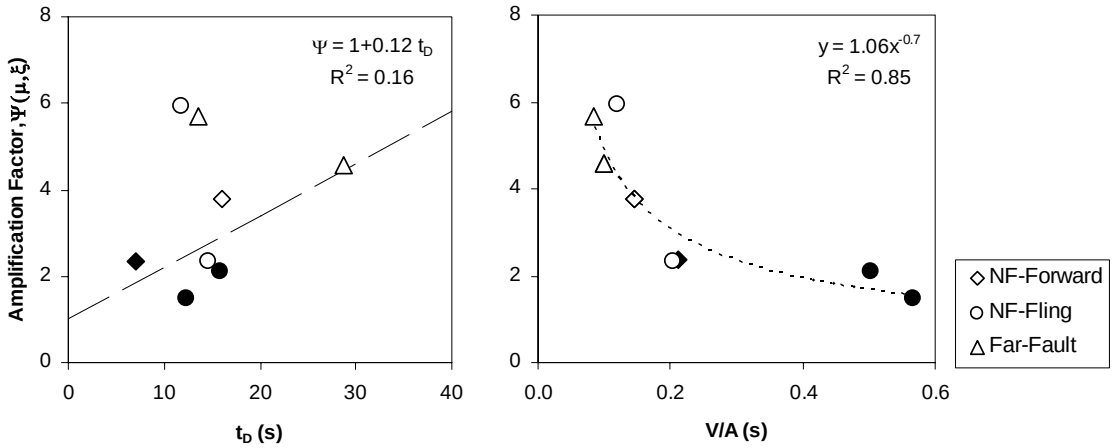

Figure 4.7 Amplification factor plotted against strong motion duration (Left) and V/A ratio (Right) (Note: Filled marks show the records having apparent acceleration pulses; dashed line (Left) represents the relation given by Uang and Bertero (1990); dotted line (Right) denotes the best fit curve)

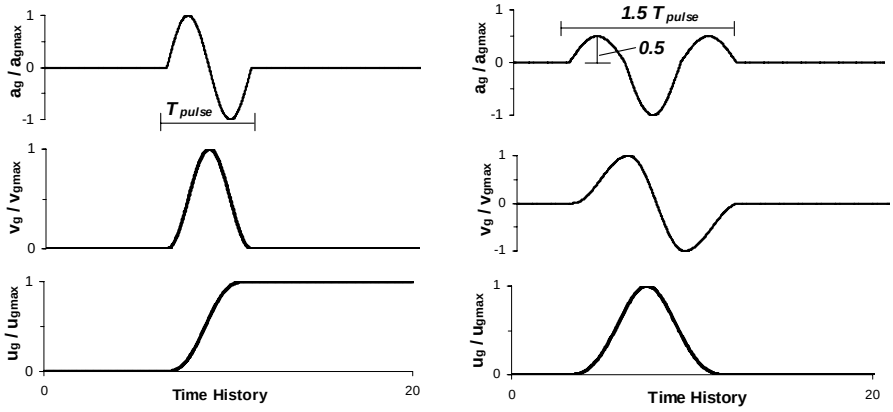

Figure 4.8 Sinusoidal wave forms to simulate near-fault forward directivity pulse (Left) and fling pulse (Right)

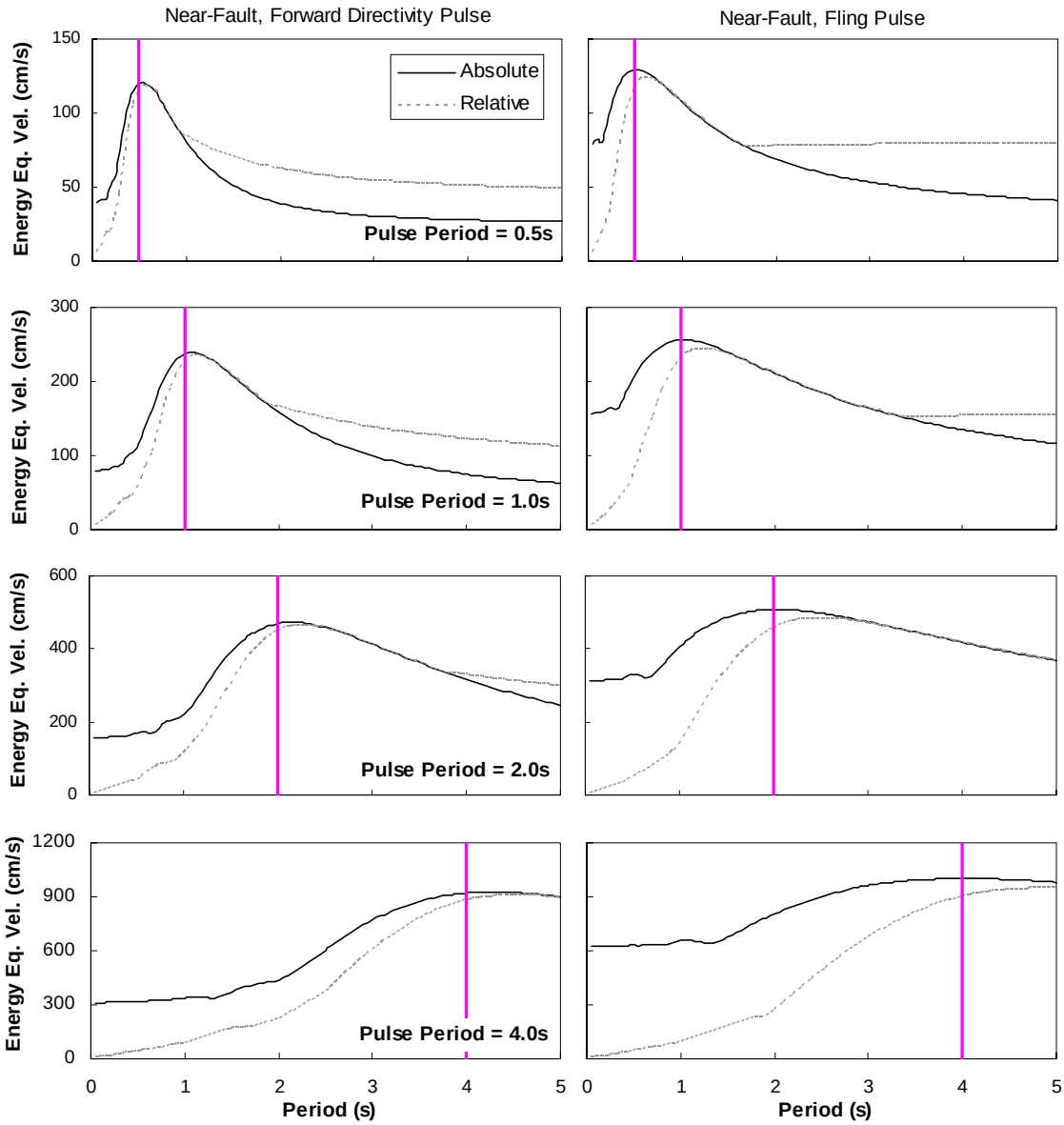

Figure 4.9 Comparison of equivalent velocity spectra (5% damping) computed using absolute and relative energy formulations for forward directivity (Left) and fling (Right) pulse models (*Vertical line in energy spectrum indicates the pulse period*)

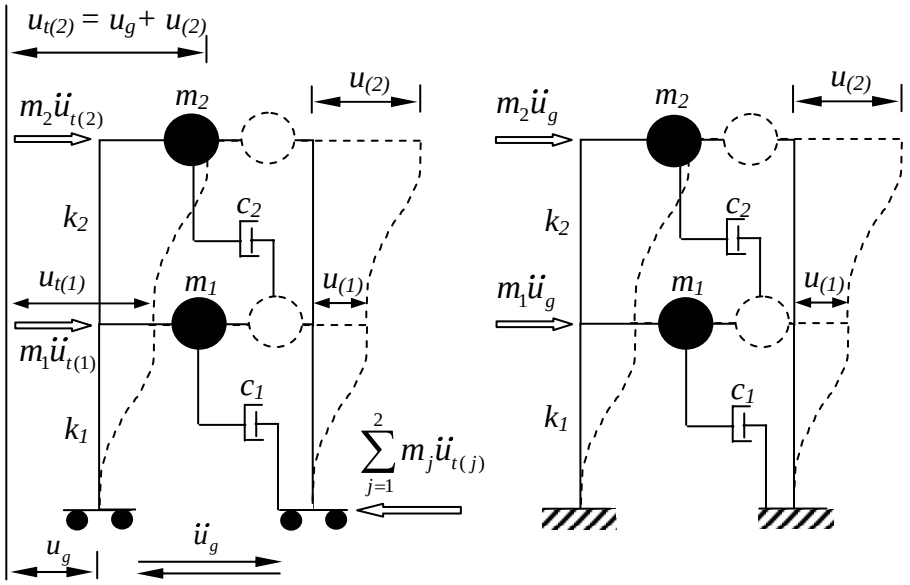

Figure 4.10 Idealized mathematical models of MDOF system used for absolute (Left) and relative energy formulations (Right)

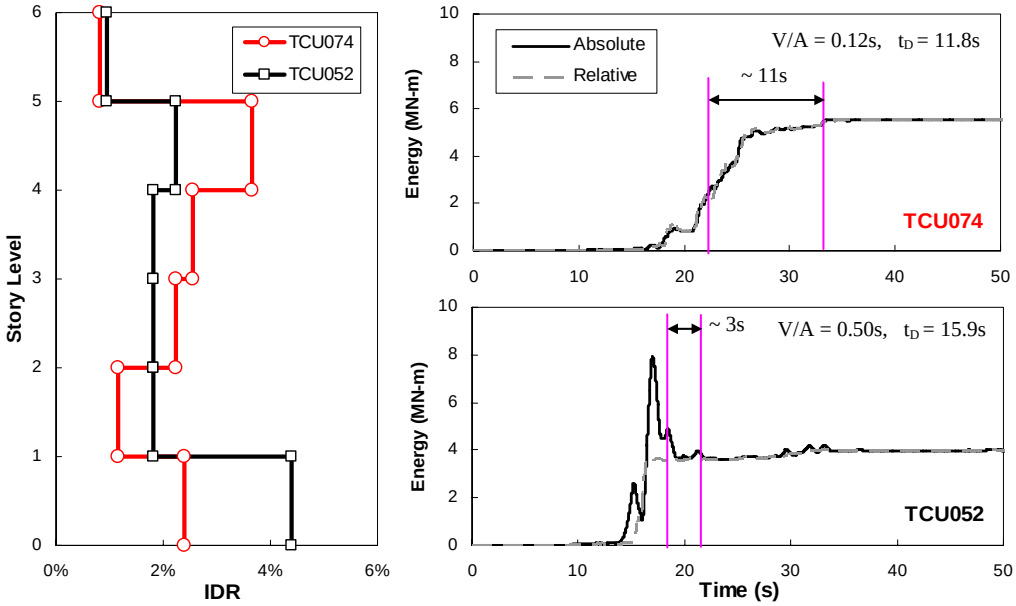

Figure 4.11 Peak interstory drift ratio (IDR) (Left) and energy time history (Right) computed for 6-story building subjected to fling records

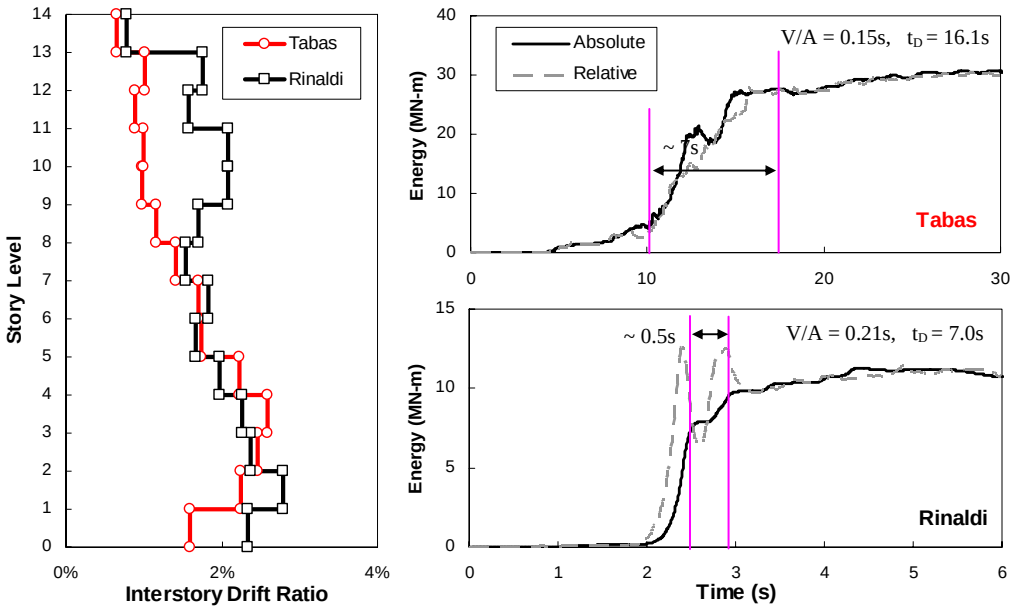

Figure 4.12 Peak interstory drift ratio (IDR) (Left) and energy time history (Right) computed for 13-story building subjected to forward directivity records

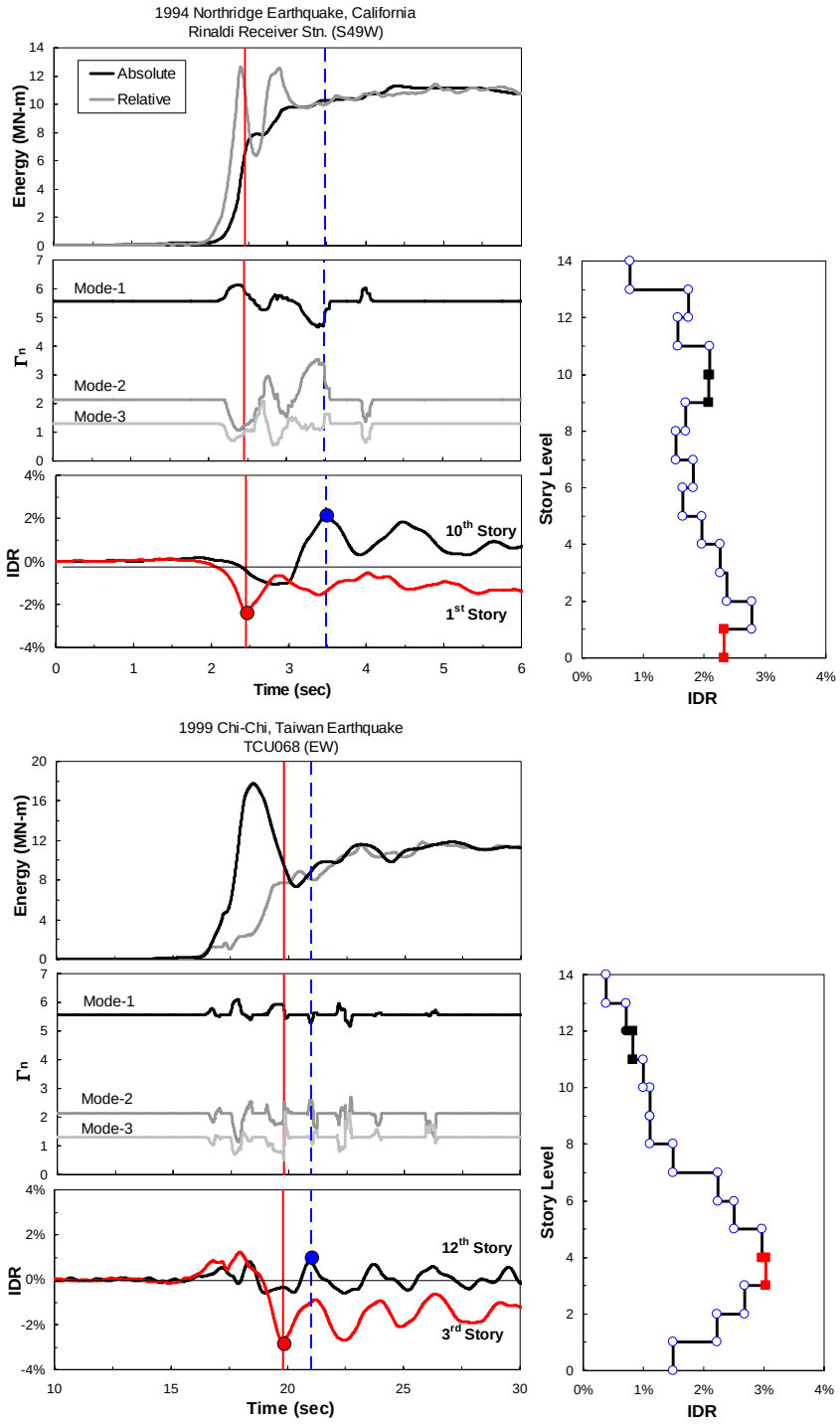

Figure 4.13 Variation of absolute and relative energy, modal participation factors and interstory drift ratio (IDR) for selected stories of 13-story building subjected to Rinaldi Receiver Stn. and scaled TCU068 records

CHAPTER 5

EFFECTIVE CYCLIC ENERGY AND RELATIONSHIP TO SEISMIC DEMAND

5.1 INTRODUCTION

A fundamental precept of performance-based seismic design is to ensure that structural components have adequate ductility and energy dissipation capacity so that damage condition in terms of interstory drift and member deformations may be controlled in limits of desired performance state when the system goes into inelastic phase. A key issue that has been confronted, however, is to identify the seismic performance of a structure associated with maximum response displacement considering ultimate capacity of yielding members, and correlation of this peak response with respective seismic demand. For its resolution, energy balance formulation appears to be effective in concept, as it permits a rational assessment of energy absorption and dissipation mechanism that can be effectively accomplished to balance the energy imposed to structural systems. Therefore, introduction of appropriate parameters formulated in terms of energy balance might lead to reliable prediction of maximum demand and also quantification of destructiveness of seismic action. Integration of these two aspects eventually emerges as a decisive prerequisite in performance-based design engineering. In recognition of this, a various response indices based on energy balance have been proposed recently (e.g., Park and

Ang 1984; Fajfar 1992; Teran-Gilmore 1999; Decanini and Mollaioli 2001; Riddell and Garcia 2001). These indices generally utilize absolute or relative energy formulations without making clear distinguish on ground motion characteristics such as cyclic nature of far-fault and impulsive feature of near-fault accelerograms.

For far fault records having cyclic nature, level of structural damage does not depend solely on maximum deformation since duration dependent low-cycle fatigue effect has also significant contribution to cumulative damage (e.g., Fajfar and Vidic 1994; Kunnath and Chai 2004; Sucuoglu and Erberik 2004; Teran-Gilmore and Jirsa 2005). That turns cumulative input energy to a convenient index parameter to effectively represent damaging potential of such records. However, majority of damage to structural components caused by near-fault records takes place in a few plastic cycles created by instantaneous energy demand associated with intense pulse effect. In this condition, effects of low-cycle fatigue become almost insignificant while the total damage becomes directly related to maximum system displacement. Additionally, using cumulative input energy as a response index may lead to uncertain results for near-fault records having apparent acceleration pulses, since peak seismic energy demand in such records renders itself as energy spikes in the early phase of energy-time response, and becomes more critical than input energy accumulated at the termination of ground movement. These energy spikes may arise either at relative or absolute energy time-histories depend upon the ratio of system period to dominant pulse period of ground motion, therefore differences between relative and absolute energy time-responses as well as resultant energy spectra become remarkable. This discrepancy brings additional complexity and uncertainty in selection of absolute or relative energy formulations to quantify the seismic

input energy. As a matter of fact, this aspect is crucial not only for assessing the reliability of various relative or absolute energy based response indices proposed to characterize the destructive power of near-fault earthquake recordings, but also and principally for the management of questions related to definition of seismic input energy. Therefore, this chapter is aimed to quantify the intensity and spectral distribution of energy demand, and express this demand in a reliable way as a function of characteristics of the ground motion and of the earthquake resisting system while being independent from absolute or relative energy definitions. To this end, an extensive number of near-fault ground motions were clustered for elaborating energy spectral parameters of inelastic SDOF systems. This effort led to definition of effective cyclic energy (ECE) expressed as the maximum value of peak-to-peak dissipated energy through damping and hysteresis loops (in a finite time interval required for reversal of system velocity). The correlation of ECE to respective maximum system displacement was verified through inelastic SDOF time-response analyses considering different hysteresis rules and ductility levels. Based on the conceptual development of ECE, non-dimensional ground motion severity index (γ_{eff}) were proposed with like formulation of earthquake damage potential index proposed by Fajfar (1992). The validity and stability of γ_{eff} in comparison with other common response indices were substantially performed through carefully sorted 107 near-fault ground motions for objective of considering aleatoric variability in near-fault earthquake recordings. Use of γ_{eff} turns out particularly advantageous in that, unlike the peak energy spectral value, its quantity takes the effective damaging energy amount into account, so that it can be regarded as the most stable parameter in energy analysis.

Finally, the ECE demand of a MDOF system is estimated through modal-energy-decomposition for elastic and inelastic SDOF systems. The concept of ECE spectrum is next proposed to estimate the modal target energy demands in MDOF systems to be directly used in performance evaluation of new and existing structures.

5.2 RELATIONSHIP BETWEEN SEISMIC INPUT ENERGY AND RESPONSE

The feasibility of defining a rational energy-based descriptor that can be related to the severity of earthquake motions and also to critical system demand parameters requires a clear understanding of the effects of seismic input energy on building structures. Therefore, peak displacements of inelastic SDOF systems subjected to an ensemble of near-fault records were compared to seismic input energy. Table 1 lists all the records used in the study. All of the selected ground motion recordings were taken in the vicinity of the causative fault and contain long-period coherent velocity pulses which are characteristic of near-fault accelerograms having fling or forward-rupture directivity. These long period coherent velocity pulses are produced either by integration of apparent acceleration pulses or a succession of high frequency acceleration peaks.

Figure 5.1 displays the acceleration and velocity time-series of representative ground motions. Notably, the Rinaldi Receiver Stn. Record contains a distinguishable acceleration pulse (shaded area) whereas the Sakarya record does not. The difference in the initiation of velocity pulse has been shown to influence the input energy on structural systems (see Chapter 4). As such, records containing apparent acceleration pulses produce instantaneous energy spikes in the early phase of response which can be

appreciably larger than the energy accumulated at the end. Conversely, for near-fault records characterized by high frequency acceleration spikes, input energy tends to accumulate progressively over time resembling typical far-fault records.

Figure 5.2 presents the energy, velocity and displacement time history and the resulting force-deformation response computed for an inelastic SDOF system subjected to the records shown in Figure 5.1. A bilinear material model with 2 percent strain-hardening (see Figure 5.4) was used to generate these results for a system with a period of 1.0s and a ductility demand of 4. Since the records were not scaled, the yield strength of the systems was adjusted to achieve the desired ductility ratio. In these figures, the energy measure used is the relative input energy ($E_I^{'}$) which is formulated as follows:

$$E_K^{'} + E_D + E_H = E_I^{'} \tag{5.1}$$

where $E_K^{'}$ is the relative kinetic energy, E_D is the damping energy, E_H is the hysteretic energy composed of elastic strain energy (E_S) and plastic strain energy (E_P) (i.e., irrecoverable hysteretic energy). It is possible to expand Equation 5.1 into its respective components:

$$\frac{m(\dot{u})^2}{2} + \int c\dot{u}du + \int f(u)du = -\int m\ddot{u}_g du = -\int m\ddot{u}_g \dot{u}dt \tag{5.2}$$

in which *m* is the mass, *c* is the damping coefficient, *f(u)* is the restoring force, *u* is the relative displacement of the SDOF system with respect to the ground and $\ddot{u}_g$ is the ground acceleration. Additionally, energy is represented as the energy equivalent velocity ($V_{eq} = \sqrt{2E_I^{'}/m}$) since this term is linearly proportional to the ground motion amplitude. For convenience, V_{eq} is henceforth referred to as input energy. The responses shown in

Figure 5.2 provide an opportunity to assess the variation of seismic demand and its correlation to different components of input energy.

Owing to the fact that damage to a structural component is directly related to dissipated energy, Figure 5.2 shows the combined effects of damping and hysteretic energy (E_H+E_D) separately in addition to the relative input energy ($E_I^{'}$) and damping energy (E_D). The plots showing the energy components indicates that the kinetic energy component vanishes during reversal of system velocity (i.e., $\dot{u}(t) = 0$ at the point of zero crossings in the velocity time-response), and the summation of damping and hysteretic energy becomes equal to the relative input energy. These time instants ($\dot{u}(t) = 0$) also refer to the corner points in the force-deformation hysteresis loops representing the absolute peak displacements during each cycle. The energy balance equation between these two peaks in the displacement response can be expressed as

$$\Delta E_D + \Delta E_H = \Delta E_I \tag{5.3}$$

where ΔE_D is the incremental energy due to viscous damping and ΔE_H includes both the incremental recoverable strain energy (ΔE_S) and irrecoverable strain energy (ΔE_P). The peak value of the term on the right hand side of the equation ($\Delta E_{I,\max}$) is hereby defined as the effective cyclic energy (ECE). The definition of ECE represents the incremental work done during the finite time interval ($\Delta t = t_2 - t_1$) required for the reversal of the effective system velocity (i.e., $\dot{u}(t_2) = 0$ and $\dot{u}(t_1) = 0$). As shown in Figure 5.2, ECE attains its largest magnitude immediately before the maximum displacement. It is also noteworthy that ECE depends not only on the ground motion characteristics but

also on the system attributes (such as period, hysteretic rule, damping, ductility etc.). Although Equations 5.1 and 5.2 are derived for relative input energy, ECE is not affected by the choice of absolute or relative energy since the difference in the two energy definitions in fact arises from the formulation of the kinetic energy term which vanishes in the ECE formulation.

5.3 EFFECTIVE CYCLIC ENERGY BASED GROUND MOTION SEVERITY INDEX

The concept of energy balance has been extensively used to identify reliable relationships between seismic energy and displacement demands, and consequently develop indices to effectively capture the destructive potential of earthquake motions. Fajfar (1992) derived the following non-dimensional parameter based on the reduction of the deformation capacity due to low-cycle fatigue.

$$\gamma = \frac{\sqrt{E_H / m}}{\omega D} \tag{5.4}$$

where E_H represents the dissipated hysteretic energy, m is the mass of the system, ω is the natural frequency and D is the maximum displacement demand. This index, which is the ratio of two equivalent velocities, has been shown to be dependent on both ground motion and system attributes but independent of damping (Fajfar and Vidic 1994). An analogous parameter (ζ) was later proposed by Teran-Gilmore (1998) whereby the hysteretic energy term (E_H) in Equation 5.1 was replaced with the absolute input energy term (E_I) as follows:

$$\zeta = \frac{\sqrt{E_I / m}}{\omega D} \tag{5.5}$$

This parameter has shown to be more stable than γ (Teran-Gilmore 1998; Decanini et al. 2000). Other response indices correlating the maximum displacement demand to seismic energy utilizes the ratio of hysteretic energy to total input energy (E_H / E_I) as used in studies by Kuwamura and Galambos (1989), Fajfar and Vidic (1994), Lawson and Krawinkler (1995) and Decanini and Mollaioli (2001) and the square root of hysteretic energy $S_H = \sqrt{E_H}$ proposed by Riddell and Garcia (2001).

Following a detailed and comprehensive study examining peak response measures and seismic energy (Figure 5.2 being a representative set) of SDOF systems, it was established that ECE (i.e., $\Delta E_{I,\max}$) is a reliable measure of the critical seismic energy transferred to a structural system and producing the maximum cyclic deformation. On the basis of this finding, the hysteretic energy term in Equation 5.4 was replaced with ECE resulting in an alternative descriptor, denoted by γ_{eff} as follows:

$$\gamma_{eff} = \frac{\sqrt{(\Delta E_{I,\max}) / m}}{\omega D} \tag{5.6}$$

The stability and accuracy of this new descriptor is investigated for 107 near-fault records. Pertinent information on the ground motion data is listed in Table 1, while the distribution of their PGA (peak-ground-acceleration) values with respect to moment magnitude (M_W) and closest fault distance are demonstrated in Figure 5.3. These ground motions were recorded from earthquakes having a magnitude range from 6.0 to 7.6 and at distances varying from 0.0 to 17.0 km to the causative fault. The records either contain forward-rupture directivity or fling; fling records in Table 1 were processed by baseline

correction only (by fitting segmental polynomials) following the removal of pre-event mean. Such a scheme is used for correction of raw data since conventional filtering techniques may distort or eliminate the true static displacement at the end of the time-history (Graizer 1989). The information on true static off-sets was retrieved from the available GPS data. The applied correction scheme guarantees that the velocity will be zero near the beginning and at the end of the time-series (see Chapter 3).

Table 1 includes another piece of useful information on the ratio of PGA to PGV (denoted as *V/A*) and strong motion duration (T_D) of the recordings. *V/A* ratio indicate the average duration of acceleration pulse provided that PGV is reached immediately following the dominant acceleration pulse. This parameter has been shown to be well correlated with the damage potential (Sucuoglu et al. 1998) and peak input energy of recordings (see Chapter 4). Strong motion duration (T_D) is another parameter used commonly to identify the severity of ground motions (e.g., Uang and Bertero 1990; Amiri and Dana 2005). It was first defined by Trifunac and Brady (1975) as the interval between times at which 5 and 95 percent of the value of the Arias intensity ($I_A = (\pi / 2g)\int_0^{t_d} \ddot{u}_g^2 dt$, where t_d is the duration of record) is achieved.

Using the ground motion records listed in Table 1, the correlation between peak seismic demand and the proposed energy (ECE) and damage (γ_{eff}) measures is evaluated and also compared to other indices. The analyses considered two different hysteretic models at four different ductility levels (μ = 1, 2, 4 and 6). A bilinear non-degrading hysteretic model and a pinching-degrading model were employed in the inelastic SDOF time-history analyses. Details of the hysteresis models are illustrated in Figure 5.4. Figure 5.5 summarizes the correlation between peak system displacement and

effective cyclic energy (ECE), absolute input energy (E_I), *V/A* ratio and strong motion duration (T_D) for two systems (T=1s and T=2s), two ductility demands and two force-deformation models. These plots indicate that ECE is better correlated to peak system deformation than parameters such as E_I, *V/A* and T_D. Both relative and absolute input energy produced similar results. Though the bilinear model resulted in slightly larger correlation coefficients (*R*) compared to the pinching-degrading model, general findings from Figure 5.5 are valid for both the ductility levels and period range (T=0.2 to T=5.0 sec) considered in the study. In contrast to ECE, a weaker correlation was observed between strong motion duration (T_D) and peak system deformation. This finding is not surprising since strong motion duration and cyclic (low-cycle fatigue) effects are not as significant for near-fault records as with far fault-records. On the other hand, *V/A* ratios are better correlated with peak deformation than T_D.

It should be also noted that the constant slope of the best-fit line in Figure 5.5 is directly related to the non-dimensional parameter γ_{eff} . To further evaluate the accuracy and stability of γ_{eff} , it is compared in Figure 5.6 with other non-dimensional response indices, namely $\gamma, \zeta,$ and E_H / E_I . Despite some dispersion at small deformations, γ_{eff} generally yields more stable results than other indices. Of the existing measures of damage potential, E_H / E_I is seen to provide the most consistent estimates. Figures 5.5 to 5.6 collectively indicate that ECE and its counterpart γ_{eff} are stable and reliable indicators of input energy and damage potential of ground shaking. Hence, the energy dissipated through inelastic deformations in an effective cycle (i.e., through damping and dissipated hysteretic energy) is a critical parameter that is most closely correlated with the peak

system response for near-fault ground motions. This suggests the feasibility of determining the maximum seismic demand from the effective cyclic energy.

5.4 EFFECTIVE CYCLIC ENERGY DEMANDS IN MDOF SYSTEMS

Absolute energy formulation for MDOF systems was initially derived by Uang and Bertero (1990). In a similar manner, it is possible to express the relative energy imparted to a MDOF system as:

$$\frac{1}{2}\dot{\boldsymbol{u}}^T\boldsymbol{m}\dot{\boldsymbol{u}} + \int \dot{\boldsymbol{u}}\boldsymbol{c}d\boldsymbol{u} + \int \boldsymbol{f}_s\, d\boldsymbol{u} = \int (\sum_{j=1}^{N} m_j \ddot{u}_g)\; d\boldsymbol{u} = \int (\sum_{j=1}^{N} m_j \ddot{u}_g \dot{u}_j)\; dt \tag{5.7}$$

$$E_K + E_D + (E_S + E_P) = E'_I \tag{5.8}$$

where $\boldsymbol{m}$ is the diagonal mass matrix, $\boldsymbol{c}$ is the damping matrix and $\boldsymbol{u}$ is the relative story displacement vector. Accordingly, $\boldsymbol{m_j}$ is the lumped mass and $\dot{u}_j$ is the relative velocity recorded at the j^{th} story, and N is the number of stories. In the above expression, E'_I corresponds to the relative work done due to the sum of inertia forces $(m_j \ddot{u}_g)$ at each storey level over the corresponding story displacement u_j. Chou and Uang (2003) showed that the hysteretic energy component of MDOF systems (i.e., E_S+E_P) can be predicted using equivalent-single-degree-of-freedom (ESDOF) systems derived from the first and second mode elastic modal properties. Based on this idea, relative input energy time-history is computed for a MDOF system and compared with the corresponding input energy of ESDOF systems. The MDOF system studied for this purpose is an existing six-story steel moment-frame building instrumented by the California Strong Motion

Instrumentation Program. Therefore, recorded acceleration time-series at different story levels were initially used in calibration of the numerical model. Details of modeling and calibrations can be found in Chapter 3. The six-story building has the elastic modal periods of 1.41, 0.51 and 0.30 s and modal participation factors of 2.57, 0.96 and 0.465 for the first, second and third mode, respectively. These properties are used to obtain corresponding ESDOF systems parameters through individual pushover analyses conducted using invariant load vectors. The load vectors correspond to height-wise distribution of inertial forces expressed as $s_n = \phi_n.\mathbf{m}$ (where ϕ_n is the elastic n^{th}-mode vector). Through equivalent bi-linearization to approximate the ESDOF parameters, spectral conversion of base-shear is achieved similar to the ATC-40 (1996) procedure, whereas spectral displacement is computed by dividing the total dissipated energy during the monotonic pushover analysis to the corresponding base shear. Thereby the ESDOF system is forced to dissipate the same energy dissipated by the MDOF system at each step of the pushover analysis. In this way, potential limitations and drawbacks of using the roof displacement as a deformation index to convert the MDOF capacity curve to the ESDOF system capacity spectrum for modes higher than first mode are eliminated. It is instructive to note that proportionality of the roof displacement to the other story displacements is only limited to the first mode. The energy-based approach for ESDOF conversion of MDOF system has been recently developed in Hernandez-Montes et al. (2005) and extended to be used in the adaptive multi-modal pushover analysis proposed later in Chapter 6.

Figure 5.7a displays the relative input energy time-variation computed through Eq. (5.7) for the MDOF system subjected to near-fault forward-rupture directivity record of

1992 Erzincan Earthquake. This record contains a coherent long period velocity pulse associated with distinct pulse content in the acceleration time-series. The record is scaled by 2.0 to create significant inelastic demands, hence the peak inter-story drift ratio exceeds 3 percent and significant yielding takes place throughout the structure. Also shown in Figure 5.7a are the relative input energy plots computed from the ESDOF systems for comparison. Relative input energy of each ESDOF system ($E'_{I(ESDOF),n}$) is calculated through inelastic time-history analysis and converted to the MDOF n^{th}-mode input energy contribution as

$$E'_{I(MDOF),n} = E'_{I(ESDOF),n}\Gamma_n^2 \tag{5.9}$$

where Γ_n is the modal participation factor. Figure 5.7a shows that the energy input to MDOF system can be estimated by summation of the energies of the first few modes (generally up to two or three modes). Thus, the total input energy to MDOF system can be expressed as

$$E'_{I(MDOF)} = \sum_{n=1,3} E'_{I(ESDOF),n}\Gamma_n^2 \tag{5.10}$$

Right side of the Eq. 10 can be interpreted as a modal-energy-decomposition approach. Figure 5.7b compares the input energy computed from the elastic SDOF with the inelastic SDOF time-history analyses (for modes 1 - 3) and also the input energy computed from nonlinear-time-history (NTH) analysis of the MDOF system. This figure implies that the abrupt intense energy jump, condensed in a short period of time (highlighted zone in Figure 5.7b) which is a characteristic of near-fault pulse-type records (see Chapter 3), can be reasonably estimated by elastic analyses. The sum of hysteretic and damping components of this abrupt energy increase (i.e., ECE) is directly associated with the peak

inelastic displacement demand since it is dissipated in a single or very few cycles. It is also clear that, following the immediate energy input, the elastic and inelastic energy curves start to deviate from each other, and the difference between them becomes the accumulated energy dissipated through plastic excursions.

It is possible to express the sum of hysteretic and damping energies as the difference between input and kinetic energies since the computation of input and kinetic energies for MDOF systems is more convenient than the computation of hysteretic and damping energies. If the relative energy is used, the following expression can be utilized to compute the sum of hysteretic and damping energy terms:

$$\Delta E_I = E_\xi - E_H = E_I^{'} - E_K = \int (\sum_{j=1}^{N} m_j \ddot{u}_g)\ \dot{u}_j dt - \frac{1}{2}\sum_{j=1}^{N} m_j (\dot{u}_j)^2 \qquad (5.9)$$

Similar to SDOF systems investigated earlier, the ECE (i.e., $\Delta E_{I,\max}$) for MDOF system is equal to the peak incremental value of the sum of viscous damping and hysteretic energies between a peak-to-peak half cycle (Figure 5.2). At these time-steps, relative and absolute energy are identical and become equal to the sum of hysteretic and damping energies. Figure 5.8a shows the time-history of relative input energy and exemplifies the computation of ECE for a MDOF system. Figure 5.8b-c shows the interstory drift ratio (IDR = relative displacement between two consecutive stories normalized by story height) time-variation for selected stories based on the peak IDR profile presented in Figure 5.8d. The IDR is selected as a representative response parameter since it is well-correlated with component deformations at that story (see Chapter 2). It is instructive to note that peak IDR for each story is associated with the ECE. To be more specific, the ECE is dissipated throughout the structure within a single

or few cycles resulting in the effective structural peak responses. This is typical for structures subjected to impulsive records (see Chapter 3)

Based on the information gained from Figures 5.7 and 5.8, it is possible to conclude that peak inelastic response parameters for near-fault earthquakes take place after the first change of state from elastic to inelastic behavior. Under these conditions, elastic SDOF systems may be potentially used to approximate the ECE input to the MDOF system (see Figure 5.7b). Figure 5.9 compares the ECE computed based on the elastic and inelastic ESDOF systems with that of the MDOF system. It should be noted that in generating the ECE, energy contributions of ESDOF systems for the first two modes are summed since energy contribution of the third mode is significantly low as shown in Figure 5.7a. This figure implies that while the ECE input to MDOF system can be best estimated using inelastic ESDOF systems, for practical purposes, elastic ESDOF systems can still be utilized since it provides reasonable predictions of ECE demand.

The good correlation obtained between the ECE of MDOF and SDOF systems allows ECE to be used directly in a spectral format. Typical ECE spectra derived for a set of representative near-fault accelerograms having forward-rupture directivity and fling are demonstrated in Figure 5.10. It is seen that ductility ratio has only a marginal effect on the energy demand while the force-deformation modeling can have a more significant impact on the spectral shape. The pinching-degrading model shows tendency to shift the ECE peaks to the lower periods compared to the stable bilinear hysteretic model.

5.5 EFFECTIVE-CYCLIC-ENERGY DEMAND ESTIMATION

ECE demands of a MDOF system is estimated based on the modal-energy-decomposition (Eq. 5.10) and the elastic ECE spectrum. The six-story building described earlier is used to illustrate the proposed concept. Two near-fault records are employed in the nonlinear time-history simulations to obtain the corresponding performance as well as the ECE of the MDOF system. Figure 5.11b compares the MDOF nonlinear time history results with the ECE demands computed based on both inelastic SDOF time history analyses and those computed from the elastic ECE spectra (Figure 5.11a). The results of inelastic SDOF time-response analyses yield the best estimates since they are more consistent with the modal ductility demands of the MDOF system. However it is seen that the elastic ECE spectrum provides reasonable predictions. This later approach requires generation of elastic ECE spectrum and limited knowledge on the basic structural characteristics of the MDOF system (i.e., period, damping and participation factor of first few elastic modes).

The modal ECE demands computed using the ECE spectrum (i.e., vertical lines in the ECE plots) are also in good agreement with the peak interstory drift profiles (Figure 5.11c) which essentially represent the overall seismic performance. Results of NTH analyses show that higher mode contributions (i.e., amplified deformations at upper or intermediate stories) to the response are significant in case of TCU068 record, whereas the Parachute Test Site record triggers a primarily first mode response and imposes the largest interstory drift exceeding 4.0 percent at the first story level. Correlation of the MDOF responses with ECE spectrum indicates that the Parachute Test Site record has a significantly larger value in the ECE spectrum close to the first mode period of the

building than at the higher modes. For the TCU068 record, the ECE spectrum indicates the likelihood of higher mode participation by providing relatively small energy difference between the first two modes. Moreover, it is evident that the ECE spectra of the records confirm the information gained from the inelastic response of the buildings suggesting the potential of the proposed ECE spectra to distinguish seismic damage potential of ground motions.

5.6 CONCLUSIONS

It is well known that the ability of structural components to dissipate energy through viscous and hysteretic damping is a primary factor contributing to structural damage during earthquakes. For far-fault records, this damage is a direct consequence of the number and amplitude of plastic deformation cycles. Hence, in quantifying the damage potential of ground motion, it is important to include the effects of the duration of strong ground shaking. In contrast, near-fault ground motions often have an impulsive feature and impose sudden and intense energy input that should be dissipated within a short period of time. This causes amplified deformation demands in structures and is associated with very few cycles of plastic deformation and, therefore, earthquake damage is related to the maximum deformation or maximum ductility. While most of the previous studies on energy demand has focused on far-fault records (or a collection of records in which ground motion characteristics were not explicitly considered), the present research is concerned primarily with near fault records. It is demonstrated that peak deformation is well correlated to effective cyclic energy (ECE), and a relationship between ECE and

maximum deformation is proposed through a severity index (γ_{eff}). This non-dimensional index can be used to include displacement parameters in seismic design procedures based on energy concepts, and also to assess the damage potential of ground motions. Since ECE is influenced by system response, the development of ECE spectra is shown to be more appropriate than conventional acceleration spectra to assess deformation demands in structures.

Finally, a procedure utilizing the modal-energy-decomposition through elastic ECE spectrum is presented to estimate the ECE demand of MDOF systems. Thereby "modal-target-energy" demands are computed to be used directly in performance evaluations without performing NTH analysis. The proposed procedure is validated for an instrumented moment frame building for forward directivity and fling records and satisfactory energy estimates are obtained. The features of ECE presented in this sutdy indicate that it can be a valuable tool in developing energy-based guidelines for performance assessment of building structures.

Table 5.1 Near-fault earthquake recordings

No.	Year	Earthquake	M_W	Mech.[1]	Station	Characteristics	Dist.[2] (km)	Site Class[3]	Data Src.[4]	Comp.	PGA (g)	PGV (cm/s)	PGD (cm)	T_D[5] (s)	V/A[6] (s)
1	1966	Parkfield	6.1	SS	Temblor	Fwd-Rup. Dir.	11.4	C	1	205	0.36	21.6	3.8	4.4	0.06
2	1966	Parkfield	6.0	SS	Cholame 2WA	Fwd-Rup. Dir.	6.6	C	1	065	0.48	75.0	22.4	7.0	0.16
3	1971	San Fernando	6.6	TH/REV	Pacoima Dam	Fwd-Rup. Dir.	2.8	B	1	254	1.16	54.3	11.7	6.7	0.05
4	1978	Tabas	7.4	TH	Tabas	Fwd-Rup. Dir.	3.0	D	1	TR	0.85	121.4	95.1	16.1	0.15
5	1979	Imperial-Valley	6.5	SS	El Centro Array #3	Fwd-Rup. Dir.	13.8	D	1	140	0.27	46.8	18.9	11.9	0.18
6	1979	Imperial-Valley	6.5	SS	El Centro Diff. Array	Fwd-Rup. Dir.	5.6	D	1	270	0.35	71.2	45.9	7.0	0.21
7	1979	Imperial-Valley	6.5	SS	El Centro Imp. Co. Cent.	Fwd-Rup. Dir.	7.6	D	1	092	0.23	68.8	39.4	13.2	0.30
8	1979	Imperial-Valley	6.5	SS	El Centro Array #4	Fwd-Rup. Dir.	8.3	D	2	S50W	0.36	80.6	72.0	10.3	0.23
9	1979	Imperial-Valley	6.5	SS	El Centro Array #6	Fwd-Rup. Dir.	3.5	D	2	S50W	0.44	113.4	72.0	8.2	0.26
10	1979	Imperial-Valley	6.5	SS	El Centro Array #7	Fwd-Rup. Dir.	3.1	D	2	S50W	0.46	113.3	47.5	4.8	0.25
11	1979	Imperial-Valley	6.5	SS	El Centro Array #8	Fwd-Rup. Dir.	4.5	D	1	140	0.60	54.3	32.4	6.8	0.09
12	1979	Imperial-Valley	6.5	SS	El Centro Array #10	Fwd-Rup. Dir.	8.7	D	2	320	0.23	46.3	26.7	12.0	0.20
13	1979	Imperial-Valley	6.5	SS	Bonds Center	Fwd-Rup. Dir.	4.4	D	1	140	0.59	45.2	16.8	9.7	0.08
14	1979	Imperial-Valley	6.5	SS	Holtville Post Office	Fwd-Rup. Dir.	8.8	D	1	225	0.25	48.8	31.6	11.8	0.20
15	1979	Imperial-Valley	6.5	SS	Brawley Airport	Fwd-Rup. Dir.	11.3	D	1	225	0.16	35.9	22.4	14.9	0.23
16	1979	Imperial-Valley	6.5	SS	EC Meloland Overpass	Fwd-Rup. Dir.	3.1	D	1	270	0.30	90.5	31.7	6.7	0.31
17	1983	Coalinga	6.5	TH/REV	Pleasant Valley P.P. Bld.	Fwd-Rup. Dir.	8.5	-	1	045	0.38	32.4	6.4	8.1	0.09
18	1984	Morgan Hill	6.1	SS	Anderson Dam	Fwd-Rup. Dir.	4.8	B	2	340	0.29	28.0	5.8	5.2	0.10
19	1984	Morgan Hill	6.1	SS	Gilroy STA #2	Fwd-Rup. Dir.	11.8	D	2	090	0.21	12.8	2.0	12.7	0.06
20	1984	Morgan Hill	6.1	SS	Gilroy STA #3	Fwd-Rup. Dir.	10.3	D	2	090	0.19	12.2	2.6	22.0	0.06
21	1984	Morgan Hill	6.1	SS	Gilroy STA #6	Fwd-Rup. Dir.	6.1	C	2	090	0.29	36.5	5.2	6.5	0.13
22	1984	Morgan Hill	6.1	SS	Coyote Lake Dam	Fwd-Rup. Dir.	1.5	B	2	285	1.16	80.3	10.5	3.4	0.07
23	1984	Morgan Hill	6.1	SS	Halls Valley	Fwd-Rup. Dir.	2.5	D	2	240	0.31	39.5	6.6	10.8	0.13
24	1985	Nahanni-Canada	6.9	-	Site 1, Stn. 6097	Fwd-Rup. Dir.	6.0	-	1	010	0.98	46.1	9.6	7.9	0.05
25	1986	N. Palm Springs	6.2	SS	Whitewater Trout Farm	Fwd-Rup. Dir.	6.1	-	1	270	0.61	31.5	4.6	3.4	0.05
26	1986	N. Palm Springs	6.2	SS	Desert Hot	Fwd-Rup. Dir.	6.8	D	1	000	0.33	29.5	5.7	6.6	0.09
27	1986	N. Palm Springs	6.2	SS	N. Palm Spr. Post Office	Fwd-Rup. Dir.	3.6	-	1	210	0.59	73.3	11.5	4.6	0.13
28	1987	Superstition Hills	6.4	SS	Parachute Test Site	Fwd-Rup. Dir.	0.7	D	1	225	0.46	112.0	52.5	10.3	0.25
29	1987	Superstition Hills	6.4	SS	El Centro Imp. Co. Cent.	Fwd-Rup. Dir.	13.9	D	1	000	0.36	46.4	17.6	32.1	0.13
30	1987	Whittier-Narrows	6.1	TH/REV	LA Vernon Ave., Cmd Terminal	Fwd-Rup. Dir.	15.7	D	1	083	0.15	13.1	1.4	11.9	0.09
31	1987	Whittier-Narrows	6.1	TH/REV	Bell LA Bulk Mail Center	Fwd-Rup. Dir.	14.9	B	2	010	0.33	13.9	1.5	7.2	0.04
32	1987	Whittier-Narrows	6.1	TH/REV	Garvey Reservoir Abutment Bld.	Fwd-Rup. Dir.	13.6	B	2	060	0.37	15.5	1.4	5.7	0.04
33	1989	Loma Prieta	7.0	OB	Gilroy Gav. Col.	Fwd-Rup. Dir.	11.6	C	1	067	0.36	28.6	6.4	5.0	0.08
34	1989	Loma Prieta	7.0	OB	Los Gatos Parent Center	Fwd-Rup. Dir.	3.5	C	1	000	0.56	94.8	41.1	10.2	0.17
35	1989	Loma Prieta	7.0	OB	Lexington Dam	Fwd-Rup. Dir.	6.3	C	2	090	0.41	94.3	36.4	4.1	0.23
36	1989	Loma Prieta	7.0	OB	Gilroy STA #1	Fwd-Rup. Dir.	2.8	B	1	090	0.47	34.0	8.1	14.7	0.07
37	1989	Loma Prieta	7.0	OB	Gilroy STA #2	Fwd-Rup. Dir.	4.5	D	1	000	0.37	32.9	7.2	11.0	0.09
38	1989	Loma Prieta	7.0	OB	Gilroy STA #3	Fwd-Rup. Dir.	6.3	D	1	000	0.56	35.7	8.2	6.4	0.07
39	1989	Loma Prieta	7.0	OB	Gilroy His. Bld.	Fwd-Rup. Dir.	12.7	-	1	090	0.28	42.0	11.1	8.9	0.15
40	1989	Loma Prieta	7.0	OB	Saratoga Aloha Ave.	Fwd-Rup. Dir.	4.1	D	2	090	0.32	44.8	28.0	8.3	0.14
41	1989	Loma Prieta	7.0	OB	Saratoga W.Valley Coll.	Fwd-Rup. Dir.	13.7	-	1	000	0.26	42.5	19.5	11.1	0.17
42	1989	Loma Prieta	7.0	OB	Capitola	Fwd-Rup. Dir.	8.6	D	1	000	0.53	35.0	9.2	11.9	0.07
43	1989	Loma Prieta	7.0	OB	Corralitos	Fwd-Rup. Dir.	5.1	D	1	000	0.64	55.2	10.8	6.9	0.09
44	1992	Cape Mendocino	7.1	TH	Petrolia, General Store	Fwd-Rup. Dir.	15.9	C	1	090	0.66	90.2	28.9	16.1	0.14
45	1992	Erzincan	6.7	SS	Erzincan	Fwd-Rup. Dir.	2.0	C	1	EW	0.50	64.3	21.9	7.3	0.13
46	1992	Landers	7.3	SS	Joshua Tree Fire Stn.	Fwd-Rup. Dir.	10.0	D	1	000	0.27	27.5	9.1	27.2	0.10
47	1989	Landers	7.3	SS	Lucerne Valley	Fwd-Rup. Dir.	2.0	B	1	275	0.72	97.7	70.4	13.1	0.14
48	1994	Northridge	6.7	TH	Rinaldi Rec. Stn.	Fwd-Rup. Dir.	8.6	D	2	S49W	0.84	174.8	33.4	7.0	0.21
49	1994	Northridge	6.7	TH	Newhall LA Fire Stn.	Fwd-Rup. Dir.	7.1	D	1	090	0.58	75.6	18.9	5.9	0.13
50	1994	Northridge	6.7	TH	Newhall Pico Canyon	Fwd-Rup. Dir.	7.1	D	1	316	0.33	67.4	16.1	9.2	0.21
51	1994	Northridge	6.7	TH	Jensen Filt. Plant	Fwd-Rup. Dir.	6.2	D	1	022	0.42	106.3	43.2	12.4	0.26
52	1994	Northridge	6.7	TH	Sepulveda Va. Hospital	Fwd-Rup. Dir.	9.5	D	1	360	0.94	75.9	15.1	8.2	0.08
53	1994	Northridge	6.7	TH	Pacoima Kagel Canyon	Fwd-Rup. Dir.	10.6	B	1	360	0.43	51.6	8.2	9.8	0.12
54	1994	Northridge	6.7	TH	Canoga Park TC	Fwd-Rup. Dir.	15.7	D	1	196	0.42	60.7	20.3	10.4	0.15
55	1994	Northridge	6.7	TH	Arieta Nordhoff Ave. Fire Stn.	Fwd-Rup. Dir.	9.5	D	1	090	0.34	40.7	15.1	13.0	0.12
56	1994	Northridge	6.7	TH	Los Angeles Dam	Fwd-Rup. Dir.	2.6	-	1	064	0.51	63.7	21.3	6.7	0.13
57	1995	Kobe	6.9	SS	KJMA	Fwd-Rup. Dir.	0.6	C	1	000	0.82	81.6	17.7	8.4	0.10
58	1978	Tabas	6.9	SS	Takatori	Fwd-Rup. Dir.	4.3	D	1	090	0.62	120.8	32.8	9.9	0.20
59	1995	San Fernando	6.7	TH	Sylmar Olive View Hospital	Fwd-Rup. Dir.	6.4	D	1	360	0.84	130.4	31.7	5.3	0.16
60	1996	Imperial-Valley	6.7	TH	Slymar Converter Sta.	Fwd-Rup. Dir.	6.2	D	1	142	0.90	102.2	45.1	7.5	0.12
61	1997	Imperial-Valley	6.7	TH	Slymar Converter Sta East	Fwd-Rup. Dir.	6.1	D	1	018	0.83	117.5	34.5	6.9	0.14
62	1999	Kocaeli	7.4	SS	Darica (ARC)	Fling	17.0	C	3	EW	0.14	45.1	66.1	29.5	0.33
63	1999	Kocaeli	7.4	SS	Duzce (DZC)	Fwd-Rup. Dir.	11.0	D	1	180	0.31	58.9	44.1	11.8	0.19
64	1999	Kocaeli	7.4	SS	Gebze (GBZ)	Fwd-Rup. Dir.	15.0	B	1	000	0.24	50.3	42.7	29.6	0.21
65	1999	Kocaeli	7.4	SS	Izmit (IZT)	Fling	4.30	B	3	EW	0.23	48.9	95.5	34.5	0.22
66	1999	Kocaeli	7.4	SS	Yarimca (YPT)	Fling	3.30	D	3	EW	0.23	88.8	184.8	33.2	0.39
67	1999	Kocaeli	7.4	SS	Yarimca (YPT)	Fling	3.30	D	3	NS	0.33	88.4	152.1	31.8	0.27
68	1999	Kocaeli	7.4	SS	Izmit (IZT)	Fling	4.30	B	3	NS	0.17	27.2	23.7	34.1	0.16
69	1999	Kocaeli	7.4	SS	Sakarya (SKR)	Fling	3.20	C	3	EW	0.41	82.1	205.9	14.6	0.20
70	1999	Duzce	7.2	SS	Bolu (Bol)	Fwd-Rup. Dir.	20.4	D	1	EW	0.82	62.1	13.6	9.0	0.08

Table 5.1 (Cont.). Near-fault earthquake recordings

No.	Year	Earthquake	M_W	Mech.[1]	Station	Characteristics	Dist.[2] (km)	Site Class[3]	Data Src.[4]	Comp.	PGA (g)	PGV (cm/s)	PGD (cm)	T_D[5] (s)	V/A[6] (s)
71	1999	Chi-Chi	7.6	TH	TCU049	Fling	3.27	D	4	NS	0.24	57.5	102.7	22.7	0.24
72	1999	Chi-Chi	7.6	TH	TCU049	Fling	3.27	D	4	EW	0.27	54.8	121.8	21.6	0.21
73	1999	Chi-Chi	7.6	TH	TCU052	Fling	1.84	D	4	EW	0.35	178.0	493.5	16.8	0.52
74	1999	Chi-Chi	7.6	TH	TCU052	Fling	1.84	D	4	NS	0.44	216.0	709.1	15.9	0.50
75	1999	Chi-Chi	7.6	TH	TCU065	Fling	2.49	D	4	NS	0.55	86.4	124.7	28.5	0.16
76	1999	Chi-Chi	7.6	TH	TCU065	Fling	2.49	D	4	EW	0.76	128.3	228.4	28.8	0.17
77	1999	Chi-Chi	7.6	TH	TCU067	Fling	1.11	D	4	NS	0.31	53.5	103.2	23.0	0.18
78	1999	Chi-Chi	7.6	TH	TCU067	Fling	1.11	D	4	EW	0.48	94.3	181.3	21.7	0.20
79	1999	Chi-Chi	7.6	TH	TCU068	Fling	3.01	D	4	EW	0.50	277.6	715.8	12.4	0.57
80	1999	Chi-Chi	7.6	TH	TCU068	Fling	3.01	D	4	NS	0.36	294.1	895.7	13.2	0.83
81	1999	Chi-Chi	7.6	TH	TCU071	Fling	4.88	D	4	NS	0.63	79.1	244.1	23.7	0.13
82	1999	Chi-Chi	7.6	TH	TCU071	Fling	4.88	D	4	EW	0.51	69.9	196.9	24.6	0.14
83	1999	Chi-Chi	7.6	TH	TCU072	Fling	7.87	D	4	NS	0.36	66.7	245.3	24.0	0.19
84	1999	Chi-Chi	7.6	TH	TCU072	Fling	7.87	D	4	EW	0.46	83.6	209.7	21.9	0.19
85	1999	Chi-Chi	7.6	TH	TCU074	Fling	13.75	D	4	EW	0.59	68.9	193.2	11.8	0.12
86	1999	Chi-Chi	7.6	TH	TCU074	Fling	13.75	D	4	NS	0.37	48.0	155.4	19.7	0.13
87	1999	Chi-Chi	7.6	TH	TCU075	Fling	3.38	D	4	NS	0.25	36.2	108.5	31.2	0.15
88	1999	Chi-Chi	7.6	TH	TCU075	Fling	3.38	D	4	EW	0.32	111.8	164.4	27.0	0.36
89	1999	Chi-Chi	7.6	TH	TCU076	Fling	3.17	D	4	NS	0.41	61.8	73.1	28.1	0.15
90	1999	Chi-Chi	7.6	TH	TCU076	Fling	3.17	D	4	EW	0.33	65.9	101.7	29.7	0.20
91	1999	Chi-Chi	7.6	TH	TCU078	Fling	8.27	D	4	NS	0.30	30.9	106.7	26.1	0.10
92	1999	Chi-Chi	7.6	TH	TCU078	Fling	8.27	D	4	EW	0.43	41.9	121.2	25.9	0.10
93	1999	Chi-Chi	7.6	TH	TCU079	Fling	10.95	D	4	NS	0.41	30.4	83.1	26.9	0.08
94	1999	Chi-Chi	7.6	TH	TCU079	Fling	10.95	D	4	EW	0.57	68.1	166.1	24.2	0.12
95	1999	Chi-Chi	7.6	TH	TCU082	Fling	4.47	D	4	NS	0.18	38.8	105.7	27.0	0.22
96	1999	Chi-Chi	7.6	TH	TCU082	Fling	4.47	D	4	EW	0.22	50.5	142.8	23.3	0.23
97	1999	Chi-Chi	7.6	TH	TCU084	Fling	11.40	C	4	EW	0.98	140.4	204.6	14.6	0.15
98	1999	Chi-Chi	7.6	TH	TCU084	Fling	11.40	C	4	NS	0.42	42.6	64.9	23.1	0.10
99	1999	Chi-Chi	7.6	TH	TCU089	Fling	8.33	C	4	NS	0.22	33.9	141.3	24.9	0.16
100	1999	Chi-Chi	7.6	TH	TCU089	Fling	8.33	C	4	EW	0.34	44.4	193.9	24.1	0.13
101	1999	Chi-Chi	7.6	TH	TCU102	Fling	1.19	D	4	NS	0.17	68.6	83.8	19.7	0.41
102	1999	Chi-Chi	7.6	TH	TCU102	Fling	1.19	D	4	EW	0.29	84.5	153.9	15.0	0.30
103	1999	Chi-Chi	7.6	TH	TCU128	Fling	9.08	C	4	NS	0.16	59.7	88.1	20.7	0.38
104	1999	Chi-Chi	7.6	TH	TCU128	Fling	9.08	C	4	EW	0.14	59.4	91.1	19.3	0.43
105	1999	Chi-Chi	7.6	TH	TCU129	Fling	2.21	D	4	EW	0.98	66.9	126.1	27.3	0.07
106	1999	Chi-Chi	7.6	TH	TCU129	Fling	2.21	D	4	NS	0.61	54.6	82.7	30.8	0.09
107	2004	Bingol	6.4	SS	Bingol (BNG)	Fwd-Rup. Dir.	6.1	D	3	NS	0.56	14.7	9.8	4.6	0.03

[1] *Faulting Mechanism = TH: Thrust; REV: Reverse; SS: Strike-slip; OB: Oblique*

[2] *Closest distance to fault rupture*

[3] *NEHRP Site Classifications => (B for V_S = 760 to 1500 m/s), (C for V_S = 360 to 760 m/s), (D for V_S = 180 to 360 m/s)*

[4] *Data Source = 1: PEER (http://peer.berkeley.edu/smcat); 2: Cosmos (http://db.cosmos-eq.org); 3: ERD (http://angora.deprem.gov.tr/); 4: http://scman.cwb.gov.tw/eqv5/special/19990921/pgadata-asci0704.htm*

[5] *T_D = Duration of motion (time interval during which accelerogram intensity increases from 5 to 95 percent of its final value)*

[6] *V/A = PGV/PGA (Indicates the average duration of acceleration pulse provided that PGV is reached immediately following the dominant acceleration pulse)*

Note: Original fling ground motions from data sources (3) and (4) were baseline corrected after removal of pre-event mean (For details see Kalkan and Kunnath 2006)

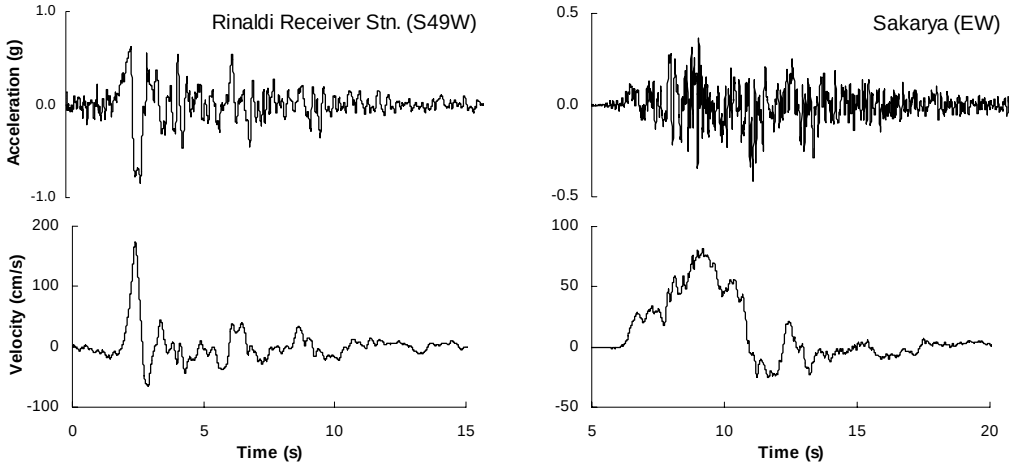

Figure 5.1 Earthquake recordings having apparent acceleration pulse (Left), and packed with random high frequency acceleration spikes (Right).

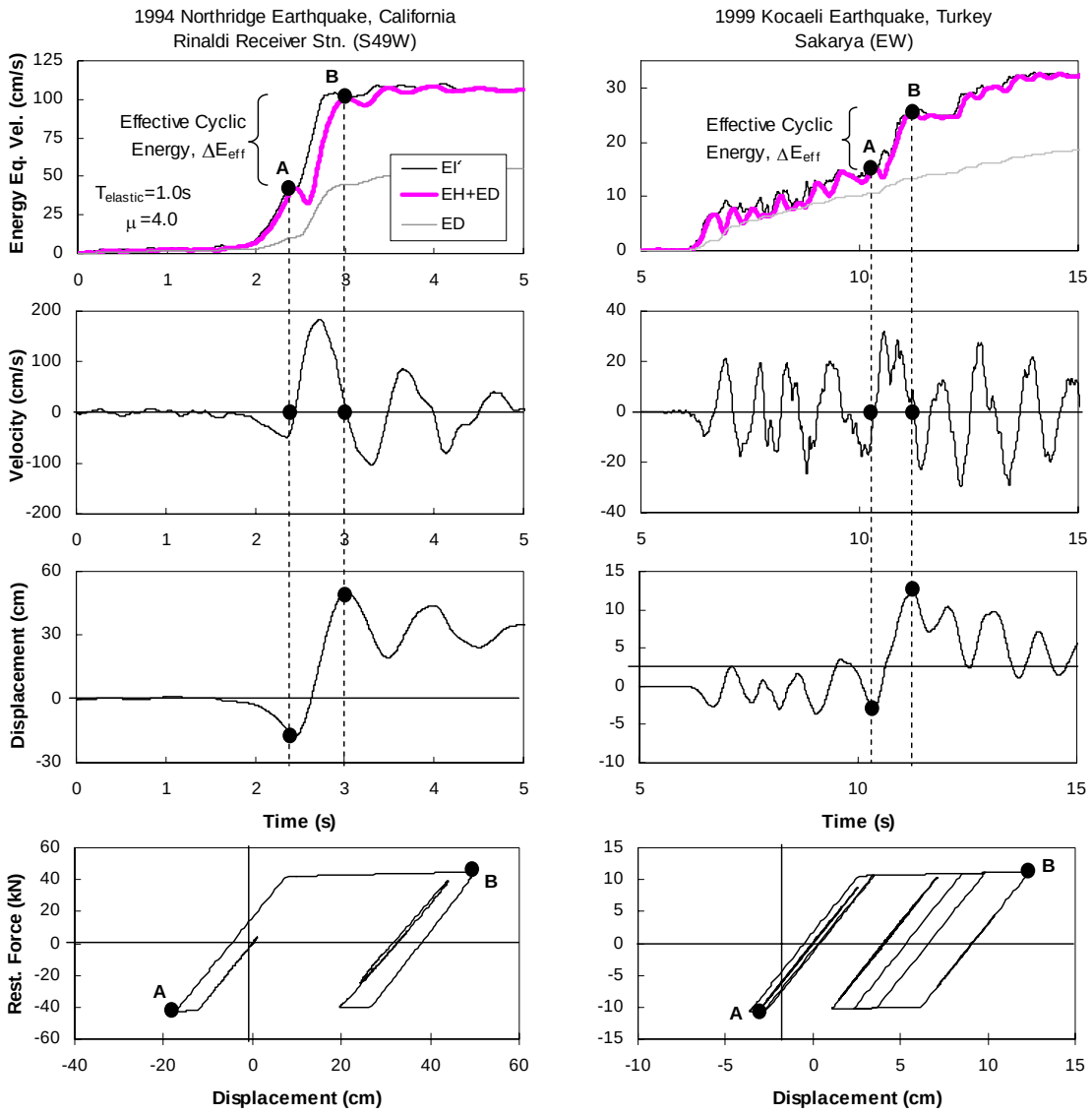

Figure 5.2 Correlation of SDOF inelastic response with computed ECE for near-fault forward directivity record of Rinaldi Rec. Stn. and fling record of Sakarya.

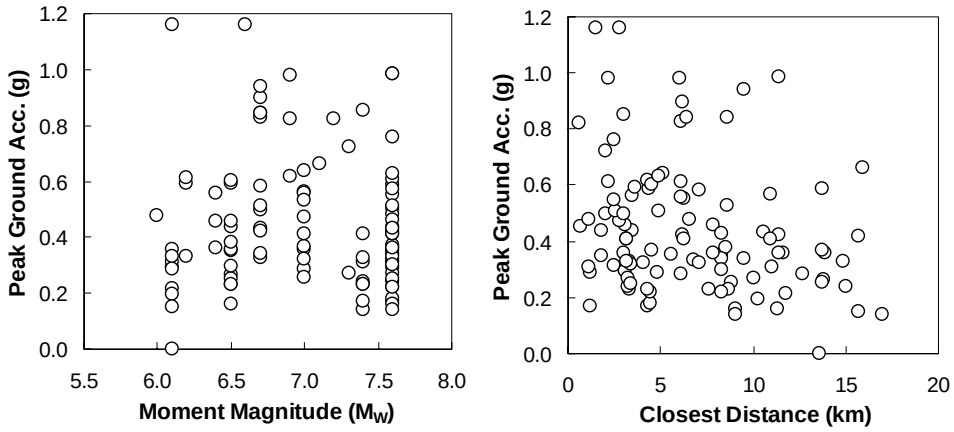

Figure 5.3 Distribution of PGA of records with respect to moment magnitude (Left) and closest distance (Right).

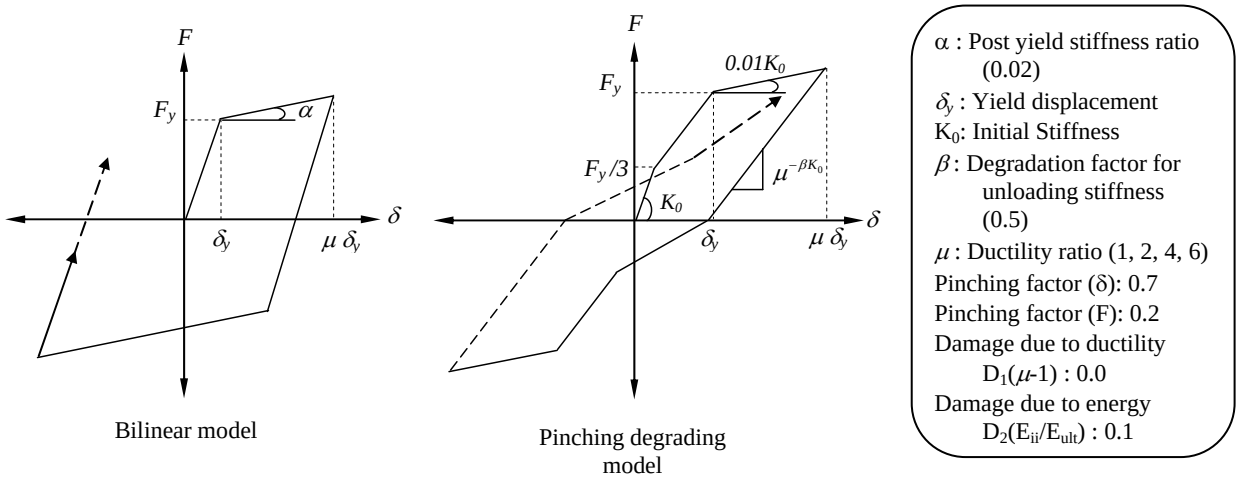

Figure 5.4 Hysteresis models.

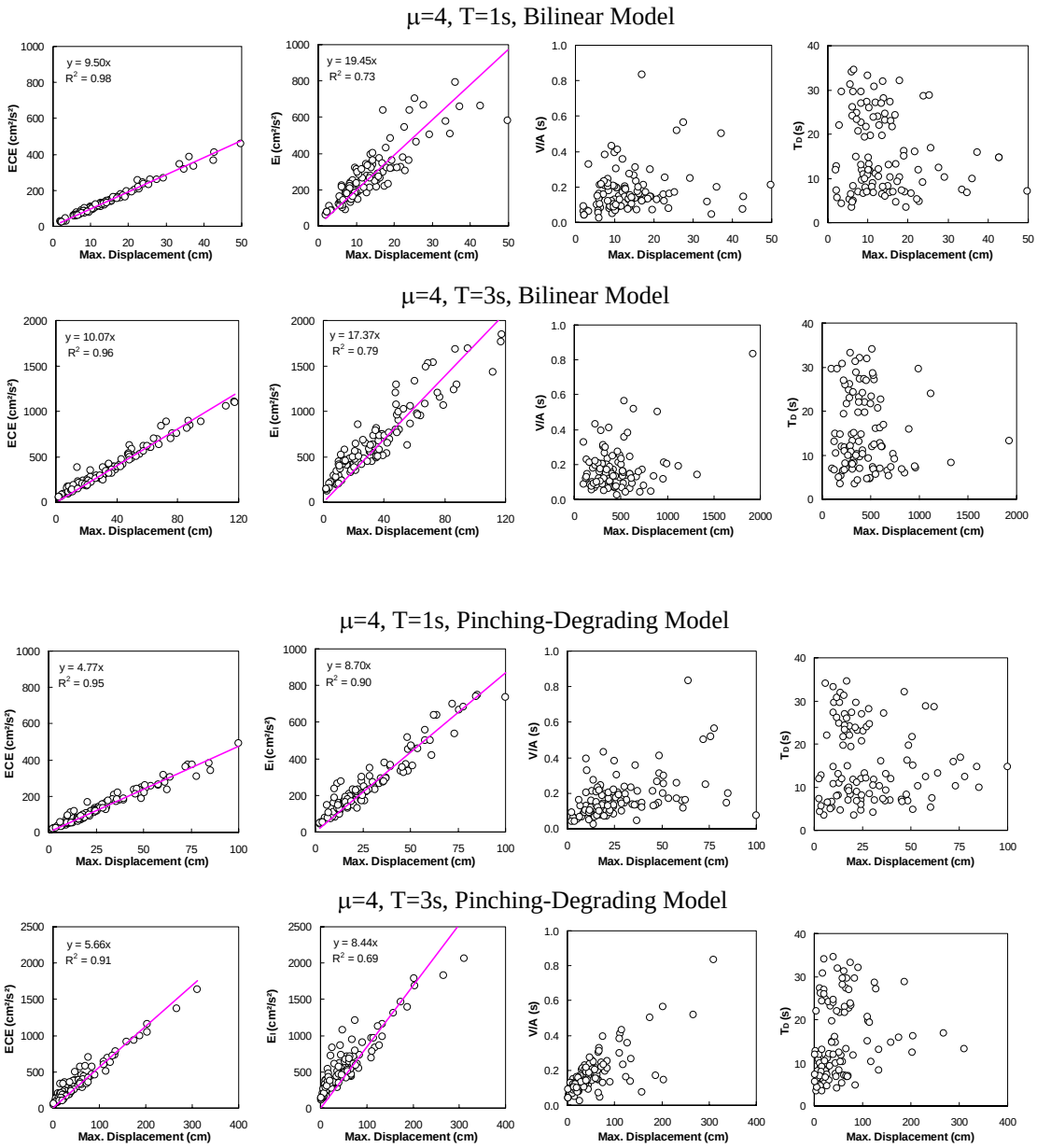

Figure 5.5 Correlation between maximum system displacement and effective cyclic energy (ECE), absolute input energy (EI), strong motion duration (TD) and ratio of PGA to PGV (V/A) (Results are based on inelastic time response analyses of SDOF system having spectral period of 1s and 3s with ductility ratio of 4).

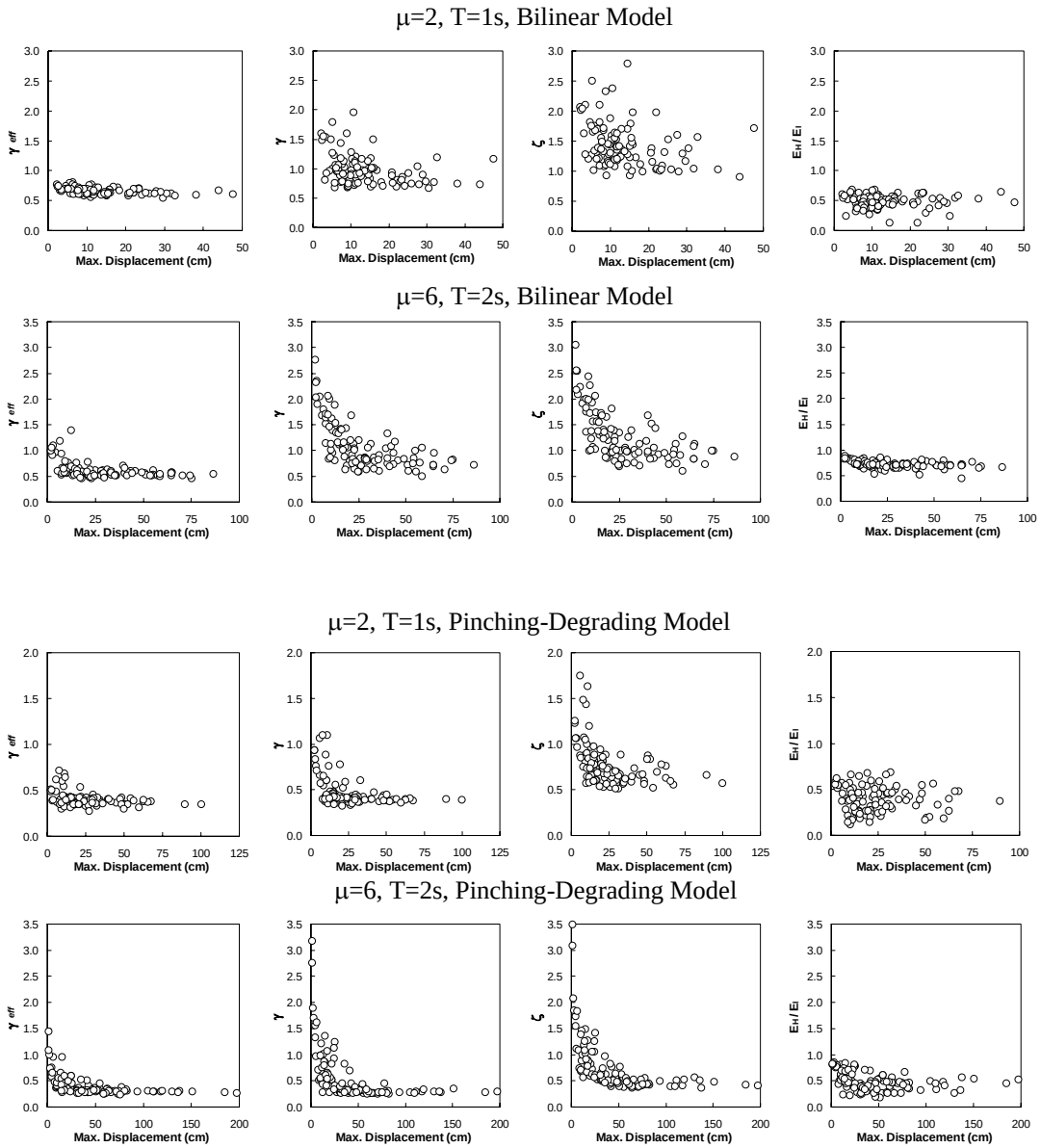

Figure 5.6 Stability of various non-dimensional response indices at constant displacement ductility levels (Results are based on inelastic time response analyses of SDOF systems having spectral period of 1s and 2s with ductility ratio of 2 and 6).

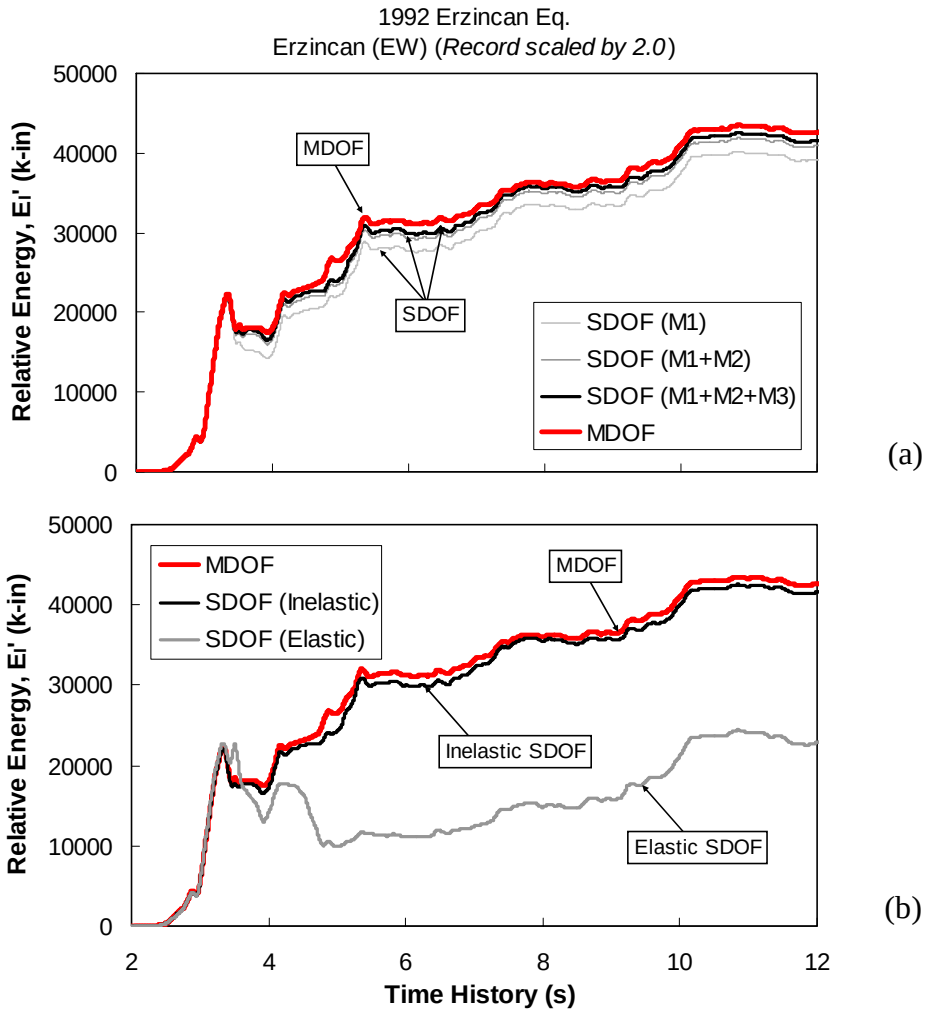

Figure 5.7 Comparison of relative input energy (M1 = Mode 1; M2 = Mode 2; M3 = Mode 3).

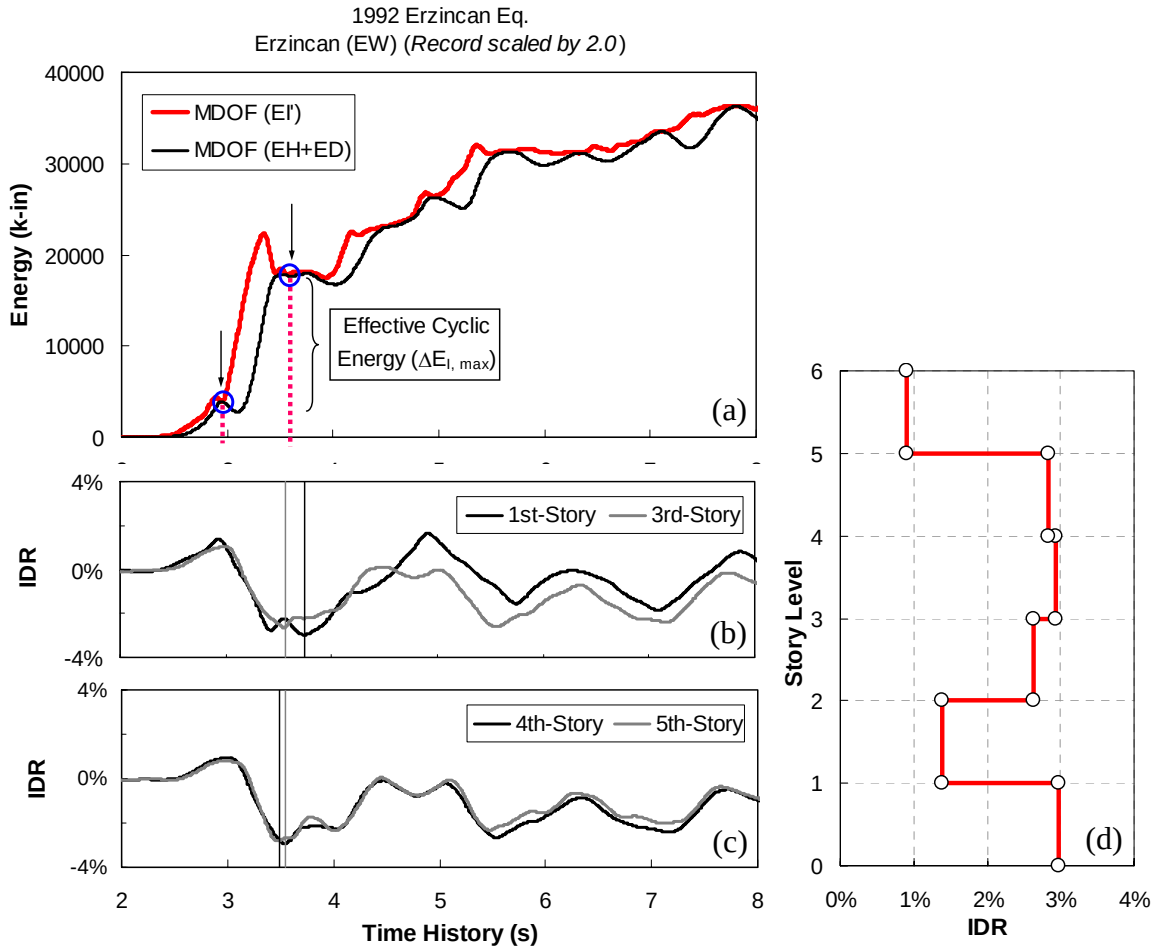

Figure 5.8 Variation of input energy and interstory drift ratio (IDR) for 6-story building and peak interstory drift profile (Note: time instants for story peak IDR are indicated by vertical lines in Figure 8b-c).

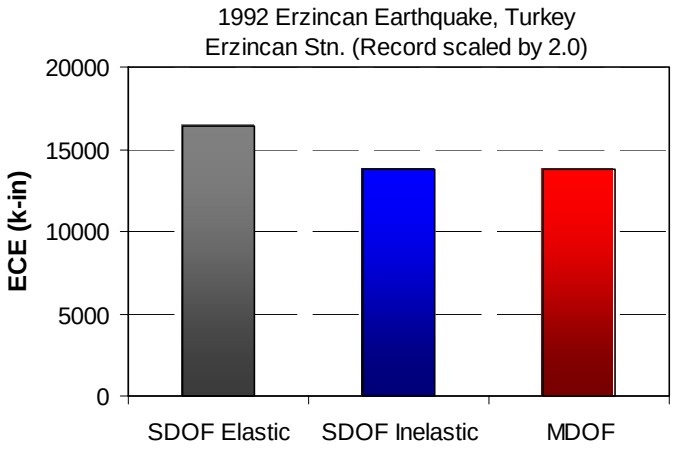

Figure 5.9 ECE computed based on MDOF and SDOF systems.

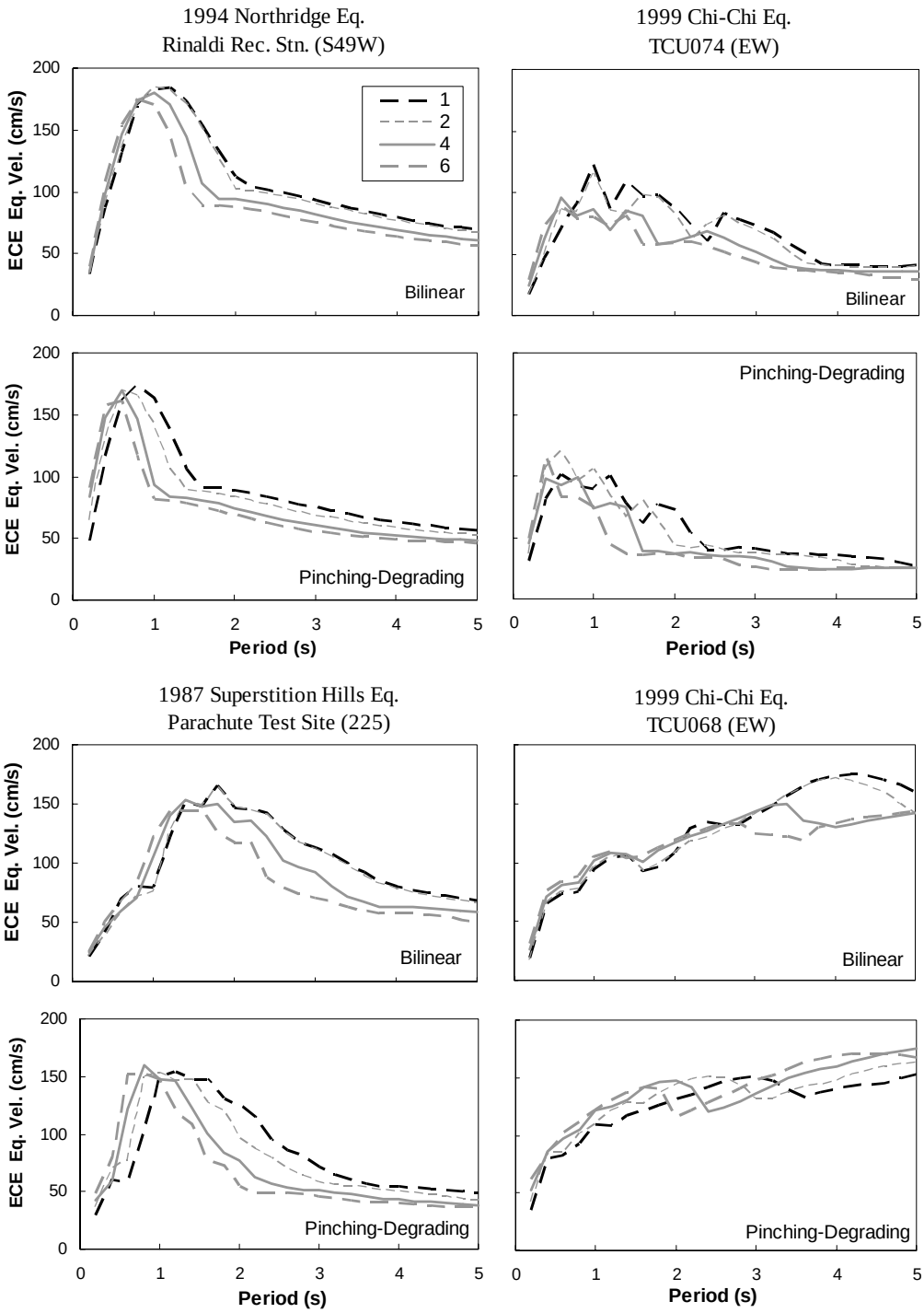

Figure 5.10 ECE spectra of representative near-fault records having forward-rupture directivity (Left) and fling (Right).

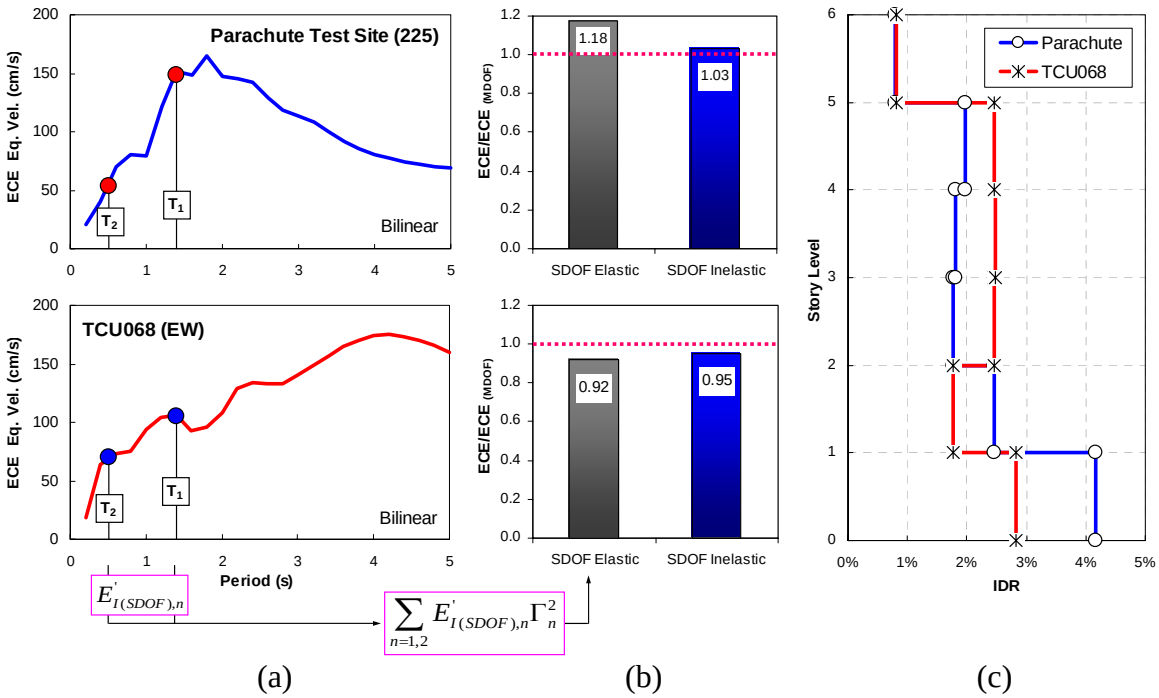

Figure 5.11 ECE demand estimates in MDOF system.

CHAPTER 6

DEVELOPMENT OF ADVANCED ANALYTICAL TOOL: ADAPTIVE MODAL COMBINATION PROCEDURE

6.1 INTRODUCTION

The introduction of performance based earthquake engineering (PBEE) concepts into recent guideline documents such as ATC-40 (1996) and FEMA-356 (2000) has led to increased utilization of nonlinear static methods to estimate seismic demands. Recently, the capacity spectrum method (CSM) of ATC-40 has been adapted as a seismic evaluation method in the Japanese structural design code for buildings (Ministry of Land, Infrastructure and Transport 2001), and the N2 method (a special form of the CSM in which the demand is represented by an inelastic spectrum) has been implemented in the draft of Eurocode-8 (2001). Both CSM and the N2 method rely on a pushover analysis using invariant lateral load patterns to estimate deformation demands under seismic loading. However, these simplified approaches to predict seismic demands are known to have major drawbacks (Kalkan and Kunnath 2004; Goel and Chopra 2004). Several researchers (Chopra et al. 2002; Jan et al. 2003) have proposed enhanced pushover procedures to account for higher mode effects while retaining the simplicity of invariant load patterns. These improved procedures utilize the concept of modal combinations

either through a single pushover analysis where the load vectors reflect the contributions from each elastic mode-shape considered or through multiple pushover analyses using invariant load patterns based on elastic mode shapes where the contribution from each mode is combined at the end. Recently, a modified version of MPA (MMPA) has been proposed in which the inelastic response obtained from first-mode pushover analysis has been combined with the elastic contribution of higher modes (Chopra et al. 2004). In order to investigate alternative schemes to represent realistic lateral force demands, a new lateral load configuration using factored modal combinations has been developed by Kunnath (2004), and evaluated for various steel building structures (Kalkan and Kunnath 2004). All these enhanced procedures have been shown to provide improved estimates of interstory drift values compared to conventional nonlinear-static-procedures (NSPs) using inverted triangular, uniform or other lateral load patterns based on direct modal combination rules suggested in FEMA-356.

The invariant load patterns used in the above-referenced procedures are based on the initial elastic dynamic properties of the structure, and the change in the modal attributes of the structure during the inelastic phase is not accounted for. Additionally, the estimation of target displacement in ATC-40 or FEMA-356, or even methods used by the enhanced procedures pose numerous limitations. While ATC-40 uses equivalent linearization and FEMA-356 uses the displacement coefficient method, enhanced pushover procedures (e.g., Chopra and Goel 2002; Jan et al. 2003; Chopra et al. 2004) either use an elastic spectrum with elastic modal periods or inelastic ESDOF dynamic responses to approximate the target displacement. It has been shown that the target displacement computed using ATC-40 or FEMA-356 can be not only significantly

different from each other but also significantly different from response history analysis for short period structures (Miranda and Akkar 2002). Furthermore, in the case of near-fault records these approximate methods as well as the other approaches based on the equal displacement rule may not be applicable for the period range of low to mid-rise buildings. Another limitation stems from the assumption that the roof displacement is assumed to be the representative of the ESDOF system response. The roof displacement as a parameter to convert the MDOF system to ESDOF system is only meaningful for the first-mode. It has been recently shown by Hernandez-Montes et al. (2004) that using roof displacement as the target parameter to obtain the ESDOF system properties of MDOF structure may lead erroneous results and proceed to propose an energy based representation of the capacity curve that overcomes some of the aforementioned problems. Though energy based computation of the capacity curve has been implemented in MPA, other issues still remain because the inelastic system properties are still obtained from elastic modal attributes, and using invariant load patterns are not compatible with the progressive yielding of the structure during the pushover analysis.

In order to incorporate change in the modal attributes of the structure during inelastic phase, Gupta and Kunnath (2000) proposed an adaptive pushover procedure based on an elastic demand spectrum. In this procedure, conventional response spectrum analysis is essentially being applied at each pushover step. Several other pushover procedures based on adaptive load patterns have also been proposed (Elnashai 2000; Antoniou et al. 2000; Antoniou and Pinho 2004).

Recognizing the merits and limitations of existing methodologies, a new adaptive pushover technique referred to as the Adaptive Modal Combination (AMC) procedure is

developed herein. The AMC procedure derives its fundamental scheme from the adaptive pushover procedure of Gupta and Kunnath (2000) by recognizing the need to modify applied lateral loads as the system responds to the applied earthquake load. The proposed procedure integrates the inherent advantages of the capacity spectrum method, modal combination and the adaptive loading scheme, while at the same time eliminating the need to pre-estimate the target displacement. The accuracy of the approach is validated by comparing predictions using the proposed method with estimates obtained from a comprehensive set of nonlinear time-history (NTH) analyses.

6.2 DEVELOPMENT OF THE AMC PROCEDURE

The primary feature of adaptive schemes is the updating of the applied story forces with respect to progressive changes in the modal properties at each step. This allows progressive system softening due to inelastic deformations to be represented more realistically in a static framework. The original adaptive method proposed by Gupta and Kunnath is a load-controlled procedure in which load increments are scaled at each pushover step using elastic spectral accelerations ($S_{ae}^{(i)}$) based on the instantaneous dynamic properties of the system. In the proposed new procedure, a displacement-controlled method is used in which the demand due to individual terms in the modal expansion of the effective earthquake forces is determined by individual adaptive pushover analyses using the inertia distribution of each mode, which is progressively updated during the process of loading. Unlike the adaptive scheme of Gupta and Kunnath where the contributions of each mode are combined at end of each step using square-root-of-sum-of-squares (SRSS), in the proposed scheme the total seismic demand of the

system is obtained at the end of the analysis by combining the individual response using SRSS.

6.2.1 Basic Elements of the Procedure

The development of the AMC procedure is motivated by the need to synthesize key elements of advanced pushover methods that have independently addressed different drawbacks identified in simplified pushover procedures. The primary concepts that have been both integrated and enhanced in the proposed methodology include:

- Establishing the target displacement: An energy-based procedure is used in conjunction with inelastic displacement spectra (expressed in spectral acceleration vs. displacement format) at a set of pre-determined ductility levels to progressively establish the target displacement as the modal pushover analyses proceeds.
- Dynamic Target Point: This concept is analogous to the performance point in CSM, however, it represents a more realistic representation of demand since inelastic response measures are used to target this demand point.
- Adaptive Modal Combination: Finally, the method recognizes the need to alter the applied lateral load patterns as the system characteristics change yet retain the simplicity of combining the response measures at the end of the analysis.

Details of the conceptual elements of the process are described in the following sections.

6.2.1.1 Energy Based Incremental Modal Displacement

The determination of the target displacement is a key element in a static pushover procedure. The Displacement Coefficient Method in FEMA-356 approximates the target

displacement by modifying the elastic SDOF demand through a set of coefficients that account for MDOF effects, inelastic behavior, degrading effects and dynamic P-delta effects. In ATC-40, the target displacement is embedded in the Capacity Spectrum Method wherein the pushover curve is transformed into ADRS format (i.e., spectral acceleration versus spectral displacement). By overlapping the transformed capacity curve with an equivalent damped elastic spectrum, the performance point can be estimated in an iterative manner and converted into roof displacement of the equivalent MDOF system. The following relationships convert the MDOF capacity curve coordinates into ADRS format:

$$S_{a,n} = \frac{V_{b,n}}{W\alpha_n} \tag{6.1}$$

$$S_{d,n} = \frac{u_{r,n}}{\Gamma_n \phi_{r,n}} \tag{6.2}$$

$$\Gamma_n = \frac{\boldsymbol{\phi}_n^{'}\mathbf{m}\boldsymbol{\iota}}{\boldsymbol{\phi}_n^{'}\mathbf{m}\boldsymbol{\phi}_n} \tag{6.3}$$

where $S_{a,n}$ and $S_{d,n}$ stand for spectral acceleration and spectral displacement, respectively, corresponding to a specific period and a fixed viscous damping ratio for the n^{th}-mode considered. W is the total weight, $V_{b,n}$ is the base shear, and α_n is the modal mass coefficient ($\alpha_n = (\boldsymbol{\phi}_n^{'}\,\mathbf{m}\boldsymbol{\iota})^2 / [(\boldsymbol{\phi}_n^{'}\,\mathbf{m}\boldsymbol{\phi}_n)\sum_n m_n]$). $u_{r,n}$ stands for the roof displacement obtained from the n^{th}-mode pushover analysis, $\phi_{r,n}$ and Γ_n are respectively, the roof component of the n^{th}-mode shape and the modal participation factor. m is the mass matrix and ι is the influence matrix. In ATC-40, n is restricted to the first mode only. It is therefore reasonable to conclude that the peak response quantities associated with the

multi-mode effects cannot be correctly predicted with a conversion technique based on a single-mode response (Akkar et al. 2004).

On the other hand, in a multi-mode procedure such as the Modal Pushover Analysis (MPA) introduced by Chopra and Goel (2002), the target displacement is obtained through converting the MDOF response into a series of bilinear ESDOF responses for the first *n* modes. It essentially extends the ATC-40 concept to multiple modes to determine the ESDOF system parameters for each mode considered. An inelastic dynamic analyses is carried out on each ESDOF system and the pertinent maximum inelastic spectral displacement demand can be obtained, and transformed back to a target displacement ($u_{n,r}$) as follows:

$$u_{r,n} = \phi_{r,n} \, \Gamma_n \, S_{d,n} \tag{4}$$

The basic limitation of this approach is that elastic modal properties are used to compute the inelastic system parameters, and the procedure may necessitate several iterations for convergence of target displacement computed from inelastic dynamic analysis. Another potential limitation arises from the fact that the roof displacement is approximated from the maximum deformation of an ESDOF system. Such an approach is only meaningful for the first mode, while for higher modes, the roof displacement does not proportionally change with the other story deformations, therefore use of the roof displacement as the pivotal parameter for the ESDOF representations may yield erroneous predictions of the target displacement. In recognition of this fact, an energy based concept has been utilized to represent the MDOF system parameters in an ESDOF system corresponding to each individual mode. In the energy based approach proposed by Hernandez-Montes et al. (2004), the abscissa of the capacity curve of the ESDOF

system is determined based on the work done at each story level (*j*) through each incremental displacement ($\Delta d_{j,n}^{(i)}$) during the pushover analysis (see Figure 6.1). The total energy increment is divided by the base shear at each step to find the incremental displacement ($\Delta D_n^{(i)}$). Hence, the sum of the incremental displacements gives the resultant displacement of the ESDOF system (i.e., spectral displacement, $S_{d,n}^{(i)}$) at any given step (*i*) of the pushover analysis.

For the adaptive approach proposed in this study, it was found that the energy based formulation results in more stable and smooth capacity curves. Another benefit of the energy formulation is that it eliminates the reversal of the higher mode capacity curves that have been observed for second and third mode pushover analyses when the roof displacement is utilized as the index parameter (Tjhin et al. 2004).

6.2.1.2 Inelastic Spectra and Dynamic Target Point

A key aspect of the proposed procedure is that a set of capacity spectra based on a series of predetermined ductility levels are used for each mode to approximate the displacement demand (referred to as the *dynamic target point*). Studies conducted by the authors indicate that the increment at which the spectra should be generated is optimal at $\Delta\mu$=0.25 (meaning ductility levels of 1.0, 1.25, 1.50, etc.) though an interval of 0.5 used in many of the simulations presented in this study was generally adequate. The peak modal inelastic spectral acceleration ($S_{a,n}^{(i)}$) and displacement ($S_{d,n}^{(i)}$) of the equivalent system associated with the instantaneous configuration of the structure is computed using the energy approach described above. The constant-ductility capacity spectra are computed based on ESDOF system properties which can be obtained from bi-

linearization of modal capacity curve. Since the yield displacement and post-yield stiffness ratio are undetermined till the capacity curve is established, a preliminary pushover analysis using a fixed post-yield stiffness (or even an elastic-perfectly-plastic model) can be carried out to establish these parameters. These pre-analysis estimates should be modified at the end of the next iteration of the pushover analysis and the process repeated till a stable yield point and post-yield stiffness are established. In each case, it will also be necessary to regenerate the constant ductility capacity spectrum curves using updated parameters. To this extent, the proposed method is an iterative procedure which requires proper calibration of the capacity curves prior to the generation of the final pushover curve.

The intersection of the modal capacity at the current state of the system and the demand spectrum (in spectral acceleration and spectral displacement format) satisfying approximately the same ductility level (as displayed in Figure 6.2) represents the associated dynamic target point. This energy based dynamic target displacement ($S_{d,n}^{(ip)}$) can be back translated from ESDOF to MDOF using the instantaneous modal properties ($\phi_{r,n}$ and Γ_n) of the system as follows:

$$u_{r,n}^{(ip)} = \phi_{r,n}^{(ip)} \, \Gamma_n^{(ip)} \, S_{d,n}^{(ip)} \tag{5}$$

Within the adaptive framework, the changing modal attributes of the inelastic system is dynamically updated during the progress of the pushover analysis, and constant-ductility capacity spectra are used to compute the dynamic target displacements for each mode considered. The dynamic target point evaluation described above is illustrated in Figure 6.2 considering only a single mode response. At any step *(i)* in the modal

pushover analysis (an ADRS plot for mode *n* is shown in Figure 6.2), the equivalent ductility (identified as $\mu_n^{(i)}$ in the figure) is determined. The target displacement is achieved when an intersection point is located on the constant ductility spectra. In the conceptual illustration in Figure 6.2, a possible intersection at a known ductility is identified as the "dynamic target point." Such a process can be extended to as many modes as necessary.

6.2.1.3 Adaptive Modal Combination

Finally, the methodology retains the fundamental premise of adaptive methods by updating the modal vectors as often as necessary to capture the variation in the dynamic characteristics of the building. In the implementation presented herein, the modal vectors are updated every time an element changes state. Practically speaking, it is possible to define threshold limits during the analysis by monitoring the relative changes in modal shapes from one step to the next. Likewise, the simplicity of the modal pushover procedure is incorporated into the procedure by carrying out the response analysis of each mode separately. Peak modal quantities of interest obtained at the end of each adaptive pushover analysis for each mode are combined using a combination rule. The SRSS combination rule is typically valid if the predominant modal frequencies are well separated while the CQC combination may be more appropriate for systems having closer modes.

6.2.2 The AMC Procedure

The proposed procedure, like all pushover methods, depends on the development of an adequate simulation model of the building system. This step is a function of the analytical tool being used in the nonlinear analysis. Once a reasonable mathematical (simulation) model is developed, the earthquake loading is specified by means of a response spectrum. The procedure consists of a series of step-by-step computations with systematic updates being performed at the end of each step, as follows:

1. Compute the modal properties of the structure (i.e., natural frequencies, $\omega_n^{(i)}$, mode-shapes, $\boldsymbol{\phi}_n^{(i)}$, and modal participation factors, $\Gamma_n^{(i)}$) at the current state of the system.

2. For the n^{th}-mode considered, construct the adaptive lateral load pattern as follows:

$$\boldsymbol{s}_n^{(i)} = \mathbf{m}\boldsymbol{\phi}_n^{(i)} \tag{6.6}$$

   where *(i)* is the step number of the incremental adaptive pushover analysis, **m** is the mass matrix of the structure. The load distribution ($\boldsymbol{s}_n^{(i)}$) can be recomputed at every step or at a set of predefined steps following an eigenvalue analysis based on the current stiffness properties of the system. Since an eigenvalue analysis can be computationally demanding, the frequency with which the load vector is updated should be established prudently with the objective of balancing computational efficiency and solution accuracy.

3. Evaluate the next incremental step of the capacity curve for each ESDOF system using the energy based approach in which the increment in the energy based displacement of the ESDOF system, $\Delta D_n^{(i)}$ can be obtained as

$$\Delta D_n^{(i)} = \Delta E_n^{(i)} / V_{b,n}^{(i)} \tag{6.7}$$

where $\Delta E_n^{(i)}$ is the increment of work done by lateral force pattern, $s_n^{(i)}$ acting through the displacement increment, $\Delta d_n^{(i)}$, associated with a single step of the n^{th}-mode pushover analysis. $V_{b,n}^{(i)}$ is the base shear which is equal to sum of the lateral forces at the i^{th} step. The spectral displacement, $S_{d,n}^{(i)}$ of the ESDOF system (i.e., abscissa of the ESDOF capacity curve) at any step of n^{th}-mode pushover analysis is obtained by the summation of $\Delta D_n^{(i)}$. The ordinate of ESDOF capacity curve is classically determined as follows:

$$S_{a,n}^{(i)} = V_{b,n} / (\alpha_n^{(i)} W) \tag{6.8}$$

where $\alpha_n^{(i)}$ is the modal mass coefficient computed at the i^{th} step of the n^{th}-mode pushover analysis (see Figure 6.1 for exemplified computation of $S_{a,n}^{(i)}$ and $S_{d,n}^{(i)}$)

4. If the response is inelastic for the i^{th} step of the n^{th}-mode pushover analysis, calculate the approximate global system ductility ($\mu_n^{(i)} = S_{d,n}^{(i)} / S_{d,n}^{(yield)}$), and post-yield stiffness ratio from modal capacity curve (see Figure 6.2). Post-yield stiffness ratio ($\lambda_n^{(i)}$) can be approximated using a bilinear representation. If the pushover curve exhibits negative post-yield stiffness, the second stiffness of the bilinear curve would be negative. As described previously, the inelastic parameters (yield point and post-yield stiffness) are yet unknown in an incremental procedure. Hence, it is typically necessary to carry out a preliminary (or dummy) pushover analysis, using adaptive

force distributions and the energy-based displacement increments but not being concerned with a target displacement, to establish these parameters.

5. For the site-specific ground motion to be used for evaluation, generate the capacity spectra in ADRS format (spectral acceleration $S_{a,n}(\mu,\zeta_n,\lambda_n)$ versus spectral displacement $S_{d,n}(\mu,\zeta_n,\lambda_n)$) for a series of predefined ductility levels. This step is required to calculate the energy based dynamic target displacement. The generation of these spectra requires the calibration of the capacity curve to establish the yield point and post-yield stiffness (see discussion in step 4 and the section on constant ductility spectra and dynamic target point).

6. Plot $S_{a,n}^{(i)}$ versus $S_{d,n}^{(i)}$ (i.e., modal capacity curve from Step 3) together with the inelastic demand spectra (from Step 5) at different ductility levels. The dynamic target point, D_n^{ip} for the n^{th}-mode pushover analysis is the intersection of ESDOF modal capacity curve with the inelastic demand spectrum (i.e., $S_{a,n}(\mu,\zeta_n,\lambda_n)$ versus $S_{d,n}(\mu,\zeta_n,\lambda_n)$) corresponding to the global system ductility (μ). While an exact match cannot be established unless inelastic spectral plots are pre-generated at refined ductility levels, a reasonable approximation is achieved by considering displacement spectrum plots in the ductility range of interest at ductility intervals of 0.5. With the known dynamic target point for the n^{th}-mode pushover analysis, the global system roof displacement can be computed as $u_{r,n}^{(ip)} = D_n^{ip}\phi_{r,n}^{(ip)}\Gamma_n^{(ip)}$, where *(ip)* is the step-number in the incremental pushover analysis at which the dynamic target point is captured.

7. Extract the values of response parameters ($r_n^{(ip)}$) desired (e.g., displacements, story drifts, member rotations, etc.) at the ip^{th} step of the n^{th}-mode pushover analysis.

Repeat Steps 1-7 for as many modes as deemed essential for the system under consideration. The first few modes are typically adequate for most low to medium rise buildings. The total response is determined by combining the peak modal responses using any appropriate combination scheme. The total response given in the following expression is obtained through SRSS combination of the modal quantities.

$$r = \max\left(\left(\sum_n (r_n^{(ip)})^2\right)^{0.5}\right) \tag{6.9}$$

If the system remains elastic in any mode considered, the computation of the response parameters will be equal to conventional response spectrum analysis. The proposed pushover procedure can be easily implemented in any structural analysis software package that allows eigenvalue computations to be performed during the analysis phase. The results of the AMC procedure reported here have been implemented using the open source finite element platform, OpenSees (2005) in conjunction with MATLAB (MathWorks, 2001) routines.

6.3 VALIDATION OF THE PROPOSED METHODOLOGY

The proposed AMC procedure has been verified for different structural configurations and ground motions having diverse characteristics. Validation studies are presented for two steel moment frame buildings and results obtained with the AMC method are compared with MMPA and first-mode FEMA-356 lateral load pattern. The results of the

different pushover analyses are then compared to benchmark results obtained from detailed nonlinear time history (NTH) analyses using an array of earthquake records having both far-fault and near-fault characteristics. The records used in the NTH analyses were carefully selected so as to induce higher mode contributions.

6.3.1 Structural Systems and Analytical Models

The buildings considered in this evaluation study are a six-story and a thirteen story steel special moment resisting frame (SMRF) system. Both buildings represent existing structures in California and were selected for this study because the simulation models used in the analyses have been previously calibrated to observed response.

6.3.2 Ground Motion Ensemble

In order to develop a set of benchmark responses against which to compare the proposed procedure, a set of records having far-fault and near-fault characteristics were populated. These records were selected with the objective of triggering higher mode responses in the buildings. The near fault records contain both fling and forward-directivity effects with coherent long period velocity pulses. The far-fault records were amplified by a scale factor to induce inelastic response in both buildings. Such a process was not required for near-fault records. The ground motions used for evaluation study are summarized in Table 6.1. The response spectra of the scaled far-fault records and original near-fault records are presented in Figure 6.4.

6.3.3 Validation Studies

In order to assess the effectiveness of the proposed methodology, each frame was subjected to the suite of ground motions listed in Table 6.1. Different scale factors were used for far fault records when analyzing the respective frames: amplification factors of 4.6 and 6.0 were used on Desert Hot and Taft records, respectively, for the six-story building; and uniform scale factors of 3.9 and 4.5 were used on Moorpark and Desert Hot records, respectively for the thirteen-story building. The computed responses using nonlinear time history analyses are referred to as the benchmark responses. Peak inelastic response quantities for each frame predicted by AMC are compared with estimates obtained from MMPA, FEMA-356 first mode NSP and results from the NTH simulations.

For the typical moment frames investigated in this study, only the first three modes were considered when applying MMPA and AMC in the demand analyses. In the MMPA, inelastic dynamic analyses based on the ESDOF system properties were conducted for the selected records by computing the corresponding first mode target displacements. ESDOF system properties were obtained through bilinear representation of the first mode capacity curve for the two buildings separately. Target displacements for the second and third modes were determined directly form the jagged 5% damped elastic spectra (see Figure 6.4) associated with each unscaled near-fault record and scaled far-fault record using the elastic modal properties of the buildings. Target displacements for conventional first-mode pushover analyses were taken directly as the peak roof displacement computed from NTH analyses. As mentioned previously, target displacements for AMC (i.e.,

dynamic target points) are implicitly estimated during the analysis process without necessitating any pre-computation.

Figure 6.5 demonstrates an example of the dynamic target point evaluation for the thirteen-story steel building subjected to JMA motion. This figure clearly shows the global system ductility computation, and how the system parameters change as the demand exceeds the yield strength. In this particular case, the third mode response remains in the elastic range, while first two modal responses require a series of inelastic spectra in order to capture the intersection point (dynamic target point). For example, in the first mode, the secant period at a system ductility level of 1.6 is approximately 3.5 sec. The corresponding intersection point on the inelastic displacement spectra must match this ductility level to have reached the target point for this mode. In this particular example, the pre-computed ductility spectra do not include a spectrum at a ductility of 1.6. Hence, the nearest spectrum at $\mu = 1.5$ is used. This level of approximation, as suggested earlier, is adequate for practical purposes. The dynamic target points are determined on plots of spectral displacement versus spectral period format rather than ADRS format. This format provides information on the variation of the secant period of the system during the inelastic response phase.

In Figures 6.6 and 6.7, the peak interstory and roof drift ratio are presented for the six-story building for both earthquake sets. In all cases, higher mode effects results in larger demand at the upper (story-5) level and in one case also at the intermediate story levels (story-3 and 4). The conventional static method utilizing elastic first mode and MMPA (which is based on the assumption that contributions from modes higher than first mode are elastic) were found to be inadequate in identifying the demands at these

levels whereas the AMC procedure provided a better fit to the dynamic envelopes obtained from NTH analyses. For both near-fault and far-fault ground motions, the dynamic response of the building shows significant demand at the fifth story level. The comparison of roof drift ratio shows that the AMC procedure overestimates the demand for one far-fault record but is similar to NTH predictions for the remaining far-fault record and both near-fault records. For near-fault records, roof drift ratio is overestimated by MMPA but is reasonable for far-fault records.

For the thirteen-story building, while MMPA captures the overall response in many cases (see Figures 6.8 and 6.9), the proposed adaptive scheme yielded results that were generally similar to NTH results at most story levels. Nevertheless, there are cases where neither MMPA nor AMC are able to reproduce the dynamic response at some story levels. The response to LGPC and Desert H. records (Figures 6.6 and 6.7) are examples where the drifts at intermediate story levels are underestimated by both methods. The dispersion serves as a reminder that complex dynamic phenomena can never be fully replaced by equivalent static schemes. Another observation, though not new, is that conventional first-mode pushover procedure not only significantly underestimates the upper story responses but also the lower story responses in some cases, even though the exact target displacements retrieved from NTH results were utilized. This implies that approximate computation of target displacement using first mode behavior may not be conservative, and may vary from one record to another. The NTH results plotted in Figures 6.7 through 6.9 highlight the order of underestimation of the structural response using conventional first-mode pushover analysis.

The results shown in Figures 6.7 – 6.9 considered the response of typical frames to selected records so as to highlight important features of structural response and examine record-to-record variability. These results represent critical cases from the entire subset of simulations wherein the largest discrepancy between pushover and time-history methods was observed. Next, the effectiveness of the proposed AMC procedure to estimate story demands is investigated statistically. Results from the overall simulation study indicate that mean estimates using the AMC procedure are comparable to NTH analyses. A detailed analysis of the response data using all records in both ground motion sets (three far fault and eight near fault records) generated the results displayed in Figures 6.10 and 6.11. Shown in these figures are the mean and standard deviations (16 to 84 percentile range) for both NTH and AMC predictions of roof drift and interstory drift demands. The mean estimates using AMC are significantly better for the 13-story frame because higher mode contributions in the inelastic phase of the response of this frame were limited. The dispersion using NTH is typically higher than AMC in both cases. These findings provide a measure of confidence in the general predictive abilities of the proposed pushover procedure.

6.4 CONCLUSIONS

The advancement of performance-based procedures in seismic design relies greatly on advancements in analytical methods to predict inelastic dynamic response of building structures. Since nonlinear time-history analyses are associated with greater uncertainties stemming from the choice of modeling parameters to the selection of ground motions, engineers are more likely to adopt static approaches before finally transitioning to time

history methods. Hence the need to evaluate existing static methods and improve the potential for seismic response prediction remains a central issue in performance-based seismic engineering.

A new pushover technique utilizing adaptive multi-modal displacement patterns is proposed in this here with the objective of retaining the advantages of both adaptive and modal pushover procedures. The proposed Adaptive Modal Combination procedure eliminates the need to pre-estimate the target displacement and utilizes an energy-based scheme to achieve stable estimates of the seismic demand in conjunction with constant-ductility inelastic spectra. It is shown to provide reasonable estimates of seismic demand in typical moment frame structures for both far-fault and near-fault records. By combining the contributions of sufficient number of modes, the response estimated by AMC is generally similar to the benchmark results obtained from rigorous nonlinear time-history analyses for typical steel moment frame buildings. Nonetheless, there are cases when the predictions at the some story levels do not match NTH response estimates. Additionally, the findings and conclusions are based on studies of regular moment frame buildings.

The proposed procedure is by no means more difficult to implement than any other enhanced pushover procedure, and requires primarily an eigenvalue solver that can be invoked when necessary during the progressive modal pushover analysis and an internal or external module to generate constant-ductility ADRS curves. Since the method builds on existing procedures and incorporates concepts in CSM and inelastic spectra that are already familiar to structural earthquake engineers, it attempts to provide a methodology

that provides a physical basis for understanding the sensitivity of structural response to strong ground motions to structural and ground motion characteristics.

Table 6.1 Ground motion ensemble

No	Year	Earthquake	M_W[1]	Mech.[2]	Recording Station	Directivity Effect	Dist.[3] (km)	Site Class[4]	Data Source[5]	Comp.	PGA (g)	PGV (cm/sec)	Scale Factors 6-Story Bld.	Scale Factors 13-Story Bld.
Far-Fault Ground Motions														
1	1952	Kern county	7.5	TH/REV	Taft	-	36.2	D	1	111	0.18	17.50	6.0	-
2	1992	Big Bear	6.4	SS	Desert Hot Spr. (New Fire Stn.)	-	40.1	D	2	090	0.23	19.14	4.6	4.5
3	1994	Northridge	6.7	TH	Moorpark (Ventura Fire Stn.)	-	26.4	D	2	180	0.29	20.97	-	3.9
Near-Fault Ground Motions														
1	1992	Erzincan	6.7	SS	Erzincan	Forward	2.0	C	1	EW	0.50	64.32	1.0	1.0
2	1992	Cape Mendocino	7.1	TH	Petrolia, General Store	Forward	15.9	C	1	090	0.66	90.16	1.0	1.0
3	1989	Loma Prieta	7.0	OB	Los Gatos Parent Center	Forward	3.5	C	1	000	0.56	94.81	1.0	1.0
4	1994	Northridge	6.7	TH	Rinaldi Receiver Stn.	Forward	8.6	D	2	S49W	0.84	174.79	1.0	1.0
5	1994	Northridge	6.7	TH	Sylmar Olive View Hospital	Forward	6.4	D	1	360	0.84	130.37	1.0	1.0
6	1995	Kobe	6.9	SS	JMA	Forward	0.6	C	1	000	0.82	81.62	1.0	1.0
7	1999	Chi-Chi	7.6	TH	TCU074	Fling *	13.8	D	3	EW	0.59	68.90	1.0	1.0
8	1999	Chi-Chi	7.6	TH	TCU079	Fling *	11.0	D	3	EW	0.57	68.06	1.0	1.0

[1] *Moment magnitude*

[2] *Faulting mechanism = TH: Thrust; REV: Reverse; SS: Strike-slip; OB: Oblique*

[3] *Closest distance to fault*

[4] *NEHRP site classifications => (C for V_S (Shear-wave velocity) = 360 to 760 m/sec), (D for V_S = 180 to 360 m/sec)*

[5] *Data source = 1: http://peer.berkeley.edu/smcat); 2: http://db.cosmos-eq.org);*
3: http://scman.cwb.gov.tw/eqv5/special/19990921/pgadata-asci0704.htm

** Raw fling records were processed using a baseline correction only to conserve the true statis offset*

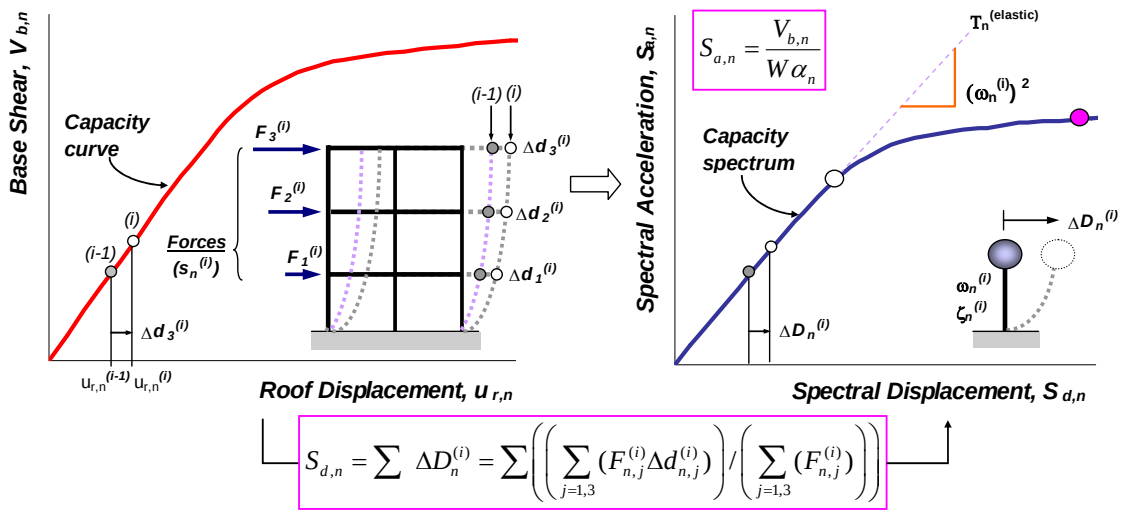

Figure 6.1 Energy-based ESDOF system representation of n^{th}-mode MDOF system capacity curve

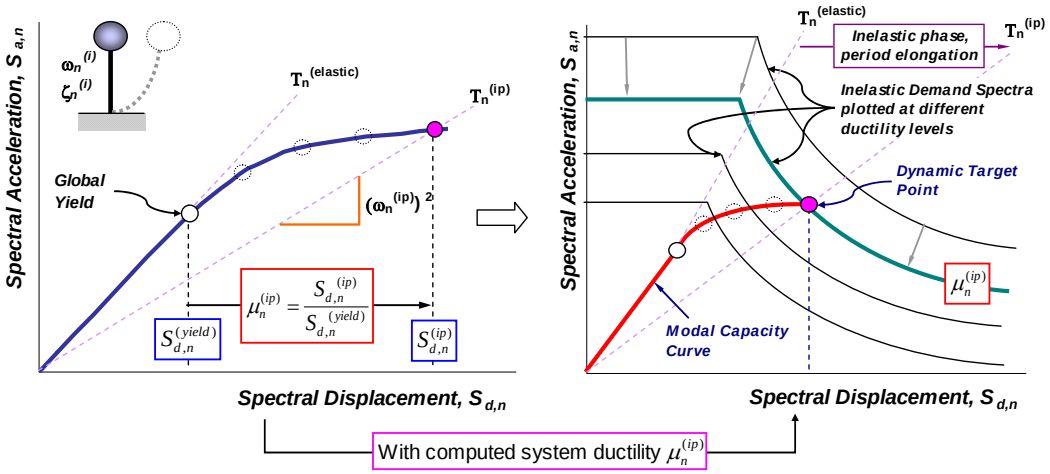

Figure 6.2 Performance point evaluation using system ductility through a set of inelastic spectra

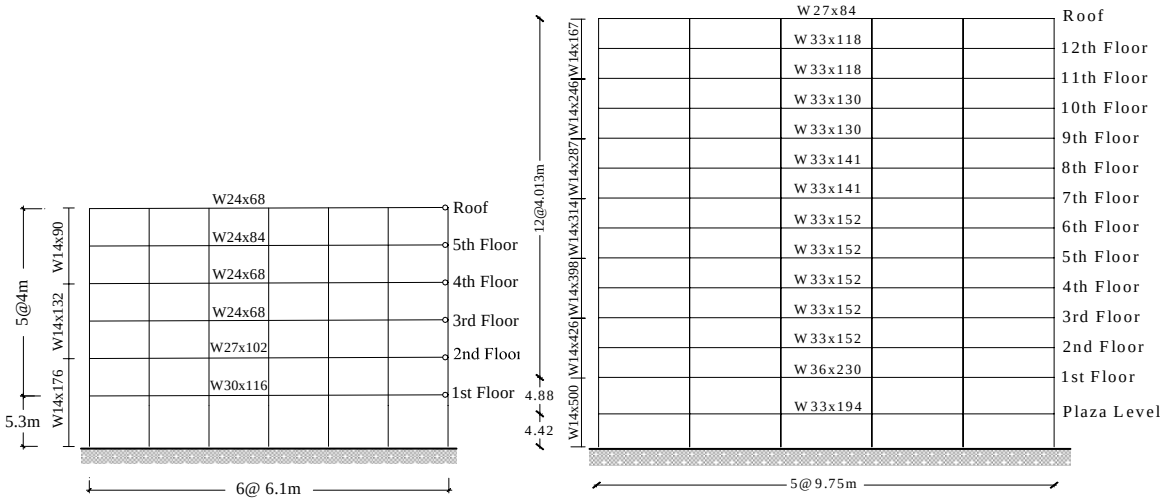

Figure 6.3 Elevation views of typical perimeter frames from six and thirteen-story steel buildings

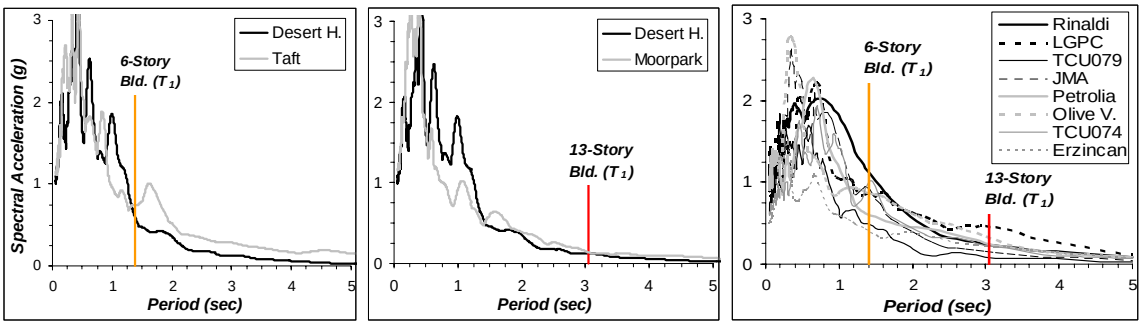

Figure 6.4 Response spectra (5 percent damped) of (a) scaled far-fault records (for six-story building); (b) scaled far-fault records (for thirteen-story building); (c) original near-fault records (*Note: Vertical lines indicate the fundamental periods of buildings*)

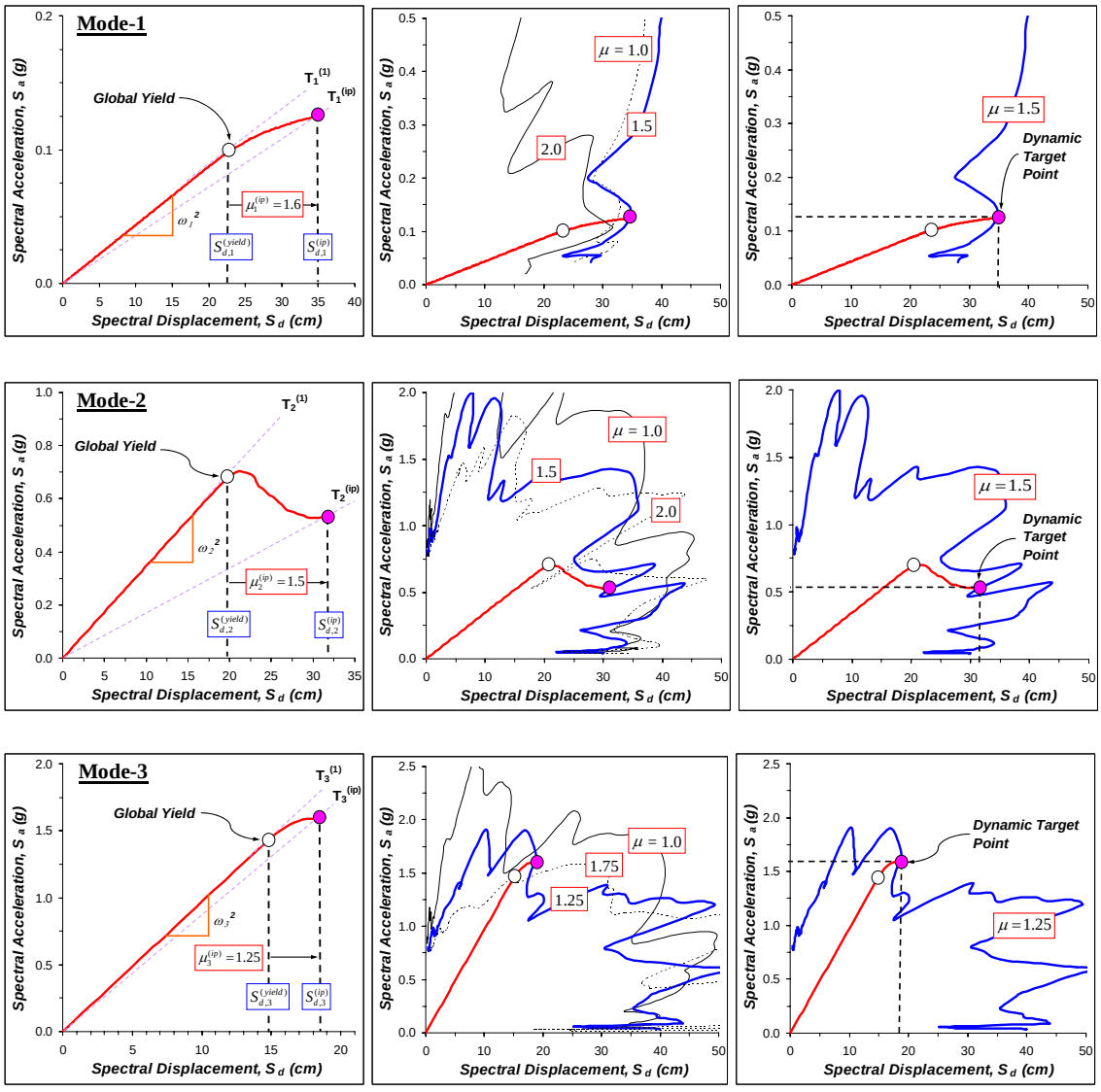

Figure 6.5 Dynamic target point evaluation in the AMC procedure

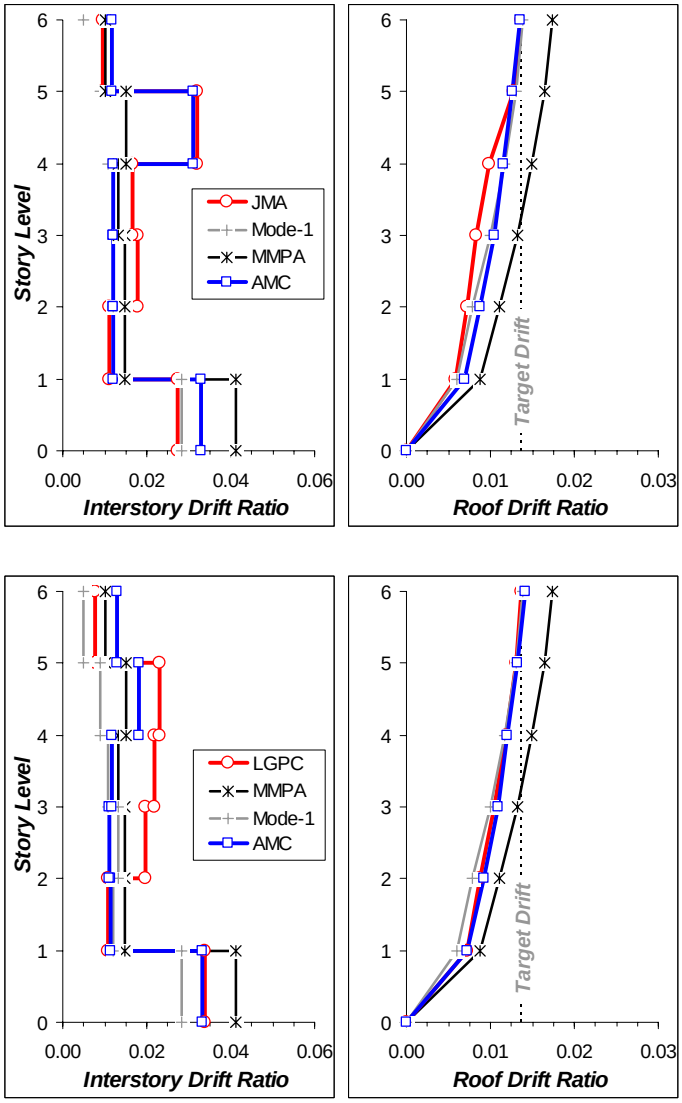

Figure 6.6 Predicted peak roof drift and interstory drift ratios by nonlinear static procedures compared to NTH analyses of near-fault records for six-story steel building

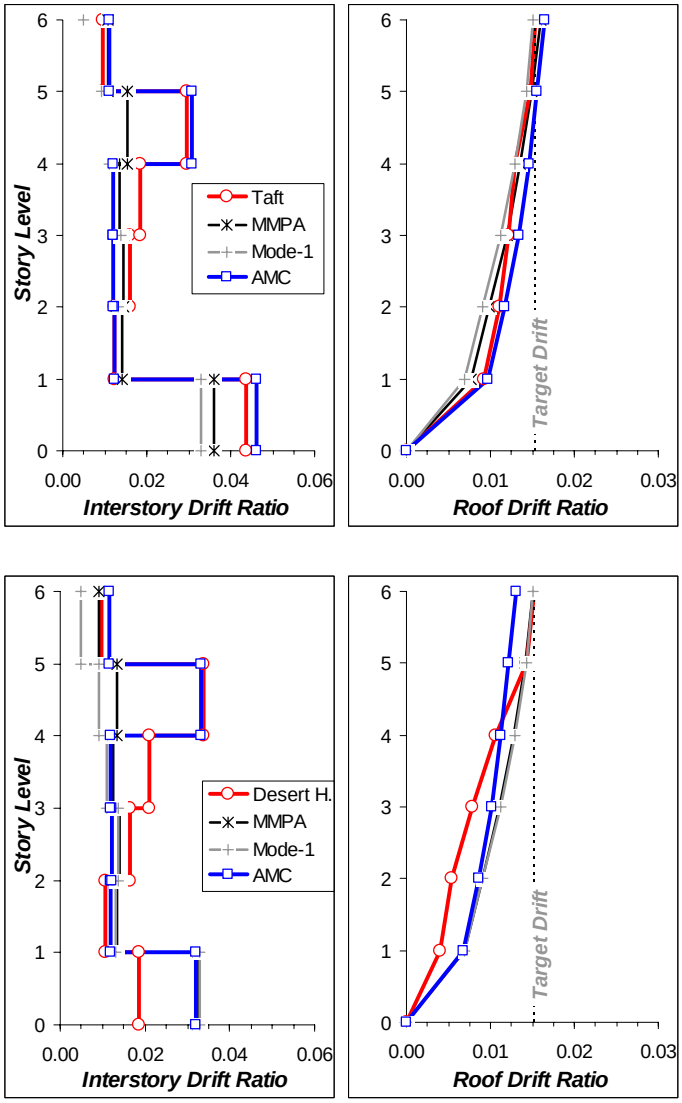

Figure 6.7 Predicted peak roof drift and interstory drift ratios by nonlinear static procedures compared to NTH analyses of far-fault records for six-story steel building

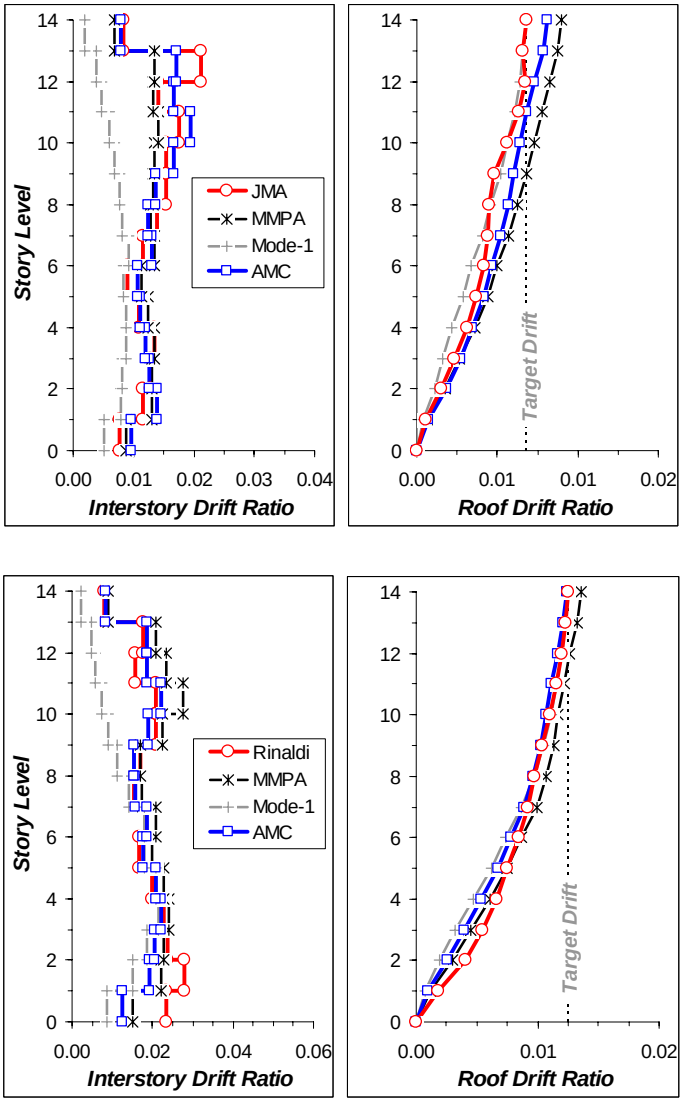

Figure 6.8 Predicted peak roof drift and interstory drift ratios by nonlinear static procedures compared to NTH analyses of near-fault records for thirteen-story steel building

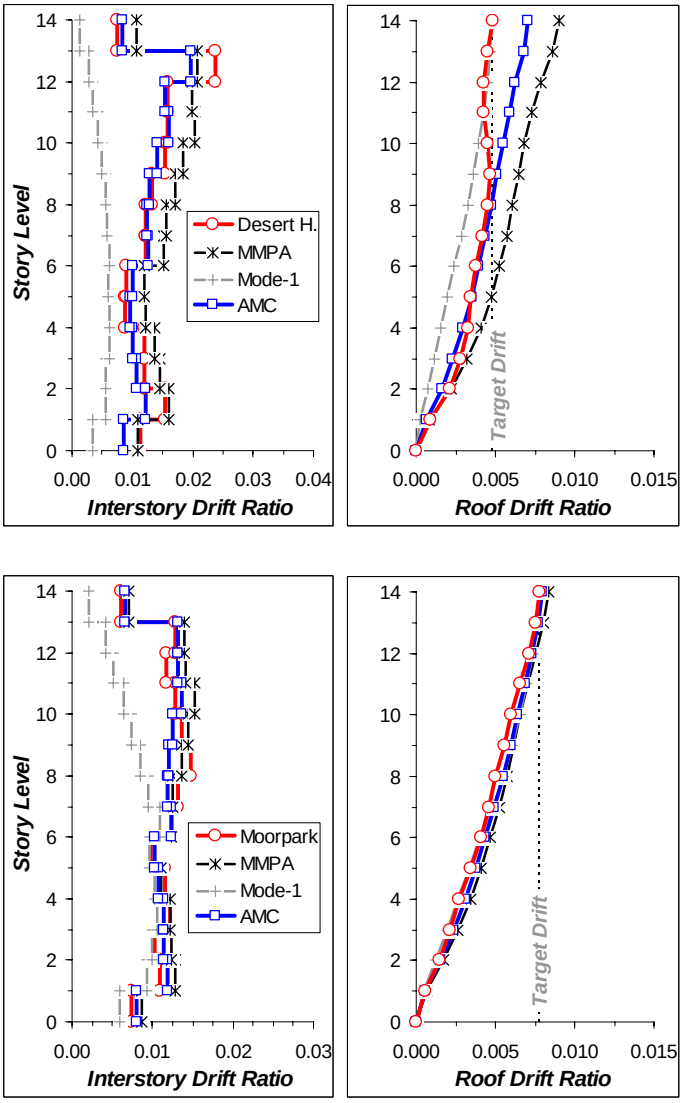

Figure 6.9 Predicted peak roof drift and interstory drift ratios by nonlinear static procedures compared to NTH analyses of far-fault records for thirteen-story steel building

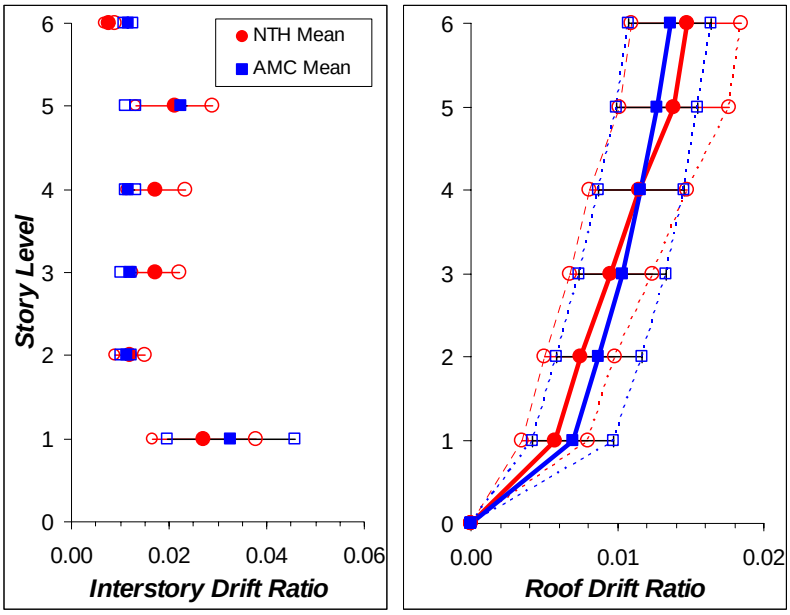

Figure 6.10 Mean and 16 / 84 percentile predictions of interstory and roof drift demands for six-story building (*Note: 16 and 84 percentile predictions are shown by unfilled markers)*

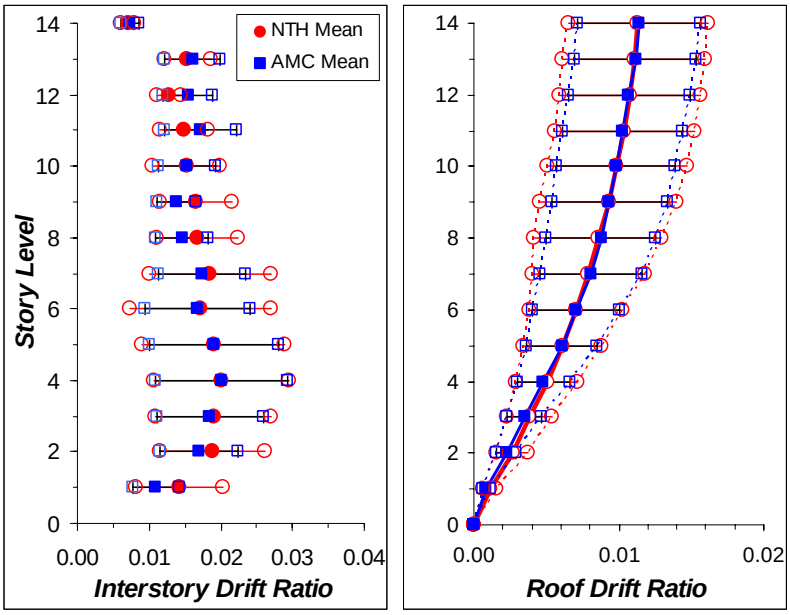

Figure 6.11 Mean and 16 / 84 percentile predictions of interstory and roof drift demands for thirteen-story steel building (*Note: 16 and 84 percentile predictions are shown by unfilled markers)*

CHAPTER 7

EVALUATION OF ADAPTIVE MODAL COMBINATION PROCEDURE FOR RC AND STEEL MOMENT FRAME BUILDINGS

7.1 INTRODUCTION

In performance assessment and design verification of building structures, approximate nonlinear static procedures (NSPs) are becoming commonplace in engineering practice as an "advanced" analysis technique to estimate seismic demands. Although seismic demands are best estimated using nonlinear time-history (NTH) analyses, NSPs are frequently used in ordinary engineering applications to avoid the intrinsic complexity and additional computational effort required by the former. As a result, simplified NSPs recommended in ATC-40 (1996) and FEMA-356 (2000) have become popular. These procedures are based on monotonically increasing predefined load patterns until some target displacement is achieved. However, it is now well-known that these simplified procedures based on invariant load patterns are inadequate to predict inelastic seismic demands in buildings when modes higher than first mode contribute to the response and inelastic effects alter the height-wise distribution of inertia forces (e.g., Gupta and Kunnath 2000; Kalkan and Kunnath 2004; Goel and Chopra 2004). In order to overcome some of these drawbacks, a number of enhanced procedures considering different loading

vectors (derived from mode shapes) were proposed. These procedures attempt to account for higher mode effects and use elastic modal combination rules while still utilizing invariant load vectors. The modal pushover analysis (MPA) of Chopra and Goel (2002), modified modal pushover analysis (MMPA) of Chopra et al. (2004), and upper-bound pushover analysis (UBPA) procedure of Jan et al. (2004) are examples of this approach.

A new adaptive modal combination (AMC) procedure, whereby a set of adaptive mode-shape based inertia force patterns is applied to the structure, has been developed in Chapter 6 where the methodology has been validated for regular moment frame buildings.

With the increase in the number of alternative pushover procedures proposed in recent years, it is useful to identify the potential limitations of these methods and compare and contrast their effectiveness in simulating seismic demands at the structure, story and component level. Following a brief overview of the major developments in nonlinear static analysis techniques, the ability of enhanced nonlinear static procedures to simulate seismic demands in a set of existing steel and reinforced concrete (RC) buildings is explored through comparisons with benchmark results obtained from a comprehensive set of NTH analyses considering ground motions having diverse characteristics. The earthquake recordings were carefully compiled so as to reflect characteristics of normal far-fault records and typical near-fault records having forward-directivity and fling effects.

7.2 REVIEW OF MAJOR NONLINEAR STATIC PROCEDURES

NSPs can be classified into three major groups based on the type of lateral load patterns applied to the structural model during the analysis: invariant single load vectors (FEMA-356); invariant multi-mode vectors (MMPA and UBPA); and adaptive load vectors (AMC). In this section, a brief overview of these typical methodologies is presented.

7.2.1 FEMA-356 Lateral Load Patterns

Currently, two sets of lateral load distributions are recommended in FEMA-356 for nonlinear static analysis. The first set consists of a vertical distribution proportional to (a) pseudo lateral load (this pattern becomes an inverted triangle for systems with fundamental period $T_1 < 0.5$sec); (b) elastic first mode shape; (c) story shear distribution computed via response spectrum analysis. The second set encompasses mass proportional uniform load pattern and adaptive load patterns (note: though the FEMA document refers to an adaptive pattern, a detailed procedure is not provided). FEMA-356 recommends that at least one load patterns from each set be used to obtain the response envelope. Therefore, in this study, the most commonly used load distributions, viz., a load vector proportional to the first mode shape and a load vector proportional to the story mass, are employed. The results shown later represents the envelope of the two distributions.

7.2.2 Modified Modal Pushover Analysis (MMPA)

The Modified Modal Pushover Analysis (MMPA), which has been recently developed by Chopra et al. (2004) is an extension of Modal Pushover Analysis (MPA), combines the

elastic influence of higher modes with the inelastic response of a first mode pushover analysis using modal combination rules (such as SRSS). The procedure involves conducting a nonlinear response history analysis (NRHA) of the first-mode SDOF system unless an inelastic response spectrum is available for the target (design) ground motion. Details of the implementation are described in Chopra et al. (2004).

7.2.3 Upper-Bound Pushover Analysis (UBPA)

Unlike the MMPA where the response is obtained from the combination of individual analyses using different mode shapes, the upper-bound pushover analysis (UBPA) proposed by Jan et al. (2004) is based on utilizing a singe load vector obtained as the combination of the first mode shape and a factored second mode shape. The spectral displacements (D_n) corresponding to elastic first and second mode periods are estimated from the elastic spectrum of the considered ground motion and the upper-bound contribution of the second mode is established using modal participation factors (Γ_n), as follows:

$$(q_2 / q_1) = \left|(\Gamma_2 D_2) / (\Gamma_1 D_1)\right| \tag{7.1}$$

The invariant load vector (F) is then computed as the combination of first and second mode shapes:

$$F = w_1^2 m\phi_1 + w_2^2 m\phi_2 (q_2 / q_1) \tag{7. 2}$$

7.2.4 Adaptive Modal Combination (AMC) Procedure

The AMC procedure was developed to integrate the essential concepts of the following three methods: the capacity spectrum method recommended in ATC-40, the direct

adaptive method of Gupta and Kunnath (2000); and the modal pushover analysis advanced by Chopra and Goel (2002). The AMC procedure accounts for higher mode effects by combining the response of individual modal pushover analyses and incorporates the effects of changing modal properties during inelastic response through its adaptive feature. A unique aspect of the procedure is that the target displacement is estimated and updated dynamically during the analysis by incorporating energy based modal capacity curves with inelastic response spectra. Hence it eliminates the need to approximate the target displacement prior to commencing the pushover analysis. The basic steps of the methodology are presented in Chapter 6.

7.3 STRUCTURAL SYSTEMS, ANALYTICAL MODELS AND GROUND MOTIONS

Existing 6 and 13 story steel moment frame buildings and 7 and 20 story RC moment frame buildings were used in the evaluation of the different NSP methods. All buildings were instrumented by the CSMIP (California Strong Motion Instrumentation Program), thus data from actual earthquake responses were used in the calibration of the mathematical models. Details of the 6 and 13 story steel moment frame buildings and their calibration examples are given in Chapter 3.3.2 and 3.3.3, while details of 7 and 20 story RC moment frame buildings are given in the following.

7.3.1 7-Story RC Building

This RC building was constructed during the mid-1960s according to 1964 Los Angeles City building code. It was suffered damage in both the 1971 San Fernando and 1994

Northridge earthquakes. The building is 20.03m in elevation and has a rectangular plan with plan dimensions of 45.72m x 18.6m. The sub-structural system consists of pile foundations. The floor system consists of RC flat slabs and perimeter beams supported by concrete columns. The lateral load is resisted by four perimeter spandrel beam-column frames. The moment frames in the longitudinal direction consists of eight bays at 5.7m. In the short direction, the two outer bays are 6.12m and the interior bay measures 6.35m. The interior frames constitute 45.7cm square columns and two way flat slabs with a thickness range of 25.4cm on the second level to 20.3cm on the roof. Materials are normal weight concrete with design strength from 21.0MPa to 35.0MPa, grade 40 steel (~280MPa) in beams and grade 60 steel (~420MPa) in columns. The details of the perimeter frame in the long direction are shown in Figure 7.1. This building was equipped with sixteen sensors by CSMIP which recorded the 1994 Northridge earthquake. A maximum PGA of 0.42g in the transverse direction and 0.45g in the longitudinal direction were recorded at the ground level.

7.3.2 20-Story Steel Building

The North Hollywood Hotel is located in Southern California and designed in accordance with 1966 Los Angeles building code. The building consists of 20 stories above ground and a basement. The rectangular plan of the building measures 60.7m x 19.1m in the longitudinal and transverse directions, respectively. The gravity load system of the building consists of 11.5 to 15.2cm concrete slab supported. Concrete used in the construction, for both beams and columns, was light weight concrete with a specified concrete strength of 28MPa for levels one through ten, and 21MPa for the remaining levels. The specified yield strength for column reinforcement up to the 10^{th} level is

420MPa and for the remaining levels is 280MPa. The building foundation consists of spread footings. The primary lateral force resisting system consists of moment-resisting frames with strong shear walls in the basement only. Details of a typical perimeter frame in the longitudinal direction are exhibited in Figure 7.2. The building was instrumented with a total of sixteen sensors, on five levels. These sensors recorded the building motion during the 1994 Northridge earthquake. It performed well during the earthquake, and only suffered damage in nonstructural components. A PGA of 0.32g in the transverse direction and 0.12g in the longitudinal direction were recorded at the roof level.

7.3.3 Analytical Model Development

Analytical models were created using the open source finite element platform, OpenSees (2005). Two-dimensional models of a single frame were developed for each building. A force-based nonlinear beam-column element (utilizes a layered fiber section) is used to model all components of the frame models. Centerline dimensions were used in the element modeling, the composite action of floor slabs was not considered, and the columns were assumed to be fixed at the base level. For the time-history evaluations, masses were applied to frame models based on the floor tributary area and distributed proportionally to the floor nodes. The simulation models were calibrated to the measured response data at the roof level of each building so as to gain confidence in the analytical results of the comparative study. Figures 7.1 and 7.2 present the typical comparisons of recorded and computed response at the roof level of 7-story and 20-story RC buildings, respectively. Based on the calibration studies, Raleigh damping of 4 percent for the first

two vibration modes of 7-story building, and 4 percent for the first and third vibration modes of 20-story building were employed.

7.3.4 Ground Motion Ensemble

In order to consider ground motions with diverse characteristics, ordinary far-fault records and near-fault ground motions having forward directivity and fling effects were used. A total of thirty records as indicated in Table 7.1 were compiled for the NTH analyses. The selection of near-fault records has two important features. First, these motions have significant PGV than ordinary far-fault records. Second, near-fault records exhibit intense coherent long period velocity pulses due to directivity effects. As opposed to near-fault forward directivity records generally producing two sided velocity pulses, near-fault fling type of records are generally characterized with a single sided velocity peak and that manifest itself as a large static offset at the end of the displacement time-history. This static offset is the indication of tectonic deformation on the rupture plane.

7.3.5 Ground Motion Scaling and Target Displacement Evaluation

In order to facilitate a rational basis for comparison of the different methodologies, the ground motion records given in Table 7.1 were scaled so that a peak roof drift ratio of 1.5 percent was achieved for the two steel buildings and the 7-story RC building while a roof drift of 1 percent was obtained for the 20-story RC building. Figure 7.3 displays the elastic mean pseudo-acceleration spectra (five-percent damped) of the building-specific scaled records. Also marked on this figure with vertical lines are the first three elastic fundamental periods of the buildings.

The target displacements used for the FEMA-356 and UBPA procedures are the predetermined peak roof displacements for each building. For the MMPA, this target displacement was used to calculate the first mode contribution. For the second and third mode contributions, the mean spectra computed for each building and ground motion set were used together with the elastic modal periods to determine the peak roof displacement levels. For AMC, the target point for the first mode was constrained to the predetermined peak roof drift, and the target point for the higher modes (i.e., 2^{nd} and 3^{rd}) were computed dynamically during the pushover analyses using the mean inelastic spectra of the records.

7.4 EVALUATION OF NONLINEAR STATIC PROCEDURES

The FEMA-356, MMPA, UBPA and AMC nonlinear static procedures are evaluated by comparing the computed roof drift ratio (maximum roof displacement normalized by building height), interstory drift ratio (relative drift between two consecutive stories normalized by story height) and member plastic rotations to nonlinear time-history results. Since the time history results are based on a set of ten simulations per record set, both the mean and the dispersion (standard deviation) about the mean value are presented in the plots.

7.4.1 Peak Displacement Profiles

Figures 7.4 and 7.5 show the mean and standard deviations (i.e., 16 and 84 percentile) of peak displacement profile estimated by NTH analyses and predictions by FEMA-356,

UBPA, MMPA and AMC procedures for each building sorted by type of record. The peak deformed shape along the heights of the buildings show that FEMA-356 pushover envelope consistently overestimates the peak story displacements in the low and intermediate story levels for all buildings and ground motions types investigated, UBPA underestimates the displacements at almost all levels with the exception of the upper stories. The AMC and MMPA procedures both result in similar estimates and generally yield better estimates of the peak displacement profile particularly for the 13-story steel and 7-story RC buildings. It is interesting that story displacement demands from nonlinear static methods (with the exception of UBPA) are always conservative. Comparing the time-history responses for the different ground motions indicates that far-fault records generally produce more variability in the demands than near-fault records. Only the 20-story RC building showed greater variability in the displacement demands for near-fault records.

7.4.2 Interstory Drift Ratio Profiles

In Figures 7.6 and 7.7, the interstory drift ratio profiles obtained with NSPs are compared to NTH estimates. For the entire set of analyzed buildings, significant higher mode contributions are evident resulting in the migration of dynamic drifts from the lower to the upper stories. The FEMA-356 methodology grossly underestimates the drifts in upper stories and overestimates them in lower stories, except the 13-story building, in which only the lower level demands were captured adequately. Conversely, the UBPA always underestimates the drifts at the lower levels and overestimates them at the upper story levels. MMPA yields better estimates of drift demands compared to FEMA-356 and

UBPA. However, in all cases, upper level demands were underestimated by MMPA, with the exception of the 13-story building, where MMPA overestimates the upper level drifts. On the other hand, AMC is shown to predict the drift profiles for all four buildings with relatively better accuracy. The AMC procedure slightly overestimates or underestimates the drift in some cases but captures the overall effects of higher mode contributions more consistently for both far fault and near fault records.

7.4.3 Member Plastic Rotation Profiles

Since each earthquake record induces different demand patterns, local demand estimates at the component level are evaluated only for a specific record in each data set (near fault with directivity, near fault with fling and far fault record). Figures 7.8 and 7.9 show the results of computed member plastic rotations at beams and columns determined by NTH and are compared to NSP estimates for the 6-story steel and 7-story RC buildings, respectively. Only the AMC and MMPA procedures are included here since the comparisons presented previously have demonstrated the limitations of the FEMA and UBPA methods.

It is seen that MMPA fails to identify column yielding in the 5^{th} level of the 6-story steel frame but does a good job at the first story level. The AMC procedure is able to identify plastic hinging at both the first and fifth levels. MMPA provides an improved prediction for the 7-story RC frame by identifying yielding in the fourth story however it is unable to capture the inelastic demands at the other levels. AMC predictions are consistent with NTH patterns though the demands are slightly overestimated for the near fault record with directivity effects. The plastic rotation estimates in MMPA are produced

essentially by the first mode pushover analysis while higher modes contributions remain elastic as per the procedure. Accordingly, MMPA generally provides better estimates of plastic rotations at the first and lower story levels.

7.5 HIGHER MODE CONTIBUTIONS TO SEISMIC DEMANDS

Higher mode effects on seismic demand are strongly dependent on both the characteristics of the ground motion and the properties of the structural system. While the former is an independent input parameter, the dynamic properties of the structural system are significantly affected by the frequency content of the ground motion. With repeated changes in system stiffness, modal attributes also experience progressive modifications. Figure 7.10 demonstrates how modal periods and modal participation factors are altered during the dynamic response of the 6-story building when subjected to JMA near-fault record. The peak interstory drift profile (Figure 7.10d) shows that the peak drift is occurring at the fifth story level, a clear indication of higher mode effects. It is instructive to note that the peaks of modal periods (associated with yielding and inelastic behavior) are associated with the peaks of the modal participation factors, and they strongly correlate to the time-steps at which the story peak demands occur (follow the vertical lines in Figure 7.11). Another important observation is that the second and third mode modal participation factors are in-phase but both these modes are out-of-phase with respect to the first mode participation factor. That implies that the peak deformation associated with the first mode (at the first story in this case) is not coupled with higher mode contributions.

Figure 7.11 demonstrates other important features of structural behavior by examining snapshots of the time history response of the same building. Shown in this figure are the inertia forces computed by multiplying story mass and story acceleration at the time instances when the peak interstory drift demands at each story level are observed. Notably, peak demands at each story occur at different time instances with significantly different inertia force patterns. Consideration of the vertical distribution of inertia forces is crucial for static procedures and such variations can only be accommodated by considering changes in the modal attributes as the system moves from the elastic to inelastic state.

Figure 7.12 shows how the mode shapes vary continuously during the response history. Mode shapes shown in this figure are from snapshots at critical time instants when the peak interstory drift occurs at each story level. In fact, these changes are also reflected in the instantaneous inertia forces described in the previous paragraph. At the time when the first story experiences its peak demand, the first mode shape resembles the FEMA invariant uniform load distribution. At the time-step when the fifth story peak drift is recorded, the first mode shape has significantly deviated from its original elastic form forcing the upper story levels to deform further rather than the lower levels. The significant contribution of the second mode to the relative drift between the fourth and fifth level is evident as the system moves from the elastic to inelastic phase. Similarly, the third mode is seen to influence the drift mostly at the mid-levels though the relative difference is not significant. These observations once again highlight the importance of considering mode shapes at different stiffness states of the system.

7.6 CONCLUSIONS

The ability of four different types of nonlinear static procedures to predict seismic demands in a set of existing buildings were examined. Each building was subjected to 30 ground motions having different characteristics. The resultant mean and standard deviations served as benchmark responses against which the NSPs were compared. A systematic evaluation of the predicted demands (such as peak displacement profile, interstory drifts and member plastic rotations) by the different NSPs forms the basis for the following conclusions:

1. The FEMA-356 method (wherein the envelope of two response measures were considered) provides inadequate predictions of peak interstory drift and peak member plastic rotations at the upper story levels when higher mode contribution are significant.
2. UBPA estimates were the poorest by far, being unable to reasonably predict even the peak displacement profile. It led to significant underestimation of story drift demands and member rotations at the lower levels and to their overestimation at the upper stories.
3. Compared to FEMA-356 and UBPA procedures, MMPA provides story drift estimates that are generally much closer to the mean NTH estimates. However, since the method ignores the inelastic contribution of higher modes, it is unable to reasonably predict plastic rotation demands in the upper stories.
4. It was also shown that NSPs based on invariant load vectors using elastic modal properties cannot capture the changes to the dynamic modes resulting from inelastic action. The inertia load distribution, which is well correlated to story

deformations, progressively changes following the variation of the modal periods and modal shapes during inelastic response. Consequently, the variation of inertial forces must be considered in static procedures that attempt to reproduce inelastic dynamic response. This can only be achieved using adaptive load vectors.

5. The AMC procedure which integrates the inherent advantages of the capacity spectrum method, modal combination and adaptive loading scheme provided the best overall comparison with NTH results. In general, the method was able to reproduce the essential response features providing a reasonable measure of the likely contribution of higher modes in all phases of the response.

Table 7.1 Details of ground motion ensemble

No	Year	Earthquake	M_W	Mech.[1]	Recording Station	Dist.[2] (km)	Site Class[3]	Data Source[4]	Comp.	PGA (g)	PGV (cm/sec)
Near-Fault Ground Motions with Forward Directivity											
1	1979	Imperial-Valley	6.5	SS	EC Meloland Overpass	3.1	D	1	270	0.30	90.5
2	1984	Morgan Hill	6.1	SS	Coyote Lake Dam	1.5	B	2	285	1.16	80.3
3	1989	Loma Prieta	7.0	OB	Saratoga Aloha Ave.	4.1	D	2	090	0.32	44.8
4	1989	Loma Prieta	7.0	OB	Lexington Dam	6.3	C	2	090	0.41	94.3
5	1992	Erzincan	6.7	SS	Erzincan	2.0	C	1	EW	0.50	64.3
6	1992	Cape Mendocino	7.1	TH	Petrolia, General Store	15.9	C	1	090	0.66	90.2
7	1994	Northridge	6.7	TH	Rinaldi Receiver Stn.	8.6	D	2	S49W	0.84	174.8
8	1994	Northridge	6.7	TH	Jensen Filtration Plant	6.2	D	1	292	0.59	99.2
9	1995	Kobe	6.9	SS	JMA	0.6	C	1	000	0.82	81.6
10	1995	Kobe	6.9	SS	Takatori	4.3	D	1	090	0.62	120.8
Near-Fault Ground Motions with Fling											
1	1999	Kocaeli	7.4	SS	Sakarya	3.20	C	3	EW	0.41	82.1
2	1999	Chi-Chi	7.6	TH	TCU068	3.01	D	4	EW	0.50	277.6
3	1999	Chi-Chi	7.6	TH	TCU072	7.87	D	4	EW	0.46	83.6
4	1999	Chi-Chi	7.6	TH	TCU074	13.8	D	4	EW	0.59	68.9
5	1999	Chi-Chi	7.6	TH	TCU084	11.4	C	4	NS	0.42	42.6
6	1999	Chi-Chi	7.6	TH	TCU129	2.2	D	4	EW	0.98	66.9
7	1999	Chi-Chi	7.6	TH	TCU082	4.5	D	4	EW	0.22	50.5
8	1999	Chi-Chi	7.6	TH	TCU078	8.3	D	4	EW	0.43	41.9
9	1999	Chi-Chi	7.6	TH	TCU076	3.2	D	4	NS	0.41	61.8
10	1999	Chi-Chi	7.6	TH	TCU079	10.95	D	4	EW	0.57	68.1
Far-Fault Ground Motions											
1	1952	Kern county	7.5	TH/REV	Taft	36.2	D	1	111	0.18	17.5
2	1989	Loma Prieta	7.0	OB	Cliff House	68.5	D	1	090	0.11	19.8
3	1992	Big Bear	6.4	SS	Desert Hot Spr. (New Fire Stn.)	40.1	D	2	090	0.23	19.1
4	1994	Northridge	6.7	TH	Moorpark (Ventura Fire Stn.)	26.4	D	2	180	0.29	21.0
8	1994	Northridge	6.7	TH	Saturn Street School	26.9	D	2	S70E	0.43	43.5
3	1971	San Fernando	6.6	TH	Castaic, Old Ridge Route	23.5	B	1	291	0.27	25.9
7	1971	Landers	7.3	SS	Boron Fire Stn.	99.3	D	1	000	0.12	13.0
8	1989	Loma Prieta	7.0	OB	Presidio	67.4	D	1	090	0.19	32.4
9	1994	Northridge	6.7	TH	Terminal Island Fire Stn. 111	57.5	D	1	330	0.19	12.1
10	1994	Northridge	6.7	TH	Montebello	44.2	D	1	206	0.18	9.4

[1] *Faulting Mechanism = TH: Thrust; REV: Reverse; SS: Strike-slip; OB: Oblique;*

[2] *Closest distance to fault*

[3] *NEHRP Site Class = B for V_S (Shear-wave velocity) = 760 to 1500 m/s; C for V_S = 360 to 760 m/s; D for V_S = 180 to 360 m/s*

[4] *Data Source = 1: PEER (http://peer.berkeley.edu/smcat); 2: Cosmos (http://db.cosmos-eq.org)*
3: ERD (http://angora.deprem.gov.tr/); 4: http://scman.cwb.gov.tw/eqv5/special/19990921/pgadata-asci0704.htm

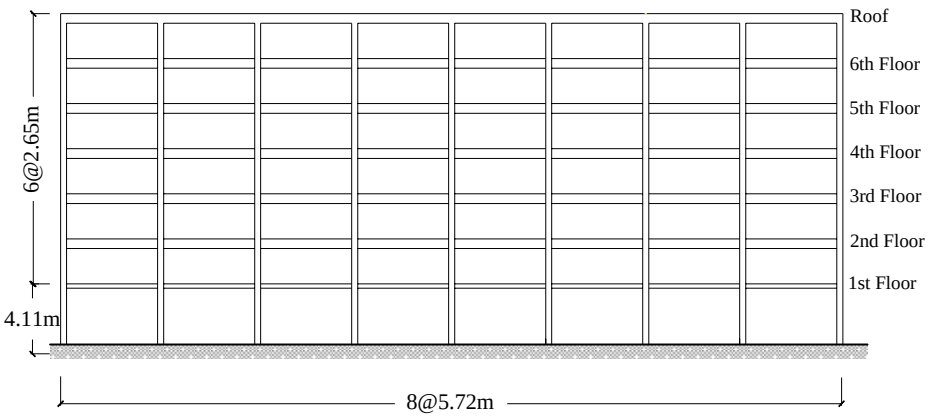

(a)

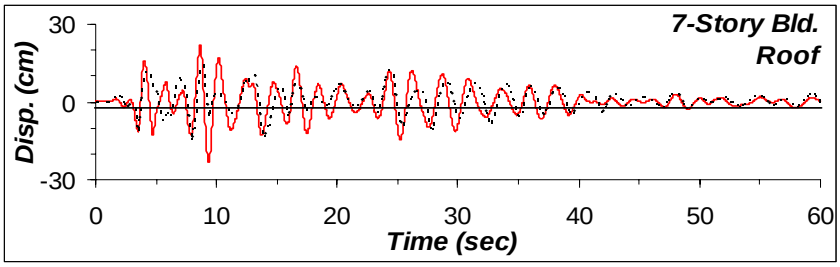

(b)

Figure 7.1 (a) Elevation of 7-story RC building, (b) recorded and computed response at the roof level

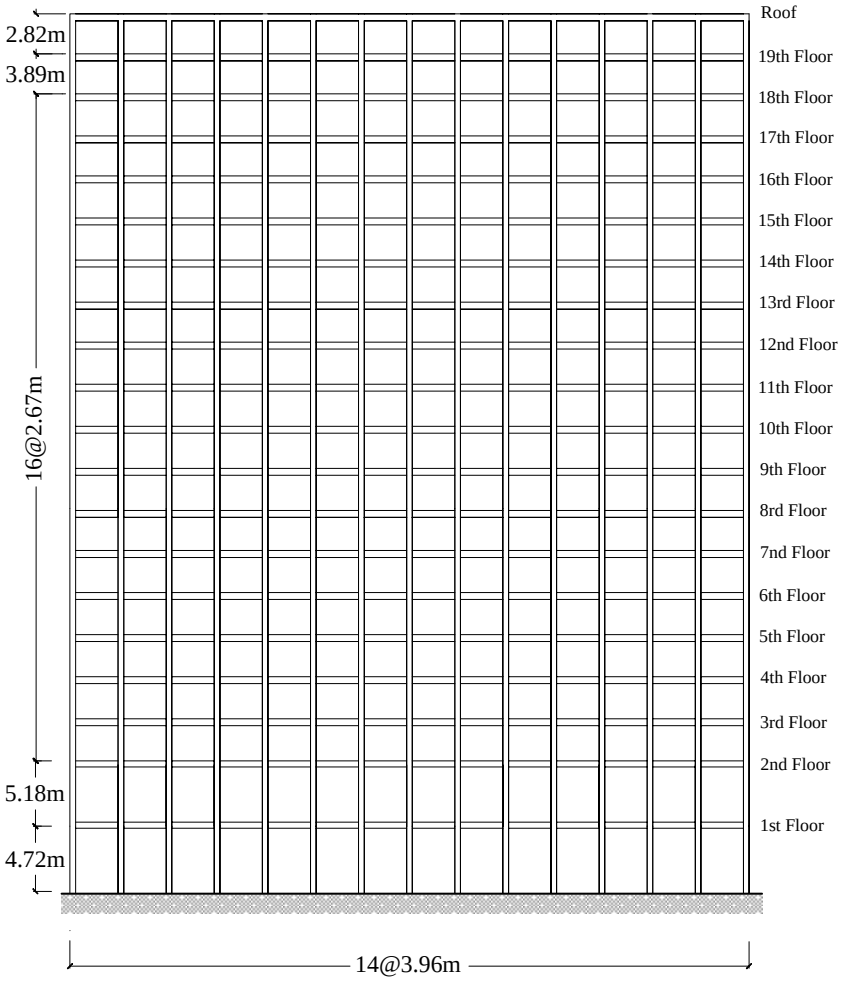

(a)

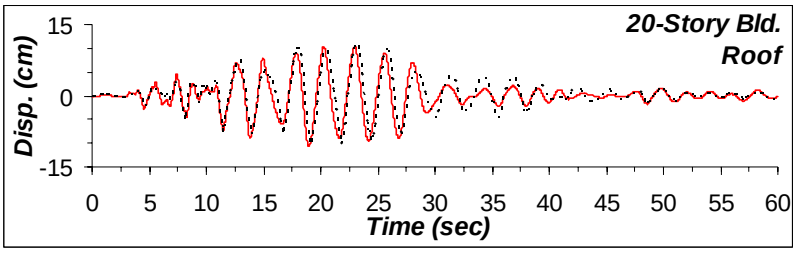

(b)

Figure 7.2 (a) Elevation of 20-story RC building, (b) recorded and computed response at the roof level

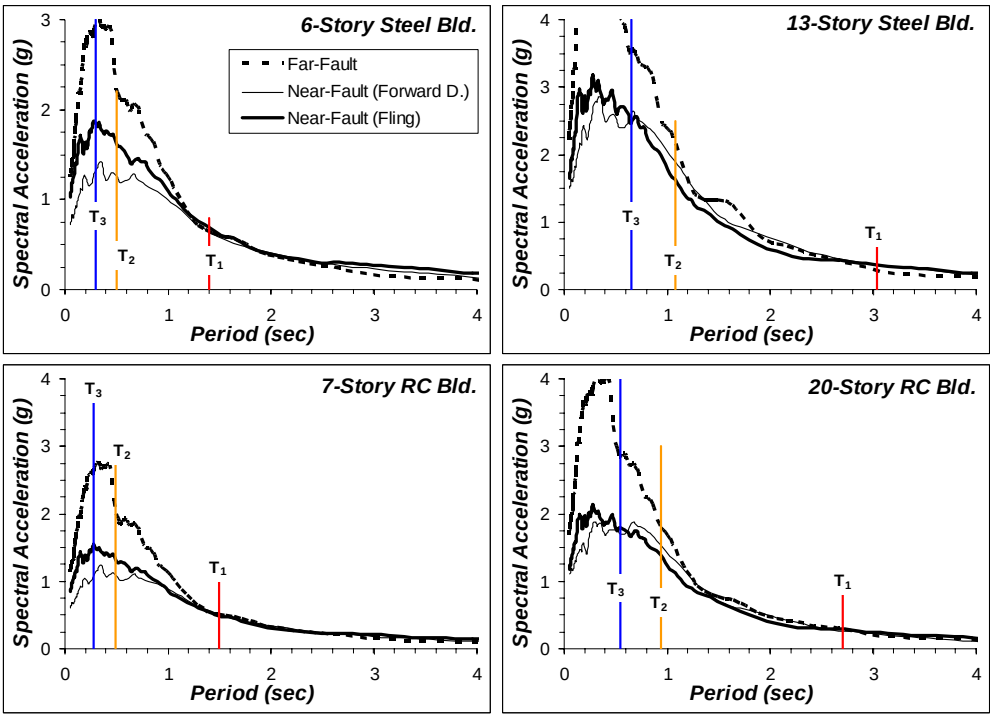

Figure 7.3 Mean pseudo-acceleration spectra of building-specific scaled ground motions

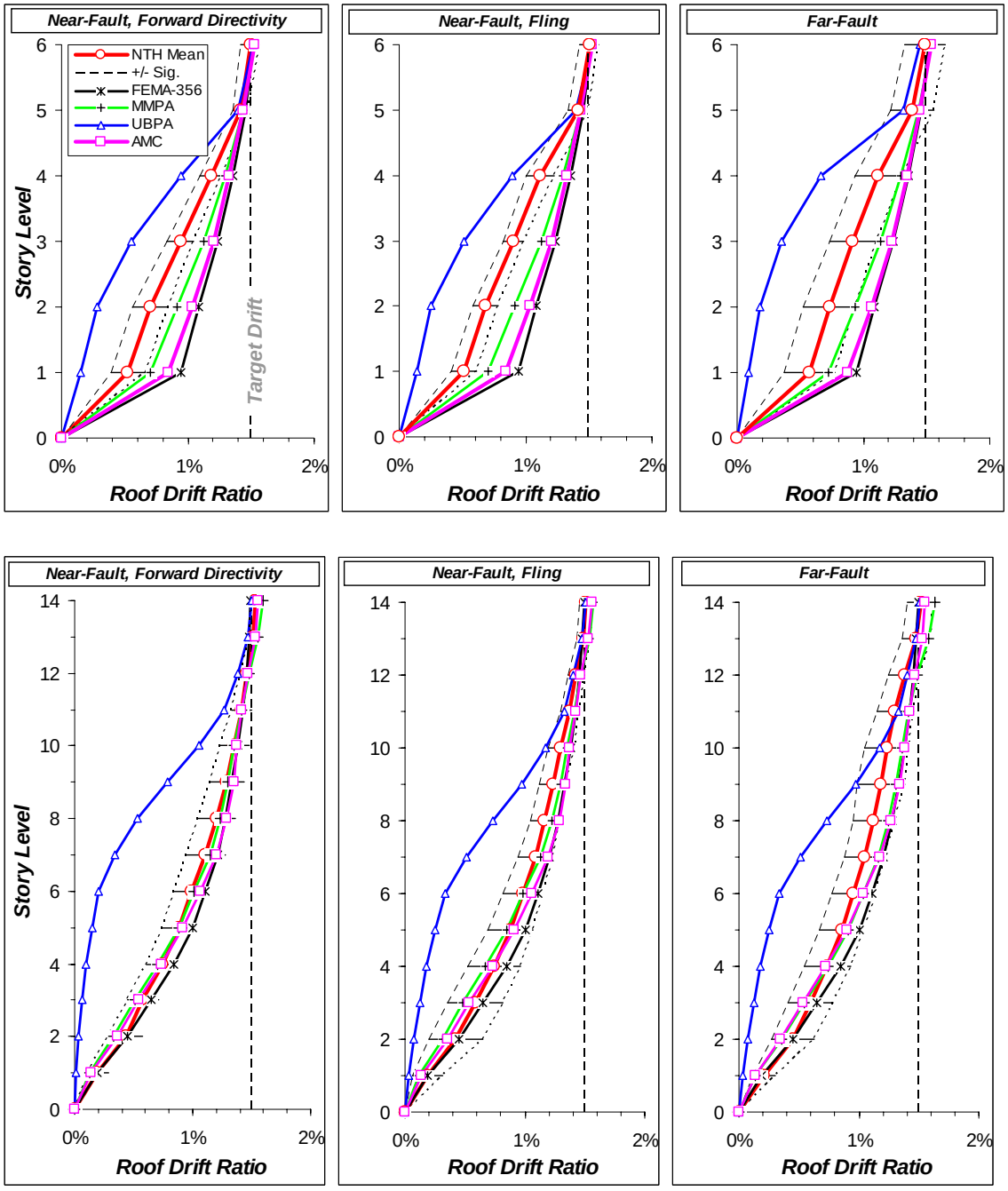

Figure 7.4 Predicted peak displacement demands by NSPs compared to NTH analyses for steel buildings

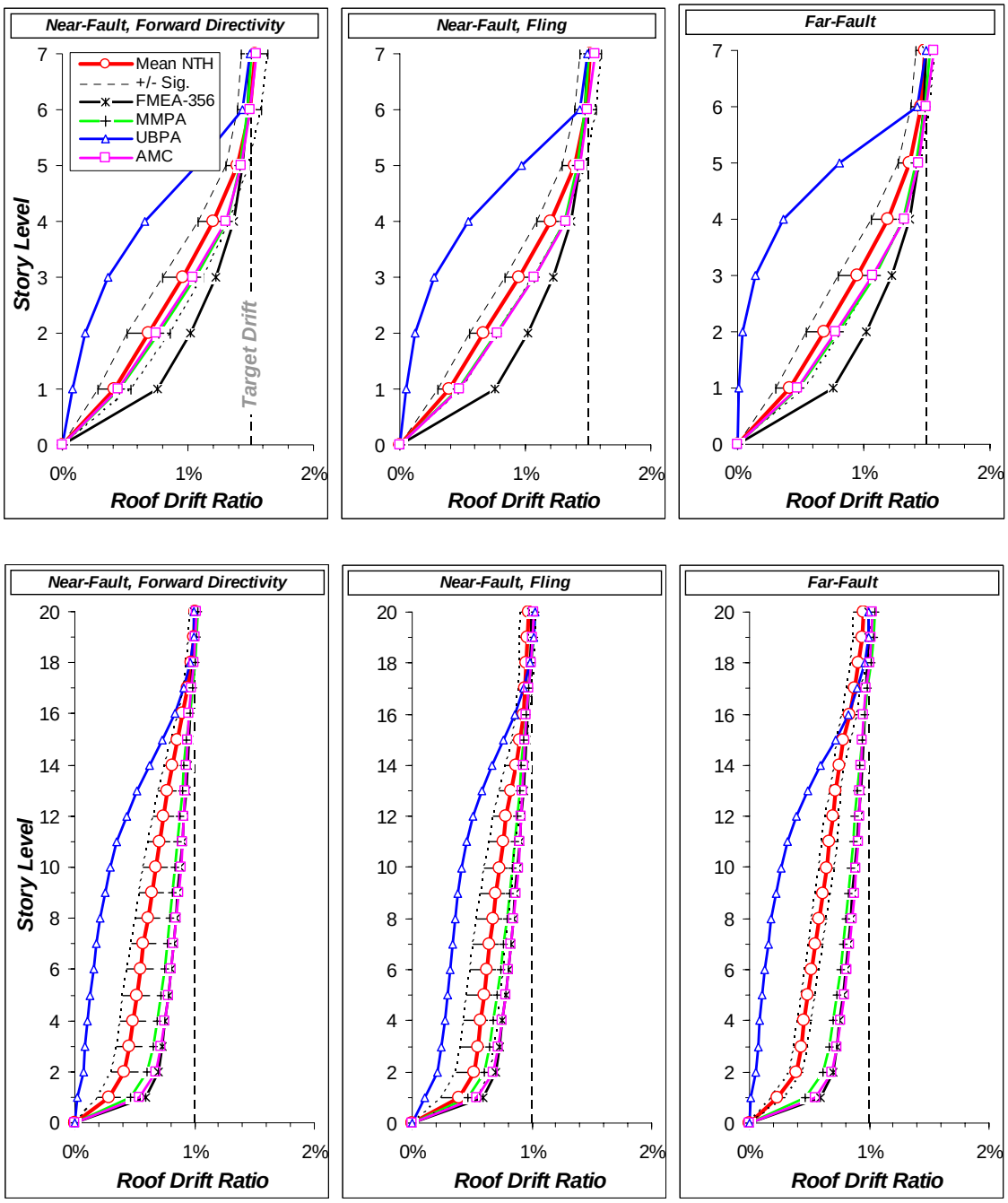

Figure 7.5 Predicted peak displacement demands by NSPs compared to NTH analyses for RC buildings

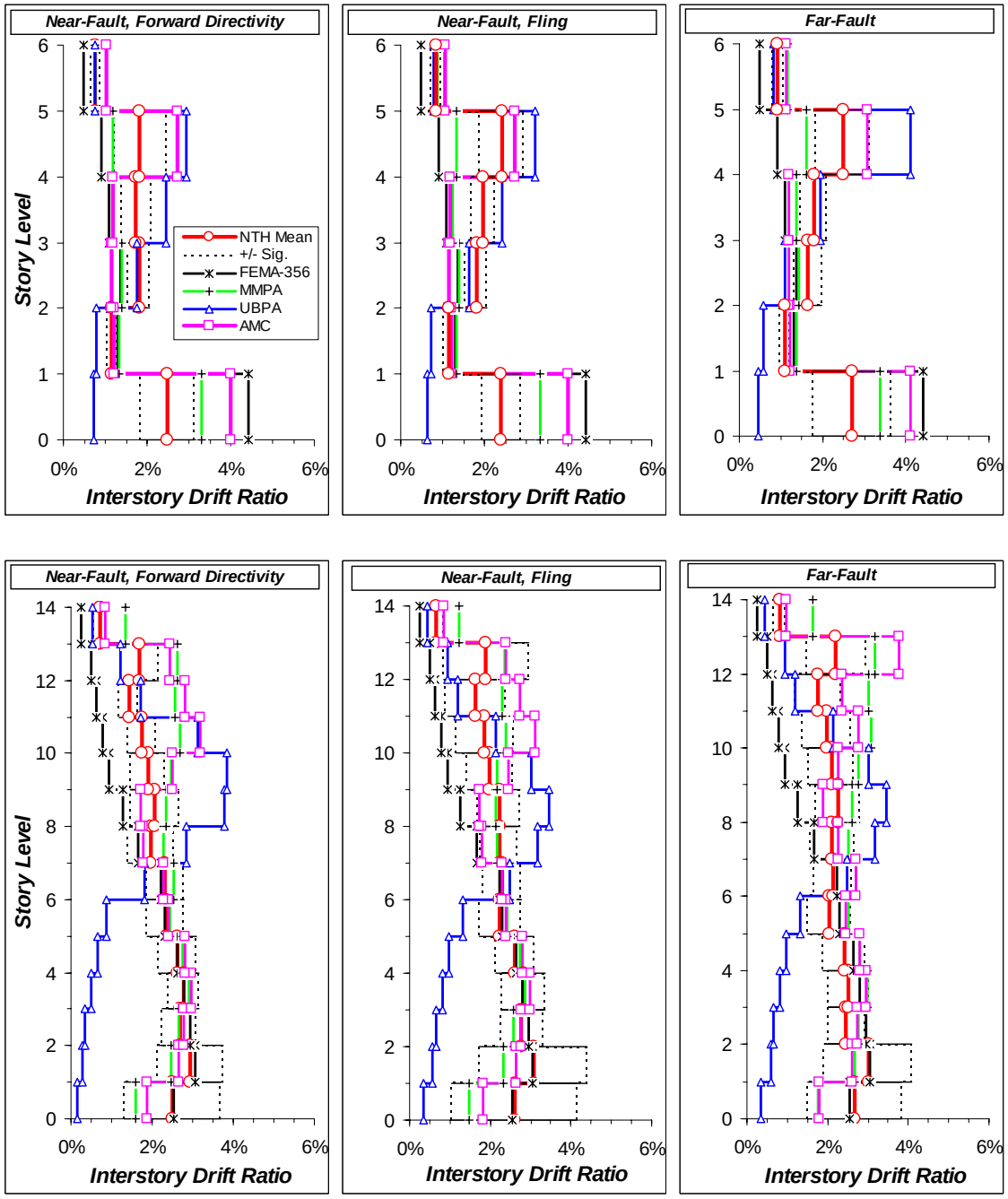

Figure 7.6 Predicted peak interstory drift demands by NSPs compared to NTH analyses for steel buildings

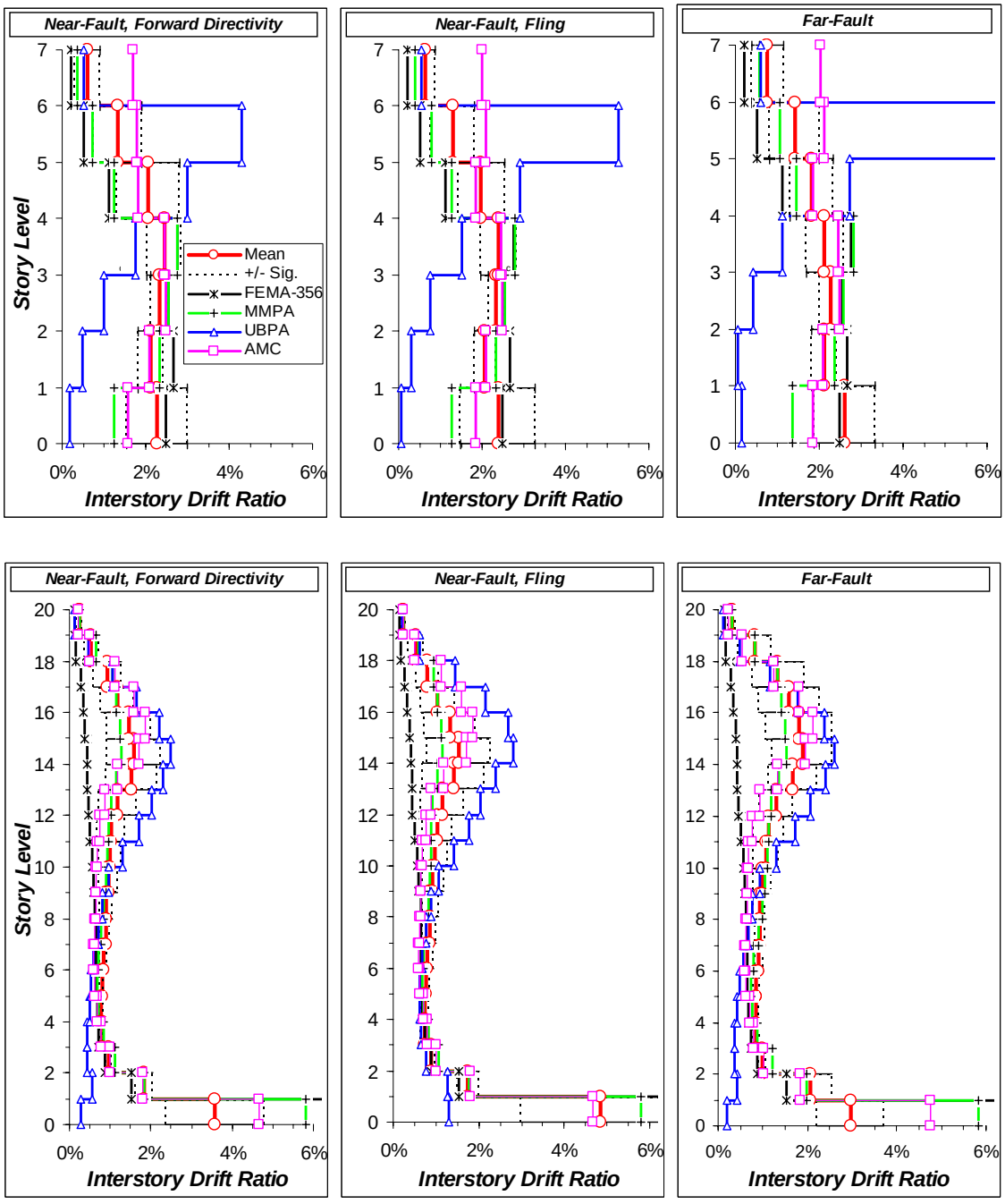

Figure 7.7 Predicted peak interstory drift demands by NSPs compared to NTH analyses for RC buildings

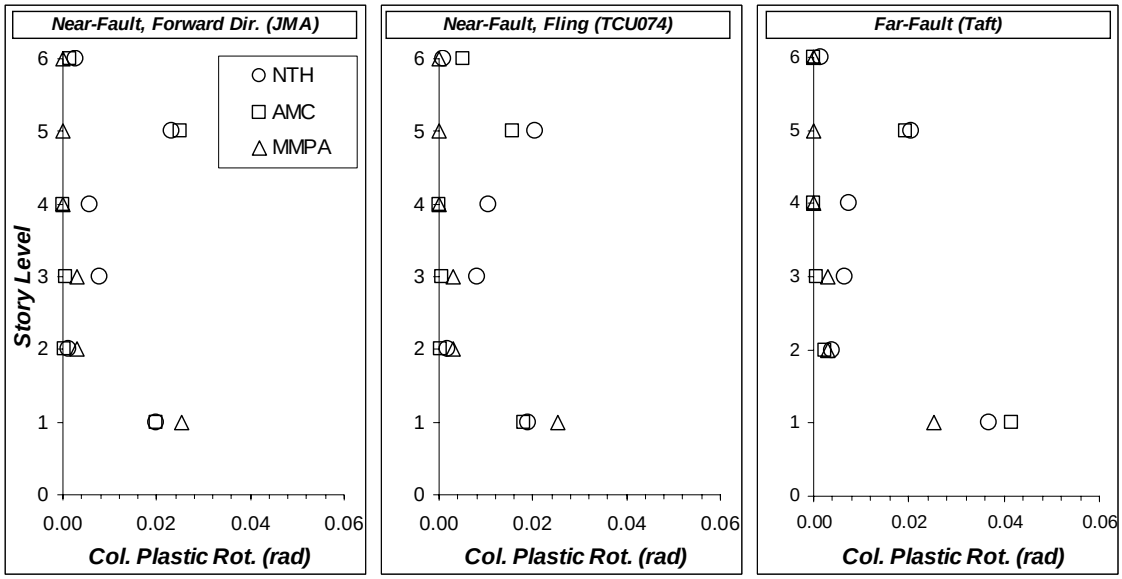

Figure 7.8 Predicted maximum column plastic rotations by AMC and MMPA compared to NTH analyses for 6-story steel building subjected to (scaled) JMA, TCU074 and Taft records

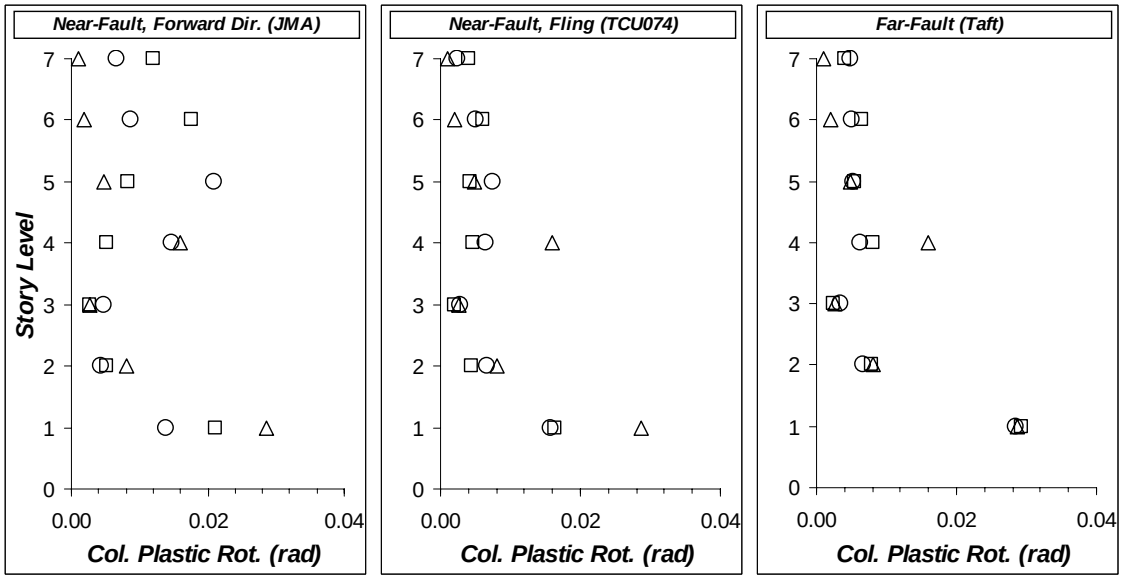

Figure 7.9 Predicted maximum column plastic rotations by AMC and MMPA compared to NTH analyses for 7-story RC building subjected to (scaled) JMA, TCU074 and Taft records

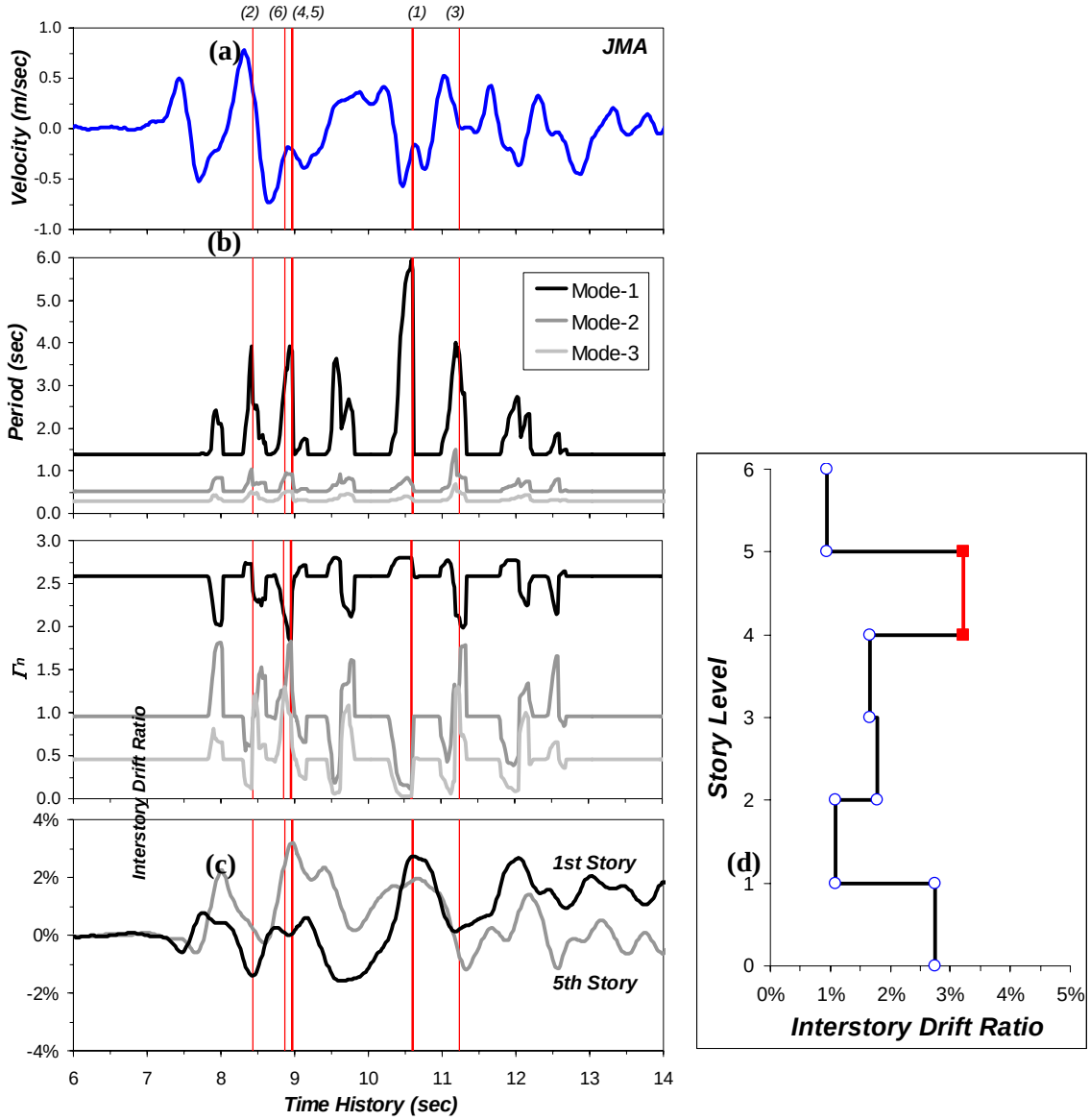

Figure 7.10 (a) Velocity time series of JMA motion; (b) variation of 6-story building modal periods and n^{th}-mode participation factor (Γ_n); (c) interstory drift history; (d) peak interstory drift profile (*Note that number in parenthesis at the top indicates the specific story that has the peak interstory drift at the time instant indicated by vertical line)*

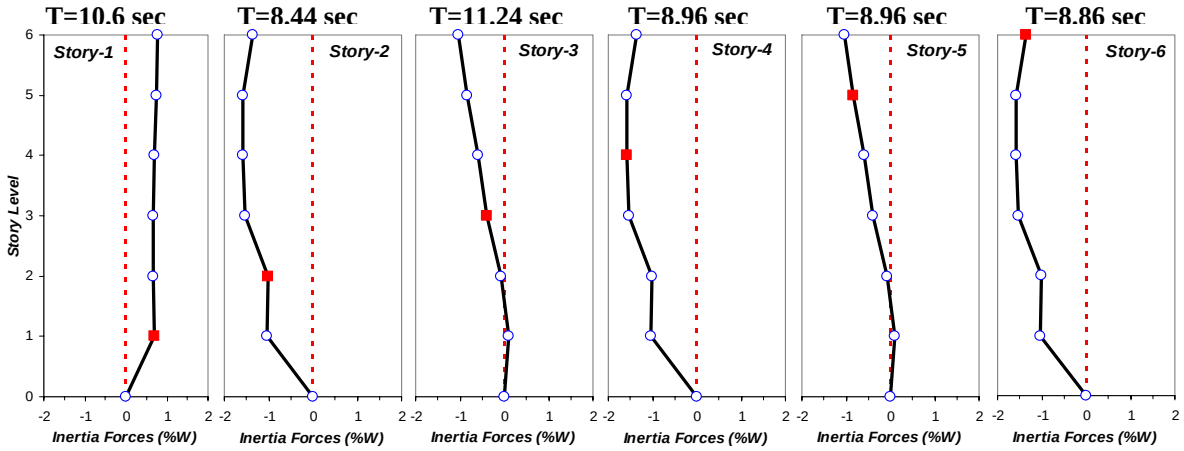

Figure 7.11 Instantaneous inertia profiles when the story maxima take place (6-story building subjected to JMA motion, 'T' indicates the time-instance in the time-history, filled square marker indicates the critical story at the specific time instant, T)

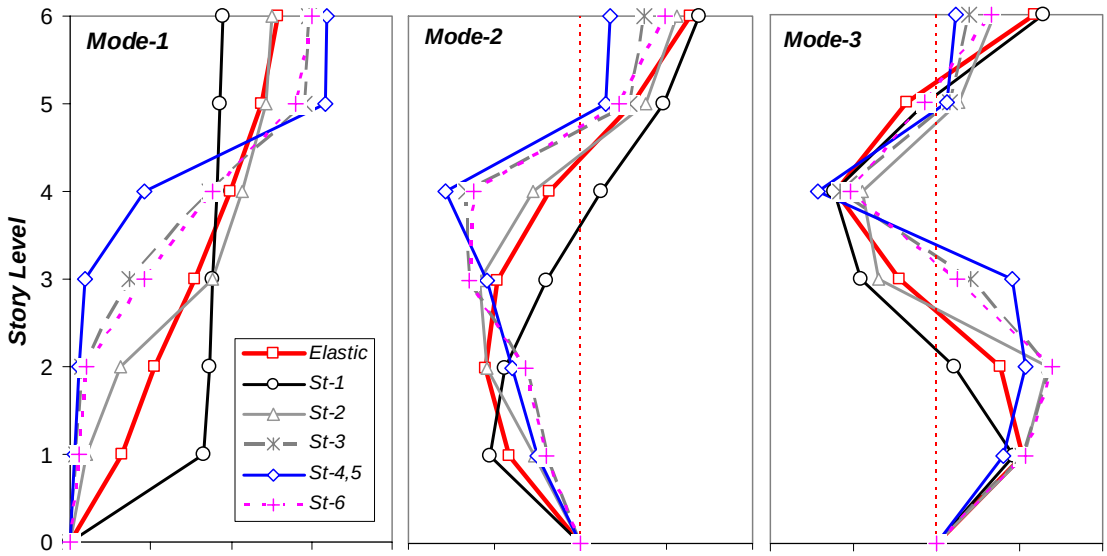

Figure 7.12 Instantaneous modal shapes at the time-instances when the story maxima take place (*6-story building subjected to JMA motion; 'St' in legend indicates story level*)

CHAPTER 8

EVALUATION OF ADAPTIVE MODAL COMBINATION PROCEDURE FOR VERTICALLY IRREGULAR STRUCTURAL SYSTEMS

8.1 INTRODUCTION

Since 1988 Uniform Building Code, earthquake design codes in U.S. have started to demarcate vertically irregular structures from regular ones based on certain limits on the ratio of strength, stiffness, mass, setbacks or offsets of one story to the corresponding value in an adjacent story. These limits are based on conducted analytical (e.g., Humar and Wright 1977; Costa et al. 1988; Estava 1992; Valmundsson and Nau 1997) and experimental (e.g., Moehle 1984; Wood 1992) studies which clearly elucidate significantly altered drift and ductility demands in the vicinity of irregularities. Recent parametric studies employed by Al-Ali and Krawinkler (1998) on two-dimensional (2D) generic frames, and by Das and Nau (2003) on code designed 2D special-moment-resisting-frames (SMRFs) further illuminate the influences of variation of vertical irregularity along the height on respective seismic performance of buildings when subjected to different types of ground motions. In recognition of diverse dynamic characteristics and behavior of vertically irregular structures compared to their regular counterparts, code recommends using dynamic analysis methods (i.e., modal analyses or

time-history analysis) to compute design forces in lieu of equivalent lateral force (ELF) procedure which is essentially applicable only for regular structures with uniform distributions of mass, stiffness and strength over the height.

Not only design issue of vertically irregular buildings, their seismic assessments also requires special attention. For regular low-rise buildings (representing first mode response), it is well documented that nonlinear static procedures recommended in FEMA-356, now standard in engineering practice in U.S., yield reasonable approximation of critical seismic demand descriptors (such as interstory drift). However, for irregular structures, Chopra and Chintanapakdee (2004) has recently demonstrated that FEMA invariant load distributions (i.e., 1st Mode, ELF, SRSS and uniform) are systematically biased in predicting story drifts when compared "exact" NTH analyses results. In their study, Chopra and Chintanapakdee considered three types of irregularity as stiffness, strength and stiffness-strength in 24 irregular generic frames having different heights.

Owing to fact that nonlinear static pushover analysis is now commonly accepted as a simpler alternative towards evolving performance based methodologies, the applicability and accuracy of developed Adaptive Modal Combination (AMC) procedure are examined for a wide range of vertically irregular SMRFs. The SMRFs used in this study includes 5, 10 and 15 stories, and represent two types of vertical irregularities, mass irregularity and vertical geometric irregularity (i.e., setback),. The building models are designed in compliance with IBC (ICBO 2000) code requirements. A total of 10 different building models are used to study the effects of changing location of irregularity along the height on salient response characteristics of buildings. Each building model is subjected to a set of 10 near-fault forward directivity ground motions for objective of computing mean and

dispersion values of interstory drift values which are used as benchmark responses to test the AMC procedure.

8.2 DESCRIPTION OF BUILDINGS AND ANALYTICAL MODELS

The primary lateral load resisting system for the buildings considered in this study are steel moment frames. Generic SMRFs with heights corresponding to 5, 10 and 10 stories and each having four bays with a bay size of 5.5 m are analyzed. Except for the first floor which is 5.5 m high, the remaining floors of each frame have a height of 3.0 m. The following two types of vertical irregularities, as specified in IBC, comprise the primary variables evaluated herein.

- Mass Irregularity: is considered to exist if the effective mass of any story is more than 150 percent of an adjacent story. A roof that is lighter than the floor below is excluded from this consideration.
- Vertical Geometric Irregularity (Setback): is considered to exist where the horizontal dimension of the lateral-force-resisting system in any story is more than 130 percent of that in an adjacent story.

In order to create a system which meets the first criterion, the first and fifth story mass values were doubled respectively to generate two cases of mass irregularity for the 5-story building. In a similar fashion, the first, fifth and tenth story mass values were doubled respectively to generate 3 cases for the 10-story building. In the case of the 15-story building, mass values were magnified by a factor of 2.0 at the first, seventh and fifteenth story levels. In order to create vertical geometric irregularity, setbacks at the

second and fifth story levels were introduced in the 10-story building models. As a result, a total of 10 vertically irregular frame models (i.e., 8 with mass irregularity and 2 with vertical setbacks) were generated. Figure 8.1 displays the different configurations considered in the study.

All frames were designed in a region of high seismicity with soil-type “D” and located about 5 km from causative fault (see Figure 8.2 for the respective IBC spectrum, and corresponding design coefficients to compute the base shear). The designs satisfy the strong column-weak beam requirement of the code and the size and shape of beams and columns were chosen to satisfy code drift limitations.

All frame structures were modeled as two-dimensional systems using the open source finite element platform, OpenSees (2005). Beam and columns were modeled as nonlinear elements with section properties specified using a fiber discretization at five integration points along the member length. A non-degrading bilinear material model with yield strength of 50 ksi and 2 percent strain hardening was assumed for all structural elements. Raleigh damping was assumed at 5 percent of critical for the first and third modes for the 5-story frame, and for the first and fourth modes for the remaining frames.

8.3 GROUND MOTION DATA

Each structural model was subjected to a set of ten near-fault forward directivity motions. Ground motions from recent major Californian earthquakes were carefully compiled so that the mean acceleration spectrum of the selected records matches the IBC design spectrum across a wide range of spectral periods. In addition, each individual record satisfies the soil and distance constraints of the design spectrum. Records were therefore

used in their original form without scaling. Relevant information on the selected ground motions is listed in Table 8.1, while the acceleration spectra, the mean spectrum of all records together with the IBC design spectrum are shown in Figure 8.2.

8.4 VALIDATION OF AMC PROCEDURE FOR IRREGULAR FRAMES

The validation process consists of comparing the peak interstory drift demands predicted by AMC procedure with those computed from nonlinear time-history analyses. The AMC procedure was applied to each of the 10 SMRF models for each of the 10 ground motions separately. This means that inelastic acceleration and displacement spectra for each record are computed and utilized in individual pushover analysis. Figure 8.3 presents the mean, 16 and 84 percentile response data of peak interstory drift profiles for the 5, 10 and 15-story frames with mass irregularities subjected to near-fault records. Also shown in the figure are response estimates computed using the proposed AMC procedure. In all cases, it is seen that the AMC procedure approximates the mean drift demands over the height of the frames with dispersion comparable to NTH analyses.

Figure 8.4 compares the drift demands computed using NTH analyses with those predicted by the AMC procedure for 10-story frames having two types of setbacks. In case of setback at the second story, the AMC procedure yields almost identical drift profiles as those from NTH simulations. For the frame with the setback at fifth story, the AMC procedure overestimates the lower level drift values up to third story; however the drift profile above this level compare very favorably with NTH estimates. The dispersion

in the demand estimates (indicated by the 16 and 84 percentile values) are comparable to NTH analyses.

In the results summarized in Figures 8.3 and 8.4, the AMC procedure was applied to each frame model considering each excitation separately. Hence inelastic spectra were generated for each record and as many simulations as NTH analyses were carried out. To investigate a more practical application, the AMC procedure was applied to the structural models by considering only a single spectrum: in this case, the mean inelastic spectra of ground motions computed at pre-defined ductility levels were utilized. Figure 8.5 compares the difference in the predictions of these two approaches compared to NTH analyses for the 15-story frame having mass irregularity at the seventh story, and the 10-story frame with setback at the second story. Prediction errors were computed by considering the difference in inter-story drift ratios (IDR) between AMC estimates and the mean of NTH analyses. Figure 8.5 shows, as expected, that using inelastic spectra of individual records yield better estimates (as indicated by lower dispersion) than using a mean spectrum. However, with the objective of minimizing computational effort, the use of mean inelastic spectra of a set of records is still satisfactory and is able to predict demands without appreciable loss of accuracy compared to NTH analyses.

Results of the study indicate that increased mass at the upper story levels exacerbates the contribution of higher modes and results in migration of demands from lower stories to upper levels. Similar effects are also observed for setback buildings, wherein the setback at the fifth story results in increased drift demands concentrated at the sixth story where a sudden change in stiffness is located. Increasing the mass at the first story level

for the 5, 10 and 15-story buildings does not produce appreciably larger drift at or adjacent to this story level.

It should also be noted that lateral inter-story drifts are limited to 2 percent in the design of frames. Despite the fact that all records are consistent with the design spectrum in terms of soil type and fault distance parameters, many individual near-fault excitations produced demands in excess of this limit at several story levels. This raises the question on the effectiveness of the near-source amplification factors (i.e., N_a and N_v) to account for the impulsive effect of near-fault ground motions. Since these factors which are used to amplify the elastic design spectrum were originally developed using far-fault ground motions, a reexamination of these amplification factors is needed.

8.5 CONCLUSIONS

The accuracy of the AMC procedure in predicting seismic response of the vertically irregular (i.e., mass irregular or setback) SMRFs using a set of forward directivity records is examined. By including the contributions of a sufficient number of modes of vibration (generally two to three), the interstory drift profiles estimated by AMC is generally similar to the "exact" results from results of NTH analyses. Therefore for the vertically irregular frames evaluated in this study, the AMC procedure has also been shown to be a significant improvement over the pushover analysis procedures currently used in structural engineering practice. The AMC method is shown to not only provide better estimates of inelastic response parameters but also eliminates the need to pre-determine the target displacement computation through utilizing energy based modal capacity curves in conjunction with inelastic spectra.

The use of inelastic spectra of individual records in the AMC procedure produces the best estimates compared to exact NTH analyses results, however to minimize computational effort, mean inelastic spectra of records were shown to be reasonably effective and thereby offers a simple and direct approach without appreciably sacrificing the accuracy of the procedure.

Table 8.1 Ground motion dataset

No	Year	Earthquake	M_W	Mech.[1]	Recording Station	Dist.[2] (km)	Data Source[3]	Comp.	PGA (g)	PGV (cm/sec)
1	1989	Loma Prieta	7.0	OB	Capitola	8.6	1	000	0.53	35.0
2	1994	Northridge	6.7	TH	Rinaldi Rec. Stn.	8.6	2	S49W	0.84	174.8
3	1994	Northridge	6.7	TH	Jensen Filt. Plant	6.2	1	022	0.42	106.3
4	1994	Northridge	6.7	TH	Slymar Converter Sta East	6.1	1	018	0.83	117.5
5	1994	Northridge	6.7	TH	Slymar Converter Sta.	6.2	1	142	0.90	102.2
6	1994	Northridge	6.7	TH	Sepulveda Va. Hospital	9.5	1	270	0.75	85.3
7	1994	Northridge	6.7	TH	Sylmar Olive View Hospital	6.4	1	360	0.84	130.4
8	1994	Northridge	6.7	TH	Newhall LA Fire Stn.	7.1	1	360	0.59	96.4
9	1994	Northridge	6.7	TH	Newhall Pico Canyon	7.1	1	046	0.45	92.8
10	2004	Parkfield	6.0	SS	Fault Zone 1	5.0	2	360	0.82	81.2

[1] *Faulting Mechanism = TH: Thrust; SS: Strike-slip; OB: Oblique;*

[2] *Closest distance to fault*

[3] *Data Source = 1: PEER (http://peer.berkeley.edu/smcat); 2: Cosmos (http://db.cosmos-eq.org)*

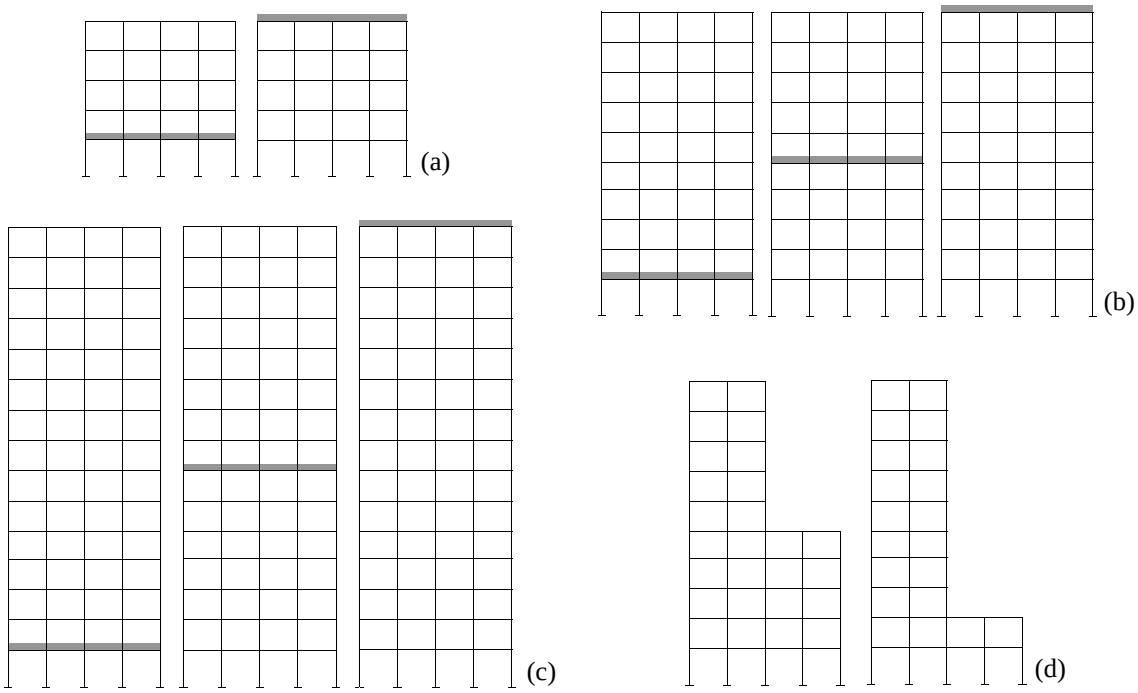

Figure 8.1 Geometric representation of mass irregular (a) 5-story, (b) 10-story, (c) 15-story SMRFs (thick shaded floors represent the location of mass irregularities) and (d-e) 10-story setback buildings.

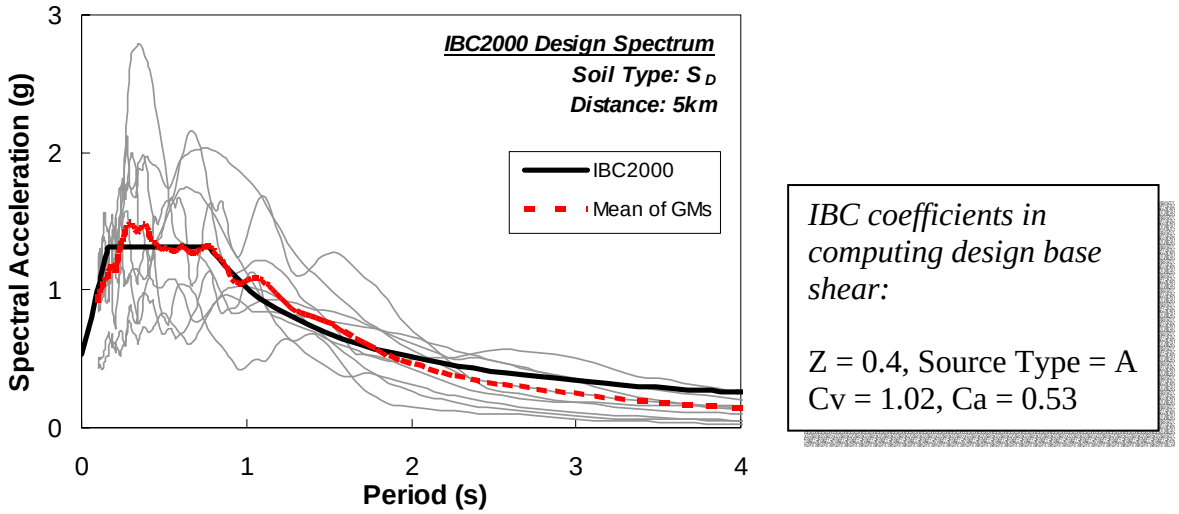

Figure 8.2 IBC (ICBO 2000) design spectrum together with pseudo-spectral acceleration spectra of near-fault forward directivity records (Left), and IBC coefficients in computing design base shear (Right).

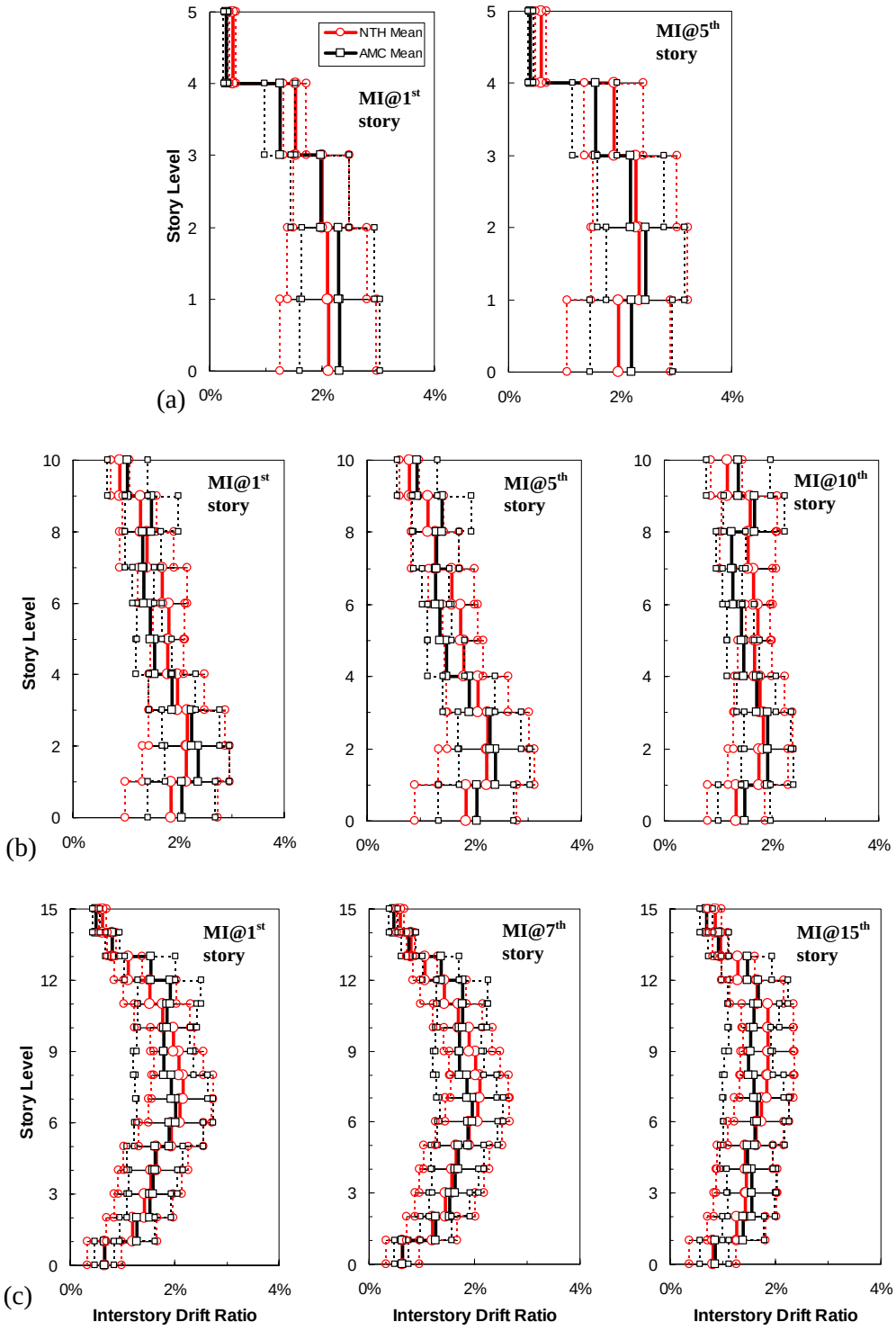

Figure 8.3 Estimated peak interstory drift profiles by AMC for (a) 5-story, (b) 10-story and (c) 15-story building with mass irregularity (MI) at various story levels.

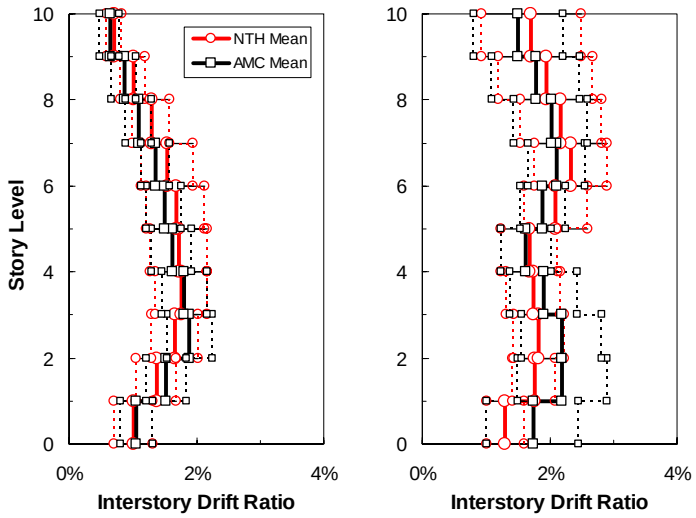

Figure 8.4 Estimated peak interstory drift profiles by AMC compared to NTH analyses results for 10-story building having setback at second story level (Left) and fifth story level (Right).

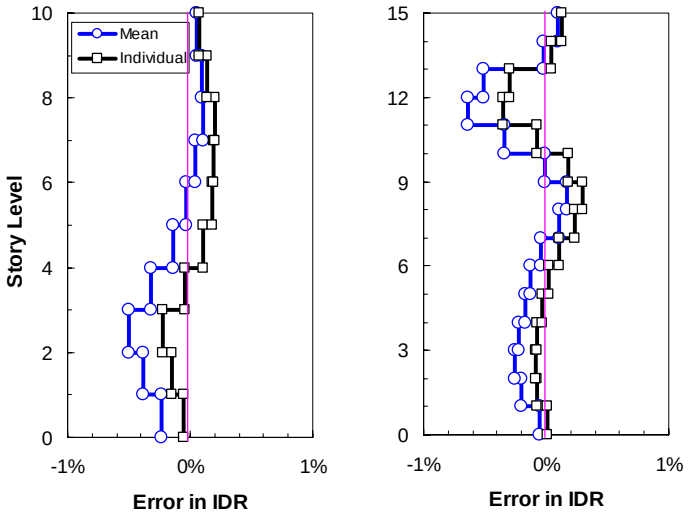

Figure 8.5 Comparison of interstory drift (IDR) estimation errors by (approach-1) utilizing "individual" spectrum for each record and (approach-2) utilizing "mean" spectra of records in AMC procedure *(Results are based on 10-story building having setback at second story level (Left) and 15-story building having mass irregularity at seventh story level (Right)).*

CHAPTER 9

CONCLUSIONS

9.1 IMPORTANT FINDINGS

The primary objectives of the investigations reported in this dissertation were to augment our understanding of the characteristics of near-fault ground motions; the nature and magnitude of seismic demands imposed by these records on structural systems; and enable the prediction of these demands through advanced nonlinear static procedures. The primary findings of this dissertation are presented in the following subsections.

9.1.1 Prediction of Seismic Demands using FEMA-356 NSPs

The validity of nonlinear static approaches introduced in FEMA-356 to estimate local demands and the correlations between component, story and global demands were critically examined. The focus of the study was not directly related to the assessment of design requirements rather it comprised an assessment of evaluation methods used to estimate seismic demands that play a major role in the design process. Findings from this investigation have led the following conclusions:

1. No consistent correlation has been found between demand estimates at the local, story and global level for the intensity level considered. The evaluations presented

were based on seismic events with a 2% probability of being exceeded in 50 years. The demands at lower intensity levels could present a different picture considering the lower demands, hence similar evaluations for different intensity levels are needed to make generalized conclusions.

2. Designing a building to achieve a certain ductility demand can result in much larger demands at the local level. Caution must be exercised when using nonlinear static procedures since the lateral load pattern used to estimate demands can have a significant influence on the computed demands. When compared to nonlinear time history estimates, pushover methods tend to underestimate demands at the upper levels signifying the relevance of high mode participation in mid to high rise structures.
3. Nonlinear response measures, using either static or dynamic analyses, are sensitive to modeling parameters such as the definition of effective stiffness, yield rotation, plastic hinge length, etc. and must be evaluated separately prior to utilizing the results of nonlinear evaluations in performance assessment.

9.1.2 Near-Fault Directivity Effects on Seismic Demands

Investigations on existing steel moment frame buildings subjected to near-fault impulsive and ordinary far-fault records provided new insight and additional data on the inelastic demands imposed by ground motions having different characteristics. Based on the extensive analytical simulations carried out, the following findings are deduced:

1. Typical steel moment frames can be subjected to large displacement demands at the arrival of the velocity pulse that require the structure to dissipate considerable

input energy in a single or relatively few plastic cycles. This demand will impact structures with limited ductility capacity.

2. Far fault motions build input energy more gradually and though the displacement demands are on average lower than the demands in near-fault records, the structural system is subjected to significantly more plastic cycles. Hence cumulative effects are more pronounced in far-fault ground motions.
3. Studies with simple pulses clearly demonstrated the migration of demands from lower to upper stories when the ratio of the pulse period to building period was below 0.8. Records with forward directivity resulted in more instances of higher mode demand while records with fling displacement almost always caused the systems to respond primarily in the fundamental mode. For all the near-fault pulses investigated in this study, the severity of the demands is controlled by the ratio of the pulse to system period.
4. Near-fault records with fling can be more damaging than far-fault records but they tend to accentuate first mode behavior.
5. A careful examination of acceleration and velocity spectra, collectively, can provide engineers with a reasonable assessment of the damage potential of near-fault records. Demands in the fundamental and higher modes must be evaluated by taking into consideration the fact that modal periods shift to the right of the spectrum as the system moves from the elastic to inelastic state.

9.1.3 Energy Contents in Near-Fault Earthquake Recordings

Fundamental precepts of two commonly used energy definitions (i.e., absolute and relative) using SDOF and MDOF systems subjected to far-fault and near-fault ground motions were examined. The main findings of this investigation can be summarized as follows:

1. For far-fault records, energy accumulates monotonically with time throughout the entire recording duration, and two energy definitions yield comparable results. As opposing, difference between relative and absolute energy can be considerable for near-fault records. The energy difference is a direct consequence of intense velocity pulses contained in near-fault records, and conditioned on the three parameters (i) the way of velocity pulse origination (ii) pulse period and (iii) pulse shape. Velocity pulse is originated either as a result of succession of high frequency single sided acceleration peaks (resembling the ordinary far-fault records) or the integral of apparent acceleration pulses. For the records without apparent acceleration pulses, both energy definitions yield comparable results. In contrast, apparent acceleration pulses have a significant impact on the imparted absolute or relative energy to structures. The record containing such acceleration pulses produces abrupt energy spike in the early phase of response being significantly larger than the energy accumulated at the termination of ground movement. Whether this instantaneous energy demand is generated by absolute or relative energy definitions depends on the period of dominant velocity pulse. According to simple pulse models studied, peak relative energy becomes larger than peak absolute energy approximately for periods larger than $2Tp$ for forward

directivity and 3*Tp* for fling. Both energy definitions are agree in the period range of *Tp* to 2*Tp* for forward directivity and *Tp* to 3*Tp* for fling records.

2. Near-fault ground motions with apparent acceleration pulses consistently exhibit large V/A ratio (i.e., average duration of dominant acceleration pulse), a parameter, which can be used to identify the impulsive character of the accelerograms. For a limited data studied, rather than strong motion duration, V/A ratio is shown to better correlate with the amplification factor (Ψ) which is the ratio of PGV to peak energy equivalent velocity.
3. For near-fault records characterized by apparent acceleration pulses, the differences in the time histories of absolute and relative energy definitions manifest itself as sudden intensive energy spikes in early phase of response. These energy spikes are originated from kinetic energy due to ground velocity and work done by ground acceleration on respective incremental system displacement. The amplitudes of energy spikes become minimal for the system whose fundamental period is close to the dominant pulse period.
4. Near-source ground motions should be characterized according to the existence of apparent acceleration pulses and directivity effects when establishing the energy dissipation capacity of structural components. For records associated with apparent acceleration pulses, whether the absolute or relative energy definition produces the peak input energy depends on the dominant velocity pulse period and system fundamental period.

9.1.4 Correlation of Seismic Input Energy with Maximum System Deformation

Based on comprehensive numerical evaluations of inelastic SDOF systems subjected to an ensemble of near-fault ground motions, maximum system displacement was correlated to the effective cyclic energy (ECE). Its non-dimensional variance γ_{eff} was proposed to represent the severity of ground motions. A set of realistic MDOF systems were examined to interrelate the ECE to interstory drift demands and generalize the findings from SDOF systems. The assessment on SDOF and MDOF systems has led to the following conclusions:

1. The energy demand on a structural system subjected to a far-fault motion tends to gradually increase over a longer duration causing an incremental buildup of input energy, thereby for far-fault earthquakes the cumulative damage effects and consequently low-cycle fatigue become more prominent and duration dependent, whereas in near-fault ground motions the maximum response concentrates in the first yielding cycle accompanied with instantaneous and high energy demand. Rather than accumulated input energy, which can be a good indicator to reflect the severity of ground motion for ordinary far-fault records, instantaneous energy-based parameters (i.e., ECE and γ_{eff}) have shown to be more appropriate to represent the damaging effect of impulsive near-fault ground motions.
2. ECE spectrum was introduced for objective of providing enhanced representation of inelastic response of MDOF systems in SDOF energy domain. Inherently, ECE is not only a unique quantity of an earthquake ground motion but also influenced

by the system response as such its peak amplitude changes with spectral system period ductility, and therefore it can be effectively used in a spectral format.

3. The development of ECE spectra is shown to be more appropriate than conventional acceleration spectra to assess deformation demands in structures. Besides, it can be effectively utilized for selection and scaling of ground motions for dynamic analysis, and as a substitute of demand spectrum in conventional performance assessment studies.
4. A proposed procedure utilizing the modal-energy-decomposition through elastic ECE spectrum is shown to be effective in predicting the ECE demand of MDOF system. Thereby “modal-target-energy” demands are computed to be used directly in performance evaluations without performing NTH analysis. The features of ECE presented in this study indicate that it can be a valuable tool in developing energy-based guidelines for performance assessment of building structures.

9.1.5 Development and Verification of AMC Procedure

A new pushover methodology utilizing adaptive multi-modal displacement patterns and retaining the advantages of both adaptive and modal pushover procedures was introduced and verified using two existing moment frame steel buildings. The major attributes of the procedure and key findings of the validation study can be summarized as follows:

1. The AMC procedure eliminates the need to pre-estimate the target displacement and utilizes an energy-based scheme to achieve stable estimates of the seismic demand in conjunction with constant-ductility inelastic spectra. It was shown to

provide reasonable estimates of seismic demand in typical moment frame structures for both far-fault and near-fault records.

2. The proposed procedure is by no means more difficult to implement than any other enhanced pushover procedure, and requires primarily an eigenvalue solver that can be invoked when necessary during the progressive modal pushover analysis and a internal or external module to generate constant-ductility spectra. The procedure is currently evaluated for earthquake hazards defined by a set of individual ground motions. However, the procedure is even more suitable for use with a target design spectrum and existing R-μ-T relations. Since the method builds on existing procedures and incorporates concepts in CSM and inelastic spectra that are already familiar to structural earthquake engineers, it attempts to provide a methodology that provides a physical basis for understanding the sensitivity of structural response to structural and ground motion characteristics.

9.1.6 Validation of the AMC Procedure and Comparison with other Nonlinear Static Procedures

The ability of four different nonlinear static procedures to predict seismic demands were examined comparatively using a set of instrumented moment frame buildings. Each building was subjected to 30 ground motions having different characteristics. The resultant mean and standard deviations of NTH analyses served as benchmark responses against which the NSPs were compared. A systematic evaluation of the predicted demands (such as peak displacement profile, interstory drifts and member plastic rotations) by the different NSPs forms the basis for the following conclusions:

1. The FEMA-356 method (wherein the envelope of two response measures were considered) provides inadequate predictions of peak interstory drift and peak member plastic rotations at the upper story levels when higher mode contribution are significant.
2. UBPA estimates were the poorest by far, being unable to reasonably predict even the peak displacement profile. It led to significant underestimation of story drift demands and member rotations at the lower levels and to their overestimation at the upper stories.
3. Compared to FEMA-356 and UBPA procedures, MMPA provides story drift estimates that are generally much closer to the mean NTH estimates. However, since the method ignores the inelastic contribution of higher modes, it is unable to reasonably predict plastic rotation demands in the upper stories.
4. It was also shown that NSPs based on invariant load vectors using elastic modal properties cannot capture the changes to the dynamic modes resulting from inelastic action. The inertia load distribution, which is well correlated to story deformations, progressively changes following the variation of the modal periods and modal shapes during inelastic response. Consequently, the variation of inertial forces must be considered in static procedures that attempt to reproduce inelastic dynamic response. This can only be achieved using adaptive load vectors.
5. The AMC procedure provided the best overall comparison with NTH results. In general, the method was able to reproduce the essential response features providing a reasonable measure of the likely contribution of higher modes in all phases of the response.

9.1.7 Evaluation of AMC Procedure for Vertically Irregular Buildings

The accuracy of the AMC procedure in predicting seismic response of vertically irregular (i.e., mass irregular or setback) buildings were evaluated using a set of near-fault forward directivity records. This validation study led to following conclusions:

1. By including the contributions of a sufficient number of modes of vibration (generally two to three), the interstory drift profiles estimated for vertically irregular buildings by AMC is generally similar to the "exact" results from results of NTH analyses.
2. For mass irregular buildings, increased mass at the upper story levels has the tendency to exacerbate the contribution of higher modes and results in migration of enhanced demands from lower stories to upper levels. Similar effects are also observed for setback buildings. As such, the setback at the mid-story level results in enhanced drift demands concentrated at the story after setback where sudden change in stiffness is located.
3. For objective of providing response statistics, use of inelastic spectra of individual record in the AMC procedure produces the best estimates compared to exact NTH analyses results, however to minimize the computational effort, mean inelastic spectra of records were shown to be effectively utilized as a direct approach without appreciably sacrificing from the accuracy.

9.2 DIRECTIONS FOR FUTURE RESEARCH

While significant advances were made in gaining a better understanding of ground motions and their effects on building structures during the course of this study, several unresolved issues still remain. These concerns are listed below and should be investigated in future research studies:

1. In this study, relatively stable hysteretic behavior was assumed in the nonlinear simulations. For steel buildings, the force-deformation response was assumed to be bilinear while moderate degrading behavior was assumed for RC structures. Incorporating degrading effects such as weld fracture in steel, severe degradation (due to shear and other brittle failure modes), and softening behavior will shed light on additional critical issues in seismic performance of existing structures.
2. Selecting ground motions that are compatible with site-specific hazards is an essential initial step in performance-based seismic evaluation. Currently, there are many methods proposed for scaling of ground motion time series so as to reduce the dispersion in response parameters such as roof drift ratio, interstory drift ratio etc. Though scaling to the same PGA or scaling to the same spectral acceleration at the first or other elastic modal periods (spectral matching is another technique recommended by some seismologists) are the most common methods used in practice, selection of records and the choice of a scaling method remain controversial. Therefore, factors such as ground motion characteristics, its frequency content and damage potential should be considered when selecting or scaling records. In this study, γ_{eff} and the ECE spectrum have been shown to be

well correlated to the maximum deformation generated by near-fault accelerograms, hence they may serve as measures for ground motion scaling methodologies.

3. The AMC procedure was evaluated for earthquake hazards defined by a set of individual ground motions or the use of mean inelastic spectra. However, the procedure is also suitable for use with a target design spectrum and existing R-μ-T relations. The application of general hazard spectra based on existing R-μ-T relations in the AMC procedure has not been investigated and is in need of further studies.
4. The accuracy of the AMC procedure to predict the demands of irregular plan buildings considering three-dimensional effects and also shear-wall buildings has not been studied. Particular attention needs to be devoted to torsion-flexible systems needs, since there is no established procedure for three-dimensional pushover analyses of buildings.
5. In current NSP procedures, roof displacement is used as a controlling deformation index to convert the MDOF capacity curve to the ESDOF system capacity spectrum. This approach has major drawbacks: (i) the roof displacement is proportional to the remaining story displacements only for the first-mode; (ii) the roof displacement may reverse direction after initiation of yielding during a higher-mode pushover analysis (Hermandez-Montes et al. 2004). Therefore, inconsistencies in higher mode ESDOF representations of MDOF system may occur when the roof displacement is used as the target parameter. In the modified modal pushover analysis (MMPA) of Chopra et al. [10], these issues are

eliminated since only the elastic contributions of higher-modes are directly used in modal combination (SRSS or CQC). However, ignoring the inelastic contribution of higher modes results in poor estimates of plastic hinge rotations and interstory drift demands in MDOF systems. The AMC procedure provides an improvement over this drawback by using energy principles in converting the ESDOF response to MDOF systems. For the next-generation simplified pushover procedures, consistency in SDOF representation of MDOF systems can be achieved by expressing seismic demand and capacity in terms of energy measures. In this case, the concept of “target energy” may emerge as a new parameter replacing the concept of “target displacement”.

BIBLIOGRAPHY

Abrahamson, N. (2001). “Incorporating effects of near fault tectonic deformation into design ground motions.” A presentation sponsored by the Earthquake Engineering Research Institute Visiting Professional Program, hosted by the State University of New York at Buffalo, 26 Oct. 2001.

Akkar, S., Yazgan, U., and Gulkan, P. (2004). “Deformation limits for simple non-degreading systems subjected to near-fault ground motions.” P*roc. of the 13th World Conf. on Eq. Eng*., Paper No.2276.

Al-Ali, A., and H., Krawinkler, (1998). *Effects of vertical irregularities on seismic behavior of building structures*, John A. Blume Earthquake Engineering Center.

Alavi, B., and Krawinkler, H. (2003). “Behavior of moment resisting frame structures subjected to near-fault ground motions.” *Earthquake Engineering and Structural Dynamics*, 33, 687-706.

Amiri, G. G., and Dana, F. M. (2005). “Introduction of the most suitable parameter for selection of critical earthquake.”, *Computers & Structures*, 83(8-9), 613-26.

Antonio, S., Rovithakis, A., and Pinho, R. (2002). “Development and verification of a fully adaptive pushover procedure.” *Proc. of the 12th European Conference on Earthquake Engineering*, Paper No. 822.

Antonio, S., and Pinho, R. (2004). “Development and verification of a displacement-based adaptive pushover procedure.” *Journal of Earthquake Engineering*, 8(5), 643-661.

Applied Technology Council (ATC) (1996). *Seismic Evaluation and Retrofit of Concrete Buildings*, Volumes 1 and 2, Report No. ATC-40, Redwood City, CA.

American Society of Civil Engineers (2000). *Prestandard and commentary for the seismic rehabilitation of buildings*. FEMA-356. Washington D.C.

Aydinoglu, M. N. (2004). “An incremental response spectrum analysis based on inelastic spectral displacement for multi-mode seismic performance evaluation.” *Bulletin of Earthquake Engineering*, 1(1), 3-36.

Berg, G. V., and Thomaides, S. S. (1960). “Energy consumption by structures in strong-motion earthquakes.” *Proc. of the 2nd World Conf. on Earthquake Eng*. Tokyo, Japan, 681-696.

Bertero, V. V. (1976). “Establishment of design earthquakes—Evaluation of present methods.” *Proc., Int. Symp. on Earthquake Structural Engineering*, St. Louis, 1, 551–580.

Bonelli, P. C. (1998). “Long seismic velocity pulses effect and damage.” *Proc., Structural Engineering World Congress (SEWC'98)*, San Francisco.

Boore, D. (2001). “Effect of baseline correction on displacements and response spectra for several recordings of the 1999 Chi-Chi, Taiwan, earthquake.” *Bull. Seismol. Soc. of Am.*, 91 (5), 1199-1211.

Boore, D., Stephens, C. D., and Joyner, W. B. (2002). “Comments on baseline correction of digital strong motion data: examples from the 1999 Hector Mine California earthquake”, *Bull. Seismol. Soc. of Am.* 92 (4), 1543-1560.

CEN (2001). *Eurocode 8 – Design of Structures for Earthquake Resistance.* Part -1, European Standard prEN 1998-1, Draft No. 4. Brussels: European Committee for Standardization, Dec.

Chai, R. Y. H., and Fajfar, P. (2000). “A procedure for estimating input energy spectra for seismic design.” *Journal of Earthquake Engineering*, 4(4), 539-561.

Chapman, M. C. (1999). “On the use of elastic input energy for seismic hazard analysis.” *Earthquake Spectra*, 15(4), 607-635.

Chopra, A. K., and Chintanapakdee, C. (2004). “Evaluation of modal and FEMA pushover analyses: vertically “regular” and “irregular” generic frames.”

Earthquake Spectra. (Tech. Note) 20(1), 255-271.

Chopra, A. K, Goel, R. K, Chintanapakdee, C. (2004). "Evaluation of a modified MPA procedure assuming higher modes as elastic to estimate seismic demands." *Earthquake Spectra*, 20(3), 757-778.

Chopra, A. K., and Goel, R. (2002). "A modal pushover analysis procedure for estimating seismic demands for buildings." *Earthquake Engineering and Structural Dynamics*, 31, 561-582.

Chou, C. C., and Uang, C. M. (2000). "Establishing absorbed energy spectra-an attenuation approach." *Earthquake Engineering and Structural Dynamics*, 29, 1441-1455.

Chou, C. C., and Uang, C. M. (2003). "A procedure for evaluation of seismic energy demand of framed structures." *Earthquake Engineering and Structural Dynamics*, 32, 229-244.

Computers and Structures Inc. (2005). *SAP2000: Integrated Software for Structural Analysis and Design*, CSI Berkeley, CA. URL: http://csiberkeley.com

Costa, A. G., Oliveria, C. S., and Duarte, R. T. (1988). "Influence of vertical irregularities on seismic response of buildings." *Proc. of the 9th WCEE*, Tokyo, Japan, 5, 491-496.

Das, S., and J. M., Nau (2003). "Seismic design aspects of vertically irregular reinforced concrete buildings." *Earthquake Spectra*, 19(3), 455-477.

Decanini, L. D., and Mollaioli, F. (2001). "An energy-based methodology for the assessment of seismic demand." *Soil Dynamics and Earthquake Engineering*, 21(2), 113-37.

Eberhard, M. O., and Sozen, M. A. (1993). "Behavior-based method to determine design shear in earthquake-resistant walls." *Journal of the Structural Division*, ASCE, 119(2), 619-640.

El-Bahy, A., Kunnath, S. K., Stone, W. C. and Taylor, A. W. (1999). "Cumulative seismic damage of circular bridge columns." *ACI Structural Journal*, 96(4), 633-641.

Elnashai,A. S. (2000). "Advanced inelastic (pushover) analysis for seismic design and assessment." *The G. Penelis Symposium,* Thessaloniki, Greece.

Estava, L. (1992). "Nonlinear seismic response of soft first-story buildings subjected to narrow-band accelerograms", *Earthquake Spectra*. 8(3), 373-389.

Fajfar, P., and Fischinger, M. (1988). "N-2 – A method for nonlinear seismic analysis of regular structures." *Proceedings of the 9th US National Conference on Earthquake Engineering*, Tokyo-Kyoto, Japan.

Fajfar, P. (1992). "Equivalent ductility factors, taking into account low-cycle fatigue.", *Earthquake Engineering and Structural Dynamics*, 23, 507-521.

Fajfar, P., and Vidic, T. (1994). "Consistent inelastic design spectra: hysteretic and input energy." *Earthquake Engineering and Structural Dynamics*, 23, 523-537.

FEMA-350 (2000). *Recommended Seismic Design Criteria for New Steel Moment-Frame Buildings*, Developed by the SAC Joint Venture for the Federal Emergency Management Agency, Washington D.C.

Freeman, S. A. (1978). "Prediction of response of concrete buildings to severe earthquake motion." *Douglas McHenry Int. Symp. on Concrete and Concrete Structures*, ACI SP-55, American Concrete Institute, Detroit, 589-605.

Galesorkhi, R., Gouchon, J. (2000). "Near-source effects and correlation to recent recorded data." *Proc. of the 6th U.S. National Conference on Earthquake Engineering*, Seattle, WA.

Goel, S. C., and Berg, G. V. (1968). "Inelastic earthquake response of tall steel frames." *J. Struct. Div.* ASCE, 94, 1907-1934.

Goel, R. K, Chopra A. K. “Evaluation of modal and FEMA pushover analyses: SAC buildings.” *Earthquake Spectra,* 20(1), 225-254.

Gupta, B., and Kunnath, S. K. (2000). “Adaptive spectra-based pushover procedure for seismic evaluation of structures.” *Earthquake Spectra*, 16(2), 367-392.

Hall, J. F., Heaton, T. H., Halling, M. W., and Wald, D. J. (1995). “Near-source ground motion and its effects on flexible buildings.” *Earthquake Spectra*, 11(4), 569–605.

Heaton, T. H., Hall, J. F., Wald, D. J., and Halling, M. W. (1995). “Response of high-rise and base-isolated buildings to a hypothetical MW 7.0 blind thrust earthquake.” *Science,* 267, 206–211.

Hernandez-Montes E., Kwon, O. S., and Aschheim, M. A. (2004). “An energy based formulation for first and multiple-mode nonlinear static (Pushover) analyses.” *Journal of Earthquake Engineering*, 8 (1), 69-88.

Housner, G. W. (1956). “Limit design of structures to resist earthquakes.” *Proc. of the 1st World Conf. Earthquake Eng*., Berkeley Calif.

Humar, J., and Wright, E. (1977). “Earthquake response of steel-framed multistory buildings with set-backs.” *Earthquake Engineering and Structural Dynamics,* 5, 15-39.

International Conference of Building Officials (ICBO) (1973). *Uniform Building Code*, Whittier, CA.

International Conference of Building Officials (ICBO) (1988). *Uniform Building Code,* Whittier, CA.

International Conference of Building Officials (ICBO) (1997). *Uniform Building Code*, Whittier, CA.

International Conference of Building Officials (ICBO) (2000). *International Building Code*, Whittier, CA.

Iwan, W. D., Moser, M. A., and Peng, C. Y. (1985). ”Some observations on strong-motion earthquake measurements using a digital accelerograph,” *Bull. Seismol. Soc. of Am..*, 75, 1225-1246.

Iwan, W. D., Chen, X. D., 1994. Important near-field ground motion data from the Landers earthquake, *Proc. of the 10th European Conference on Earthquake Engineering*, Vienna, Austria, Aug. 28 - Sept. 2.

Iwan, W. D. (1997). “Drift spectrum: measure of demand for earthquake ground motions.” *J. Struct. Eng.,* ASCE, 123(4), 397–404

Iwan, W. D. (1999). “Implications of near-fault ground motion for structural design.” *US-Japan Workshop on Performance-Based Earthquake Engineering Methodology for RC Building Structures*, Maui, Hawaii (available from PEER, UC Berkeley).

Jan, T. S., Liu, M. W., Kao, Y. C. (2004). “An upper-bound pushover analysis procedure for estimating seismic demands of high-rise buildings.” *Engineering Structures*, 26, 117-128.

Kalkan, E., Adalier, K., and Pamuk, A. (2004). “Near field effects and engineering implications of recent earthquakes in Turkey.” *Proc. of the 5th International Conference on Case histories in Geotechnical Engineering*, New York, NY April 13-17.

Kalkan, E., and Kunnath S. K. (2004). “Lateral load distribution in nonlinear static procedures for seismic design.” *ASCE Structures 2004 Congress*, Nashville, TN.

Krawinkler, H. (1987). “Performance assessment of steel components.” *Earthquake Spectra*, 3, 27-41.

Krawinkler, H., and Seneviratna, G. D. P. K. (1998). “Pros and cons of a pushover analysis for seismic performance evaluation.” *Engineering Structures*, 20(4-6), 452-464.

Krawinkler, H., and Alavi, B. (1998). “Development of improved design procedures for near-fault ground motions.” *SMIP 98, Seminar on Utilization of Strong Motion Data*, Oakland, CA.

Krawinkler, H., and Al-Ali, A. (1996). “Seismic demand evaluation for a 4-story steel frame structure damaged in the Northridge earthquake.” *The Structural Design of Tall Buildings*, 5 (1), 1-27.

Kunnath, S. K., and Gupta, S. K. (2000). “Validity of deformation demand estimates using nonlinear static procedures.” *US-Japan Workshop on Performance-Based Earthquake Engineering Methodology for RC Building Structures*. Sapporo, Japan.

Kunnath, S. K., and John, Jr. A. (2000). “Validity of static procedures in performance-based seismic design.” *Proc. of the ASCE Structures Congress*, Philadelphia, May.

Kunnath, S. K, Nghiem Q., El-Tawil, S. (2004). “Modeling and response prediction in performance-based seismic evaluation: case studies of instrumented steel moment-frame buildings.” *Earthquake Spectra*, 20(3), 883-915.

Kunnath, S. K. (2004). “Identification of modal combinations for nonlinear static analysis of building structures.” Computer-*Aided Civil and Infrastructure Engineering*, 19, 282-295.

Kunnath, S. K., and Chai, R. Y. H. (2004). “Cumulative damage-based inelastic cyclic demand spectrum.” *Earthquake Engineering and Structural Dynamics*, 33, 499-520.

Kuwamura, H., and Galambos, T. V. (1989). “Earthquake load for structural reliability.” *Journal of Structural Engineering*, ASCE, 115, 1446-62.

Lawson, R. S. and Krawinkler, H. (1995). “Cumulative damage potential of seismic ground motion.” *Prof. of the 11th World Conference on Earthquake Engineering*, Wien: Balkema, 1079-86.

Leelataviwat, S., Goel, S. C., and Stojadinovic, B. (2002). “Energy-based seismic design of structures using yield mechanism and target drift.” *J. Struct. Eng*., ASCE, 28(8), 1046-1054.

Mahin, S. A., and Lin, J. (1983). *Construction of inelastic response spectrum for single degree of freedom system*, Report No. UCB/EERC-83/17, Earthquake Engineering Research Center, Berkeley, Calif.

Makris, N., Chang, S. (2000). “Effect of viscous, viscoplastic and friction damping on the response of seismic isolated structures”, *Earthquake Engineering and Structural Dynamics*, 29, 85-107.

Makris, N., and Black, C. (2004). ”Evaluation of peak ground velocity as a 'good' intensity measure for near-source ground motions.” *Journal of Engineering Mechanics*, ASCE, 130(9), 1032-1044.

Mander, J. B., and Cheng, C. T. (1995). “Renewable hinge detailing for bridge columns.” *Pacific Conference on Earthquake Engineering*, Melbourne, Australia.

Manfredi, G., Polese, M., and Cozenza, E. (2000). “Cyclic demand in the near-fault area.” *Proc. of the 6th U.S. National Conference on Earthquake Engineering*, Seattle, WA.

MathWorks (2001). MATLAB – Version 6.1. The MathWorks Inc., Natick, MA.

Mavroeidis, G. P., Papageorgiou, A. S. (2003). “A mathematical expression of near-fault ground motions.” *Bull. Seismol. Soc. of Am.*, 93 (3), 1099-1131.

Mavroeidis, G. P., Dong, G., and Papageorgiou, A. S. (2004). “Near-fault ground motions, and the response of elastic and inelastic single-degree-freedom (SDOF) systems.” *Earthquake Engineering and Structural Dynamics*, 33, 1023-1049.

McCabe, S. L., and Hall, W. J. (1989). “Assessment of seismic structural damage.” *J. Str. Eng.*, ASCE, 115, 2166-2183.

Minami, T., and Osawa, Y. (1988). “Elastic-plastic response spectra for different hysteretic rules.” *Earthquake Engineering and Structural Dynamics,*16, 555-568.

Ministry of Land, Infrastructure and Transport (2001). *Design Example and Commentary for the Calculation of Response and Limit Strength.* (In Japanese).

Miranda, E., and Akkar, S. D. (2002) “Evaluation of approximate method to estimate target displacements in PBEE.” *The Fourth U.S. - Japan Workshop on Performance-Based Earthquake Engineering Methodology for Reinforced Concrete Building Structures,* PEER Report No. 2002/21, 75-86.

Moehle, J. P. (1984). “Seismic response of vertically irregular structures.” *J. Struct. Div*. 110(9), 2002-2014.

Mwafy, A. M., and Elnashai, A. S. (2001). “Static pushover versus dynamic collapse analysis of RC buildings.” *Engineering Structures,* 23(5), 407-424.

Ordaz, M., Huerta, B., and Reinoso, E. (2002). “Exact computation of input-energy spectra from fourier amplitude spectra.” *Earthquake Engineering and Structural Dynamics,* 32(4), 597-605.

OpenSees (2005). *Open System for Earthquake Engineering Simulation*, URL: http://opensees. berkeley.edu.

Otani, S., and Ye, L. (1999). “Maximum seismic displacement of inelastic systems based on energy concept.” *Earthquake Engineering and Structural Dynamics*, 28, 1483-99.

Pamuk, A., Kalkan, E., and Ling, H. L. (2005). “Structural and geotechnical impacts of surface rupture on highway structures.” *Soil Dynamics and Earthquake Engineering*, 25(7), 581-589.

Park, Y. J. Ang, A. H. S., and Yen, Y. K. (1984). “Seismic damage analysis and damage-limiting design of RC buildings.” *Civil Engineering Series*, UIUC.

Park, Y. J. and Ang, A. H. S. (1985). “Mechanistic seismic damage model for reinforced concrete.” *Journal of Structural Engineering* ASCE, 111 (ST4), 722-739.

Riddell, R. and Garcia, E. J. (2001). “Hysteretic energy spectrum and damage control.”, *Earthquake Engineering and Structural Dynamics*, 30, 1791-1816.

Sasaki, K. K., Freeman, S. A. and Paret, T. F. (1998) “Multimode pushover procedure (mmP) – a method to identify the effects of higher modes in a pushover analysis.” *Proc. 6th US National Conference on Earthquake Engrg*., Seattle, WA.

Sasani, M., and Bertero, V. V. (2000). “Importance of severe pulse-type ground motions in performance-based engineering: historical and critical review.” *Proc. of the 12th World Conf. on Eq. Eng.*, New Zealand.

Satyarno, I., Carr, A. J., and Restrepo, J. (1998). “Refined pushover analysis for the assessment of older reinforced concrete buildings.” Proc. New Zealand National Society for Earthquake Engineering, Technical Conference, Waiarakei, 75-82.

SEAOC (2000). *Seismic design manual, Volume III, – Building Design Examples: Steel Concrete and Cladding*, Structural Engineers Association of California, Sacramento, CA.

Shoji, Y., Tanii, K., and Kamiyama, M. (2005). “A study on the duration and amplitude characteristics of earthquake ground motions.” *Soil Dynamics and Earthquake Engineering*, (article in press).

Somerville, P. G., and Smith, N. F., Graves, R. W., and Abrahamson, N. A. (1997). “Modification of empirical strong ground motion attenuation relations to include the amplitude and duration effects of rupture directivity.” *Seismological Research Letters*, 68(1), 199-222.

Somerville, P., Smith, N., Punyamurthula, S., and Sun., J. (1997). *Development of ground motion time histories for phase 2 of the FEMA/SAC steel project*, Report No: SAC/BD-97-04.

Somerville, P. G. (1998). Development of an improved representation of near-fault ground motions, *SMIP98 Proceedings of the Seminar on Utilization of Strong-Motion Data*, Oakland, CA, Sept. 15, California Division of Mines and Geology, Sacramento, 1-20.

Sucuoglu, H., Yucemen, S., Gezer, A., and Erberik, A. (1998). "Statistical evaluation of the damage potential of earthquake ground motions.", *Structural Safety*, 20, 357-378.

Sucuoglu, H., and Erberik, A. (2004). "Energy-based hysteresis and damage models for deteriorating systems.", *Earthquake Engineering and Structural Dynamics*, 33, 69-88.

Takewaki, I. (2004). "Bound of earthquake input energy." *J. Struct. Engrg*., ASCE, 130, 1289-1297.

Tembulkar, J. M., and Nau, J. M. (1987). "Inelastic modeling and seismic energy disspation.", *J. Str. Eng.*, ASCE, 113, 1373-1377.

Teran-Gilmore, A. (1998). "A parametric approach to performance-based numerical seismic design.", *Earthquake Spectra*, 14(3), 501-520.

Teran-Gilmore, A., and Jirsa, J. O. (2005). "A damage model for practical seismic design that accounts for low cycle fatigue." *Earthquake Spectra*, 21(3), 803-832.

Trifunac, M. D., and Brady, A. G. (1975). "On the correlation of seismic intensity scales with the peaks of recorded ground motion.", *Bulletin of the Seismological Society of America*, 65, 139-62.

The Ministry of Land, Infrastructure and Transport (2001). *Design example and commentary for the calculation of response and limit strength.* (In Japanese)

Tjhin, T., Aschheim, M., and Hernandez-Montes, E. (2004). "Estimates of peak roof displacement using equivalent single degree of freedom systems." *Journal of Structural Engineering* (Tech. Note), 131(3), 517-522.

Tso, W. K. and Moghadam, A. S. (1998). “Pushover procedure for seismic analysis of buildings.” *Progress in Structural Engineering and Materials*, 1(3), 337-344.

Uang, C. M. and Bertero, V. V. (1990). “Evaluation of seismic energy in structures.” *Earthquake Engineering and Structural Dynamics*, 19, 77-90.

Uang, C. M., Yu, Q. S., Sadre, A., Youseff, N., and Vinkler, J. (1997). “Seismic response of an instrumented 13-story steel frame building damaged in the 1994 Northridge Earthquake.” *Earthquake Spectra* 13 (1), 131-149.

Valmundsson, E. G., and Nau, J. M. (1997). “Seismic response of building frames with vertical structural irregularities”, *J. Struct. Engrg*. 123(30), 30-41.

Wight, J. K., Burak, B., Canbolat, B. A., and Liang, X. (1999). *Modeling and Software Issues in Pushover Analysis of RC Structures*. Report Peer-1999/10, US-Japan Workshop on Performance-Based Earthquake Engineering Methodology for Reinforced Concrete Building Structures, Pacific Earthquake Engineering Research Center, Berkeley, CA.

Williams, M. S., and Sexsmith, R. G. (1995). “Seismic damage indices for concrete structures: a state-of-the-art review.” *Earthquake Spectra*, 11(2), 319-350.

Wood, S. L. (1992). “Seismic response of R/C frames with irregular profiles.” *J. Struct. Engrg*. 118(2), 545-566.